

Rui Lima
Yohsuke Imai
Takuji Ishikawa
Mónica S. N. Oliveira *Editors*

Visualization and Simulation of Complex Flows in Biomedical Engineering

Lecture Notes in Computational Vision and Biomechanics

Volume 12

Series Editors

João Manuel R. S. Tavares, Porto, Portugal
R. M. Natal Jorge, Porto, Portugal

Editorial Advisory Board

Alejandro Frangi, Sheffield, UK
Chandrajit Bajaj, Austin, USA
Eugenio Oñate, Barcelona, Spain
Francisco Perales, Palma de Mallorca, Spain
Gerhard A. Holzapfel, Stockholm, Sweden
J. Paulo Vilas-Boas, Porto, Portugal
Jeffrey A. Weiss, Salt Lake City, USA
John Middleton, Cardiff, UK
Jose M. García Aznar, Zaragoza, Spain
Perumal Nithiarasu, Swansea, UK
Kumar K. Tamma, Minneapolis, USA
Laurent Cohen, Paris, France
Manuel Doblaré, Zaragoza, Spain
Patrick J. Prendergast, Dublin, Ireland
Rainald Lohner, Fairfax, USA
Roger Kamm, Cambridge, USA
Shuo Li, London, Canada
Thomas J. R. Hughes, Austin, USA
Yongjie Zhang, Pittsburgh, USA

For further volumes:

<http://www.springer.com/series/8910>

The research related to the analysis of living structures (Biomechanics) has been a source of recent research in several distinct areas of science, for example, Mathematics, Mechanical Engineering, Physics, Informatics, Medicine and Sport. However, for its successful achievement, numerous research topics should be considered, such as image processing and analysis, geometric and numerical modelling, biomechanics, experimental analysis, mechanobiology and enhanced visualization, and their application to real cases must be developed and more investigation is needed. Additionally, enhanced hardware solutions and less invasive devices are demanded.

On the other hand, Image Analysis (Computational Vision) is used for the extraction of high level information from static images or dynamic image sequences. Examples of applications involving image analysis can be the study of motion of structures from image sequences, shape reconstruction from images and medical diagnosis. As a multidisciplinary area, Computational Vision considers techniques and methods from other disciplines, such as Artificial Intelligence, Signal Processing, Mathematics, Physics and Informatics. Despite the many research projects in this area, more robust and efficient methods of Computational Imaging are still demanded in many application domains in Medicine, and their validation in real scenarios is matter of urgency.

These two important and predominant branches of Science are increasingly considered to be strongly connected and related. Hence, the main goal of the LNCV&B book series consists of the provision of a comprehensive forum for discussion on the current state-of-the-art in these fields by emphasizing their connection. The book series covers (but is not limited to):

- Applications of Computational Vision and Biomechanics
- Biometrics and Biomedical Pattern Analysis
- Cellular Imaging and Cellular Mechanics
- Clinical Biomechanics
- Computational Bioimaging and Visualization
- Computational Biology in Biomedical Imaging
- Development of Biomechanical Devices
- Device and Technique Development for Biomedical Imaging
- Digital Geometry Algorithms for Computational Vision and Visualization
- Experimental Biomechanics
- Gait & Posture Mechanics
- Multiscale Analysis in Biomechanics
- Neuromuscular Biomechanics
- Numerical Methods for Living Tissues
- Numerical Simulation
- Software Development on Computational Vision and Biomechanics
- Grid and High Performance Computing for Computational Vision and Biomechanics
- Image-based Geometric Modeling and Mesh Generation
- Image Processing and Analysis
- Image Processing and Visualization in Biofluids
- Image Understanding
- Material Models
- Mechanobiology
- Medical Image Analysis
- Molecular Mechanics
- Multi-Modal Image Systems
- Multiscale Biosensors in Biomedical Imaging
- Multiscale Devices and Biomems for Biomedical Imaging
- Musculoskeletal Biomechanics
- Sport Biomechanics
- Virtual Reality in Biomechanics
- Vision Systems

Rui Lima · Yohsuke Imai
Takuji Ishikawa · Mónica S. N. Oliveira
Editors

Visualization and Simulation of Complex Flows in Biomedical Engineering

 Springer

Editors

Rui Lima
ESTiG, Polytechnic Institute of Bragança
Bragança
Portugal

and

CEFT, Faculdade de Engenharia da
Universidade do Porto (FEUP)
Porto
Portugal

Yohsuke Imai
Department of Biomedical Engineering
and Robotics, Graduate School
of Biomedical Engineering
Tohoku University
Sendai
Japan

Takuji Ishikawa
Department of Bioengineering
and Robotics, Graduate School
of Engineering
Tohoku University
Sendai
Japan

Mónica S. N. Oliveira
James Weir Fluids Lab, Department of
Mechanical and Aerospace Engineering
University of Strathclyde
Glasgow
UK

ISSN 2212-9391

ISBN 978-94-007-7768-2

DOI 10.1007/978-94-007-7769-9

Springer Dordrecht Heidelberg New York London

ISSN 2212-9413 (electronic)

ISBN 978-94-007-7769-9 (eBook)

Library of Congress Control Number: 2013949598

© Springer Science+Business Media Dordrecht 2014

This work is subject to copyright. All rights are reserved by the Publisher, whether the whole or part of the material is concerned, specifically the rights of translation, reprinting, reuse of illustrations, recitation, broadcasting, reproduction on microfilms or in any other physical way, and transmission or information storage and retrieval, electronic adaptation, computer software, or by similar or dissimilar methodology now known or hereafter developed. Exempted from this legal reservation are brief excerpts in connection with reviews or scholarly analysis or material supplied specifically for the purpose of being entered and executed on a computer system, for exclusive use by the purchaser of the work. Duplication of this publication or parts thereof is permitted only under the provisions of the Copyright Law of the Publisher's location, in its current version, and permission for use must always be obtained from Springer. Permissions for use may be obtained through RightsLink at the Copyright Clearance Center. Violations are liable to prosecution under the respective Copyright Law. The use of general descriptive names, registered names, trademarks, service marks, etc. in this publication does not imply, even in the absence of a specific statement, that such names are exempt from the relevant protective laws and regulations and therefore free for general use.

While the advice and information in this book are believed to be true and accurate at the date of publication, neither the authors nor the editors nor the publisher can accept any legal responsibility for any errors or omissions that may be made. The publisher makes no warranty, express or implied, with respect to the material contained herein.

Printed on acid-free paper

Springer is part of Springer Science+Business Media (www.springer.com)

Preface

Over the years, flow visualization techniques have been applied in an effort to make the invisible visible with the help of experimental and computational technology. These tools have become indispensable to understand, and be able to control, the flow behavior of different types of complex biological fluids (e.g., DNA solutions, microorganisms, blood, and other physiological fluids) in living systems and biomedical devices. This book focuses on the most recent advances in visualization and simulation methods to understand the flow behavior of complex fluids used in biomedical engineering and other related fields, including mechanical, chemical, and materials engineering. It considers the physiological flow behavior in large arteries, microcirculation, respiratory systems, and in biomedical microdevices.

This book is aimed mainly at graduate students and researchers in the field of bioengineering seeking to provide a better understanding of the current state of the art and hopefully encourage the readers to grow their understanding beyond the specific topics addressed here. The book is composed of 13 chapters organized into three main sections. The first section of the book presents numerical studies on the hemodynamics at the macro-scale level. The second part covers *in vivo*, numerical, and *in vitro* studies applied to hemodynamics at the micro- and cellular-scale. The last part of the book addresses the study of ciliary flow by using both numerical and *in vivo* methods.

Rui Lima
Takuji Ishikawa
Yohsuke Imai
Mónica S. N. Oliveira

Contents

A Survey of Quantitative Descriptors of Arterial Flows	1
Diego Gallo, Giuseppe Isu, Diana Massai, Francesco Pennella, Marco A. Deriu, Raffaele Ponzini, Cristina Bignardi, Alberto Audenino, Giovanna Rizzo and Umberto Morbiducci	
Fluid–Structure Interaction Modeling of Patient-Specific Cerebral Aneurysms	25
Kenji Takizawa and Tayfun E. Tezduyar	
A Full-Eulerian Approach for the Fluid–Structure Interaction Problem	47
Satoshi Ii, Kazuyasu Sugiyama, Shu Takagi and Yoichiro Matsumoto	
Physiological Significance of Cell-Free Layer and Experimental Determination of its Width in Microcirculatory Vessels	75
Bumseok Namgung, Leo Hwa Liang and Sangho Kim	
Computational Simulation of NO/O₂ Transport in Arterioles: Role of Cell-Free Layer	89
Seungkwan Cho, Swe Soe Ye, Hwa Liang Leo and Sangho Kim	
Flow-Induced Deformation of a Capsule in Unbounded Stokes Flow	101
Toshihiro Omori, Takuji Ishikawa, Yohsuke Imai and Takami Yamaguchi	
Cell-Free Layer (CFL) Measurements in Complex Geometries: Contractions and Bifurcations	119
Susana Novais, Diana Pinho, David Bento, Elmano Pinto, Tomoko Yaginuma, Carla S. Fernandes, Valdemar Garcai, Ana I. Pereira, José Lima, Maite Mujika, Ricardo Dias, Sergio Arana and Rui Lima	

Image Processing in the Tracking and Analysis of Red Blood Cell Motion in Micro-Circulation Experiments.	133
Ana João and Alberto Gambaruto	
Flow of Red Blood Cells Suspensions Through Hyperbolic Microcontractions	151
Vera Faustino, Diana PINHO, Tomoko Yaginuma, Ricardo C. Calhelha, Geyong M. Kim, Sergio Arana, Isabel C. F. R. Ferreira, Mónica S. N. Oliveira and Rui Lima	
Responses of Living Cells to Hydrodynamic Stimuli Due to Fluid Flow	165
Naoya Sakamoto	
The Effect of a Static Magnetic Field on the Flow of Iron Oxide Magnetic Nanoparticles Through Glass Capillaries.	181
N. Pereira, M. Mujika, S. Arana, T. Correia, A. M. T. Silva, H. T. Gomes, P. J. Rodrigues and R. Lima	
Three-Dimensional Simulations of Ciliary Flow	197
Raymond Quek, Kian Meng Lim and Keng Hwee Chiam	
Flow on the Surface of the Tracheal Lumen by Ciliary Motion of Asymmetric Axonemal Structures	219
Hironori Ueno	
Index	237

A Survey of Quantitative Descriptors of Arterial Flows

Diego Gallo, Giuseppe Isu, Diana Massai, Francesco Pennella, Marco A. Deriu, Raffaele Ponzini, Cristina Bignardi, Alberto Audenino, Giovanna Rizzo and Umberto Morbiducci

Abstract Knowledge of blood flow mechanics is a critical issue (1) for an in depth understanding of the relationships between hemodynamic factors and arterial homeostasis and (2) for the identification of those flow features that lead to changes in the function and health of vessels. While from one side there is clear evidence that regions of disrupted flow are correlated to, e.g., the localization of atherosclerosis, the development of aneurysms and non-physiological transport of

D. Gallo (✉) · G. Isu · D. Massai · F. Pennella · M. A. Deriu · C. Bignardi · A. Audenino · U. Morbiducci

Department of Mechanics and Aerospace Engineering, Politecnico di Torino, 24 Corso Duca degli Abruzzi 10129, Turin, Italy
e-mail: diego.gallo@polito.it

G. Isu
e-mail: giuseppe.isu@polito.it

D. Massai
e-mail: diana.massai@polito.it

F. Pennella
e-mail: francesco.pennella@polito.it

M. A. Deriu
e-mail: marco.deriu@polito.it

C. Bignardi
e-mail: cristina.bignardi@polito.it

A. Audenino
e-mail: alberto.audenino@polito.it

U. Morbiducci
e-mail: umberto.morbiducci@polito.it

R. Ponzini
HPC and Innovation Unit, CINECA, Via R. Sanzio, 4 20090, Milan, Segrate, Italy

G. Rizzo
IBFM, Research National Council, LITA Building—Via Fratelli Cervi, 93 20090, Milan, Segrate, Italy

species, on the opposite cause-effect links still do not emerge clearly. To allow for a more effective and valuable understanding of blood flow structures and mechanisms in complex four-dimensional cardiovascular flows, in recent years a large number of hemodynamic parameters have surfaced in the literature, enabling the understanding of arterial hemodynamics and of the role of streaming blood in the development of pathological events. In this work, a survey of the currently adopted methods to characterize blood flow structures in arteries is presented and open questions (1) on their clinical utility and (2) on the inherent limitations in their *in silico* and *in vivo* application are discussed.

1 Introduction

The study of cardiovascular flows is of great interest because of the role of hemodynamics in cardiovascular diseases, the single largest cause of death worldwide and responsible for more than half of mortality in the developed countries. Several tools were developed for the interpretation and analysis of arterial hemodynamics. As a first approach, the study of arterial hemodynamics has relied in the past on simplification of the physics of the problem. For example, in 1775 Euler developed a series of equations which are nowadays widely adopted for the study of pressure wave propagation phenomena in the vascular tree (Euler 1775), or Poiseuille's Law has been used to model and represent blood flow motion (therefore ignoring pulsatility and simplifying the blood velocity profile shaped as parabolic). Another contribution was given by Womersley, whose description of pulsating flows allows to model and represent more complex flow patterns than the simple parabolic shape (Womersley 1955).

By late 1960s, Caro and others (1969) had shown that the localization of vascular diseases at arterial branches and bends could be explained by the presence of complex blood flow patterns at these sites. Subsequent studies have shown that the local flow behaviour of blood is implicated in the formation of atherosclerotic plaques and of phenomena such as thrombogenesis, atherogenesis, endothelial damage, intimal thickening and hyperplasia (Karino and Goldsmith 1985; Ku et al. 1985; Giddens et al. 1993; Moore et al. 1994). The unfavourable hemodynamic environment is often referred to with the vague expression "disturbed flow", that is usually used to imply mechanisms such as (1) the modulation of the friction forces at the vascular luminal surface (Sun et al. 2007) and the consequent effects on endothelial functions, and (2) the regulation/alterations in the mass transfer and in the residence time near the wall of atherogenic particles.

In this context, the importance of the knowledge of accurate local blood flow factors emerged, clearly requiring for methods with the capability of characterizing the blood flow dynamics to ease the clinical interpretation of the disturbed flow. Thus, the research on the role of the hemodynamics in vascular disease could take advantage of methods of data reduction that allow quantitative assessments

and comparisons. A variety of hemodynamic descriptors has been proposed over the years to (1) reduce the inherent complexity of the four-dimensional blood flow fields, (2) simplify the understanding of the flow dynamics, and (3) quantify hemodynamic disturbances as potential indicators of vascular wall dysfunction.

In the past, the majority of the studies on this subject focused primarily on wall shear stress (WSS, i.e., the force per unit area the flowing blood exerts on the endothelial cells lining the vessel lumen) as quantitative indicator of disturbed flow (Ku et al. 1985; Giddens et al. 1993). A large variety of parameters based on WSS has been proposed over the years and employed in a relevant number of studies. Only recently the interest in the role played by the bulk flow in the development of the arterial disease has grown. Thus, descriptors with the capability of quantifying phenomena depending on the complexity of the blood flow in the bulk are of great interest as they can offer insights, complement, integrate and extend the information given by the WSS-based descriptors.

Here we present a review of the currently adopted methods to characterize and classify blood flow structures in arteries. After a brief introduction about the importance of WSS and its role in vascular wall pathologies, established descriptors based on WSS, proposed over the years to quantify flow disturbances, are presented. Then, the role of bulk flow in arterial hemodynamics is discussed and different descriptors used to characterize bulk flow dynamics are introduced. Finally, examples of the applications of the reviewed descriptors are reported and the utility and perspective use of the introduced hemodynamic descriptors in the clinical practice are discussed.

2 On the Importance of Wall Shear Stress (WSS)

The fluid forces acting on the vessels' walls are thought to be capable of stimulating the endothelium to produce several cellular factors that can inhibit or promote inflammatory events (Yoshizumi et al. 2003). In vitro and in vivo studies on endothelial cells have shown contrasting effects between laminar shear flow with a definite direction (e.g., as seen in the straight part of the arterial tree) and the "disturbed" shear (e.g., as seen at arterial branch points and curved regions) in terms of their signal transduction, gene expression, structure, and functions (Chien 2007; Chiu and Chien 2011). Evidence from in vitro and in vivo studies suggests that both low WSS and highly oscillatory patterns of WSS cause intimal wall thickening (Caro et al. 1969; Friedman et al. 1981; Ku et al. 1985; Glagov et al. 1988; Moore et al. 1994; Pedersen et al. 1997; Malek et al. 1999), as seen at sites with such characteristics as curvatures, bifurcations, tortuosity and branching (in general where flow velocity and shear stress are reduced and flow departs from unidirectional patterns) (De Bakey et al. 1985). WSS can change the morphology and orientation of the endothelial cell layer: endothelial cells subjected to a laminar flow with high levels of WSS tend to elongate and align in the direction of flow, whereas in areas of low and oscillatory WSS, endothelial cells look more

polygonal without a clear orientation, with a lack of organization of the cytoskeleton and intercellular junctional proteins (Galbraith et al. 1998). In addition, it has been hypothesized that low WSS and the resultant stagnation of blood permit prolonged contact of the vessel wall with platelets, granulocytes, and metabolites that influence vascular homeostasis (Glagov et al. 1988; Shaaban and Duerinckx 2000). An overview of the current knowledge on vascular mechanobiology from a cellular to a tissue scale is reported by Chiu and Chien (2011). Indeed, the importance of shear stress oscillation at the wall for the physiology of the mechanosensitive endothelial cells has been pointed out by several authors, often providing indices to quantify these occurrences.

2.1 Metrics for Quantitative Hemodynamics: Hemodynamic Wall Descriptors

Various metrics have been proposed over the years to quantify WSS disturbances by using metrics originally focused on WSS magnitude. The hemodynamic wall parameters (HWP) have then incorporated the information about spatial gradients of WSS and about the temporal variations of WSS time-varying profiles evaluating their harmonic content (Lee et al. 2009). Among the proposed HWPs, we report in the followings the most used ones.

1. Time Averaged Wall Shear Stress (TAWSS)

$$\text{TAWSS} = \frac{1}{T} \int_0^T |\mathbf{WSS}| \cdot dt \quad (1)$$

where T is the time interval during which the values of the WSS vector are measured. Low TAWSS values (lower than 0.4 N/m^2) are known to stimulate a proatherogenic endothelial phenotype and are associated with intima/media complex thickening, whereas moderate (greater than 1.5 N/m^2) TAWSS values induce quiescence and an atheroprotective gene expression profile (Malek et al. 1999). Higher TAWSS values (greater than $10 \div 15 \text{ N/m}^2$, relevant from $25 \div 45 \text{ N/m}^2$) can lead to endothelial trauma and hemolysis (Kessler 2002).

2. Oscillatory Shear Index (OSI)

$$\text{OSI} = 0.5 \left[1 - \left(\frac{\left| \int_0^T \mathbf{WSS} \cdot dt \right|}{\int_0^T |\mathbf{WSS}| \cdot dt} \right) \right] \quad (2)$$

OSI is used to identify regions on the vessel wall subjected to highly oscillating WSS directions during the cardiac cycle. Low OSI values occur at sites where flow disruption is minimal, whereas high OSI values (with a maximum of 0.5) highlight sites where the instantaneous WSS deviates from the main flow direction in a large fraction of the cardiac cycle, inducing perturbed endothelial

alignment (He and Ku 1996). Although the OSI can identify regions of flow reversal, it is insensitive to shear magnitude. Sites where the TAWSS is low may be characterized by significant OSI but not necessarily, indeed low shear can result from flow expansion, which may follow from pulsatility, without any local flow reversal. Similarly, strongly oscillatory flows can exhibit the same OSI as very slow flows with the same waveform. As stated by Himburg et al. (2004), it seems unlikely that endothelial cells sense OSI per se. Several investigators, using histological data (Keynton et al. 2001; Goubergrits et al. 2002), demonstrated that only the presence of low and oscillating WSS favours the atherosclerotic plaque formation, while if TAWSS is next to the physiological range ($1 \div 2 \text{ N/m}^2$), the intimal thickness is normal. These considerations suggest that OSI might better be employed in combination with other shear measures, rather than as a stand-alone index.

3. Relative Residence Time (RRT)

$$\text{RRT} = \frac{1}{(1 - 2 \cdot \text{OSI}) \cdot \text{TAWSS}} = \frac{1}{\left| \int_0^T \mathbf{WSS} \cdot dt \right|} \quad (3)$$

RRT is inversely proportional to the magnitude of the time-averaged WSS vector (i.e., the term in the numerator of the OSI formula). Himburg et al. (2004) demonstrated that the residence time of particles near the wall is proportional to a combination of OSI and TAWSS. RRT is simply another type of time-averaged WSS, but inverted and with a more tangible connection to the biological mechanisms underlying atherosclerosis (Himburg et al. 2004). Indeed, Lee and colleagues (Lee et al. 2009) recommended RRT as a robust single metric of “low and oscillatory” shear.

4. WSS Spatial Gradient (WSSG)

$$\text{WSSG} = \frac{1}{T} \int_0^T \sqrt{\left(\frac{\partial \mathbf{WSS}_p}{\partial p} \right)^2 + \left(\frac{\partial \mathbf{WSS}_n}{\partial n} \right)^2} \cdot dt \quad (4)$$

where p and n are the directions respectively parallel and normal to the direction of the time-averaged WSS vector. Thus, WSSG is calculated starting from the WSS gradient tensor components. Proposed by De Paola et al. (1992), the WSSG may be considered a marker of endothelial cell tension. Large sustained WSS gradients produce endothelium dysfunction due to the aggravating effects of spatially changing hemodynamic forces.

5. WSS Angle Gradient (WSSAG)

$$\text{WSSAG} = \frac{1}{T} \frac{D}{\pi} \int_0^T |\nabla \Phi_n| \cdot dt \quad (5)$$

where D is the vessel diameter, and Φ_n is the scalar field of WSS angle deviations:

$$\Phi_n = \arccos\left(\frac{\mathbf{WSS}_i \cdot \mathbf{WSS}_j}{|\mathbf{WSS}_i| |\mathbf{WSS}_j|}\right) \quad (6)$$

where \mathbf{WSS}_i is the WSS vector at the location of interest and subscript j is an index for the surrounding stress vectors. Longest and Kleinstreuer (2000) proposed the WSSAG to highlight regions exposed to large spatial variations in the mean WSS direction, irrespective of magnitude. Areas with high WSSG are thought to be related to intimal hyperplasia (Bunchanan and Kleinstreuer 1998): significant and sustained WSSAG values tend to handicap the endothelial cell response initiating the process of atherosclerosis.

6. Dominant Harmonic (DH)

$$\text{DH} = \max\left(F_{|\text{WSS}|}\left(n \frac{2\pi}{T}\right)\right), n \in \mathbf{N}^+ \quad (7)$$

where $F_{|\text{WSS}|}$ is the Fourier-transform of the time-varying waveform of the WSS magnitude and n is a positive integer. The DH is thus obtained through the Fourier decomposition of the WSS magnitude profiles along the cardiac cycle and it is defined as the harmonic with the highest amplitude. Himburg and Friedman (2006), proposing this descriptor, suggested that the frequency spectrum of WSS time-varying profiles could play a role in the atherosclerotic lesion development.

7. Harmonic Index (HI)

$$\text{HI} = \frac{\sum_{n=1}^{\infty} F_{|\text{WSS}|}\left(n \frac{2\pi}{T}\right)}{\sum_{n=0}^{\infty} F_{|\text{WSS}|}\left(n \frac{2\pi}{T}\right)}, n \in \mathbf{N}^+ \quad (8)$$

The descriptor HI, whose value ranges from zero to one, was proposed by Gelfand et al. (2006) as a measure of the relative contribution to the harmonic amplitude spectrum of non-stationary intensity to the overall signal intensity. In this way, it is possible to evaluate the relative contribution of the pulsatile component of the WSS magnitude.

For practical purposes, many of the proposed HWPs provide essentially the same information and therefore can be considered redundant. Lee et al. (2009), adopting a computational dataset made of 50 carotid bifurcation models, tested for correlations among a large variety of HWPs. Their comprehensive evaluation demonstrated that RRT can be used as single marker of low and oscillatory shear, and issues are questioned about the harmonic-based HWPs, related to their definition in the presence of strongly non-axial flows (Lee et al. 2009). Thus, we here iterate their recommendation to adopt RRT to localize areas of disturbed shear on the vessel wall.

3 On the Importance of Bulk Flow

Most mechanisms promoting degenerative phenomena and pathologies affecting vascular districts deal with three- and four-dimensional phenomena. In addition, the bulk flow plays a key role in determining WSS patterns. Notwithstanding, the focus of the most part of the studies in the literature is almost exclusively on WSS-based metrics as quantitative indicators of disturbed flow. In the past, the potential role of bulk flow in the development of arterial disease was scarcely investigated. This is partially due to the scarcity of robust quantitative descriptors of bulk flow with the ability of operating a reduction of the inherent complexity associated to four-dimensional flow fields in realistic geometries.

Recently, several studies both *in silico* and *in vitro* (Stonebridge et al. 1996; Grigioni et al. 2005; Morbiducci et al. 2007a, b; Fan et al. 2008; Chen et al. 2009; Liu et al. 2009; Zheng et al. 2009; Zhan et al. 2010) have renewed with quantitative results the presumption that arterial bulk flow could elicit the fluid-wall interaction processes leading to the onset of vessel wall pathologies (Ku and Giddens 1983; Caro et al. 1996; Stonebridge et al. 1996; Malek et al. 1999; Grigioni et al. 2005; Augst et al. 2007; Morbiducci et al. 2007a, b; Caro et al. 2009). These studies, in light of the observation that unfavourable effects like alterations in mass transfer and particle residence times are strictly related to bulk flow effects, especially when blood flow is complex, suggest that WSS-based analysis should be complemented by a quantitative description of the bulk flow and that such a description represents a potential source of information.

In order to investigate the relationships between particular blood flow patterns and physiopathological events, helicity has recently gained recognition as able to describe the arrangement of blood streams in complex patterns (Morbiducci et al. 2007b). The use of helicity to analyse bulk flow features has been applied by several groups to different cardiovascular districts (see for example Morbiducci et al. 2007b; Fan et al. 2008; Chen et al. 2009; Liu et al. 2009; Morbiducci et al. 2009a, 2010, 2011; Liu et al. 2010, 2011; Zhan et al. 2010; Lorenz et al. 2012). Helicity is a measure of the alignment of the velocity and the vorticity vectors (Moffatt 1969) and it represents the potential for helical flow, i.e., flow with a corkscrew-like pattern, to evolve. Helical flow is the product of the composition of translational and rotational motion and its role in vascular hemodynamics has long been debated.

In the past, it was postulated that helical flow has a relevant importance in the physiology of the vessel, preventing stagnation zones and flow separation at the arterial walls. In the 1990s, researchers put forward hypotheses on the theoretical advantages derived from helical blood flow (Stonebridge et al. 1996). Frazin et al. (1990) put forward the idea of a relationship between the shear forces caused by rotational flow and both the deposition of atherosclerotic plaque and the direction and extent of aortic dissection. In the aortic arch, Kilner et al. (1993) suggested that the stability induced by helical flow in the upper aortic arch spares this region from the tendency for plaques to form, whereas more unstable flow patterns

predispose to atherosclerosis; Bogren and Buonocore (1999) observed the presence of helical flow regardless the age of the volunteers. Houston and colleagues (Houston et al. 2003) found that carotid atheromatous disease is associated with a reduction in the prevalence of a systolic helical flow pattern in the aortic arch. Helical flow may also account for a significant amount of normal organ perfusion (Frazin et al. 1996) from branch vessels due to the centripetal spin (i.e., imparted tangential velocities) induced in blood. Moreover, an absence of aortic helical flow might be a predictor of renal impairment deterioration in patients with renal artery stenosis (Houston et al. 2004). In 2007, Morbiducci and colleagues (Morbiducci et al. 2007b), investigating the existence of a relationship between helical flow structures and vascular wall indexes of atherogenesis in aortocoronary bypass models, found that an arrangement of the flow field in helical patterns may elicit a damping in shear stress effects on the vessel wall. Chen and colleagues (Chen et al. 2009) found that intentional induction of helical flow in an endovascular stent reduced the size of the disturbed flow zones, enhanced the average wall shear stress, and lowered wall shear stress oscillations, which are adverse factors involved in the development of arterial restenosis after stent deployment; the same group (Liu et al. 2010) observed that the helical flow in the aorta may have great influence on the distribution of the luminal surface concentration of low density lipoproteins and, as a consequence, on the spatial distribution of atheromatous plaques. Very recently, Gallo and colleagues demonstrated that a high amount of helical flow suppresses the disturbed shear at the normal carotid bifurcation, but this beneficial effect is moderated when one direction of rotation is predominant in the flow field (Gallo et al. 2012a).

From a phenomenological viewpoint, an arrangement of the bulk flow in complex helical patterns might play a significant role in the tuning of the cells mechano-transduction pathways. It is likely that for highly helical flows, the conservation laws within the Navier–Stokes equation inhibit the transfer of helicity down the length scales, and thus the process through which energy is transferred (Ditlevsen and Giuliani 2000). As a result of this inhibition, helical energy may affect the focal contact between endothelial cell and the monocyte within the flow, i.e., helical structures could elicit the convective dispersion of monocytes within the vessel at all scales, due to the complex three-dimensional flow pattern. Furthermore, the stability induced by helical flow and the decrease in laterally directed forces may reduce turbulence in the tapering branching arterial tree and at stenoses (Caro et al. 2002). Several authors emphasize the existence of a relationship between helical flow patterns and transport phenomena affecting blood–vessel wall interaction (Pritchard et al. 1995); Hsiai et al. 2003; Morbiducci et al. 2007b; Zhan et al. 2010). These processes are fundamental to the initiation of inflammatory responses, due to alterations in the residence time of atherogenic particles (Caro et al. 1971; Friedman et al. 1987). Moreover, bulk flow structures are primarily responsible for mass transfer (Caro et al. 1969; Ma et al. 1997), in particular for those species within blood that take advantage of mixing induced by convection. For example, several studies identify the oxygen flux to the arterial wall to be another factor involved in the localization of atherogenesis (Santilli

et al. 1995; Sluimer et al. 2008), while recent studies has provided evidence for the existence of a relationship between shear-induced activation of platelets (Kroll et al. 1996) and metrics that give measures for the alignment of the local velocity and vorticity vectors (Morbiducci et al. 2009b; Massai et al. 2012).

According to these observations, it is clear that helical flow represents a natural feature of arterial hemodynamics and that a thorough understanding of the generation and disappearance of helical structures in the streaming blood is of great interest. In particular, helical flow could be used as a fluid dynamic signature for the identification of sites prone to fibrointimal thickening and atherosclerotic plaque formation (Gallo et al. 2012a).

3.1 Metrics for Quantitative Hemodynamics: Hemodynamic Bulk Flow Descriptors

Helicity can provide a better understanding of the role of pitches and torsions in the development of complex flow fields, describing and revealing the global organization of the flow.

By definition, the helicity $H(t)$ of a fluid flow confined to a domain D of three-dimensional Euclidean space \mathbf{R}^3 is the integrated internal product of the local velocity vector and the local vorticity vector, and, being related to the magnitude of the nonlinear term in the Navier–Stokes equation (and geometrically characterizing the knottedness of vortex lines), it has a great influence on the evolution and stability of both turbulent and laminar flows (Moffatt and Tsinober 1992).

$$H(\mathbf{x}, t) = \int_D \mathbf{v}(\mathbf{x}, t) \cdot \boldsymbol{\omega}(\mathbf{x}, t) dV = \int_D H_k(\mathbf{x}, t) dV \quad (9)$$

where $\mathbf{v}(\mathbf{x}, t)$ and $\boldsymbol{\omega}(\mathbf{x}, t)$ are the velocity and the vorticity vector, respectively, and their internal product H_k is the helicity density.

A useful indicator of how velocity field is oriented with respect to the vorticity field is given by the local value of the cosine of the angle between the velocity and vorticity vectors, obtained through the normalization of the helicity density H_k . In the past, the quantity Localized Normalized Helicity (LNH) has been proposed (Shtilman et al. 1985), defined as:

$$\text{LNH}(\mathbf{x}; t) = \frac{\mathbf{v}(\mathbf{x}; t) \cdot \boldsymbol{\omega}(\mathbf{x}; t)}{|\mathbf{v}(\mathbf{x}; t)| |\boldsymbol{\omega}(\mathbf{x}; t)|} = \cos \varphi(\mathbf{x}; t) \quad (10)$$

$$-1 \leq \text{LNH} \leq 1$$

where \mathbf{v} is the velocity vector, $\boldsymbol{\omega}$ the vorticity vector, \mathbf{x} is the position and t the time instant. The non-dimensional quantity LNH is the local value of the cosine of the angle $\varphi(\mathbf{x}; t)$, between the velocity and vorticity vectors: the absolute value of LNH can range between one, when the flow is purely helical, and zero, in general,

in presence of reflectional symmetry in the flow. Moreover, the sign of LNH is a useful indicator of the direction of rotation. Hence, LNH is a useful descriptor of changes in the direction of the rotation of flow into vessels during the cardiac cycle, because a local right/left-handed rotation can be identified by a change in sign of the local value of LNH.

The definition of the bulk flow quantities introduced in this section can be considered both as Eulerian or Lagrangian specifications of flow. In fact, a picture of the spatial distribution of them is known at each instant of time (i.e., they are function of position and time). On the other hand, they can be used to describe the dynamical path history of a fluid element, identified by its position at some initial time.

3.1.1 Eulerian Approach

Current in vivo (e.g., phase-contrast magnetic resonance imaging, PC MRI), in vitro (e.g., particle image velocimetry), and computational methods used for quantifying blood flow produce as output Eulerian velocity data, typically. The velocity field itself has limited clinical relevance, typically the interest relies in the transport of the fluid or in the forces produced by the fluid motion. The quantities defined in Eqs. 9 and 10 can be calculated in an Eulerian field, starting from the velocity field.

It is possible to define helicity bulk flow descriptors according to a Eulerian approach. Basic characteristics of helical structures, like their intensity, the balance between counter-rotating structures, and their size can be evaluated by using the following descriptors:

$$h_1 = \frac{1}{TV} \int_T \int_V H_k dV dt \quad (11a)$$

$$h_2 = \frac{1}{TV} \int_T \int_V |H_k| dV dt \quad (11b)$$

$$h_3 = \frac{h_1}{h_2} \quad (11c)$$

$$h_4 = |h_3| = \frac{|h_1|}{h_2} \quad (11d)$$

$$h_5 = \frac{\max(V_+, V_-)}{\min(V_+, V_-)} = \frac{V_d}{V_m} \quad (11e)$$

$$h_6 = \frac{\frac{1}{V_d} \int_T \int_{V_d} H_k dV dt}{\frac{1}{V_m} \int_T \int_{V_m} H_k dV dt} \quad (11f)$$

where V is the volume of fluid, V_+ (V_-) is the total volume of the helical structures rotating in the direction identified by the positive (negative) sign. The volumes V_+ and V_- identify the volume occupied by the dominant direction of rotation V_d and the volume occupied by the minor direction of rotation V_m . The descriptor h_1 is the time-averaged value of the helicity, normalized with respect to the volume of integration. By definition, h_1 equals 0 in the presence of reflectional symmetry in the fluid domain, for instance if the flow arrangement in the domain consists in symmetric counter-rotating helical structures, while when it has signed values, its sign indicates the predominant direction of rotation. The helicity intensity, given by the integration of the absolute value of H_k , defines descriptor h_2 and it is an indicator of the total amount of helical flow in the fluid domain, irrespective of direction. Descriptor h_3 is a non-dimensional quantity ranging between -1 and 1 : its value equals -1 when only left-handed helical structures are present in the domain, it equals $+1$ when only right-handed structures are present and it equals 0 in case of reflectional symmetry. The focus on the balance between counter-rotating structures, neglecting what is the major direction of rotation, is given by descriptor h_4 , defined as the absolute value of h_3 and thus ranging between 0 and $+1$. The descriptor h_5 is the ratio between the volumes of the helical structures in the dominant direction of rotation V_d and the minor direction of rotation V_m . The ratio of the helicity intensities in volumes V_d and V_m is given by descriptor h_6 .

This approach has been adopted in a very recent study (Gallo et al. 2012a, b). Adopting a computational dataset composed of 50 normal carotid bifurcations, they calculated the six descriptors h_i and explored the relationship between the helicity-based Eulerian descriptors and the overall burden of abnormal WSS. The regression analysis underlined the importance of two descriptors (h_2 and h_4) quantifying the total helicity intensity in the domain and the ratio between the helicity intensity of the counter-rotating helical structures. Thus, a high amount of helicity in the carotid bifurcation flow field is instrumental in suppressing flow disturbances. However this protective effect can be moderated when one direction of rotation is dominant in the flow field. Hence, the onset of helical flow into the carotid bifurcation could avoid atheroprone hemodynamics, contributing to limit flow separation leading to low and oscillatory shear (Gallo et al. 2012a).

The advantages of a Eulerian specifications of those bulk flow quantities reside mainly in the attractiveness of this approach for clinicians, due to its immediateness. Eulerian quantities in fact have a simpler definition, allows real-time analysis and can give a picture of the entire flow field. Although is often reasonable to infer the bulk fluid motion from inspection of the velocity data, a quantification of the flow structures in unsteady flows (i.e., when the time history of the velocity field has to be taken into account also) could be difficult and could result in misinterpretations.

3.1.2 Lagrangian Approach

Hemodynamic quantities such as residence times of individual fluid particles, particle deposition, and particle shear exposure can be evaluated according to Lagrangian specifications because they rely on knowledge of the dynamical path history of a fluid element, and the Lagrangian characterization identifies the element by its position at some initial time. They hence differ from other hemodynamic quantities such as WSS, which can be addressed using Eulerian specifications because a picture of the spatial distribution of these quantities is known at each instant of time (i.e., they are functions of position and time).

Since the very first eminent studies, in order to extract Lagrangian hemodynamic information, a one-way coupled Eulerian/Lagrangian method was proposed, in which the effect of a particle's motion on the surrounding flow field is neglected (Ehrlich and Friedman 1977; Perktold and Resch 1990): in this way the Lagrangian approach simply reduced to computing the particle trajectories from the pre-computed Eulerian flow field.

In principle, to model blood flow in large arteries, particle-seeding scheme reflecting the physiological distribution of blood corpuscles should be used. However, the concentration of particles required to model the physiological situation would present extreme computational demands: the concentrations make the computational cost of the particle motion modelling unfeasible (Tambasco and Steinman 2001, 2002). Hence, these limitations force to employ alternative approaches for the computation of meaningful path-dependent hemodynamic quantities for arterial models of blood flow. Among them, the most cost-effective seems to be the statistical approach, consisting of extracting the relevant quantities from ensemble averages over a sufficient set of particles.

In general, Lagrangian derived parameters can be used in the study in a wide range of arterial models of quantities of interest such as particle deposition, particle stress history (e.g., to investigate blood trauma) and, very recently, the level of pitch and torsion in the flow development, obtained through helicity (Hyun et al. 2000, 2001; Kleinstreuer et al. 2001, Tambasco and Steinman 2001, 2002; Hyun et al. 2004; Grigioni et al. 2005; Morbiducci et al. 2007a, b).

Recently a four-dimensional descriptor, the Helical Flow Index (HFI), has been introduced in order to get a "measure" of the helical structure in the blood flow. Originally developed and applied to computational models (Grigioni et al. 2005, Morbiducci et al. 2007a, b), and very recently tested in vivo on 4D PC-MRI measurements in the human aorta (Morbiducci et al. 2009a, 2011), the HFI represents the content of helical motion by clustering the information according to a Lagrangian analysis of the flow. Previous studies demonstrated that HFI is an effective synthetic flow descriptor of complex, fully four-dimensional flow fields (Morbiducci et al. 2007a, b, 2011).

Technically, the HFI is defined using the LNH as basic quantity. Considering the trajectory described by the generic particle k moving in a vessel, its dynamics can be characterized by means of the quantity:

$$hfi_k = \frac{1}{(t_k^{end} - t_k^{start})} \int_{t_k^{start}}^{t_k^{end}} |\text{LNH}_k(\zeta)| d\zeta \quad (12)$$

Equation 12 is the integral sum, in time, of the LNH values experienced by the k -th particle moving during the time interval $(t_k^{end} - t_k^{start})$.

Over the N_p ($k = 1, \dots, N_p$) particles moving in the fluid domain, the HFI can be calculated as:

$$\text{HFI} = \frac{1}{N_p} \sum_{k=1}^{N_p} hfi_k \quad (13)$$

$$0 \leq \text{HFI} \leq 1$$

The previous hemodynamic quantities (Eqs. 12, 13) are considered Lagrangian specifications of flow since they depend on knowledge of the dynamical path history of a piece of fluid element.

The Lagrangian approach, that allows to extract path dependent quantities tracking the fluid particle, in conjunction with visualization techniques, is particularly useful for characterizing unsteady flow patterns, and for highlighting important hemodynamic features. Particle traces offer three-dimensional visualization of flow patterns which have proven to be useful tools to interrogate complex flow fields in vessels and in general to reveal global organization of the flow (Steinman 2000; Morbiducci et al. 2007a, b; 2009a, b), making easier to detect by visual inspection the relevant flow features and to understand the true fluid motion. The definition of path dependent quantities allows the investigation of dynamical path histories and could offer a practical way to divide the particles into groups regardless of position (e.g., using threshold for visualization). On the other hand, the main disadvantages of a Lagrangian approach are a high computational cost, the convectiveness of the particles, resulting in a poor control over the zone of investigation that is determined by the particle motion and accumulation. Furthermore, the influence of particle distributions and of particle seeding schemes on quantities of interest is poorly investigated. Finally, adopting a Lagrangian approach it is difficult to get a complete picture of the flow at specific time instants.

Alternatively to fluid motion tracking by computing particle trajectories through velocity data integration, it is worth mentioning the recently proposed use of the finite-time Lyapunov exponent (FTLE) to characterize flow kinematics of unsteady flows. The FTLE measures the maximum linearized growth rate of the distance between initially adjacent fluid particles, tracked over a finite time interval (Haller 2001), and its calculation yields a scalar field derived from fluid trajectories. Ridges of local maxima in the FTLE fields are able to reveal flow features, identifying Lagrangian coherent structures (Shadden et al. 2005; Shadden and Taylor 2008). For example, Shadden and Taylor (2008) and Vetel et al. (2009) adopted this approach to visualize helical structures, vortex boundaries, flow recirculation and flow separation regions in the human carotid artery.

4 Hemodynamic Descriptors: Examples of *in silico* and *in vivo* Applications, Their Significance and Limitations

Nowadays, the coupling of medical imaging and computational fluid dynamics (CFD) is used to obtain a realistic detailed description of the local hemodynamics. This kind of image-based analysis is applied to study vascular districts with marked predilection to vascular pathologies (Taylor and Steinman 2010), like the carotid artery and the thoracic aorta. In the followings, we report two example of image-based in *silico* and *in vivo* calculation of the introduced hemodynamic descriptors.

As a first example, we adopted the anatomically realistic computational model of a human carotid artery developed by Morbiducci and colleagues (Morbiducci et al. 2010). Exhaustive details about the geometry reconstruction, the computational setup and the CFD simulations can be found in (Morbiducci et al. 2010).

In Fig. 1 we show different ways of visualizing the flow patterns within the vessel. All the panels are representations of the same data, but the information conveyed is different. From the observation of Fig. 1, it can be noticed that OSI (panel A), TAWSS (panel B) and RRT (panel C) capture flow disturbances at the same sites of the bifurcation, highlighting the bifurcation bulb site as the surface area exposed to a higher risk. Helicity in the bulk flow can be visualized with a Eulerian static depiction (Fig. 1, panel D) or a Lagrangian dynamic depiction (Fig. 1, panel E). The Eulerian representation of LNH isosurfaces (Fig. 1, panel D) is representative of the flow arrangement within the volume of the bifurcation, going into detail about the formation of helical blood structures: counter-rotating coherent helical structures arise at the base of the daughter vessels in correspondence of the bulb. The particle traces, coloured by means of instantaneous value of LNH, highlight the onset of a recirculation region and a flow separation region in correspondence of the bifurcation bulb, qualitatively in accordance with the localization given by the HWPs (Fig. 1, panel E).

A second example regards the evaluation of the HWPs in a CFD model of thoracic aorta. Details are given in Gallo et al. (2012b) and Morbiducci et al. (2013). TAWSS, OSI, and RRT distributions mainly capture flow disturbances at the same sites, even though differences are present. In detail, they identify, as regions of disturbed shear, areas on the curvature of the arch and focal regions in the distal descending aorta (Fig. 2).

In the same subject, an *in vivo* evaluation of HFI was performed (Morbiducci et al. 2009a, 2011). The particle traces in Fig. 3 show that the flow arrangement is strongly characterized by the onset of coherent helical structures. Two large counter-rotating helical structures arise in the proximal region of the outer wall and develop towards the inner wall of the arch (Fig. 3).

This simple example demonstrates that it is possible to quantify arterial bulk flow features *in vivo* with techniques that are mature for the application in the clinical practice. This opens an intriguing scenario. In order to perform large scale

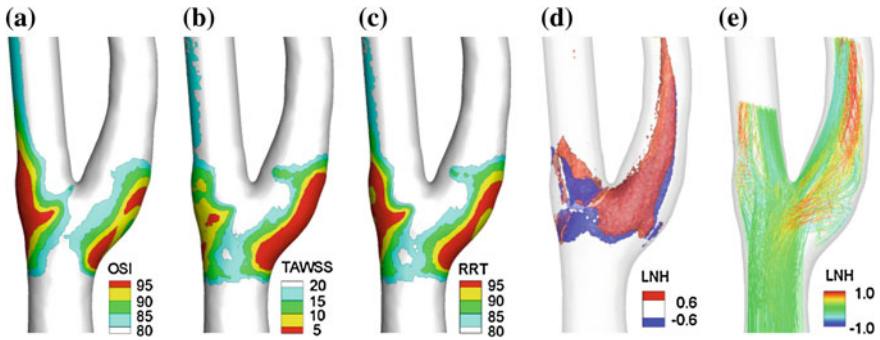


Fig. 1 Synoptic representation of the presented approaches. *Panel a, b and C* depict OSI, TAWSS and RRT distributions, respectively. *Colour-code* indicates areas exposed to OSI and RRT values above the 80th, 85th, 90th and 95th percentile values over the bifurcation surface area (*panel a* and *c*), and areas exposed to TAWSS values above the 5th, 10th, 15th and 20th percentile values (*panel b*). *Panel d* shows a Eulerian representation of bulk flow helicity using LNH iso-surfaces at the beginning of the cardiac cycle. *Panel e* displays a Lagrangian representation of helicity: particles injected at the beginning of the systole are tracked during the entire cardiac cycle. Each particle trace is colour-coded with respect to LNH values

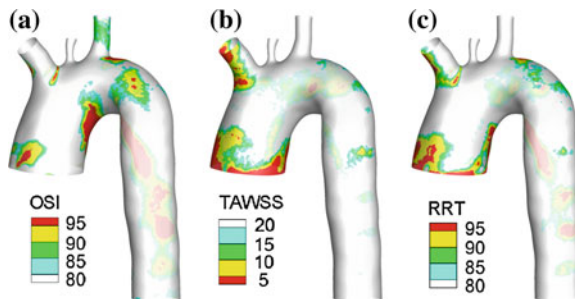


Fig. 2 *Panel a, b and c* depict OSI, TAWSS and RRT distributions, respectively. *Colour-code* indicates areas exposed to OSI and RRT values above the 80th, 85th, 90th and 95th percentile values over the bifurcation surface area (*panel a* and *c*), and areas exposed to TAWSS values above the 5th, 10th, 15th and 20th percentile values (*panel b*)

studies of hemodynamic risk in vessel wall pathologies, the ideal descriptors should be easily measurable *in vivo*. The use of routinely-acquired clinical data from which it is possible to infer the amount of disturbed flow would allow to investigate the hemodynamic risk of vessel pathologies in large-scale studies and in the clinical practice. Although great advances have been made in the area of image-based CFD, such models are still cumbersome, time-consuming to construct and use, and affected by a certain number of assumptions.

In vivo WSS estimate has been recently proposed, mainly by four-dimensional phase contrast MRI (4D PC MRI), through which it is possible to directly acquire 3D and three-directional data on blood flow over time. However, several

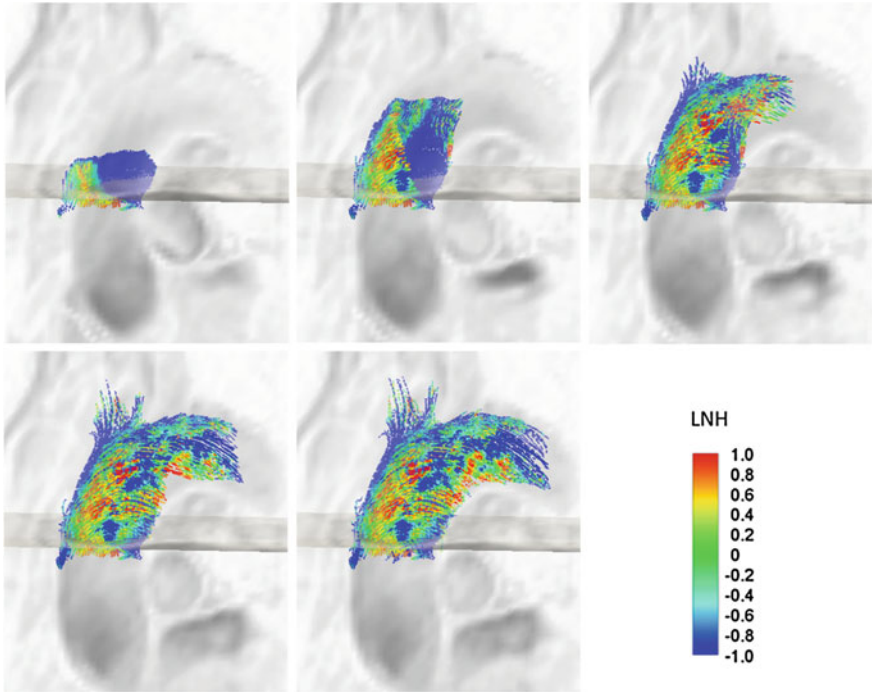


Fig. 3 Evolution of particle sets emitted during the flow deceleration phase in the thoracic aorta. *Color-coding* of the particle traces was used to display the instantaneous LNH value. The evolution is pictured at time intervals of 0.152 s

limitations affect the accuracy of the results. Since WSS depends on the spatial velocity gradient at the vessel wall, it can be calculated from the MRI-measured velocity fields, but limited spatial and temporal resolution, limited signal-to-noise ratio, the difficulty of accurately segmenting the moving vessel lumens, partial volume effects, and numerical derivation of the velocity field are likely to introduce inaccuracies in the estimations of WSS.

To evaluate *in vivo* WSS, the main image parameters (in-plane pixel size, slice thickness, number of time frames per cardiac cycle) must be selected according to conflicting constraints. On one hand, they must be able to capture the flow features within the vascular site of interest. On the other hand, the technological limitations of MRI scanners bind the achievable image resolution in clinical practice, where a trade-off policy is pursued by minimizing the overall costs and scanning time to ensure the minimal requirements for diagnostic purposes. These clashing constraints become critical when the advanced processing of *in vivo* blood flow datasets required to evaluate WSS is attempted. In fact, the application of numeric algorithms including, for example, data interpolation, requires not only low noisy data, but also spatial and temporal sampling rates sufficient to avoid the introduction of a consistent source of numerical errors. In general, the definition of the

optimal in vivo data sampling rate is challenging, since it depends on the complexity of the sampled field and on the ‘regularity’ of the data, which is not well defined a priori. At the moment, the environments traditionally used for validating protocols, such as in vitro or theoretical models, do not give definitive solutions to the problem, due to inherent limitations. In vitro validation is limited by costs, time consumption, proper experimental setup to be built, intrinsic source of noise and/or artefacts such as eddy currents, concomitant gradients, displacement, misregistration, partial volume effects, intra-voxel phase dispersion and aliasing. As for theoretical models, they remain extremely simplistic descriptors of cardiovascular flows.

Frydrychowicz et al. (2011) in their excellent review underlined that WSS estimates from 4D PC MRI measurements are restricted by a spatial resolution between 1.4 and 2.4 mm that produces a WSS underestimation of one order of magnitude when compared to CFD WSS maps (Frydrychowicz et al. 2011). Bousset et al. (2009) stated that “Although 4D MRI can provide a rough estimate of WSS, it is not currently capable of providing accurate absolute measurements”, and Markl et al. (2010) affirmed that the current spatiotemporal resolution of flow-sensitive 4D MRI can considerably underestimate the true WSS magnitude, thus limiting the accuracy of wall parameter calculations.

The main problems arising from WSS in vivo calculations are the followings:

- MR measurements show poor sensitivity to low values of velocities. The sensitivity is governed by the setting chosen for the velocity encoding level (VENC). It is usual for the VENC to be set sufficiently high to avoid aliasing in regions with the highest velocity; but in this way the velocity to noise ratio is compromised in regions of slow flow, generally located at the boundary of the lumen. Zhao et al. (2002) showed that MR measurements in a carotid bifurcation phantom produced spurious velocity vectors in the near-wall region. Given the fact that WSS is a function of near wall velocity gradients, they concluded that WSS evaluated directly from the MR data might not be reliable at certain locations. These limitations are only partially overcome by the recent diffusion of systems with multiple VENCs. Another problem is signal loss due to intra-voxel dephasing in regions of complex flow (Papathanasopoulou et al. 2003). Unfortunately, these are precisely the regions of most interest.
- In addition to sources of errors in velocity measurement, the relatively low spatial and temporal resolution of MRI results in an averaging of the measured velocities which strongly impacts the calculated values of the velocity gradients. The effects of spatial averaging resulting from limited spatial resolution are particularly evident in regions with a broad distribution of velocities within a single voxel, such as at the edge of vessels. Temporal resolution is also an important factor. Indeed, current implementations of 4D MRI have relatively low temporal resolution. Temporal averaging consists in velocity averaging through time, reducing the ability of MRI to estimate transient events, and in a substantial smoothing of the shear values particularly when these values are high, i.e., in regions of rapid spatial change in velocity. To overcome resolution

limitations, a longer time scan would permit an improvement of the resolution but it also increases the likelihood of patient motion, which can substantially degrade the measurements. Imaging at high field strengths would provide increased signal-to-noise ratio which could be used either to reduce imaging time by the use of higher acceleration factors, or to improve resolution, although errors in velocity measurements that result from scanner imperfections at higher field strengths are not yet well characterized.

- WSS calculation relies on lumen edge definition on the magnitude image of the PC MRI which is often difficult to delineate. The precise identification of the blood vessel wall boundary within the image pixel is difficult due to limited resolution, and because that pixel may be partially covered with moving blood and partially covered by the stationary vessel wall (Shaaban and Duerinckx 2000). Inadequate spatial resolution leads to partial volume effects at the vessel walls and a limited number of velocity data points from which to estimate the wall position. This results in errors in wall position and in local surface orientation, degrading the WSS calculation. This is exacerbated when noise is included from surrounding structures which is particularly pronounced if that structure has little or no magnetization (e.g., air). Morbiducci et al. (2012) observed, using a synthetic PC MRI dataset, that image processing steps involving spatial and temporal interpolation of local velocity values to reconstruct the vessel wall could lead to unreliable direct estimation of WSS from PC MRI in vivo data. Fatemi and Rittgers (1994) compared polynomial curve fitting from first through eighth order, and found that while lower-order polynomials fail to capture important velocity profile information, higher-order approximations result in unpredictable results due to oscillations of the fitting functions. Moreover, WSS calculation requires a selection of velocity vectors close to the wall, and it is important to use a reasonable estimate of that distance as it can affect the results. Results from Long et al. (2004) indicate that shear rate determined at 250–300 μm from the wall will underestimate WSS by about 10 %.

Hence, direct accurate estimation of WSS from MR measured velocities is not a viable option for in vivo applications just yet. A number of issues need to be resolved. Developments in hardware are expected to reduce, though not entirely eliminate, these effects but WSS in vivo estimation remains a significant technical challenge.

As described previously, in recent years the computation of bulk flow quantities has emerged as a possible strategy to describe the temporal and spatial complexity of arterial blood flow and complement WSS-based atherogenic hemodynamic classification (Morbiducci et al. 2010). Morbiducci et al. (2012) have demonstrated using a synthetic PC MRI dataset the reliability of measured bulk flow hemodynamics at spatial and temporal resolutions that can be adopted in the clinical practice. They also showed that the higher reliability of bulk flow quantities with respect to WSS-based descriptors could make the calculation of 4D bulk flow

descriptors an outcome which is less sensitive to the image resolution and might be more suitable for in vivo application (Morbiducci et al. 2012).

Very recently, several authors successfully quantified helicity-derived quantities in vivo from time resolved phase-contrast measurements. Morbiducci and colleagues (Morbiducci et al. 2009a, 2011) quantified helical flow in vivo in the human thoracic aorta according to a Lagrangian approach: particle traces were calculated from velocity data and characterized calculating the LNH. Harloff et al. (2009) visualized and quantified helical flow from MRI measurements in carotid artery, even though helical flow was categorized only based on the direction of rotation (qualitative analysis). Lorenz et al. (2012) quantified in vivo the temporal average of the normalized mean helicity on cross-sections in thoracic aorta, by using helicity density and applying schemes previously tested in silico (Grigioni et al. 2005).

5 Conclusions and Future Directions

The purpose of this chapter was to give an overview on the existing methods for quantifying disturbed flow in arterial hemodynamics. Rather than providing a comprehensive list of all the available approaches, we tried to organize this wide matter in lights of the recent developments and the perspective use of these quantities. Our aim was to provide the reader with the means for choosing the best descriptor for the specific problem at hand. An important issue to be explored in the future is the incorporation of hemodynamic descriptors (i.e., based on fluid dynamics information) in appropriate measures of performance for surgical interventions, device optimization, follow-up studies on subjects undergoing surgical procedures (Marsden et al. 2008).

References

- August AD, Ariff B, Thom SA, Xu XY, Hughes AD (2007) Analysis of complex flow and the relationship between blood pressure, wall shear stress, and intima-media thickness in the human carotid artery. *Am J Physiol Heart Circ Physiol* 293:H1031–H1037
- Bogren HG, Buonocore MH (1999) 4D magnetic resonance velocity mapping of blood flow patterns in the aorta in young vs. elderly normal subjects. *J Magn Reson Imaging* 10:861–869
- Boussel L, Rayz V, Acevedo-Bolton G, Lawton MT, Higashida R, Smith WS, Young WL, Saloner D (2009) Phase-contrast magnetic resonance imaging measurements in intracranial aneurysms in vivo of flow patterns, velocity fields, and wall shear stress: comparison with computational fluid dynamics. *Magn Reson Med* 61(2):409–417
- Buchanan JR, Kleinstreuer C (1998) Simulation of particle-hemodynamics in a partially occluded artery segment with implications to the initiation of microemboli and secondary stenoses. *J Biomech Eng* 120(4):446–454
- Caro CG, Fitz GJ, Schroter RC (1969) Arterial wall shear and distribution of early atheroma in man. *Nature* 223:1159–1160

- Caro CG, Fitzgerald JM, Schroter RC (1971) Atheroma and arterial wall shear stress. Observation, correlation, and proposal of a shear dependent mass transfer mechanism for atherogenesis. *Proc Roy Soc B* 177:109–159
- Caro CG, Doorly DJ, Tarnawski M, Scott KT, Long Q, Dumoulin CL (1996) Non-planar curvature and branching of arteries and non-planar-type flow. *Proc R Soc Lond A* 452:185–197
- Caro CG, Watkins NW, Sherwin SJ, Pitt R, Giordana S, Franke PT, Peiro J, Doorly DJ, Papaharilaou Y, Chesire N, Jackson M, Bicknell C (2002) Swirling circulatory and respiratory flow: biological/pathological implications. *IFMBE Proc, EMBEC 2002*, 18–116
- Caro CG (2009) Discovery of the role of wall shear in Atherosclerosis. *Arterioscler Thromb Vasc Biol* 29:158–161
- Chen ZS, Fan YB, Deng XY, Xu Z (2009) Swirling flow can suppress flow disturbances in endovascular stents: a numerical study. *Am Soc Artif Int Organ J* 55(6):543–549
- Chien S (2007) Mechanotransduction and endothelial cell homeostasis: the wisdom of the cell. *Am J Physiol Heart Circ Physiol* 292:H1209–H1224
- Chiu JJ, Chien S (2011) Effects of disturbed flow on vascular endothelium: pathophysiological basis and clinical perspectives. *Physiol Rev* 91:327–387
- De Bakey ME, Lawrie GM, Glaeser DH (1985) Patterns of Atherosclerosis and their Surgical Significance. *Ann Surg* 201:115–131
- De Paola N, Gimbrone MA Jr, Davies PF, Dewey CF Jr (1992) Vascular endothelium responds to fluid shear stress gradients. *Arterioscler Thromb* 12(11):1254–1257
- Ditlevsen PD, Giuliani P (2000) Anomalous scaling in a shell model of helical turbulence. *Phys A* 280:69–74
- Ehrlich LW, Friedman MH (1977) Particle paths and stasis in unsteady flow through a bifurcation. *J Biomech* 10:561–568
- Euler L (1775) *Principia pro motusanguinis per arterias determinando. Opera posthumamathematica et physica anno 1844 detecta. Ediderunt P.H. Fuss et N. Fuss Petropoli; Apud Eggers et Socios*
- Fan Y, Xu Z, Jiang W, Deng X, Wang K, Sun A (2008) An S-type bypass can improve the hemodynamics in the bypassed arteries and suppress intimal hyperplasia along the host artery floor. *J Biomech* 41:2498–2505
- Fatemi RS, Rittgers SE (1994) Derivation of shear rates from near-wall LDA measurements under steady and pulsatile flow conditions. *J Biomech Eng* 116(3):361–368
- Frazin LJ, Lanza G, Vonesh M, Khasho F, Spitzzeri C, McGee S, Mehlman D, Chandran KB, Talano J, McPherson D (1990) Functional chiral asymmetry in descending thoracic aorta. *Circulation* 82(6):1985–1994
- Frazin LJ, Vonesh MJ, Chandran KB, Shipkowitz T, Yaacoub AS, McPherson DD (1996) Confirmation and initial documentation of thoracic and abdominal aortic helical flow, An ultrasound study. *Am Soc Artif Int Organ J* 42(6):951–956
- Friedman MH, Hutchins GM, Barger CB, Deters OJ, Mark FF (1981) Correlation between intimal thickness and fluid shear in human arteries. *Atheroscler* 39:425–436
- Friedman MH, Barger CB, Deters OJ, Hutchins GM, Mark FF (1987) Correlation between wall shear and intimal thickness at a coronary artery branch. *Atheroscler* 68:27–33
- Frydrychowicz A, Franc-ois CJ, Turski PA (2011) Four-dimensional phase contrast magnetic resonance angiography: potential clinical applications. *Eur J Radiol* 80:24–35
- Galbraith CG, Skalak R, Chein S (1998) Shear stress induces spatial reorganization of the endothelial cell cytoskeleton. *Cell Motil Cytoskelet* 40:317–330
- Gallo D, Steinman DA, Bijari PB, Morbiducci U (2012a) Helical flow in carotid bifurcation as surrogate marker of exposure to disturbed shear. *J Biomech* 45(14):2398–2404
- Gallo D, De Santis G, Negri F, Tresoldi D, Ponzini R, Massai D, Deriu MA, Segers P, Verheghe B, Rizzo G, Morbiducci U (2012b) On the use of in vivo measured flow rates as boundary conditions for image-based hemodynamic models of the human aorta. Implications for indicators of abnormal flow. *Ann Biomed Eng* 40(3):729–741

- Gelfand BD, Epstein FH, Blackman BR (2006) Spatial and spectral heterogeneity of time-varying shear stress profiles in the carotid bifurcation by PC-MRI. *J Magn Reson Imaging* 24(6):1386–1392
- Giddens DP, Zarins CK, Glagov S (1993) The role of fluid mechanics in the localization and detection of atherosclerosis. *J Biomech Eng* 115(4B):588–595
- Glagov S, Zarins C, Giddens DP, Ku DN (1988) Hemodynamics and atherosclerosis, insights and perspective gained from studies of human arteries. *Arch Pathol Lab Med* 112:1018–1029
- Goubergrits L, Affeld K, Fernandez-Britto J, Falcon L (2002) Atherosclerosis and flow in carotid arteries with authentic geometries. *Biorheol* 39(3–4):519–524
- Grigioni M, Daniele C, Morbiducci U, Del Gaudio C, D’Avenio G, Balducci A, Barbaro V (2005) A mathematical description of blood spiral flow in vessels: application to a numerical study of flow in arterial bending. *J Biomech* 38:1375–1386
- Haller G (2001) Distinguished material surfaces and coherent structures in three-dimensional fluid flows. *Phys D* 149:248–277
- Harloff A, Albrecht F, Spreer J, Stalder AF, Bock J, Frydrychowicz A, Schollorn J, Hetzel A, Schumacher M, Hennig J, Markl M (2009) 3D blood flow characteristics in the carotid artery bifurcation assessed by flow-sensitive 4D MRI at 3T. *Magn Reson Med* 61:65–74
- He X, Ku DN (1996) Pulsatile flow in the human left coronary artery bifurcation: average conditions. *ASME J Biomech Eng* 118(1):74–82
- Himburg HA, Grzybowski DM, Hazel A, LaMack JA, Li XM, Friedman MH (2004) Spatial comparison between wall shear stress measures and porcine arterial endothelial permeability. *Am J Physiol Heart Circ Physiol* 286(5):H1916–H1922
- Himburg HA, Friedman MH (2006) Correspondence of low mean shear and high harmonic content in the porcine iliac arteries. *J Biomech Eng* 128(6):852–856
- Houston JG, Gandy SJ, Sheppard DG, Dick JBC, Belch JJJ, Stonebridge PA (2003) Two-dimensional flow quantitative MRI of aortic arch blood flow patterns: effect of age, gender and presence of carotid atheromatous disease on the prevalence of spiral blood flow. *J Magn Reson Imaging* 18(2):169–174
- Houston JG, Gandy SJ, Milne W, Dick JB, Belch JJ, Stonebridge PA (2004) Spiral laminar flow in the abdominal aorta: a predictor of renal impairment deterioration in patients with renal artery stenosis? *Nephrol Dial Transplant* 19(7):1786–1791
- Hsiai TK, Cho SK, Wong PK, Ing M, Salazar A, Sevanian A, Navab M, Demer LL, Ho CM (2003) Monocyte recruitment to endothelial cells in response to oscillatory shear stress. *Faseb J* 17(12):1648–1657
- Hyun S, Kleinstreuer C, Archie JP (2000) Computer simulation and geometric design of endarterectomized carotid artery bifurcations. *Crit Rev Biomed Eng* 28:53–59
- Hyun S, Kleinstreuer C, Archie JP (2001) Computational particle-hemodynamics analysis and geometric reconstruction after carotid endarterectomy. *Comp Biol Med* 31:365–384
- Hyun S, Kleinstreuer C, Longest PW, Chen C (2004) Particle-hemodynamics simulations and design options for surgical reconstruction of diseased carotid artery bifurcations. *J Biomech Eng* 126(4):118–195
- Karino T, Goldsmith HL (1985) Particle flow behavior in models of branching vessels. II. Effects of branching angle and diameter ratio on flow patterns. *Biorheol* 22:87–104
- Kessler M (2002) *Biocompat. Nephrol Dial Transplant* 17(7):32–44
- Keynton RS, Evancho MM, Sims RL, Rodway NV, Gobin A, Rittgers SE (2001) Intimal hyperplasia and wall shear in arterial bypass graft distal anastomoses: an in vivo model study. *J Biomech Eng* 123(5):464–473
- Kilner PJ, Yang GZ, Mohiaddin RH, Firmin DN, Longmore DB (1993) Helical and retrograde secondary flow patterns in the aortic arch studied by three-directional magnetic resonance velocity mapping. *Circ* 88:2235–2247
- Kleinstreuer C, Hyun S, Buchanan JR, Longest PW, Archie JP, Truskey GA (2001) Hemodynamic parameters and early intimal thickening in branching blood vessels. *Crit Rev Biomed Eng* 29:1–64

- Kroll MH, Hellums JD, McIntire LV, Schafer AL, Moake JL (1996) Platelets and shear stress. *Blood* 88(5):1525–1541
- Ku DN, Giddens DP (1983) Pulsatile flow in a model carotid bifurcation. *Arterioscler* 3:31–39
- Ku DN, Zarins CK, Giddens DP, Glagov S (1985) Hemodynamics of the normal human carotid bifurcation: in vitro and in vivo studies. *Ultrasound Med Biol* 11:13–26
- Lee SW, Antiga L, Steinman DA (2009) Correlations among indicators of disturbed flow at the normal carotid bifurcation. *J Biomech Eng* 131(6):061013-1-7
- Liu X, Pu F, Fan Y, Deng X, Li D, Li S (2009) A numerical study on the flow of blood and the transport of LDL in the human aorta: the physiological significance of the helical flow in the aortic arch. *Am J Physiol Heart Circ Physiol* 297:H163–H170
- Liu X, Fan Y, Deng X (2010) Effect of spiral flow on the transport of oxygen in the aorta: a numerical study. *Ann Biomed Eng* 38:917–926
- Liu X, Fan Y, Deng X, Zhan F (2011) Effect of non-Newtonian and pulsatile blood flow on mass transport in the human aorta. *J Biomech* 44(6):1123–1131
- Long DS, Smith ML, Pries RA, Ley K, Damiano ER (2004) Microviscometry reveals reduced blood viscosity and altered shear rate and shear stress profiles in microvessels after hemodilution. *Proc Natl Acad Sci USA* 101(27):10060–10065
- Longest PW, Kleinstreuer C (2000) Computational haemodynamics analysis and comparison study of arterio-venous grafts. *J Med Eng Technol* 24(3):102–110
- Lorenz R, Benk C, Stalder AF, Korvink JG, Hennig J, Matkl M (2012) Closed circuit MR compatible pulsatile pump system using a ventricular assist device and pressure control unit. *Magn Reson Med* 67:258–268
- Ma P, Li X, Ku DN (1997) Convective mass transfer at the carotid bifurcation. *J Biomech* 30:565–571
- Malek AM, Alper SL, Izumo S (1999) Hemodynamic shear stress and its role in atherosclerosis. *J Am Med Ass* 282:2035–2042
- Markl M, Wegent F, Zech T, Bauer S, Strecker C, Schumacher M, Weiller C, Hennig J, Harloff A (2010) In vivo wall shear stress distribution in the carotid artery: effect of bifurcation geometry, internal carotid artery stenosis, and recanalization therapy. *Circ Cardio Imaging* 3:647–655
- Marsden AL, Feinstein JA, Taylor CA (2008) A computational framework for derivative-free optimization of cardiovascular geometries. *Comp Methods Appl Mech Eng* 197(21–24):1890–1905
- Massai D, Soloperto G, Gallo D, Xu XY, Morbiducci U (2012) Shear-induced platelet activation and its relationship with blood flow topology in a numerical model of stenosed carotid bifurcation. *Eur J Mech-B/Fluids* 35:92–101
- Moffatt HK (1969) The degree of knottedness of tangled vortex lines. *J Fluid Mech* 35(1):17–29
- Moffatt HK, Tsinober A (1992) Helicity in laminar and turbulent flow. *Annu Rev Fluid Mech* 24:281–312
- Moore JE Jr, Xu C, Glagov s, Zarins CK, Ku DN (1994) Fluid wall shear stress measurements in a model of the human abdominal aorta: oscillatory behavior and relationship to atherosclerosis. *Atheroscler* 110(2):225–240
- Morbiducci U, Lemma M, Ponzini R, Boi A, Bondavalli L, Antona C, Montevecchi FM, Redaelli A (2007a) Does flow dynamics of the magnetic vascular coupling for distal anastomosis in coronary artery bypass grafting contribute to the risk of graft failure? *Int J Artif Organs* 30:628–639
- Morbiducci U, Ponzini R, Grigioni M, Redaelli A (2007b) Helical flow as fluid dynamic signature for atherogenesis in aortocoronary bypass, a numeric study. *J Biomech* 40:519–534
- Morbiducci U, Ponzini R, Rizzo G, Cadioli M, Esposito A, De Cobelli F, Del Maschio A, Montevecchi FM, Redaelli A (2009a) In vivo quantification of helical blood flow in human aorta by time-resolved three-dimensional cine phase contrast MRI. *Ann Biomed Eng* 37:516–531

- Morbiducci U, Ponzini R, Nobili M, Massai D, Montecocchi FM, Bluenstein D, Redaelli A (2009b) Blood damage safety of prosthetic heart valves. Shear-induced platelet activation and local flow dynamics: a fluid-structure interaction approach. *J Biomech* 42(12):1952–1960
- Morbiducci U, Gallo D, Ponzini R, Massai D, Antiga L, Redaelli A, Montecocchi FM (2010) Quantitative analysis of bulk flow in image-based haemodynamic models of the carotid bifurcation: the influence of outflow conditions as test case. *Ann Biomed Eng* 38(12):3688–3705
- Morbiducci U, Ponzini R, Rizzo G, Cadioli M, Esposito A, Montecocchi FM, Redaelli A (2011) Mechanistic insight into the physiological relevance of helical blood flow in the human aorta: an in vivo study. *Biomech Model Mechano biol* 10:339–355
- Morbiducci U, Ponzini R, Rizzo G, Biancolini ME, Iannaccone F, Gallo D, Redaelli A (2012) Synthetic dataset generation for the analysis and the evaluation of image-based hemodynamics of the human aorta. *Med Biol Eng Comput* 50(2):145–154
- Morbiducci U, Ponzini R, Gallo D, Bignardi C, Rizzo G (2013) Inflow boundary conditions for image-based computational hemodynamics: impact of idealized versus measured velocity profiles in the human aorta. *J Biomech* 46(1):102–109
- Papathanasopoulou P, Zhao S, Köhler U, Robertson MB, Long Q, Hoskins P, Yun Xu X, Marshall I (2003) MRI measurement of time-resolved wall shear stress vectors in a carotid bifurcation model, and comparison with CFD predictions. *J Magn Reson Imaging* 17:153–162
- Pedersen EM, Agerbaek M, Kristensen IB, Yoganathan AP (1997) Wall shear stress and early atherosclerotic lesions in the abdominal aorta in young adults. *Eur J Vasc Endovasc Surg* 13:443–451
- Perktold K, Resch M (1990) Numerical flow studies in human carotid artery bifurcations: basic discussion of the geometric factor in atherogenesis. *J Biomed Eng* 12(2):111–123
- Pritchard WF, Davies PF, Derafshi Z, Polacek DC, Tsao R, Dull RO, Jones SA, Giddens DP (1995) Effects of wall shear stress and fluid recirculation on the localization of circulating monocytes in a three-dimensional flow model. *J Biomech* 28(12):1459–1469
- Santilli SM, Stevens RB, Anderson JG, Payne WD, Caldwell MD (1995) Transarterial wall oxygen gradients at the dog carotid bifurcation. *Am J Physiol Heart Circ Physiol* 268:H155–H161
- Shaaban AM, Duerinckx AJ (2000) Wall shear stress and early atherosclerosis: a review. *Am J Roentgenol* 174:1657–1665
- Shadden SC, Lekien F, Marsden JE (2005) Definition and properties of Lagrangian coherent structures from finite-time Lyapunov exponents in two-dimensional aperiodic flows. *Phys D* 212(3–4):271–304
- Shadden SC, Taylor CA (2008) Characterization of coherent structures in the cardiovascular system. *Ann Biomed Eng* 36(7):1152–1162
- Shtilman L, Levich E, Orszag SA, Pelz RB, Tsinober A (1985) On the role of helicity in complex fluid flows. *Phys Lett* 113A:32–37
- Sluimer JC, Gasc JM, van Wanroij JL, Kisters N, Groeneweg M, SollewijnGelpke MD, Cleutjens JP, van den Akker LH, Corvol P, Wouters BG, Daemen MJ, Bijnens AP (2008) Hypoxia, hypoxia-inducible transcription factor, and macrophages in human atherosclerotic plaques are correlated with intraplaque angiogenesis. *J Am Coll Cardiol* 51:1258–1265
- Steinman DA (2000) Simulated pathline visualization of computed periodic blood flow patterns. *J Biomech* 33(5):623–628
- Stonebridge PA, Hoskins PR, Allan PL, Belch JF (1996) Spiral laminar flow in vivo. *Clin Sci* 91:17–21
- Sun N, Wood NB, Hughes AD, Thom SAM, Xu XY (2007) Effects of transmural pressure and wall shear stress on LDL accumulation in the arterial wall: a numerical study using a multilayered model. *Am J Physiol Heart Circ Physiol* 292:H3148–H3157
- Tambasco M, Steinman DA (2001) Calculating particle-to-wall distances in unstructured computational fluid dynamic models. *Appl Math Model* 25:803–814
- Tambasco M, Steinman DA (2002) On assessing the quality of particle tracking through computational fluid dynamic models. *J Biomech Eng* 124:166–175

- Taylor CA, Steinman DA (2010) Image-based modeling of blood flow and vessel wall dynamics: applications, methods and future directions. *Ann Biomed Eng* 38(3):1188–1203
- Vetel J, Garon A, Pelletier D (2009) Lagrangian coherent structures in the human carotid artery bifurcation. *Exp Fluid* 46(6):1067–1079
- Womersley JR (1955) Method for the calculation of velocity, rate of flow and viscous drag in arteries when the pressure gradient is known. *J Physiol* 127:553–563
- Yoshizumi M, Abe J, Tsuchiya K, Berk BC, Tamaki T (2003) Stress and vascular responses: atheroprotective effect of laminar fluid shear stress in endothelial cells: possible role of mitogen-activated protein kinases. *J Pharmacol Sci* 91:172–176
- Zhan F, Fan Y, Deng X (2010) Swirling flow created in a glass tube suppressed platelet adhesion to the surface of the tube: Its implication in the design of small-caliber arterial grafts. *Thromb Res* 125(5):413–418
- Zhao SZ, Ariff B, Long Q, Hughes AD, Thom SA, Stanton AV, Xu XY (2002) Inter-individual variations in wall shear stress and mechanical stress distributions at the carotid artery bifurcation of healthy humans. *J Biomech* 35(10):1367–1377
- Zheng T, Fan Y, Xiong Y, Jiang W, Deng X (2009) Hemodynamic performance study on small diameter helical grafts. *Am Soc Artif Int Organ J* 55:192–199

Fluid–Structure Interaction Modeling of Patient-Specific Cerebral Aneurysms

Kenji Takizawa and Tayfun E. Tezduyar

Abstract We provide an overview of the special techniques developed earlier by the Team for Advanced Flow Simulation and Modeling (T★AFSM) for fluid–structure interaction (FSI) modeling of patient-specific cerebral aneurysms. The core FSI techniques are the Deforming-Spatial-Domain/Stabilized Space–Time formulation and the stabilized space–time FSI technique. The special techniques include techniques for calculating an estimated zero-pressure arterial geometry, a special mapping technique for specifying the velocity profile at an inflow boundary with non-circular shape, techniques for using variable arterial wall thickness, mesh generation techniques for building layers of refined fluid mechanics mesh near the arterial walls, a recipe for pre-FSI computations that improve the convergence of the FSI computations, techniques for calculation of the wall shear stress and oscillatory shear index, and arterial-surface extraction and boundary condition techniques. We show, with results from earlier computations, how these techniques work. We also describe the arterial FSI techniques developed and implemented recently by the T★AFSM and present a sample from a wide set of patient-specific cerebral-aneurysm models we computed recently.

K. Takizawa (✉)

Department of Modern Mechanical Engineering and Waseda Institute for Advanced Study,
Waseda University, 1-6-1 Nishi-Waseda, Shinjuku-ku, Tokyo 169-8050, Japan
e-mail: Kenji.Takizawa@tafsm.org

T. E. Tezduyar

Mechanical Engineering, Rice University, 6100 Main Street, Houston, TX 77005, USA
e-mail: tezduyar@rice.edu

1 Introduction

Arterial fluid mechanics computations involve a number of challenges. One of the major computational challenges is accurate and efficient modeling of the fluid–structure interactions (FSI) between the blood flow and arterial walls. The preferred method of handling the moving interfaces involved in FSI modeling has mostly been the Arbitrary Lagrangian–Eulerian (ALE) finite element formulation (Hughes et al. 1981). One of the earliest space–time formulations targeting FSI modeling is the Deforming-Spatial-Domain/Stabilized Space–Time (DSD/SST) formulation (Tezduyar 1992). The DSD/SST formulation was introduced by the Team for Advanced Flow Simulation and Modeling (T★AFSM) as a general-purpose interface-tracking (i.e. moving-mesh) technique for computation of flow problems with moving interfaces. The formulation is based on the Streamline-Upwind/Petrov–Galerkin (SUPG) (Brooks and Hughes 1982) and Pressure-Stabilizing/Petrov–Galerkin (PSPG) (Tezduyar 1992) methods.

Patient-specific arterial FSI modeling with the DSD/SST formulation was first reported by Torii et al. in a 2004 journal article (Torii et al. 2004) published by the Japan Society of Mechanical Engineers. Over the years following that, Torii et al. conducted one of the most extensive series of patient-specific arterial FSI modeling of cerebral aneurysms (see Torii et al. 2011) and references therein). The cases studied in these articles by Torii et al. were almost all for middle cerebral arteries, and the geometries were constructed from computed tomography images. In these arterial FSI computations the DSD/SST formulation was used together with the mesh update methods (Johnson and Tezduyar 1994; Tezduyar et al. 1993) developed by the T★AFSM and was implemented with block-iterative coupling (Tezduyar 2004) (see (Tezduyar et al. 2006) for the terminology). The inflow boundary condition used in the computations is a pulsatile velocity profile, which closely represents the measured flow rate during a heartbeat cycle. A brief, chronological review of the computations reported was provided in (Tezduyar et al. 2007b).

New generation DSD/SST formulations, with increased scope, robustness and efficiency, were introduced by the T★AFSM in (Tezduyar and Sathe 2007). The stabilized space–time FSI (SSTFSI) technique, which is based on the new-generation DSD/SST formulations, was also introduced in Tezduyar and Sathe (2007). The SSTFSI technique was extended by the T★AFSM in Takizawa et al. (2010a, b; Tezduyar et al. 2007b, 2008, 2009, 2010) to arterial FSI modeling, with emphasis on arteries with aneurysm. The arterial geometries were approximations to patient-specific image-based geometries, mostly to those reported by Torii et al. A number of special techniques for arterial FSI were developed by the T★AFSM in conjunction with the SSTFSI technique. These include techniques for calculating an estimated zero-pressure (EZP) arterial geometry (Takizawa et al. 2010a, b; Tezduyar et al. 2007a, 2008), a special mapping technique for specifying the velocity profile at an inflow boundary with non-circular shape (Takizawa et al. 2010a), techniques for using variable arterial wall thickness (Takizawa et al. 2010a,

b), mesh generation techniques for building layers of refined fluid mechanics mesh near the arterial walls (Takizawa et al. 2010a, b; Tezduyar et al. 2009), a recipe for pre-FSI computations that improve the convergence of the FSI computations (Tezduyar et al. 2007b, 2008), the Sequentially Coupled Arterial FSI (SCAFSI) technique (Tezduyar et al. 2008, 2007c, 2009, 2010) and its multiscale versions (Tezduyar et al. 2009, 2010), and techniques (Takizawa et al. 2010b) for the projection of fluid–structure interface stresses, calculation of the wall shear stress (WSS) and calculation of the oscillatory shear index (OSI). In FSI modeling of three cerebral artery segments with aneurysm reported by the T★AFSM in Takizawa et al. (2011), the arterial geometries came from 3D rotational angiography (3DRA). In Takizawa et al. (2011), the T★AFSM also addressed the computational challenges related to extraction of the arterial-lumen geometry from 3DRA, generation of a mesh for that geometry, and building a good starting point for the FSI computations. In addition to these computational challenges common to all three cases, the computational challenges encountered in some of these cases individually were addressed in Takizawa et al. (2011).

In this chapter we provide an overview of the special techniques developed earlier by the T★AFSM for space–time FSI modeling of patient-specific cerebral aneurysms and present results from earlier computations. We also describe the arterial FSI techniques developed and implemented recently by the T★AFSM and present a sample from a wide set of patient-specific cerebral-aneurysm models we computed recently. The governing equations and the finite element formulations, including the DSD/SST and SSTFSI techniques, can be found in (Tezduyar et al. 2011). The special FSI techniques are described in Sect. 2. In Sect. 3, we describe how we extract the arterial-lumen geometry from 3DRA and generate the mesh. The fluid (blood) and structure (arterial wall) properties and boundary conditions are given in Sect. 4. The pre-FSI computations are described in Sect. 5. We present the test computations in Sect. 6, and give our concluding remarks in Sect. 7.

2 Special Techniques

2.1 Mapping Technique for Inflow Boundaries

The special mapping technique for inflow boundaries was introduced in Takizawa et al. (2010a). We repeat here from Takizawa et al. (2010a) how the technique works.

Some inflow profiles require the inlet to be circular, however the inlets in many of the geometries we encounter are not circular. Furthermore, as the artery deforms, the inlet shape changes. Thus, even if the inlet is initially circular, it will not remain so. The technique introduced in Takizawa et al. (2010a) to meet this requirement maps the inflow boundaries from non-circular shapes to circular shapes. The actual inflow profile $U(\mathbf{z}, t)$, where \mathbf{z} is the coordinate vector in the inflow plane, is obtained by mapping from a preferred inflow profile $U^P(r, t)$. Here

r is the circular coordinate and $0 \leq r \leq r_B$, where r_B is the average radius of the inflow cross-sectional area, which comes from the image-based data. It is calculated by dividing that area by π and taking the square-root of that.

The technique involves two steps:

1. Map \mathbf{z} to r and calculate a “trial” velocity:

$$r(\mathbf{z}) = \frac{\|\mathbf{z} - \mathbf{z}_C\|}{\|\mathbf{z} - \mathbf{z}_B\| + \|\mathbf{z} - \mathbf{z}_C\|} r_B, \quad (1)$$

$$U^T(\mathbf{z}, t) = U^P(r, t), \quad (2)$$

where subscripts “C” and “B” denote the centroid and the closest boundary, respectively, as shown in Fig. 1, and the superscript “T” stands for “trial”.

2. Adjust the velocity:

$$U(\mathbf{z}, t) = \frac{Q(t)}{\int_{\Gamma_{\text{INFL}}} U^T(\mathbf{z}, t) d\Gamma} U^T(\mathbf{z}, t), \quad (3)$$

where Q is the flow rate and Γ_{INFL} is the discretized inflow area; i.e. the integration area in the finite element space.

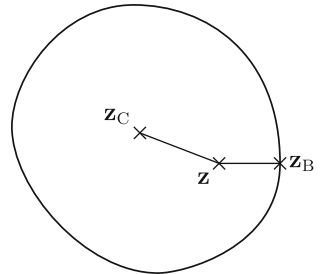
2.2 Wall Shear Stress Calculation

A new technique for calculating the wall shear stress (WSS) was proposed in Takizawa et al. (2010b). We provide the description of the technique from Takizawa et al. (2010b).

We first decompose the spatial version of $(\mathbf{w}_{11}^h)_{n+1}^-$ into its two components:

$$\mathbf{w}_{11}^h = (\mathbf{w}_{11}^h)^W + (\mathbf{w}_{11}^h)^R, \quad (4)$$

Fig. 1 Special mapping technique



where $(\mathbf{w}_{\text{II}}^h)^{\text{R}}$ is the part associated with the rim nodes at the lumen ends, and $(\mathbf{w}_{\text{II}}^h)^{\text{W}}$ is the part associated with the rest of the fluid mechanics nodes at the arterial wall. We then calculate $(\mathbf{h}_v^h)_{\text{II}}$ as follows:

$$\int_{\Gamma_h} (\mathbf{w}_{\text{II}}^h)^{\text{W}} \cdot (\mathbf{h}_v^h)_{\text{II}} d\Gamma = \int_{\Omega} 2\mu \boldsymbol{\varepsilon} \left((\mathbf{w}_{\text{II}}^h)^{\text{W}} \right) : \boldsymbol{\varepsilon}(\mathbf{u}) d\Omega + \sum_{e=1}^{(n_e)_n} \int_{\Omega^e} (\mathbf{w}_{\text{II}}^h)^{\text{W}} \cdot \nabla \cdot (2\mu \boldsymbol{\varepsilon}(\mathbf{u})) d\Omega, \quad (5)$$

$$\int_{\Gamma_h} (\mathbf{w}_{\text{II}}^h)^{\text{R}} \cdot ((\mathbf{n} \times \mathbf{e}^{\text{R}}) \cdot \nabla) (\mathbf{h}_v^h)_{\text{II}} d\Gamma = 0, \quad (6)$$

where \mathbf{e}^{R} is the unit vector along the rim.

2.3 Oscillatory Shear Index

The oscillatory shear index (OSI) is a measure of the degree to which WSS oscillates during a heart beat cycle. It is defined (see (Taylor et al. 1998)) as follows:

$$\text{OSI} = \frac{1}{2} \left(1 - \frac{(\mathbf{h}_v^h)_{\text{II}}^{\text{NM}}}{(\mathbf{h}_v^h)_{\text{II}}^{\text{MN}}} \right), \quad (7)$$

where, following the notation from Takizawa et al. (2010b), “NM” and “MN” stand for “norm of the mean” and “mean of the norm”, and

$$(\mathbf{h}_v^h)_{\text{II}}^{\text{NM}} = \frac{1}{T} \left\| \int_0^T (\mathbf{h}_v^h)_{\text{II}} dt \right\|, \quad (8)$$

$$(\mathbf{h}_v^h)_{\text{II}}^{\text{MN}} = \frac{1}{T} \int_0^T \| (\mathbf{h}_v^h)_{\text{II}} \| dt. \quad (9)$$

Here T is the period of the cardiac cycle. Higher OSI indicates larger flow direction variation in a cardiac cycle. As pointed out in Takizawa et al. (2010b), calculating the OSI based on a fixed reference frame is not the best way, because, for example, if an artery segment undergoes rigid-body rotation, that should not influence the OSI. Two methods that exclude rigid-body rotation from the OSI calculation were proposed in Takizawa et al. (2010b).

Method 1

$$(\mathbf{h}_v^h)_{\text{II}}^\Delta = \mathbf{J}\mathbf{F}^{-1}(\mathbf{h}_v^h)_{\text{II}}, \quad (10)$$

where \mathbf{F} is the deformation gradient tensor associated with the deformation of the fluid–structure interface (not the volumetric deformation gradient of the fluid-domain motion), and $J = \det\mathbf{F}$.

Method 2

$$(\mathbf{h}_v^h)_{\text{II}}^\Delta = \mathbf{R}^T(\mathbf{h}_v^h)_{\text{II}}, \quad (11)$$

where \mathbf{R} is the rotation tensor coming from the decomposition of \mathbf{F} as

$$\mathbf{F} = \mathbf{R}\mathbf{U}, \quad (12)$$

and \mathbf{U} is the right stretch tensor.

For both methods, $(\mathbf{h}_v^h)_{\text{II}}^\Delta$ is calculated as follows:

$$\int_{(\Gamma_{\text{II}})_{\text{ROSI}}} \mathbf{w}_{\text{II}}^h \cdot (\mathbf{h}_v^h)_{\text{II}}^\Delta d\Gamma = \int_{(\Gamma_{\text{II}})_{\text{ROSI}}} \mathbf{w}_{\text{II}}^h \cdot \mathcal{R}(\mathbf{h}_v^h)_{\text{II}} d\Gamma, \quad (13)$$

where $\mathcal{R} = \mathbf{J}\mathbf{F}^{-1}$ or $\mathcal{R} = \mathbf{R}^T$, and $(\Gamma_{\text{II}})_{\text{ROSI}}$ is a reference configuration of the fluid–structure interface used in the OSI calculations. In Eqs. (8) and (9), we replace $(\mathbf{h}_v^h)_{\text{II}}$ with $(\mathbf{h}_v^h)_{\text{II}}^\Delta$.

Remark 1 A similar concept can be found in Green and Naghdi (1976) as the corotated Cauchy stress, $\mathbf{R}^T\boldsymbol{\sigma}\mathbf{R}$.

Remark 2 The OSI calculations reported in this chapter are based on Eq. (10).

Remark 3 As pointed out in Takizawa et al. (2010b), the reference configuration used in Eq. (13) is not necessarily the unstressed configuration of the fluid–structure interface. For the calculations reported in this book chapter, it is the configuration corresponding to the instant when the pressure is at its time-averaged value (on the way up, i.e. at the ascending part of the pressure curve).

3 Arterial Geometry, Mesh Generation and Estimated Zero-Pressure Geometry

3.1 Arterial-Surface Extraction from Medical Images

In our current arterial FSI research the arterial geometries come as voxel data from 3D rotational angiography (3DRA) performed at one of the neuroangiography suites at the Memorial Hermann Hospital at the Texas Medical Center. This is

done on a biplane neuroangiographic unit (Allura FD20/10; Philips Medical System, Best, the Netherlands). Adjusting the contrast ratio for this voxel data allows us to visualize and create a triangular surface mesh using a marching cubes algorithm. The vertices of the surface mesh are then passed through a Gaussian smoothing filter to eliminate any high frequency noise and obtain a smooth surface. At the artery inlets and outlets, we select cutting planes that are approximately perpendicular to the flow direction. As pointed out in (Takizawa et al. 2011), this provides better inflow and outflow planes for specifying the fluid mechanics boundary conditions and is also important for imposing proper slip boundary conditions at the inlets and outlets for the structural mechanics and fluid mesh motion (see Sect. 4.5 in Tezduyar et al. 2011). This entire process is carried out using software originally designed by Warren and McPhail for the purpose of interactively imaging the pulmonary structure of the human lung McPhail and Warren (2008).

3.2 Mesh Generation and Estimated Zero-Pressure Arterial Geometry

We use the arterial lumen geometry as input to ANSYS Meshing Tools to generate a quadrilateral surface mesh. As mentioned in Takizawa et al. (2011), at locations where the arteries have large curvature we use more mesh refinement. Based on the surface mesh, we go through a process of determining the arterial wall thickness, generating a hexahedral structural mechanics mesh for the arterial wall (typically with two layers of elements across the arterial wall), and calculating the estimated zero-pressure (EZP) arterial geometry Takizawa et al. (2010a, b; Tezduyar et al. 2008).

The concept of EZP geometry was introduced in Tezduyar et al. (2008). Quite often, the image-based geometries are used as arterial geometries corresponding to zero blood pressure. As pointed out in Tezduyar et al. (2008), it is more realistic to use that image-based geometry as the arterial geometry corresponding to the time-averaged value of the blood pressure. Given that arterial geometry at the time-averaged pressure value, an estimated arterial geometry corresponding to zero blood pressure needs to be constructed. This is where the need for an EZP arterial geometry comes from. In estimating that geometry, the time-averaged value of the blood pressure, obtained by averaging over a cardiac cycle, is 92 mm Hg.

In Takizawa et al. (2011), different wall-thickness ratios are tried with the zero-pressure shape until, approximately, a 10 % wall-thickness ratio (relative to the diameter of the arterial lumen) is obtained at the inflow. At each iteration, the trial wall-thickness ratio is globally uniform (which comes out to be in the range 12–13 % when the iterations end), but the base length scales for the “patches” are defined individually, with a smooth transition between the patches. The patches are

identified as the regions associated with the inflow trunk, each of the outflow branches, and the aneurysm/bifurcation area. The length scales for the inflow and outflow patches are the lumen diameters at those ends. The length scale for the aneurysm/bifurcation patch is a factor times the lumen diameter at the inflow, where the factor was less than one and varied between the three different patient-specific artery models used in Takizawa et al. (2011). The zero-pressure shape at each EZP iteration is obtained by shrinking the surface mesh generated in the surface-extraction process (see Sect. 3.1) by an amount equal to the trial wall-thickness described above. It was pointed out in Takizawa et al. (2011) that this was a simplified implementation and it was proposed to calculate the shrinking amount not with such direct dependence on the trial wall-thickness, but based on a more sophisticated rule of dependence or based on an independent trial objective.

In Takizawa et al. (2010a, b) and Tezduyar et al. (2010) the EZP geometry was calculated in a simpler way. The zero-pressure shape used at each EZP iteration was simply the surface mesh generated in the surface-extraction process, without any shrinking. The calculation was even simpler in Tezduyar et al. (2008, 2009), where the entire artery segment was treated as a single patch.

Following the calculation of the EZP geometry, the structure is inflated to a pressure corresponding to the pressure at the start of our computation cycle (cardiac cycle). After that, we generate, with ANSYS Meshing Tools, a fluid mechanics surface mesh associated with the inflated arterial-wall structure. Then, using that surface mesh, we generate a desired number of layers of refined fluid mechanics volume mesh near the arterial walls. The rest of the fluid mechanics volume mesh is generated with the T★AFSM automatic mesh generator. Layers of refined fluid mechanics volume mesh near the arterial walls were used in T★AFSM computations as early as the computations reported in Tezduyar et al. (2009), followed by the computations reported in Takizawa et al. (2010a, b, 2011) and Tezduyar et al. (2010).

In Takizawa et al. (2011), the layers of refined mesh have locally variable thickness (with smooth transition between areas of different thickness), because some artery branches have very small diameters. The thickness of the layers of refined mesh is determined basically in the same way as the arterial wall thickness is determined in Takizawa et al. (2011). The layers of refined mesh were generated in a simpler way in Takizawa et al. (2010a, b) and Tezduyar et al. (2009, 2010), where the entire artery segment was treated as a single patch. The number of layers was 6 in Tezduyar et al. (2009), with a progression factor of approximately 1.25, and 4 in Takizawa et al. (2010a, b, 2011) and Tezduyar et al. (2010), with a progression factor of 1.75.

In this book chapter we also present results obtained with new techniques for determining the shrinking amount in the EZP process, the arterial wall thickness, and the thickness of the layers of refined fluid mechanics volume mesh near the arterial walls. These techniques were proposed in Remark 2 of Takizawa et al. (2011). Instead of using (nearly) patch-wise constant values (with a smooth transition between the patches) for the EZP shrinking amounts, the wall thicknesses, and the thickness of the layers of refined mesh, we determine the local

values of all three based on the solution of the Laplace’s equation over the surface mesh covering the lumen. In each of the three cases, the Laplace’s equation is solved with values specified at the inflow and outflow boundaries and for the shrinking amount and wall thickness, as needed,¹ at a set of inter-patch points (i.e. points that are considered to be at the boundaries between the patches). The trial ratios for the shrinking amount and wall thickness are no longer globally uniform but are defined individually for the inflow and outflow boundaries (which still come out to be in the range 12–13 % for the wall thickness when the iterations end), and the values specified at the inter-patch points are not directly related to these ratios. Furthermore, instead of targeting just a 10 % wall-thickness ratio at the inflow, we take some additional considerations into account, such as targeting a 10 % wall-thickness ratio also at the outflow boundaries, targeting a wall-thickness for the aneurysm or a set inter-patch points, reasonableness of the aneurysm size and overall shape, and the mesh quality. The trial shrinking is applied, as needed, in multiple steps, with surface remeshing between the steps. Because the parameter space is wider and the targets are multiple, the process involves more user experience, intuition and judgment. Still, of course, the objective in iterating on the values for the shrinking amount and wall thickness is to have an EZP geometry that after inflation to average pressure gives us a shape that closely resembles the lumen geometry from the 3DRA. We note that the trial ratios specified at the boundaries for the shrinking amount and wall thickness are not independent quantities, but related by the incompressibility constraint. In generating the refined fluid mechanics volume mesh near the arterial walls, the number of layers is 4 and the progression factor is 1.75.

Remark 4 The original version of the technique for calculating an EZP geometry was introduced in a 2007 conference paper (Tezduyar et al. 2007a) and the 2008 journal (Tezduyar et al. 2008) as “a rudimentary technique” for addressing the issue. Newer techniques have been introduced since then, such as the new versions we described above and the approach given in Bazilevs et al. (2010). In the approach given in Bazilevs et al. (2010), the geometry of the vessel is left unchanged and a state of pre-stress is found, which puts the artery in equilibrium with the cardiac-cycle-averaged pressure (and viscous forces). The pre-stress is then directly employed for the blood vessel wall tissue modeling in the FSI computations.

Remark 5 A technique for wall-thickness prescription, based on the solution of the Laplace’s equation over the fluid volume mesh, was developed in Bazilevs et al. (2009). The idea of using the Laplace’s equation over the surface mesh covering the lumen to determine the local values of the EZP shrinking amount, the arterial

¹ In some cases where the outflow diameters significantly differ, the solution obtained from the Laplace’s equation for shrinking amount and wall thickness for the aneurysm/bifurcation area could have an undesirable distribution. The need for specifying values at a set of inter-patch points comes from seeking a better distribution in that area.

wall thickness, and the thickness of the layers of refined mesh was motivated by this earlier wall-thickness determination work.

4 Fluid and Structure Properties and Boundary Conditions

4.1 Fluid and Structure Properties

As it was done for the computations reported in Torii et al. (2004, 2011), the blood is assumed to behave like a Newtonian fluid (see Sect. 2.1 in Tezduyar et al. 2008). The density and kinematic viscosity are set to $1,000 \text{ kg/m}^3$ and $4.0 \times 10^{-6} \text{ m}^2/\text{s}$. The material density of the arterial wall is known to be close to that of the blood and therefore set to $1,000 \text{ kg/m}^3$. The arterial wall is modeled with the continuum element made of hyperelastic (Fung) material. The Fung material constants D_1 and D_2 (from Huang et al. 2001) are $2.6447 \times 10^3 \text{ N/m}^2$ and 8.365, and the penalty Poisson's ratio is 0.45. Cerebral arteries are surrounded by cerebrospinal fluid, and we expect that to have a damping effect on the structural dynamics of the arteries. Therefore we add a mass-proportional damping, which also helps in removing the high-frequency modes of the structural deformation. The damping coefficient η is chosen in such a way that the structural mechanics computations remain stable at the time-step size used. It is $1.5 \times 10^4 \text{ s}^{-1}$.

4.2 Boundary Conditions

At the inflow boundary we specify the velocity profile as a function of time, by using the technique introduced in Takizawa et al. (2010a). Here we describe the technique from (Takizawa et al. 2010a). We use a velocity waveform which represents the cross-sectional maximum velocity as a function of time. Assuming that the maximum velocity occurs at $r = 0$, the artery is rigid and the cross-sectional shape is a perfect circle, we can apply the Womersley (1955) solution as follows:

$$U^P(r, t) = A_0 \left(1 - \left(\frac{r}{r_B} \right)^2 \right) + \sum_{k=1}^N A_k \frac{J_0(\mathcal{Y}\sqrt{k}i^{\frac{3}{2}}) - J_0\left(\mathcal{Y}\sqrt{k}\left(\frac{r}{r_B}\right)i^{\frac{3}{2}}\right)}{J_0(\mathcal{Y}\sqrt{k}i^{\frac{3}{2}}) - 1} \exp\left(i2\pi k \frac{t}{T}\right), \quad (14)$$

where N is the number of Fourier coefficients (we use $N = 20$), $A_k \in \mathbb{C}$ are the Fourier coefficients of the waveform, T is the period of the cardiac cycle, J_0 is the

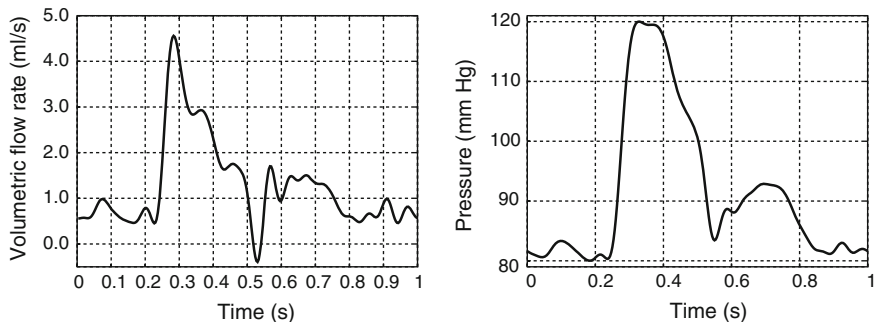


Fig. 2 Sample volumetric flow rate (*left*) and outflow pressure profile (*right*) corresponding to the sample flow rate

Bessel functions of the first kind of order 0, i is the imaginary number, and \mathcal{Y} is the Womersley parameter:

$$\mathcal{Y} = r_B \sqrt{\frac{2\pi}{\nu T}}. \quad (15)$$

We use the special mapping technique described in Sect. 2.1 for non-circular shapes. Figure 2 shows a sample volumetric flow rate as a function of time.

Remark 6. In the current T★AFSM computations, the volumetric flow rate (which was calculated based on a velocity waveform that represents the cross-sectional maximum velocity) is scaled by a factor. The scaling factor is determined in such a way that the scaled flow rate, when averaged over the cardiac cycle, yields a target WSS for Poiseuille flow over an equivalent cross-sectional area. The target WSS is 10 dyn/cm^2 in the current T★AFSM computations.

At all outflow boundaries of an artery segment, we specify the same traction boundary condition. The traction boundary condition is based on a pressure profile computed as described in (Takizawa et al. 2010a). In that computation, the pressure profile, as a function of time, is determined based on the flow rate and by using the Windkessel model (Frank, 1899). From Eq. (14), we obtain the flow rate as follows:

$$Q(t) = \int_0^{r_B} 2\pi r U^P(r, t) dr \quad (16)$$

$$= \pi r_B^2 \frac{A_0}{2} + \pi r_B^2 \sum_{n=1}^N A_k \frac{J_0(\mathcal{Y}\sqrt{k}i^{\frac{3}{2}}) - 2(\mathcal{Y}\sqrt{k}i^{\frac{3}{2}})^{-1} J_1(\mathcal{Y}\sqrt{k}i^{\frac{3}{2}})}{J_0(\mathcal{Y}\sqrt{k}i^{\frac{3}{2}}) - 1} \exp\left(i2\pi k \frac{t}{T}\right) \quad (17)$$

$$= \sum_{k=0}^N B_k \exp\left(i2\pi k \frac{t}{T}\right), \quad (18)$$

where J_1 is the Bessel functions of the first kind of order 1, and for notational convenience we introduce another set of coefficients, $B_k \in \mathbb{C}$. The pressure, based on the Windkessel model, can be written as follows:

$$p(t) = \exp\left(-\frac{t}{RC}\right) \int_0^t \frac{1}{C} Q(\tau) \exp\left(\frac{\tau}{RC}\right) d\tau + p_0, \quad (19)$$

where C and R are the compliance and resistance of the distal arterial networks, and p_0 is a constant of integration. Substituting Eq. (18) into Eq. (19), we obtain the following:

$$p(t) = \sum_{k=0}^N \frac{B_k}{i2\pi k \frac{C}{T} + \frac{1}{R}} \left[\exp\left(i2\pi k \frac{t}{T}\right) - \exp\left(-\frac{t}{RC}\right) \right] + p_0. \quad (20)$$

After a sufficient number of periods, the $\exp\left(-\frac{t}{RC}\right)$ term in Eq. (20) goes to 0:

$$p(t) = \frac{T}{C} \sum_{k=0}^N \frac{B_k}{i2\pi k + \frac{T}{RC}} \exp\left(i2\pi k \frac{t}{T}\right) + p_0. \quad (21)$$

Here $\frac{T}{RC}$ is only a profile factor, because it is a parameter that only acts on each Fourier coefficient. We set $\frac{T}{RC}$ to 18.2, and the other parameters, $\frac{T}{C}$ and p_0 , are set in such a way that the range for the pressure profile is from 80 to 120 mm Hg for normal blood pressure. Figure 2 shows the pressure profile corresponding to the sample flow rate.

On the arterial walls, we specify no-slip boundary conditions for the flow. In the structural mechanics part, as boundary condition at the ends of the arteries, we set the normal component of the displacement to zero (see Sect. 4.5 in Tezduyar et al. 2011), and for one of those nodes we also set to zero the tangential displacement component that needs to be specified to preclude rigid-body motion.

5 Simulation Sequence

Recipes for pre-FSI computations that provide a good starting point for the FSI computations and improve their convergence were introduced in Tezduyar et al. (2007b). Now, in all arterial simulations carried out by the T★AFSM, the FSI computations are preceded by a set of pre-FSI computations. These pre-FSI computations include fluid-only and structure-only computations. The recipes introduced in (Tezduyar et al. 2007b) were used also in Tezduyar et al. (2008,

2009). A slightly modified recipe was introduced in Takizawa et al. (2010a), resulting in a simulation sequence called “S → F→S → FSI”, and this is the one that the T★AFSM has been using in its arterial simulations since then.

Structure → Fluid → Structure → FSI (S → F→S → FSI) sequence

Step 1: Generate the structure mesh based on the shape of the unstressed structure.

Step 2: Compute the structural deformation with a uniform fluid pressure held steady at a value close to 80 mm Hg.

- Structural deformation can be determined with a steady-state computation or a time-dependent computation that eventually yields a steady-state solution.
- For the steady-state computation, $\Delta t \rightarrow \infty$ and $\alpha = 0$ in Eq. (23) in Tezduyar et al. (2011), the number of time steps is one, and the initial displacement, velocity and acceleration are set to zero.

Step 3: Generate the fluid mesh based on the shape of the deformed structure.

Step 4: Compute a developed flow field while holding the structure from Step 2 rigid.

- The outflow traction is set to a value close to 80 mm Hg.
- The inflow velocity is set to a value corresponding to the outflow traction.

Step 5: Recompute the structural deformation, with the fluid stresses at the interface held steady at their values from Step 4, and simultaneously update the fluid mesh.

- Structural deformation can be determined with one of the two choices we had in Step 2.

Step 6: Compute the FSI with the same inflow and outflow conditions used in Step 4, with the initial condition for the flow velocity coming from Step 4.

Step 7: Compute the FSI with the inflow and outflow conditions pulsating.

6 Computational Results

All computations were carried out in a parallel computing environment and were completed without any remeshing. The fully discretized, coupled fluid and structural mechanics and mesh-moving equations are solved with the quasi-direct coupling technique (see Sect. 5.2 in Tezduyar and Sathe 2007). In solving the linear equation systems involved at every nonlinear iteration, the GMRES search technique (Saad and Schultz 1986) is used with a diagonal preconditioner.

6.1 WSS Calculations with Refined Meshes

The two different fluid mechanics meshes used in Tezduyar et al. (2010) were a “coarse” mesh with 15,850 nodes and 88,573 four-node tetrahedral elements, and a

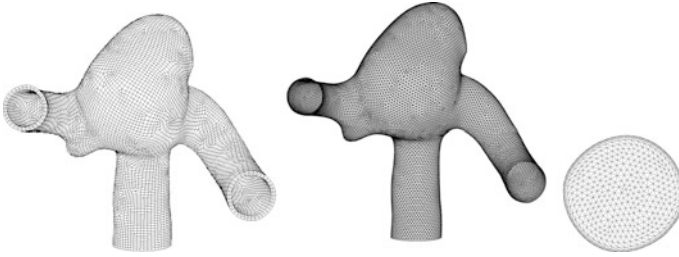


Fig. 3 A bifurcating middle cerebral artery segment with aneurysm. Fine structural mechanics mesh when the outflow pressure is maximum (*left*). Fine fluid mechanics mesh at the fluid–structure interface (*center*) and the inflow plane (*right*)

“medium” mesh with 22,775 nodes and 128,813 four-node tetrahedral elements. The medium mesh has four layers of elements with higher refinement near the arterial wall, with the thickness of the first layer being approximately 0.02 mm. The progression factor is 1.75. The coarse mesh has one layer of elements with a uniform thickness of approximately 0.2 mm. The coarse and medium meshes have the same number of nodes and elements at the fluid–structure interface: 3,057 nodes and 6,052 three-node triangular elements. The computations reported in Takizawa et al. (2010b) were based on the same artery model as the one used in Tezduyar et al. (2010) and involved basically three new features. The new features were (a) carrying out higher-resolution FSI computations with more refined fluid and structure meshes, (b) calculating the WSS with a new technique, as described in Sect. 2.2, and c) reporting OSI values that were calculated with a new technique, as described in Sect. 2.3. We describe the computations from Takizawa et al. (2010b). Two structural mechanics meshes are used. The “coarse” structure mesh consists of 8,067 nodes and 5,316 eight-node hexahedral elements, with 2,689 nodes and 2,658 four-node quadrilateral elements on the fluid–structure interface. The “fine” structure mesh consists of 30,732 nodes and 20,366 eight-node hexahedral elements, with 10,244 nodes and 10,183 four-node quadrilateral elements on the fluid–structure interface and two layers of elements across the arterial wall. It is shown in Fig. 3. The reason behind using a more refined fluid mechanics mesh in the higher-resolution FSI computations reported in Takizawa et al. (2010b) was to increase the accuracy of the WSS calculations by increasing the fluid mechanics mesh refinement also on the arterial wall, not just in the normal direction near the arterial wall. As pointed out in Takizawa et al. (2010b), this would normally make sense only if the structural mechanics mesh has comparable refinement. The refined structural mechanics mesh introduced in Takizawa et al. (2010b), which is shown in Fig. 3, served that purpose. The “fine” fluid mechanics mesh has 138,713 nodes and 823,756 four-node tetrahedral elements. It has 11,713 nodes and 23,304 threenode triangular elements at the fluid–structure interface, which is shown in Fig. 3. The fine mesh, just like the medium mesh, has four layers of elements with higher refinement near the arterial wall. The thickness of the first layer is approximately 0.02 mm and the progression factor is 1.75 (see Fig. 3).

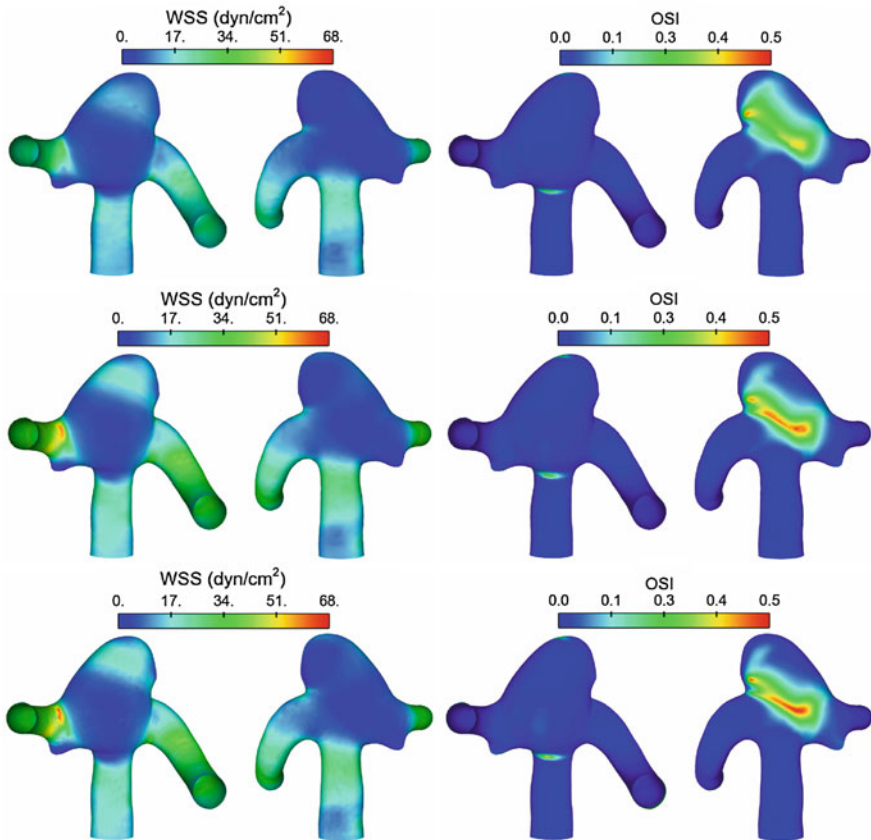


Fig. 4 A bifurcating middle cerebral artery segment with aneurysm. Time-averaged WSS (*left*) and OSI (*right*) for the coarse (*top*), medium (*middle*) and fine (*bottom*) meshes

The computations were carried out with the SSTFSI-TIP1 technique (see Remarks 8 and 16 in (Tezduyar et al. 2011)) and the SUPG test function option WTSA (see Remark 2 in (Tezduyar et al. 2011)). The stabilization parameters used are those given by Eqs. (12)–(18) in Tezduyar et al. (2011). The time-step size is 3.333×10^{-3} s for the coarse and medium meshes and 1.667×10^{-3} s for the fine mesh. For all three meshes the number of nonlinear iterations per time step is 6. For the fluid + structure block the number of GMRES iterations per nonlinear iteration is 300 for the coarse and medium meshes and 600 for the fine mesh. For all six nonlinear iterations the fluid scale is set to 1.0 and the structure scale to 50. For the mesh moving block the number of GMRES iterations is 30. Good mass balance is achieved in all computations. This was verified by comparing the rate of change for the artery volume and the difference between the volumetric inflow and outflow rates. The pictures showing that can be found in Takizawa et al. (2010b). Figure 4 shows, for the three meshes, the time-averaged WSS and the OSI.

Table 1 A bifurcating middle cerebral artery segment with aneurysm

Mesh	Peak systole		Time average		
	Max	Mean	Max	Mean	Min
Coarse	102	37	32	12.53	0.16
Medium	237	54	60	16.76	0.32
Fine	263	53	68	16.53	0.24

WSS (dyn/cm^2) for the coarse, medium and fine meshes. Spatial maximum and mean at peak systole, and spatial maximum, mean and minimum of time-averaged values.

Fig. 5 A bifurcating middle cerebral artery segment with aneurysm. Streamlines computed with the fine mesh at $t = 0.268$ s (*left*) and $t = 0.448$ s (*right*). The *streamlines* illustrate the WSS direction changes

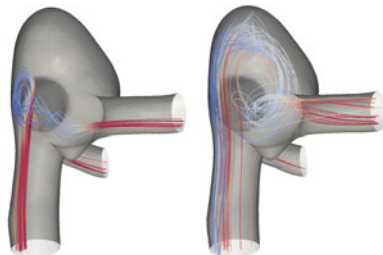


Table 1 shows the maximum, mean and minimum values of the WSS for the three meshes. The higher OSI region indicates flow direction changes over the cardiac cycle. The medium and fine mesh results are in good agreement. Figure 5 shows typical streamlines around the higher OSI region at $t = 0.268$ s (accelerating flow) and $t = 0.448$ s (decelerating flow). When the flow accelerates, a vortex forms, which results in a downward WSS. Conversely, when the flow decelerates, the vortex dissipates and the flow creates an upward WSS. As pointed out in Takizawa et al. (2010b), one of the reasons behind this change in flow characteristics is the motion of the aneurysm. We observe an aneurysm movement towards the left in Fig. 5 when the flow accelerates.

6.2 Computations with the New Techniques for the EZP Geometry, Wall Thickness and Boundary-Layer Element Thickness

We present a sample from a wide set of patient-specific cerebral-aneurysm models used in (Takizawa et al. 2012), where the shrinking amount in the EZP process, the arterial wall thickness, and the thickness of the layers of refined fluid mechanics mesh are determined based on the solution of the Laplace's equation over the surface mesh covering the lumen (see Sect. 3.2). The length scales used in conjunction with the trial ratios for the inflow and outflow boundaries are the lumen diameters at those ends. The value specified for the thickness of the first layer of

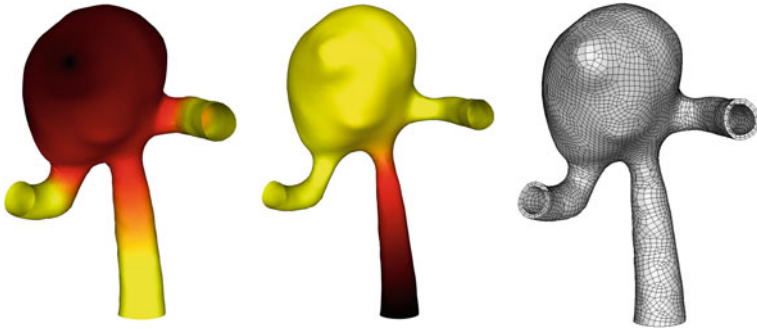


Fig. 6 Model-M6Acom. EZP shrinking amount over the surface (lumen) extracted from the medical image (*left*), wall thickness over the shrunk lumen (*middle*), and structure mesh at zero pressure (*right*). The *color range* represents a value range that increases from *light* to *dark*

elements at the inflow and outflow boundaries is $0.007 \times$ (lumen diameter at those ends). In these computations, the volumetric flow rate is specified by using the scaling technique introduced in Remark 6. Figure 6 shows the EZP shrinking amount, wall thickness, and structure mesh for the arterial model, which we call Model-M6Acom. The diameter of the arterial lumen is 3.13 mm at the inflow end, and 2.12 and 2.11 mm at the outflow ends. The structure mesh has two layers of elements across the arterial wall. For the layers of refined fluid mechanics mesh near the arterial wall, the progression factor is 1.75. Figure 7 shows the fluid mechanics mesh at the lumen, thickness of the first layer of elements near the arterial wall, and the mesh at the inflow plane. The node and element numbers for the model are given in Table 2. The Womersley parameter (defined in Sect. 4.2) is 2.0. This is based on the duration of one cardiac cycle (1 s) and the representative

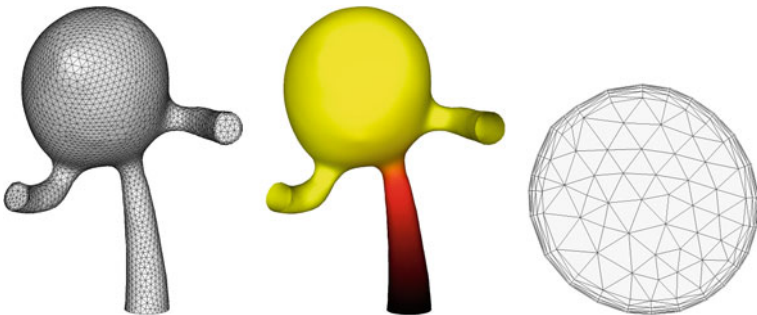
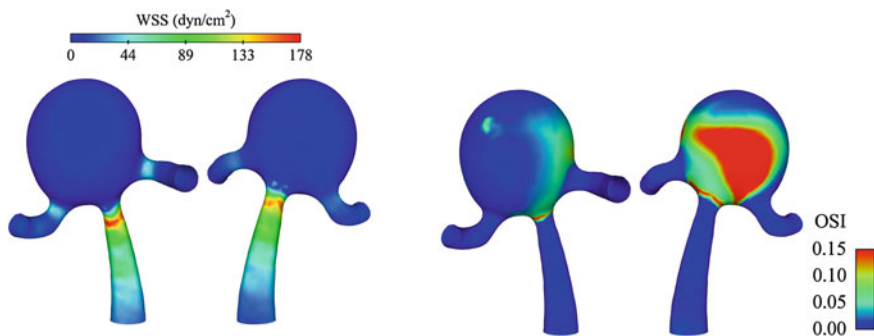


Fig. 7 Model-M6Acom. Fluid mechanics mesh at the lumen and outflow planes (*left*), thickness of the first layer of elements near the arterial wall (*middle*), and the mesh at the inflow plane (*right*). All pictures are from the starting point of our computation cycle. The *color range* represents a value range that increases from *light* to *dark*

Table 2 Model-M6Acom. Number of nodes and elements. Here nn and ne are number of nodes and elements, respectively

		M6Acom	
Structure	Volume	nn	17,574
		ne	11,650
	Interface	nn	5,858
		ne	5,825
Fluid	Volume	nn	33,040
		ne	192,112
	Interface	nn	3,528
		ne	6,996

**Fig. 8** Model-M6Acom. WSS when the volumetric flow rate is maximum and OSI

diameter is calculated from the inflow area corresponding to the shape when inflated to the average pressure.

The computations were carried out with the SSTFSI-TIP1 technique (see Remarks 8 and 16 in Tezduyar et al. 2011) and the SUPG test function option WTSA (see Remark 2 in Tezduyar et al. 2011). The stabilization parameters used are those given by Eqs. (12)–(18) in Tezduyar et al. (2011). The SSP option is used fully (see Remarks 21 and 22 in Tezduyar et al. 2011). The time-step size is 3.333×10^{-3} s. The number of nonlinear iterations per time step is 6. The number of GMRES iterations per nonlinear iteration for the fluid + structure block was chosen such that mass balance is satisfied to within at most 5 % for each case. The number of GMRES iterations is 300, and this was sufficient for obtaining good mass balance. For all six nonlinear iterations the fluid scale is 1.0 and the structure scale is 100. For the mesh moving block the number of GMRES iterations is 30. Figure 8 shows the WSS when the volumetric flow rate is maximum and the OSI. The OSI is calculated with the technique that excludes rigid-body rotations from the calculation (see Sect. 2.3).

7 Concluding Remarks

We presented an overview of the special techniques developed earlier by the T★AFSM for FSI modeling of patient-specific cerebral aneurysms. The core techniques are the DSD/SST and SSTFSI methods. The special FSI techniques developed in conjunction with the core techniques include (a) techniques for calculating an EZP geometry, (b) a special mapping technique for specifying the inflow velocity profile, (c) techniques for using variable arterial wall thickness, (d) techniques for building layers of refined fluid mechanics mesh near the arterial walls, (e) pre-FSI computation techniques that improve the convergence of the FSI computations, (f) techniques for calculation of the WSS and OSI, and (g) arterial-surface extraction and boundary condition techniques. With results from earlier computations carried out by the T★AFSM, we demonstrated how these techniques work. We also presented the special arterial FSI techniques developed and implemented very recently by the T★AFSM and the computational results obtained with these techniques. Overall, this review article shows that the space–time arterial FSI techniques developed by the T★AFSM can deal effectively with the computational challenges involved in arterial fluid mechanics problems.

Acknowledgments This work was supported in part by a seed grant from the Gulf Coast Center for Computational Cancer Research funded by John & Ann Doerr Fund for Computational Biomedicine. It was also supported in part by the Rice Computational Research Cluster funded by NSF Grant CNS-0821727. The 3DRA research at the Memorial Hermann Hospital University of Texas Medical School at Houston was supported by generous a funding from the Weatherhead Foundation. We thank Dr. Ryo Torii (University College London) for the inflow velocity data used in the computations and the arterial geometry used in [Sect. 6.1](#).

References

- Bazilevs Y, Hsu M-C, Benson D, Sankaran S, Marsden A (2009) Computational fluid–structure interaction: methods and application to a total cavopulmonary connection. *Comput Mech* 45:77–89
- Bazilevs Y, Hsu M-C, Zhang Y, Wang W, Kvamsdal T, Hentschel S, Isaksen J (2010) Computational fluid–structure interaction: methods and application to cerebral aneurysms. *Biomech Model Mechanobiol* 9:481–498
- Brooks AN, Hughes TJR (1982) Streamline upwind/Petrov–Galerkin formulations for convection dominated flows with particular emphasis on the incompressible Navier–Stokes equations. *Comput Methods Appl Mech Eng* 32:199–259
- Frank O (1899) Die grundform des arteriellen pulses. *Zeitung fur Biologie* 37:483–586
- Green AE, Naghdi PM (1976) A derivation of equations for wave propagation in water of variable depth. *J Fluid Mech* 78:237–246

- Huang H, Virmani R, Younis H, Burke AP, Kamm RD, Lee RT (2001) The impact of calcification on the biomechanical stability of atherosclerotic plaques. *Circulation* 103:1051–1056
- Hughes TJR, Liu WK, Zimmermann TK (1981) Lagrangian–Eulerian finite element formulation for incompressible viscous flows. *Comput Methods Appl Mech Eng* 29:329–349
- Johnson AA, Tezduyar TE (1994) Mesh update strategies in parallel finite element computations of flow problems with moving boundaries and interfaces. *Comput Methods Appl Mech Eng* 119:73–94
- McPhail T, Warren J (2008) An interactive editor for deforming volumetric data. International conference on biomedical engineering 2008, Singapore, pp 137–144
- Saad Y, Schultz M (1986) GMRES: a generalized minimal residual algorithm for solving nonsymmetric linear systems. *SIAM J Sci Stat Comput* 7:856–869
- Takizawa K, Brummer T, Tezduyar TE, Chen PR (2012) A comparative study based on patient-specific fluid–structure interaction modeling of cerebral aneurysms. *J Appl Mech* 79:010908
- Takizawa K, Christopher J, Tezduyar TE, Sathe S (2010a) Space–time finite element computation of arterial fluid–structure interactions with patientspecific data. *Int J Numer Methods Biomed Eng* 26:101–116
- Takizawa K, Moorman C, Wright S, Christopher J, Tezduyar TE (2010b) Wall shear stress calculations in space–time finite element computation of arterial fluid–structure interactions. *Comput Mech* 46:31–41
- Takizawa K, Moorman C, Wright S, Purdue J, McPhail T, Chen PR, Warren J, Tezduyar TE (2011) Patient-specific arterial fluid–structure interaction modeling of cerebral aneurysms. *Int J Numer Meth Fluids* 65:308–323
- Taylor CA, Hughes TJR, Zarins CK (1998) Finite element modeling of three-dimensional pulsatile flow in the abdominal aorta: relevance to atherosclerosis. *Ann Biomed Eng* 158:975–987
- Tezduyar T, Aliabadi S, Behr M, Johnson A, Mittal S (1993) Parallel finite-element computation of 3D flows. *Computer* 26(10):27–36
- Tezduyar TE (1992) Stabilized finite element formulations for incompressible flow computations. *Adv Appl Mech* 28:1–44
- Tezduyar TE (2004) Finite element methods for fluid dynamics with moving boundaries and interfaces. In: Stein E, Borst RD, Hughes TJR (eds) *Encyclopedia of computational mechanics*, vol 3: Fluids, Chap. 17. John Wiley & Sons, New York
- Tezduyar TE, Cragin T, Sathe S, Nanna B (2007a) FSI computations in arterial fluid mechanics with estimated zero-pressure arterial geometry. In: Onate E, Garcia J, Bergan P, Kvamsdal T (eds) *Marine 2007*. CIMNE, Barcelona
- Tezduyar TE, Sathe S (2007) Modeling of fluid–structure interactions with the space–time finite elements: Solution techniques. *Int J Numer Meth Fluids* 54:855–900
- Tezduyar TE, Sathe S, Cragin T, Nanna B, Conklin BS, Pausewang J, Schwaab M (2007b) Modeling of fluid–structure interactions with the space–time finite elements: arterial fluid mechanics. *Int J Numer Meth Fluids* 54:901–922
- Tezduyar TE, Sathe S, Keedy R, Stein K (2006) Space–time finite element techniques for computation of fluid–structure interactions. *Comput Methods Appl Mech Eng* 195:2002–2027
- Tezduyar TE, Sathe S, Schwaab M, Conklin BS (2008) Arterial fluid mechanics modeling with the stabilized space–time fluid–structure interaction technique. *Int J Numer Meth Fluids* 57:601–629
- Tezduyar TE, Schwaab M, Sathe S (2007c) Arterial fluid mechanics with the sequentially-coupled arterial FSI technique. In: Onate E, Papadrakakis M, Schrefler B (eds) *Coupled problems 2007*. CIMNE, Barcelona

- Tezduyar TE, Schwaab M, Sathé S (2009) Sequentially-coupled arterial fluid–structure interaction (SCAFSI) technique. *Comput Methods Appl Mech Eng* 198:3524–3533
- Tezduyar TE, Takizawa K, Brummer T, Chen PR (2011) Space–time fluid–structure interaction modeling of patient-specific cerebral aneurysms. *Int J Numer Methods Biomed Eng* 27:1665–1710
- Tezduyar TE, Takizawa K, Moonman C, Wright S, Christopher J (2010) Multiscale sequentially-coupled arterial FSI technique. *Comput Mech* 46:17–29
- Torii R, Oshima M, Kobayashi T, Takagi K, Tezduyar TE (2004) Influence of wall elasticity on image-based blood flow simulation. *Jpn Soc Mech Eng J A* 70:1224–1231 (in Japanese)
- Torii R, Oshima M, Kobayashi T, Takagi K, Tezduyar TE (2011) Influencing factors in image-based fluid–structure interaction computation of cerebral aneurysms. *Int J Numer Meth Fluids* 65:324–340
- Womersley JR (1955) Method for the calculation of velocity, rate of flow and viscous drag in arteries when the pressure gradient is known. *J Physiol* 127:553–563

A Full-Eulerian Approach for the Fluid–Structure Interaction Problem

Satoshi Ii, Kazuyasu Sugiyama, Shu Takagi and Yoichiro Matsumoto

Abstract A fixed-mesh method is developed for the fluid–structure interaction problem, based on a fully Eulerian formulation. A material phase for an elastic solid/membrane immersed in a fluid field is represented by a volume-fraction function (or phase function) without any material point. In addition, its material deformation at a current configuration is given by solving a transport equation for the left Cauchy-Green deformation tensor on a fixed Eulerian mesh. A set of partial differential equations in a mixture form is monolithically discretized by a finite difference/volume method which has been developed in the field of the multiphase flow analysis. The present fully Eulerian method does not require a mesh generation, mesh moving and remeshing (or reconnection) procedures, thus it straightforwardly addresses not only biological problems in which geometric data are given by a measurement image, but also suspension flows in which soft materials are largely moved and deformed in a fluid, e.g. blood flow with multiple red blood cells and platelets, without any numerical or technical modification. A numerical accuracy of the present method is well investigated in a grid refinement manner and also in comparisons with that of the existing Lagrangian methods.

S. Ii (✉)

Graduate School of Engineering Science, Osaka University, 1-3 Machikaneyama,
Toyonaka 560-8531, Japan
e-mail: sii@me.es.osaka-u.ac.jp

K. Sugiyama

Advanced Center for Computing and Communication, RIKEN, 2-1 Hirosawa,
Wako 351-0198, Japan
e-mail: kazuyasu.sugiyama@riken.jp

S. Takagi · Y. Matsumoto

Department of Mechanical Engineering, The University of Tokyo, 7-3-1 Hongo,
Tokyo 113-8656, Japan
e-mail: takagi@mech.t.u-tokyo.ac.jp

Y. Matsumoto

e-mail: ymats@fel.t.u-tokyo.ac.jp

1 Introduction

Computational studies for the fluid–structure interaction (FSI) problem are required in many fields, e.g. biological systems, and industrial processes. Conventionally, the computational fluid dynamics is more commonly described in an Eulerian way, whereas the computational structure dynamics is more straightforward and described in a Lagrangian way. The coupling of the fluid and structure dynamics is a formidable task because of the difference in the numerical framework.

Concerning a simulation scale, the nonzero Reynolds number flows require that the computational mesh is set out over the entire domain if the partial differential equation is numerically solved for FSI problems. There are currently several major approaches classified, with respect to the computational treatment, on how the kinematic and dynamic interactions are coupled on the moving interface. One of the most accurate approaches is raised as arbitrary Lagrangian–Eulerian (ALE) (Hirt et al. 1974; Belytschko 1980; Hughes et al. 1981) or deforming-spatial-domain/stabilized space–time (DSD/SST) (Tezduyar et al. 1992a, b, 2007; Takizawa and Tezduyar 2011) technique, in which the body-fitted mesh is used. These approaches are referred to as an interface-tracking approach, in which the surface mesh is shared between the fluid and solid phases, and thus automatically satisfies the kinematic condition. However, the computational domain has to be remeshed as the object is greatly distorted, and it is not always an easy task to keep the load of each computational core balanced.

An alternative to the interface-tracking approach is an Eulerian–Lagrangian approach, in which the fluid and solid phases are separately formulated on the fixed Eulerian and Lagrangian grids, respectively. A noticeable contribution is the development of the immersed boundary (IB) method by Peskin (1972, 2002), who introduces a smoothed approximation of Dirac δ function for communication between the Eulerian and Lagrangian quantities, and demonstrated the landmark simulation of the blood flow around heart valves (Peskin 1972). The fictitious domain (FD) method (Glowinski et al. 1999; Yu 2005) and PHYSALIS (Takagi et al. 2003) for specific multiphase flow problems with circular or spherical particles are also classified into the Eulerian–Lagrangian approach. The IB and FD methods have been applied to a variety of studies, for example, moving rigid particles (Glowinski et al. 1999; Yuki et al. 2007), moving flexible bodies (Mori and Peskin 2008; Zhao et al. 2008), elastic membrane (Eggleton and Popel 1998; Lac et al. 2004; Bagchi 2007; Sui et al. 2008; Takagi et al. 2009; Gong et al. 2009), and restricted diffusion with permeable interfaces (Huang et al. 2009). The IB method has also inspired many researchers to propose a number of improved methods (Zhang et al. 2004; LeVeque and Li 1994; Li and Lai 2001; Takeuchi et al. 2010).

Considering the utilization of voxel data converted from the medical image data of MRI or CT, it is straightforward to develop the full Eulerian finite difference methods, which directly access the voxel data to describe the boundary on the fixed Cartesian mesh and avoid difficulty in mesh generation and reconstruction. Several

Eulerian solvers for modeling the solid deformation have been proposed for linear elastic materials (Xiao and Yabe 1999), for elasto-plastic materials (Udaykumar et al. 2003; Okazawa et al. 2007), for hyperelastic materials (Van Hoogstraten et al. 1991; Liu and Walkington 2001; Dunne 2006; Cottet et al. 2008; Richter and Wick 2010).

Recently, Sugiyama et al. (2010a, 2011) has developed a novel full-Eulerian FSI solver for biological problems, and it has been extended to a fluid and wavy wall interaction (Nagano et al. 2010), fluid and stiff material interaction (Ii et al. 2011) and fluid and membrane interaction (Ii et al. 2012a, b). Considering that the voxel data contain the volume fractions of fluid and solid, we apply the volume-of-fluid/volume-fraction (VOF) formulation (Hirt and Nichols 1981) to describing the multicomponent geometry. Because the Eulerian formulation lacks of the material points to link between the reference and current configurations, we need to devise a method to quantify the level of deformation. To this end, we introduce the left Cauchy-Green deformation tensor defined on each grid point, and temporally update it. The full-Eulerian method has been reviewed by Takagi et al. (2012).

In this Chapter, a basic formulation of the full-Eulerian FSI method proposed by Sugiyama et al. (2011) is described, and numerical results are discussed. Moreover, further developments of the full-Eulerian FSI method are shown in respect to the numerical method for the fluid–membrane interaction (Ii et al. 2012a), less-dissipative advection method (Ii et al. 2012c), quasi-implicit formulation (Ii et al. 2011) and particle-in-cell based approach (Sugiyama et al. 2010b), and also application for a suspension flow of the multiple flexible capsules (Ii et al. 2012b).

2 Full-Eulerian Approach for the Fluid–Solid Interaction

2.1 Eulerian Versus Lagrangian Frames

2.1.1 Material Phase

Let's consider that Ω_f is a fluid region and Ω_s is a solid region, and introduce an indicator function $I_s(\mathbf{x}, t)$, which is being to either 0 or 1 for $\mathbf{x} \in \Omega_f$ or $\mathbf{x} \in \Omega_s$. Then, on a control volume $\delta V(\mathbf{x})$, the volume-fraction or volume-of-fluid (VOF) function of a solid is defined as

$$\phi_s(\mathbf{x}, t) = \frac{1}{|\delta V(\mathbf{x})|} \int_{\delta V(\mathbf{x})} I_s(\mathbf{x}', t) d\mathbf{x}', \quad (1)$$

According to a kinematic relation:

$$d_t \mathbf{x} = \mathbf{v}, \quad (2)$$

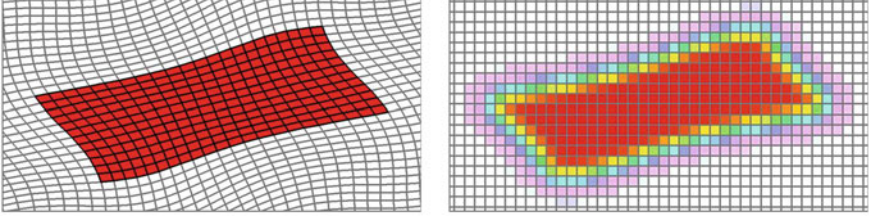


Fig. 1 Comparison for a material phase (volume fraction ϕ_s) in Lagrangian versus Eulerian frames

(d_t indicates a material derivative, i.e. $\partial_t + \mathbf{v} \cdot \nabla$, with a partial temporal-derivative ∂_t), the VOF function is updated by solving a following advection equation given in the Eulerian form.

$$\partial_t \phi_s + \mathbf{v} \cdot \nabla \phi_s = 0. \quad (3)$$

Here, $\mathbf{v}(\mathbf{x}, t)$ is the velocity vector defined in the field. Expressions (1) and (2) are mathematically equivalent to describe the material interface with a same initial condition and velocity field, except for a difference of numerical treatments.

In a simple deformation problem, in which a square solid is deformed by a given velocity field, it is confirmed that the material phases based on both Lagrangian (2) and Eulerian (3) ways are in good agreement (Fig. 1). It therefore shows the material phase can be addressed in the Eulerian way as far as an appropriate numerical method to update the VOF function.

2.1.2 Solid Deformation

Based on a basic theory on a finite deformation (e.g. Belytschko 1980; Holzapfel 2000, HolBonet and Wood 2008), the deformation gradient tensor is defined as

$$\mathbf{F} = \frac{\partial \mathbf{x}}{\partial \mathbf{X}}, \quad (4)$$

where, \mathbf{X} and \mathbf{x} denote a reference and current coordinate systems. Due to a kinematic relation (2), the deformation tensor \mathbf{F} is updated by

$$\partial_t \mathbf{F} + \mathbf{v} \cdot \nabla \mathbf{F} = \nabla \mathbf{v}^T \cdot \mathbf{F}. \quad (5)$$

Then, the left Cauchy-Green deformation tensor $\mathbf{B} = \mathbf{F} \cdot \mathbf{F}^T$, which is explicitly shown to describe the Cauchy stress of a hyperelastic material (described later in detail), is updated by a following transport equation (based on the upper-convected time derivative or Oldroyd derivative) in the Eulerian way.

$$\partial_t \mathbf{B} + \mathbf{v} \cdot \nabla \mathbf{B} = \mathbf{B} \cdot \nabla \mathbf{v} + \nabla \mathbf{v}^T \cdot \mathbf{B}. \quad (6)$$

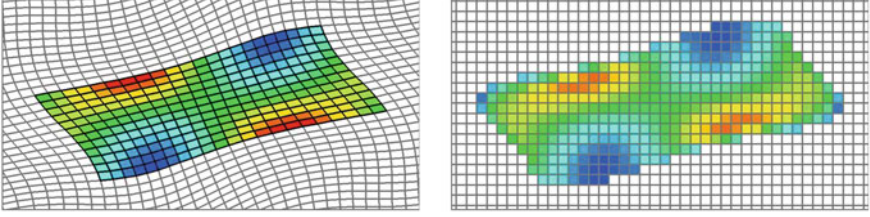


Fig. 2 Comparison for a deformation (the first invariant of the left Cauchy-Green deformation tensor, $\text{tr}(\mathbf{B})$) in Lagrangian versus Eulerian frames

Similarly, a numerical difference between both Lagrangian and Eulerian approaches is considerable. In the Lagrangian way, \mathbf{F} is first calculated by using the material points updated by (2) in a local coordinate system ξ with a bilinear basis function on a quadrangular mesh, that is $\mathbf{F} = (\partial \mathbf{x} / \partial \xi) \cdot (\partial \mathbf{X} / \partial \xi)^{-1}$, and then \mathbf{B} is calculated by $\mathbf{F} \cdot \mathbf{F}^T$. In the Eulerian way, \mathbf{B} is directly updated by solving (6). Figure 2 shows distributions of the first invariant of \mathbf{B} , i.e. $\text{tr}(\mathbf{B})$. It is also found that numerical solutions at a certain time are competitive except for the material interface due to a cut-off manipulation (described later).

2.2 Basic Formulation

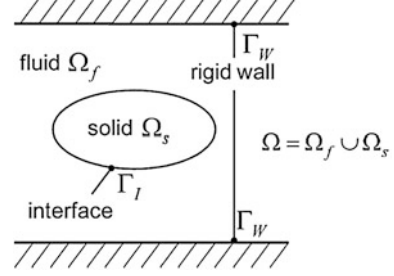
2.2.1 Governing Equations and Fluid–Solid Mixture Representations

Figure 3 shows the notation of the fluid–structure systems to be addressed. Let us consider an incompressible hyperelastic domain Ω_s submerged in an incompressible fluid domain Ω_f , which is bounded with rigid flat walls. Hereafter, the suffices f and s stand for the fluid and solid phases, respectively. We focus on the system, where the walls are in contact with only fluid at the boundary Γ_w , and the moving wall drives the fluid and solid motions. Both fluid and solid are homogeneous, i.e. the material properties are uniform inside each phase. We shall restrict our attention to the kinematic and dynamic interactions at the fluid–structure interface Γ_I . The fluid and solid densities are assumed to be identical ($\rho_f = \rho_s = \rho$) as in many analyses for biological systems. For incompressible fluid and solid, the governing equations consist of the mass and momentum conservations:

$$\begin{aligned} \nabla \cdot \mathbf{v}_f &= 0, \quad \mathbf{x} \in \Omega_f, \\ \nabla \cdot \mathbf{v}_s &= 0, \quad \mathbf{x} \in \Omega_s, \end{aligned} \quad (7)$$

$$\begin{aligned} \rho(\partial_t \mathbf{v}_f + \mathbf{v}_f \cdot \nabla \mathbf{v}_f) &= \nabla \cdot \boldsymbol{\sigma}_f, \quad \mathbf{x} \in \Omega_f, \\ \rho(\partial_t \mathbf{v}_s + \mathbf{v}_s \cdot \nabla \mathbf{v}_s) &= \nabla \cdot \boldsymbol{\sigma}_s, \quad \mathbf{x} \in \Omega_s, \end{aligned} \quad (8)$$

Fig. 3 Abstract setting for the FSI problem considered in the present study



where \mathbf{v} denotes the velocity vector, t the time, ρ the density, and $\boldsymbol{\sigma}$ the Cauchy stress tensor. The no-slip condition is imposed on the fluid-wall boundary, namely

$$\mathbf{v}_f = \mathbf{V}_W, \quad \mathbf{x} \in \Gamma_W, \quad (9)$$

where \mathbf{V}_W denotes the wall velocity. The kinematic and dynamic interactions between the fluid and solid phases are determined by continuity in the velocity and in the traction force at the fluid–structure interface, namely

$$\mathbf{v}_f = \mathbf{v}_s, \quad \mathbf{x} \in \Gamma_I, \quad (10)$$

$$\boldsymbol{\sigma}_f \cdot \mathbf{n} = \boldsymbol{\sigma}_s \cdot \mathbf{n}, \quad \mathbf{x} \in \Gamma_I, \quad (11)$$

where \mathbf{n} denotes the unit normal vector at the interface.

In the practical numerical procedure based on the full Eulerian perspective, instead of separately partitioned two velocity fields \mathbf{v}_f and \mathbf{v}_s respectively in Ω_f and in Ω_s , it is convenient to introduce a monolithic velocity vector \mathbf{v} applied to the entire domain $\Omega (= \Omega_f \cup \Omega_s)$. In multiphase flow simulations, one set of governing equations for the whole flow field, known as a one-fluid formulation (Tryggvason et al. 2007), is often employed to be discretized on a fixed grid. In the present study, such an idea is applied to the fluid–structure system by using \mathbf{v} , that is here referred to as a one-continuum formulation. The one-continuum formulation would immediately satisfy (10) because \mathbf{v} is supposed to be continuous across the interface Γ_I . Following the volume averaging procedure (Takeuchi et al. 2010), we establish the velocity field \mathbf{v} as $\mathbf{v} = (1 - \phi_s)\mathbf{v}_f + \phi_s\mathbf{v}_s$, where ϕ_s is the volume fraction of solid inside a computation cell:

$$\phi_s(x, y, z) = \frac{1}{\Delta_x \Delta_y \Delta_z} \int_{-\Delta_x/2}^{\Delta_x/2} d\hat{x} \int_{-\Delta_y/2}^{\Delta_y/2} d\hat{y} \int_{-\Delta_z/2}^{\Delta_z/2} d\hat{z} I_s(x + \hat{x}, y + \hat{y}, z + \hat{z}), \quad (12)$$

where Δ_α ($\alpha = x, y, z$) denotes the grid size, the suffices x, y and z stand for the respective directions.

We may regard the volume fraction ϕ_s as a smoothed Heaviside function at the grid scale. The distribution of the volume fraction reveals $\phi_s = 0$ in fluid, $\phi_s = 1$ in solid, and $0 < \phi_s < 1$ for the grid involving the fluid–solid interface. The

mixture representation is employed in the present study. Taking the weighted average with respect to ϕ_s , we write the mixture stress $\boldsymbol{\sigma}$ as

$$\boldsymbol{\sigma} = -p\mathbf{I} + (1 - \phi_s)\boldsymbol{\sigma}'_f + \phi_s\boldsymbol{\sigma}'_s, \quad \mathbf{x} \in \Omega, \quad (13)$$

where \mathbf{I} denotes the unit tensor, and the prime on the second-order tensor stands for the deviatoric tensor, e.g. $\mathbf{T}' = \mathbf{T} - \text{tr}(\mathbf{T})/3$ for a tensor \mathbf{T} . For incompressible continua, the pressure p may be regarded as of a Lagrangian multiplier imposing the solenoidal condition over the whole velocity field. The Poisson equation will be solved to find the pressure field p , written in the one-continuum form, over the entire domain Ω . Since ϕ_s is smoothed at the grid scale and $\boldsymbol{\sigma}$ is supposed to be smoothly distributed over the entire domain, the expression (13) at $\phi_s = 1/2$ would satisfy the continuity of the traction force (11). Throughout this Chapter, the fluid component is assumed to be Newtonian, and thus the deviatoric stress of fluid is given by

$$\boldsymbol{\sigma}'_f = 2\mu_f\mathbf{D}, \quad (14)$$

where μ_f denotes the dynamic viscosity of fluid, and $\mathbf{D} = (\nabla\mathbf{v} + \nabla\mathbf{v}^T)/2$ the strain rate tensor. Instead of (7) and (8) with (10), (11) and (13), we solve the following equations in the one-continuum form over the entire domain:

$$\nabla \cdot \mathbf{v} = 0, \quad \mathbf{x} \in \Omega, \quad (15)$$

$$\rho(\partial_t\mathbf{v} + \mathbf{v} \cdot \nabla\mathbf{v}) = -p\mathbf{I} + (1 - \phi_s)\boldsymbol{\sigma}'_f + \phi_s\boldsymbol{\sigma}'_s, \quad \mathbf{x} \in \Omega, \quad (16)$$

with the updating equations for ϕ_s and \mathbf{B} in (3) and (6), respectively.

2.2.2 Constitutive Equations for Solid

We consider incompressible visco-hyperelastic materials undergoing only the isochoric motion. The deviatoric Cauchy stress of solid is expressed as

$$\boldsymbol{\sigma}'_s = 2\mu_s\mathbf{D} + \boldsymbol{\sigma}'_{sh}, \quad (17)$$

where the first term on the right-hand-side corresponds to the viscous contribution with dynamic viscosity μ_s . The second term $\boldsymbol{\sigma}'_{sh}$ corresponds to the hyperelastic contribution to be derived below. To formulate the constitutive equation, we refer to the general theories (e.g. Trapp 1971; Gurtin and Guidugli 1973; Simo et al. 1985) of constrained material. Choosing the Mooney–Rivlin expression (Mooney 1940; Rivlin 1948), and considering the nonlinearity up to $O(\mathbf{B}^2)$ in the deviatoric Cauchy stress, we write the hyperelastic strain energy potential W as

$$W(\mathbf{I}_B, \mathbf{\Pi}_B) = c_1(\mathbf{I}_B - 3) + c_2(\mathbf{\Pi}_B - 3) + c_3(\mathbf{I}_B - 3)^2, \quad (18)$$

where $I_B = \text{tr}(\mathbf{B})$ and $\Pi_B = (\text{tr}(\mathbf{B})^2 - \text{tr}(\mathbf{B} \cdot \mathbf{B}))/2$ denote invariants of the left/right Cauchy-Green deformation tensor. Utilizing the equivalence of the invariants between the left and right Cauchy-Green deformation tensors $\mathbf{C}(= \mathbf{F}^T \cdot \mathbf{F})$, we write the deviatoric Cauchy stress tensor as

$$\boldsymbol{\sigma}'_{sh} = 2 \left(\mathbf{F} \cdot \frac{\partial W}{\partial \mathbf{C}} \cdot \mathbf{F}^T \right)' = 2 \left(c_1 \mathbf{B}' + c_2 (I_B \mathbf{B} - \mathbf{B} \cdot \mathbf{B})' + 2c_3 (I_B - 3) \mathbf{B}' \right). \quad (19)$$

We will give several demonstrations afterward for some specific cases based on the *linear* Mooney–Rivlin, neo-Hookean and incompressible Saint–Venant–Kirchhoff materials. Note that all these materials obey (19). Linear Mooney–Rivlin material (Mooney 1940; Rivlin 1948) is given by setting $c_3 = 0$, and the neo-Hookean material, which is a particular case of the linear Mooney–Rivlin material, is given with the coefficients $c_1 = G/2$, $c_2 = 0$, $c_3 = 0$. As another typical hyperelastic material, we consider Saint–Venant–Kirchhoff material (Bonet and Wood 2008), which often models a thin but finite volume membrane. The constitutive equation is expressed as a simple extension of Hooke’s law, as defined by $c_1 = \mu_{\text{Lamé}}$, $c_2 = -\mu_{\text{Lamé}}/2$, $c_3 = (\lambda_{\text{Lamé}} + 2\mu_{\text{Lamé}})/8$, where $\mu_{\text{Lamé}}$ and $\lambda_{\text{Lamé}}$ are the Lamé constants.

It should be noted that when the tensor field \mathbf{B} is determined in a purely Eulerian manner, all the equations will be closed in the Eulerian form. One may use the transport Eq. (6) to update the \mathbf{B} field, however, it should be noticed that it is quite cumbersome to solve (6) from a numerical viewpoint, because \mathbf{B} exhibits rough distribution in the fluid domain Ω_f (Liu and Walkington 2001). The fluid element subject to a shearing motion is likely to elongate toward the extensional direction. Such an elongation causes a temporally exponential growth of some components of \mathbf{B} . To avoid the numerical instability brought by the exponential growth, we define the modified left Cauchy-Green deformation tensor:

$$\tilde{\mathbf{B}} = \phi^{1/2} \mathbf{B}, \quad (20)$$

and update it by solving

$$\partial_t \tilde{\mathbf{B}} + \mathbf{v} \cdot \nabla \tilde{\mathbf{B}} = \tilde{\mathbf{B}} \cdot \nabla \mathbf{v} + \nabla \mathbf{v}^T \cdot \tilde{\mathbf{B}}, \quad (21)$$

with the initial condition $\phi_s^{0.5} \mathbf{I}$. Further, to avoid the inevitable exponential growth at the cell near the interface Γ_I containing the fluid–solid mixture, and to obtain a viable compromise between the numerical consistency and stability, we introduce a threshold ϕ_{\min} and enforce

$$\tilde{\mathbf{B}} = 0, \quad \text{for } \phi_s < \phi_{\min}. \quad (22)$$

In the present study, we set ϕ_{\min} between 0.01 and 0.1. From (21), the resulting deviatoric stress of solid multiplied by ϕ_s , which is involved in (17) with (19), is expressed as

$$\phi_s \boldsymbol{\sigma}'_s = 2\phi_s \mu_s \mathbf{D} + 2 \left(c_1 \phi_s^{1/2} \tilde{\mathbf{B}} + c_2 (\text{tr}(\tilde{\mathbf{B}}) \tilde{\mathbf{B}} - \tilde{\mathbf{B}} \cdot \tilde{\mathbf{B}}) + 2c_3 (\text{tr}(\tilde{\mathbf{B}}) - 3) \tilde{\mathbf{B}} \right)', \quad (23)$$

which can be evaluated together with the temporally updated modified left Cauchy-Green deformation tensor from (21).

2.2.3 Numerical Methods

The basic equations are solved by a finite difference method on a fixed Cartesian grid. We follow the simplified MAC (SMAC) algorithm (Amsden and Harlow 1970) to find the pressure field and simultaneously to satisfy the solenoidal condition (15) with the staggered arrangement (Harlow and Welch 1965), where the velocity component is located on the cell face, and the pressure and solid volume fraction at the cell center. For the tensor component, the diagonal components are defined on the cell center, while the non-diagonal components are on the cell apex.

Here, the time-stepping algorithm to update the variables at the $(n + 1)$ th time level from the (n) th time level is briefly explained. Following the SMAC method, corresponding to a standard incompressible fluid flow algorithm, with an incremental pressure correction applied to the finite difference scheme, we decompose the time-stepping into three steps. In the first step, the volume fraction and the modified left Cauchy-Green deformation tensor are updated by

$$\phi_s^{n+1} = \phi_s^n + \Delta t R_\phi(\phi_s^n, \phi_s^{n-1}, \mathbf{v}^n, \mathbf{v}^{n-1}), \quad (24)$$

$$\tilde{\mathbf{B}}^{n+1} = \tilde{\mathbf{B}}^n + \Delta t R_{\mathbf{B}}(\tilde{\mathbf{B}}^n, \tilde{\mathbf{B}}^{n-1}, \mathbf{v}^n, \mathbf{v}^{n-1}), \quad (25)$$

where R_ϕ and $R_{\mathbf{B}}$ indicate the advection and right-hand-side terms of Eqs. (3) and (21) in the discretization level with adequate spatial and temporal methods. In the second step, the velocity field is temporarily calculated by

$$\mathbf{v}^* = \mathbf{v}^n + \frac{\Delta t}{\rho} (R_p(p^n) + R_v(\mathbf{v}^n, \mathbf{v}^{n-1}, \phi^{n+1}, \phi^n, \tilde{\boldsymbol{\sigma}}^*, \tilde{\boldsymbol{\sigma}}^n)), \quad (26)$$

$$\tilde{\boldsymbol{\sigma}}^* = (1 - \phi_s^{n+1}) \mu_f (\nabla \mathbf{v}^* + \nabla \mathbf{v}^{*T}) + \phi_s^{n+1} \left(\mu_s (\nabla \mathbf{v}^* + \nabla \mathbf{v}^{*T}) + \boldsymbol{\sigma}'_{sh}(\tilde{\mathbf{B}}^{n+1}) \right), \quad (27)$$

where \mathbf{v}^* denotes the temporal velocity, and R_p and R_v denote the discretization terms of the momentum equation in terms of the pressure and deviatoric Cauchy stress terms. Finally, pressure, solenoidal velocity vector, and stress tensor are updated during the projection step by

$$p^{n+1} = p^n + \varphi, \quad (28)$$

$$\mathbf{v}^{n+1} = \mathbf{v}^n - \frac{\Delta t}{\rho} \nabla \varphi, \quad (29)$$

$$\tilde{\sigma}^{n+1} = \tilde{\sigma}^n + \delta_{\sigma}(\phi^{n+1}, \varphi), \quad (30)$$

where the incremental pressure φ is determined by solving the Poisson equation:

$$\nabla^2 \varphi = \frac{\nabla \cdot \mathbf{v}^*}{\Delta t}, \quad (31)$$

and δ_{σ} is a stress increment tensor depending on a time-integration method employed in (26) (see Sugiyama et al. (2011) for the detailed formulation).

The spatial derivatives are approximated by the second-order central differences, except for those of the advection terms in (3) and (21), to which the fifth-order WENO scheme (Liu et al. 1994; Jiang and Shu 1996) is applied. For the momentum equation, following the spirit in the energy conservation methods (Kajishima 1994; Ikeno and Kajishima 2007), we discretize the advection terms to satisfy the identity $\nabla \cdot (\mathbf{v}\mathbf{v}) = (\mathbf{v} \cdot \nabla)\mathbf{v} + \mathbf{v}(\nabla \cdot \mathbf{v})$ in the discretized space, that would make the energy highly conserved. The time integrations are basically approximated by the second-order Adams–Bashforth method, except for the viscous stress term in the momentum Eq. (27), to which the second-order Crank–Nicolson method is applied. More details about the advection scheme, etc., are given in the literatures (Kajishima et al. 2001; Kajishima and Takiguchi 2002).

2.3 Numerical Examples

2.3.1 Reversibility in Shape of a Circular Hyperelastic Material

We here deal with a shear flow between two plane plates involving a hyperelastic particle. The distance between the plates is $L_y = 2$. The computational extent in x direction is set to $L_x = 8$. The upper and lower plates are located at $y = 1$ and $y = -1$, respectively. Initially, the system is at rest. An unstressed solid particle is initially circular with a radius of 0.75, and centered at the middle position (0, 0) between the plates as depicted in Fig. 4a. The no-slip condition is imposed on the plates, whereas the periodic condition is applied in x direction. We fix the material properties $\rho = 1$, $\mu_f = 1$ and $\mu_s = 0$. We consider two kinds of materials: one is the linear Mooney–Rivlin material with $c_1 = 4$, $c_2 = 2$ and $c_3 = 0$, and the other is the Saint–Venant–Kirchhoff material with $\lambda_{\text{Lamé}} = 6$ and $\mu_{\text{Lamé}} = 4$ (i.e. $c_1 = 4$, $c_2 = -2$ and $c_3 = 1.75$). The system motion is controlled as follows. Within a period of $t \in [0, 4]$, the upper and lower plates move at speeds of $V_{W(\text{upper})} = 1$ and $V_{W(\text{lower})} = -1$ in x direction, respectively, to drive the fluid and solid motions. After $t = 4$, the moving plates stop (i.e. $V_{W(\text{upper})} = V_{W(\text{lower})} = 0$) to release the particle from the shearing force.

Figure 4 visualizes the particle deformation and the flow field for six consecutive time instants with a grid resolution of 1024×256 . As the shear flow is induced by the moving plates, the shearing force is imposed on the solid particle, and causes the particle elongation toward the extensional direction. In the transient

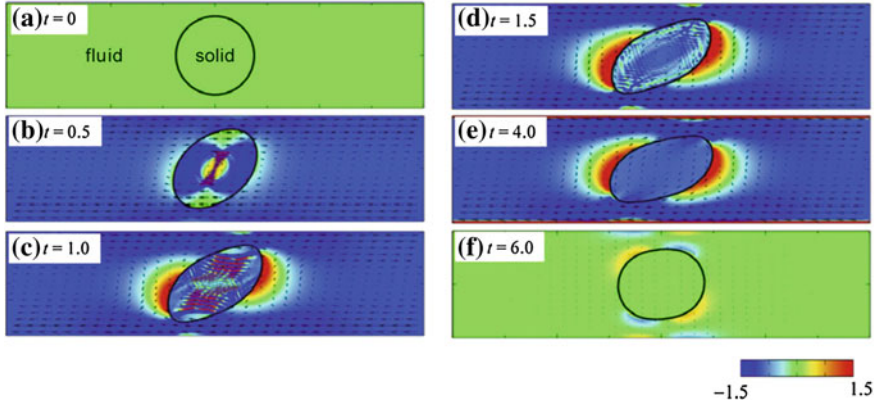


Fig. 4 Snapshots of the velocity (*arrows*) and vorticity (*color*) fields involving a circular particle in the imposing-releasing shear flow between two parallel plates. The figures are reproduced with permission from Sugiyama et al. (2011)

state during the development of the deformation, it is observed in Fig. 4b and c that the transverse elastic waves travel inside the solid, and are reflected by the fluid–structure interface. The wave amplitude is damped through the repetitious reflections with time as shown in Fig. 4d and e. As examined by Gao and Hu (2009), the elastic wave propagation inside the particle may play an important role on the deformation. As shown in Fig. 4e, the vorticity inside the particle at $t = 4$ is negative, indicating that the particle experiences a tank-treading like motion. After the shearing force is released by setting the wall velocities to be zero at $t = 4$, the fluid flow rapidly decays and the deformed particle gradually recovers the circular shape. At $t = 6$ as shown in Fig. 4f, the vorticity in the bulk fluid is almost zero, while the non-zero vorticity forms near the fluid–structure interface, indicating the particle shape is under recovery.

To directly demonstrate whether the reversibility can be captured, the distributions of the tracers for four consecutive time instants are shown in Fig. 5. As depicted in Fig. 5a, the tracers are initially seeded on the concentric circles inside the solid to demonstrate the local displacements inside the solid. The bilinear interpolation to the tracer location is applied to identifying its velocity, and its position is temporally updated in a Lagrangian way. Figure 5b shows the tracer distribution at the most deformed instant $t = 4$ when the particle is under the tank-treading like motion. After the wall velocities is set to be zero at $t = 4$, the tracer particles gradually move back toward the initial concentric circles with time. It should be noted that because the degree of freedom corresponding to the rigid rotation is allowed, the tracer distributions in Fig. 5c and d turn in the clockwise directions about 80° with respect to the initial distribution in Fig. 5a. At the instant $t = 8$, when the same period as the shear-imposing stage (four unit time) has elapsed after the walls stop, the discrepancy between the tracer location and the concentric circle is clearly shown in Fig. 5c, indicating that the recovery in the

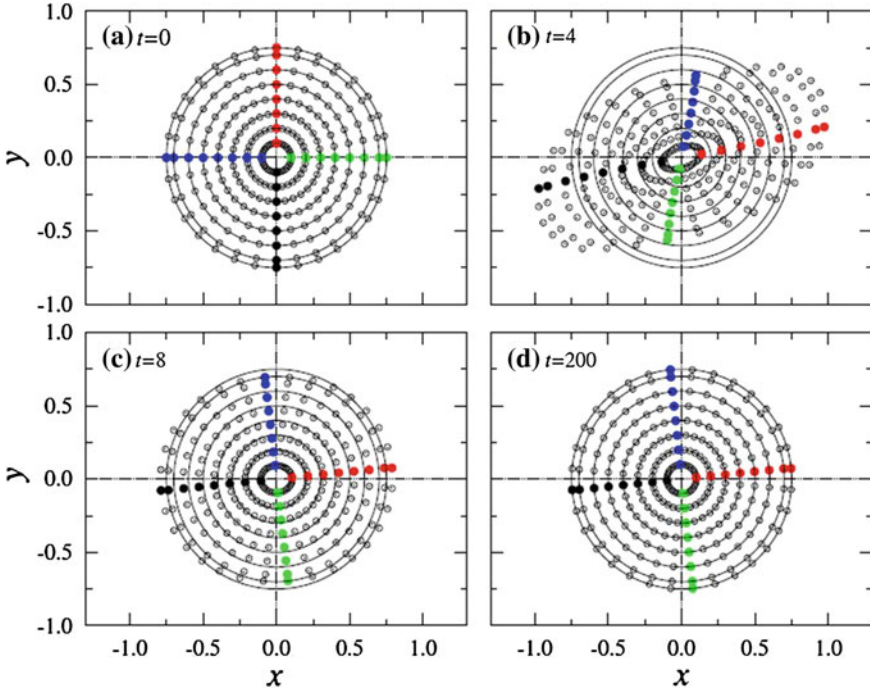


Fig. 5 Material point distribution in the imposing-releasing shear flow involving a circular particle between two parallel plates mesh. The conditions are the same as those of Fig. 4. The (colored) filled circles are distributed to demonstrate the rotation. Reproduced with permission from Sugiyama et al. (2011)

particle shape is still underway. After a sufficiently long time ($t = 200$), the tracers are found to be back in the concentric circles as shown in Fig. 5d. We may say that the present Eulerian approach can capture the reversibility in shape under certain right circumstances.

2.3.2 Two Particles Interaction in a Couette Flow

We here make a comparison with the available numerical analysis of the interaction between two deformable particles in a Couette flow performed by Gao and Hu (2009), who adopted body-fit Lagrangian mesh. The computational extent is $L_x \times L_y = 8 \times 4$, which is the same as the reference. Initially, the system is at rest. Two unstressed solid particles are initially circular with a radius of 0.5, and centered at $\mathbf{x}_{c,A} = (2, 2.5)$ and $\mathbf{x}_{c,B} = (6, 1.5)$ as depicted in Fig. 6a. The upper and lower plates located at $y = 4$ and $y = 0$, respectively, start to move impulsively to drive the fluid and solid motions at speeds of $V_{W(\text{upper})} = 1$ and $V_{W(\text{lower})} = -1$ in x direction.

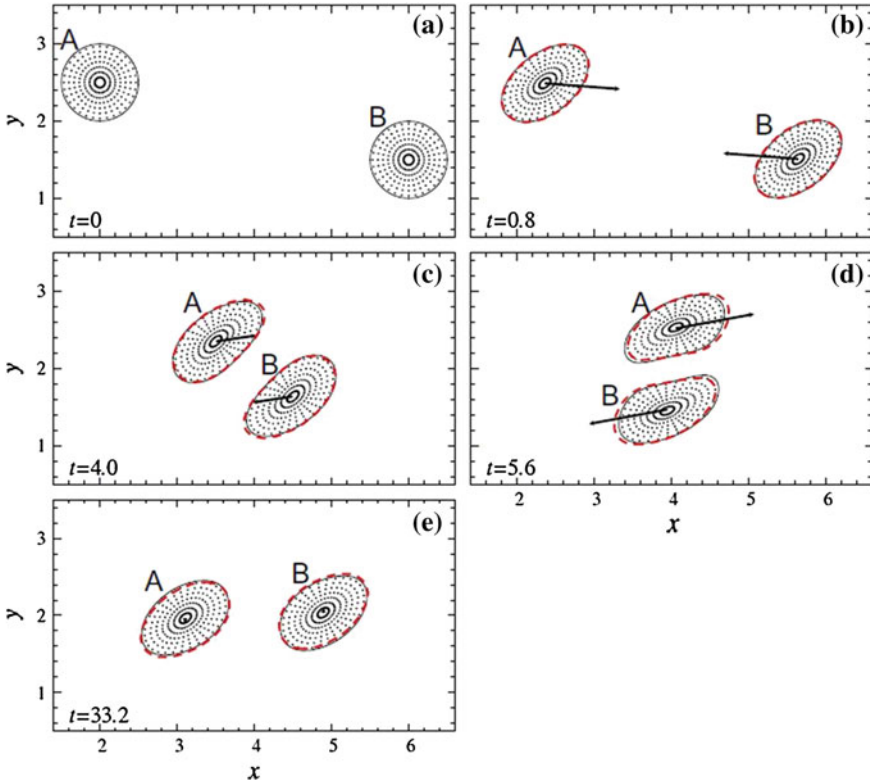


Fig. 6 Comparison of particle–particle interactions in a Couette flow with the existing data (*dashed line*) by Gao and Hu (2009), in which the body-fit Lagrangian mesh was used to solve the FSI problem. The dotted material points and the solid outline correspond to the present simulation results based on the full Eulerian approach with a mesh $1,024 \times 512$. Reproduced with permission from Sugiyama et al. (2011)

The no-slip condition is imposed on the plates, while the periodic condition is applied in x direction. The solid component is purely hyperelastic. The material properties are $\rho = 1$, $\mu_f = 20$, $\mu_s = 0$, $c_2 = 40$ and $c_1 = c_3 = 0$. Figure 6 visualizes the two-particle shape for five time instants. The dotted markers are, again, to represent the solid deformations and those markers are not used for computing solid stress or strain. The arrows at the particle centers are the instantaneous translating velocity vectors. The dashed curve in Fig. 6 represents the outline of the particles obtained by Gao and Hu (2009). The particles experience somehow complicated interactions involving the “roll over” and “bounce back” modes. The solid shape obtained by the present Eulerian simulation is again in agreement with the well-validated result by Gao and Hu, indicating that the particle–particle interaction is also reasonably captured by the present approach.

Fig. 7 Variations of particle y_c -position as functions of time for various number of grid points. Comparison with the result of Gao and Hu (2009). Reproduced with permission from Sugiyama et al. (2011)

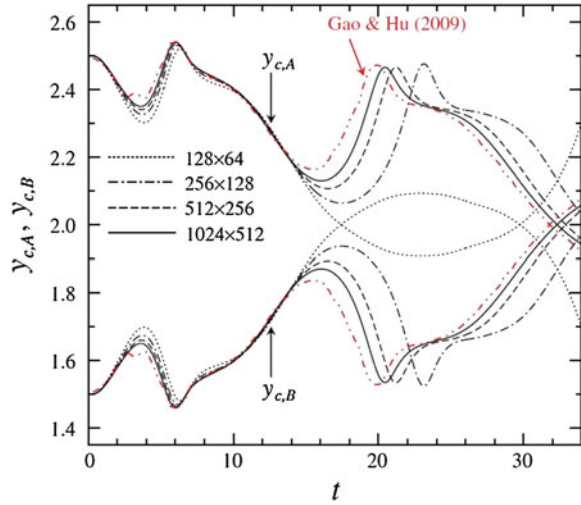


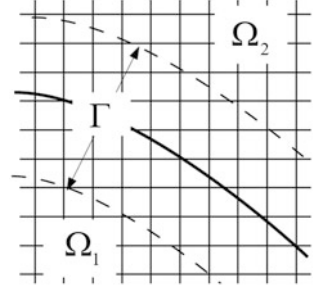
Figure 7 shows the temporal evolution of the y_c -position of the particle centroid for various grid resolutions ($N_x \times N_y = 128 \times 64, 256 \times 128, 512 \times 256, 1024 \times 512$). In the full Lagrangian computation, the finite element mesh is refined within the particle–particle gap, whereas in the present Eulerian simulation, the grid size is uniform and fixed. When the plot shows peaks around $t = 3.0, t = 16.0$ and $t = 20.0$, the gap between the particles is narrow, and the particle undergoes relatively strong hydrodynamic force owing to a squeezing effect. Such a narrow-gap effect is less resolved by the present method than the full Lagrangian method especially for the low spatial resolution cases, that is reflected on the larger deviations from the result by Gao and Hu preferentially at the peaks. In the higher spatial resolution, the profiles of the present simulation get closer to the full Lagrangian result.

3 Further Developments

3.1 Full-Eulerian Fluid–Membrane Coupling Method

In coupling methods for a fluid and elastic membrane typified by the immersed boundary method (Peskin 1972, 2002), the Lagrangian description is employed for the membrane motion, whereas the Eulerian description is employed for the fluid. However, there is an open question for a numerical stability in a long time run without any numerical stabilization. For that reason, rather than using the Lagrangian particles, field variables to identify the membrane interface are introduced and utilized for interaction between the fluid and membrane on the Eulerian mesh. Cottet and Maitre (2006) introduced the level-set function to identify the

Fig. 8 The compactly supported or smoothed interface region Γ immersed in the Cartesian mesh



interface, in addition, the membrane stretching or variation of the surface area was obtained from the information of the level-set function. As a result, the membrane force was successfully obtained on the Eulerian mesh without using the interfacial material points. However, since the constitutive law of the membrane elasticity is limited to a model which only involves a variation of the surface area, it has not been applied yet for more general membrane models which depend on the principal strains.

A novel full Eulerian fluid–membrane interaction method has been proposed (Li et al. 2012a, b), as an extension of the general idea by Sugiyama et al. (2011). It is assumed that a closed membrane is immersed in a field Ω , where inner and ambient regions Ω_1 and Ω_2 are filled with the incompressible Newtonian fluids ($\Omega = \Omega_1 \cup \Omega_2$). A material phase to describe each fluid is expressed by a smoothed volume fraction (VOF) function ϕ , which distributes from zero to one within a few computational meshes. Then a membrane transition region Γ defined as $|\nabla\phi| \leq \varepsilon$, where $|\nabla\phi|$ is regarded as a smoothed Delta function (e.g. Brackbill et al. 1992) and ε is an arbitrarily value depending on the mesh size, is introduced as in Fig. 8.

By making use of a basic theory on the finite deformation (Skalak et al. 1973; Barthés-Biesel and Rallison 1981), a set of governing equations with a mixture formulation is given as follows in the Eulerian frame.

$$\nabla \cdot \mathbf{v} = 0, \quad \mathbf{x} \in \Omega, \quad (32)$$

$$\rho(\partial_t \mathbf{v} + \mathbf{v} \cdot \nabla \mathbf{v}) = -\nabla p + \nabla \cdot (\mu(\nabla \mathbf{v} + \nabla \mathbf{v}^T)) + |\nabla \phi| \mathbf{f}_s, \quad \mathbf{x} \in \Omega, \quad (33)$$

$$\partial_t \phi + \mathbf{v} \cdot \nabla \phi = 0, \quad \mathbf{x} \in \Omega, \quad (34)$$

$$\partial_t \mathbf{B}_s + \mathbf{v} \cdot \nabla \mathbf{B}_s = \mathbf{B}_s \cdot \nabla_s \mathbf{v} + \nabla_s \mathbf{v}^T \cdot \mathbf{B}_s, \quad \mathbf{x} \in \Gamma, \quad (35)$$

$$\partial_t J_s + \mathbf{v} \cdot \nabla J_s = J_s \nabla_s \cdot \mathbf{v}, \quad \mathbf{x} \in \Gamma, \quad (36)$$

$$\partial_t \kappa_R + \mathbf{v} \cdot \nabla \kappa_R = 0, \quad \mathbf{x} \in \Gamma, \quad (37)$$

where $\nabla_s = \mathbf{P} \cdot \nabla$ is the *surface* gradient operator with a surface projection tensor $\mathbf{P} = \mathbf{I} - \mathbf{nn}$, where \mathbf{n} is a unit normal vector of a membrane surface, $\mathbf{B}_s = \mathbf{P} \cdot \mathbf{B} \cdot \mathbf{P}_R$ the *surface* left Cauchy–Green deformation tensor (subscript R denotes a reference coordinate), J_s the surface Jacobian (i.e. ratio A/A_0 between an initial surface area

A_0 and current area A), κ_R the reference mean curvature and \mathbf{f}_s the surface singular force (force per area) of the membrane given by

$$\mathbf{f}_s = \nabla_s \cdot (\boldsymbol{\tau}_s + \boldsymbol{\tau}_b), \quad (38)$$

where $\boldsymbol{\tau}_s$ is an in-plane stress tensor, e.g. the neo-Hookean material (Barthés-Biesel and Rallison 1981):

$$\boldsymbol{\tau}_s = \frac{E_s}{3(\Lambda_1 + 1)} \left(\mathbf{B}_s - \frac{1}{(\Lambda_1 + 1)^2} \mathbf{P}_s \right), \quad (39)$$

and the Evans–Skalak material (Evans and Skalak 1980):

$$\boldsymbol{\tau}_s = \frac{E_s}{(\Lambda_1 + 1)^2} \mathbf{B}_s + \left(E_s \Lambda_1 - C_s \frac{\Lambda_2 + 1}{\Lambda_1 + 1} \right) \mathbf{P}_s, \quad (40)$$

where,

$$\Lambda_1 = J_s - 1, \quad \Lambda_2 = \frac{\text{tr}(\mathbf{B}_s)}{2J_s} - 1. \quad (41)$$

Here, E_s is the shear modulus, C_s the area dilation modulus. $\boldsymbol{\tau}_b$ is a bending stress tensor proposed by Pozrikids (2001):

$$\begin{aligned} \boldsymbol{\tau}_b &= \mathbf{q}_s \mathbf{n}, \\ \mathbf{q}_s &= (\nabla_s \cdot \mathbf{m}_s) \cdot \mathbf{P}, \quad \mathbf{m}_s = k_s (\boldsymbol{\kappa}_s - \kappa_R \mathbf{P}), \end{aligned} \quad (42)$$

where K_s is the bending modulus and $\boldsymbol{\kappa}_s = \nabla_s \mathbf{n}$ the Cartesian curvature tensor. The outward unit normal vector defined as $\mathbf{n} = -\nabla \phi / |\nabla \phi|$, and $\boldsymbol{\kappa}_s$ (and also κ_R) are calculated in the Eulerian meshes. A set of PDEs is discretized by the finite difference/volume manner, and the SMAC algorithm (Amsden and Harlow 1970) is employed to couple with the pressure and velocity fields with the staggered arrangement. More detailed description on the numerical methods, see literatures (li et al. 2012a, b).

For the sake of validation, a shear-induced deformation problem for a spherical capsule obeying the neo-Hookean law (39) is simulated. A capsule with a diameter of $d = 2$ is located on a computational domain, $[-4, 4] \times [-2, 2] \times [-4, 4]$. An opposite velocity of $\pm V$ that results in a shear rate $\gamma = 2V/H_z$, where $H_z = 8$ is a vertical height of the domain, is imposed on each top/bottom wall in z direction. The periodic boundary conditions are imposed on other x and y directions. The viscosity $\mu (= \mu_1 = \mu_2)$ is given by Reynolds number $Re = \rho \gamma d^2 / (4\mu)$, and the membrane stiffness is given by capillary number $Ca = \gamma d / (2E_s)$. In this test, $\rho = 1$, $\gamma = 1$ and $Re = 0.001$ are fixed, therefore, the membrane stiffness only depends on the capillary number Ca . Here, the bending force is neglected and the capillary number is varied as 0.0125, 0.025, 0.05, 0.1 and 0.2. Numerical results at steady state with a mesh size $\Delta_x = d/32$ are shown in Fig. 9, where the time

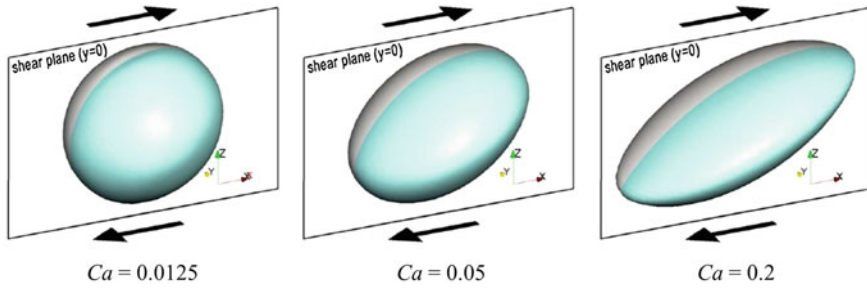


Fig. 9 The fully-developed deformed surface of the neo-Hookean membrane subjected to the linear shear flow for various capillary numbers $Ca = 0.0125, 0.05$ and 0.2 . The “shear plane” indicates a plane at $y = 0$, and the arrows indicate a schematic of the imposed shear velocities. Reproduced with permission from Ii et al. (2012b)

increment $\Delta t = 0.0025$ is used. It is confirmed that the deformation becomes larger as the capillary number increases.

Here, time history of a deformation parameter $D = (l - s)/(l + s)$, where l and s denote the semi-major and semi-minor axes of an ellipse fitting to an obtained interface in “shear plane”, i.e. x - z cross-section passing through $y = 0$, is shown in Fig. 10. The mesh lengths $\Delta_x = d/16$ and $d/32$ are employed, where the time increments $\Delta t = 0.005$ and 0.0025 are used. In this regard, numerical solutions given by the immersed boundary (IB) method (Eggleton and Popel 1998) and the boundary element method (BEM) (Pozrikidis 1995) are also shown. As compared with the well-validated results of the IB method and BEM, the present results converge to the reference solutions by increasing the spatial resolution.

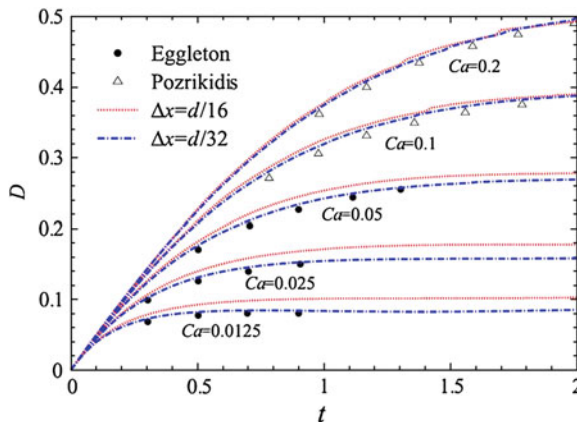


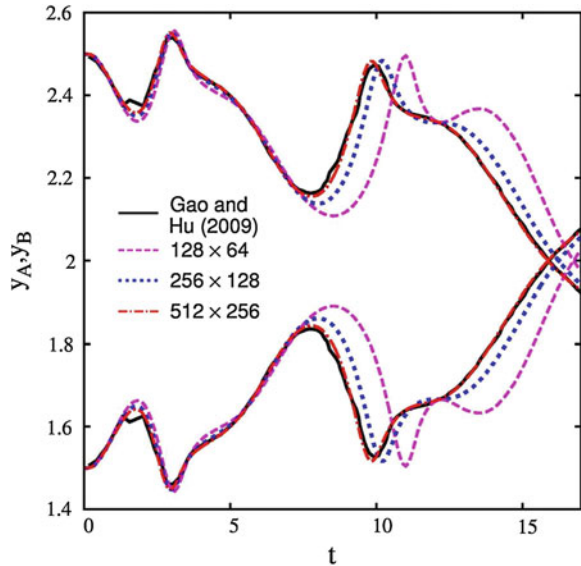
Fig. 10 Deformation parameter D vs. time t for various capillary numbers $Ca = 0.0125, 0.025, 0.05, 0.1$ and 0.2 . The lines are the present solutions with the mesh sizes of $\Delta_x = d/16$ and $d/32$, the filled-circles indicate the solutions by means of the immersed boundary method by Eggleton and Popel (1998), and open-triangles show those of the boundary element method by Pozrikidis (1995). Reproduced with permission from Ii et al. (2012b)

3.2 Less-Dissipative Treatment for Updating the VOF Function

The updating equation of the VOF function $\phi_s(\mathbf{x}, t)$ is derived from the advection Eq. (3). From a numerical point of view, an accurate treatment is necessary to numerically obtain the flux $\mathbf{v}\phi_s$ in a conservative form without the numerical dissipation and oscillation. In other words, an accurate approximate function $F(\mathbf{x}, t)$ is desirable for the indicator function $I_s(\mathbf{x}, t)$. In the discretization, the approximate function $F(\mathbf{x}, t)$ is piecewisely reconstructed in a single mesh ijk , that is F_{ijk} . In the present Eulerian FSI method especially for the coupling with the membrane including a diffusive membrane region, a numerical method is required to ensure the diffusive transition region between respective material-phases (fluid and solid regions or inner/outer fluid region of the membrane) without numerical dissipation over time. In order to satisfy solving such a requirement, a continuous interface capturing method, namely MTHINC method (Ii et al. 2012c), has been proposed developed by the method by Xiao et al. (2005), in which a (multi-dimensional) hyperbolic tangent function is utilized for the approximation of the cell-wisely indicator function.

In order to check the effect of the non-dissipative (MTHINC) method on the full-Eulerian FSI solver, we again carry out a simulation on the two particles interaction problem shown in Sect. 2.3.2. The temporal evolutions of the y_c -position of the particle centroids for various grid resolutions ($N_x \times N_y = 64 \times 32, 128 \times 64, 256 \times 128, 512 \times 256$) are shown in Fig. 11. The present solutions with the MTHINC method are excellently competitive to the full Lagrangian result

Fig. 11 Similar with Fig. 7, but the MTHINC method is employed for updating the VOF function ϕ_s



(Gao and Hu 2009) with lower grid resolutions as compared with the results with the fifth-order WENO method (Fig. 7 in Sect. 2.3.2), inferring that the less-dissipative numerical method for updating the VOF function is very important to maintain an overall accuracy on the coupling problem based on the Eulerian formulation.

3.3 Quasi-Implicit Formulation for a Stiff Material

For the soft material or membrane, of which the propagation speed of the elastic wave is comparable to the advection speed, the explicit time-marching is completed with no small time increment Δt , whereas for the hard one, it suffers from the expensive computational cost because of a huge number of time steps with the sufficiently small Δt to capture the high-speed elastic wave. For the latter situation, an implicit treatment is required to relax the stability restriction because of the stiffness. A geometric nonlinearity appears in a general finite deformation problem, thus a nonlinear system should be solved in an implicit manner. However, the above-mentioned instability mainly comes from the stiffness of the material, i.e. high-speed elastic wave. It is therefore expected that the system becomes stable drastically with the implicitly treated wave propagation even if the interface motion is explicitly treated, inferring that no nonlinear system is solved.

In the employed fractional step approach, the effect of the elastic wave propagation appears in a coupling with (26) and (26, 27). Therefore, the stress tensor of the solid is approximated as

$$\sigma'_{sh}(\mathbf{B}^{n+1}) \approx \sigma'_{sh}(\mathbf{B}^n) + \underbrace{\frac{\partial \sigma'_{sh}(\mathbf{B}^n)}{\partial \mathbf{B}^n}}_{\mathbf{J}_B} \cdot \Delta \mathbf{B}^*, \quad (43)$$

where \mathbf{J}_B is the fourth-order Jacobian tensor and the time increment of the modified left Cauchy-Green deformation tensor $\Delta \mathbf{B}^*$ is approximated as

$$\Delta \mathbf{B}^* \approx \frac{\Delta t}{2} (\mathbf{B}^n \cdot (\nabla \mathbf{v}^n + \nabla \mathbf{v}^*) + (\nabla \mathbf{v}^n + \nabla \mathbf{v}^*)^T \cdot \mathbf{B}^n). \quad (44)$$

As compared with the explicit (or semi-implicit) estimation (25), Eq. (44) involves the temporal velocity vector \mathbf{v}^* . It is therefore shows that, by substituting Eqs. (43) with (43) into (27), a linear system (26) for \mathbf{v}^* is obtained based on the quasi-implicit treatment for the solid stress tensor. Detailed expressions are shown in literatures (Ii et al. 2011, 2012a).

It was confirmed in the literature (Ii et al. 2011) the present implicit method offers a unified treatment for both soft and hard materials, enabling simulation over a broad range of elastic moduli (including a severe near-rigid condition) within a feasible computation time without switching the numerical procedures depending on the moduli.

3.4 Particle-In-Cell Approach

The Eulerian FSI simulation provides significant advances in our understanding of the geometrical flexibility, however, one inevitably encounters a numerical diffusion problem. The VOF function is able to be accurately updated by using the less-dissipative interface-capturing method, e.g. the MTHINC method (Ii et al. 2012c) described in Sect. 3.2, on the other hand, there are no sophisticated methods for updating the deformation tensor because of its definition. Even if a high-order scheme is chosen, the fluid–structure interface is smeared out gradually with time. One of the methods to retain the sharp interface and the numerical stability is a particle-in-cell (PIC) or material-point approach (Harlow 1988), in which a moving object is discretized into Lagrangian markers accompanying the status data for the individual small regions. The PIC method and its variants have been proven to their merits in coping with, for example, solid dynamics (Sulsky et al. 1995; Huang and Savage 1998; Guilkey and Weiss 2003; Wallstedt and Guilkey 2008) and fluid-membrane interaction (York et al. 2000) problems.

A novel PIC-based Eulerian FSI solver has been proposed by Sugiyama et al. (2010b), in which the Lagrangian markers are introduced to describe the solid shape and deformation level, whereas the force-coupling is addressed in the Eulerian mesh. A centroid $\mathbf{x}_p^{(l)}$ of a marker l with a volume $\chi_p^{(l)}$ and a modulus $G_p^{(l)}$, which is related to the prescribed velocity by

$$\frac{d\mathbf{x}_p^{(l)}}{dt} = \mathbf{v}(\mathbf{x}_p^{(l)}), \quad l \in [1, N_p], \quad (45)$$

where N_p is the total number of particles. The left Cauchy-Green deformation tensor $\mathbf{B}_p^{(l)}$, is temporally updated by

$$\frac{d\mathbf{B}_p^{(l)}}{dt} = \mathbf{B}_p^{(l)} \cdot \mathbf{L}^T(\mathbf{x}_p^{(l)}) + \mathbf{L}(\mathbf{x}_p^{(l)}) \cdot \mathbf{B}_p^{(l)}, \quad l \in [1, N_p]. \quad (46)$$

Here, $\mathbf{v}(\mathbf{x}_p^{(l)})$ and $\mathbf{L}(\mathbf{x}_p^{(l)}) = (\nabla \mathbf{v}(\mathbf{x}_p^{(l)}))^T$ are interpolated from the Eulerian mesh to the marker position $\mathbf{x}_p^{(l)}$. Following an idea of a component-weighted average (Drew and Passman 1999), we compute the hyperelastic stress field $\phi_s \boldsymbol{\sigma}_{sh}$, e.g. $\phi_s G \mathbf{B}$ in the neo-Hookean material, on the fixed mesh through an extrapolation from the marker points to satisfy

$$\phi_s G \mathbf{B}(\mathbf{x}_c) = \frac{1}{V_c} \sum_{l=1}^{N_p} \int_{V_c} d^3 \mathbf{x} G_p^{(l)} \chi_p^{(l)} \mathbf{B}_p^{(l)} \delta(\mathbf{x} - \mathbf{x}_p^{(l)}). \quad (47)$$

where V_c is the computational cell volume, \mathbf{x}_c is its centroid, and $\delta(\dots)$ is the Dirac delta function.

The proposed PIC-based Eulerian FSI analysis offers an excellent agreement with theoretical analyses in some problems (Sugiyama et al. 2010b), and possibility to solve the suspension flow of flexible bodies in an elastic tube with a

narrow constriction, in which a higher spatial resolution is required to address an interaction between both flexible bodies and wall in case of a pure full-Eulerian approach.

4 Suspension of Biconcave Capsules and Spheroid Solids in a Capillary Tube

Human blood is composed of biological cells (erythrocyte, leukocyte and thrombocyte, i.e., red blood cell, white blood cell and platelet), proteins and plasma. Especially, the deformable red blood cell (RBC) highly occupies a blood, where its volume ratio ranges from 30 to 50 %, thus the dynamic motions of the multiple RBCs play an important role in a capillary vessel when its size (or diameter D) is comparable to a RBC size (diameter $d \sim 8 \mu\text{m}$). In such a small vessel, the blood is no longer accordance with the Newtonian fluid due to the presence of the high-density RBCs. When the vessel size D is close to the RBC size d for $D > d$, it has been observed that a flow rate increases even if a same driving pressure is enforced, that is commonly known as the Fåhræus–Lindqvist effect (Fåhræus and Lindqvist 1931). Due to a hydrodynamic effect, the deformable RBCs axially aggregate and the RBC-rich core region is created around an axial center, resulting in a cell-free layer (or plasma occupying layer) near the vessel wall. In a primary stage of the thrombus formation (or blood clotting) that stops the bleeding in homeostatic mechanism, the platelets immediately accumulate on an injured vessel wall. Therefore, it is quite important to know how many platelets are confined and drift in the cell-free layer.

In this section, a suspension flow of the multiple RBCs and platelets in an elastic capillary vessel and study the feasibility of the blood flow analysis based on the full-Eulerian approaches. Here, to simplify the analysis, the platelet is regarded as the elastic solid with a stiff elastic modulus, whereas the RBC is treated as the elastic membrane obeying an adequate constitutive law with experimentally given parameters (Hochmuth and Waugh 1987).

4.1 Analysis Setup

A suspension of the RBCs and platelets is enclosed by the elastic vessel tube with a radius of $D = 20 \mu\text{m}$, obeying the solid material of the neo-Hookean law (18). Here, 30 RBCs are randomly distributed to that a relevant hematocrit H_t is approximately 20 %. The Evans-Skalak model (40) and Pozrikidis bending model (42) are employed for the RBC. Meanwhile 10 platelet-like elastic solids are randomly distributed within a range of $r_c \leq 8 \mu\text{m}$ (r_c is a centroid of the platelet in a radial direction) to reveal how the centrally-located platelets behave due to the

presence of the RBCs. Initial shapes of the RBC and platelet are of biconcave discoid (Evans and Fung 1972) and spheroid, respectively. A flow is induced by a pressure-gradient as a body force, and a periodic boundary condition is imposed on a streamwise direction x , and wall boundary conditions are employed for both spanwise and vertical directions, y and z , respectively. Computational conditions are referred to Table 1 of literature (Ii et al. 2012b).

4.2 Results and Discussion

4.2.1 Dynamic Motions of the RBCs

Snapshots of numerical results at $t = 7.5, 30$ and 75 ms are shown in Fig. 12. It is found that the initially-distributed RBCs are mixed over time. Each of RBCs has a different shape such as a parachute shape or slipper one reported in both a numerical simulation (Zhao et al. 2010) and experiment (Gaetgens et al. 1980). The deformed RBCs aggregate into large masses around the axial center due to a hydrodynamic effect, causing a plasma phase near the wall, so-called the cell-free layer.

To clarify the development of the cell-free layer, a spatial occupancy of the RBCs in a streamwise direction x is plotted in Fig. 13. It is confirmed that the cell-free layer (or non-existing region of the RBC near the wall) becomes larger and a RBC-rich core region is created around a tube center over time. It has been reported that the RBC-rich core region is sufficiently created at $t = 87.5$ ms in a

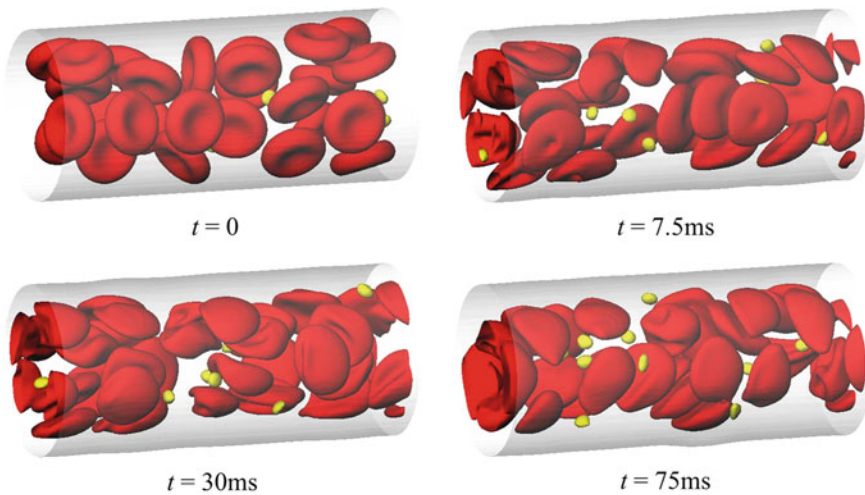
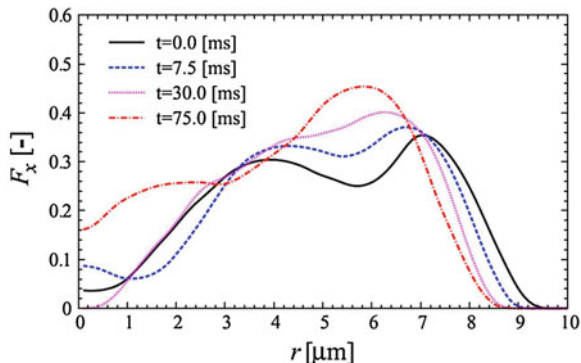


Fig. 12 Snapshots of the numerical results at $t = 0, 7.5, 30$ and 75 ms. Reproduced with permission from Ii et al. (2012b)

Fig. 13 Spatial occupancy of the RBC versus axial position at different time. Reproduced with permission from Li et al. (2012b)



2D simulation (Zhang et al. 2008), in which the computational conditions are totally different (i.e., 2 and 3D, rigid parallel plate and elastic tube, $H_t \approx 30$ and $H_t \approx 20$ %). Nevertheless, the present result is physically comparable to the existing result (Zhang et al. 2008) in terms of a time constant for creating the RBC-rich core region. In a bounded flow subjected to a pressure gradient, it is known that a laterally-located RBC follow a tank-treading motion due to a strong shear rate near the wall (Zhao et al. 2010; Zhang et al. 2008; Crowl and Fogelson 2010, 2011). This tendency has been also reported by Doddi and Bagchi (2009) (Fig. 11 of the literature) whose simulation employs a parallel plate in 3D. However, the present result is given by a specific configuration (one initial distribution), therefore further discussions for the development of the RBC aggregation will be necessary using various initial distributions.

4.2.2 Platelet Motion

Trajectories of the respective platelets in a radial direction are plotted in Fig. 14(left). Each platelet moves in a flow undergoing a fluctuation in a radial direction, especially, such a fluctuation seems to be large around the tube center ($r \leq 4$ μm). As the above discussion in Sect. 4.2.1, it is considered that the axially-aggregating RBCs push out the platelets together with the plasma, and the laterally-migrated platelets drift with a less fluctuation. Taking the distribution of the RBCs into account, it is assumed that the RBC-rich core region induces a mixing effect of the flow, which results in a higher fluctuation in respect to the medially-located platelets, whereas the cell-free layer restricts the radial motions of the laterally-located platelets. Furthermore, a specific separation is observed between the axial center ($r \leq 4$ μm) and near the wall (6 $\mu\text{m} \leq r \leq 8$ μm) for $t \leq 75$ ms. In the 2D simulation results (Crowl and Fogelson 2010, 2011), this separation has relevance to the multiple behaviors of the RBCs playing the tank-treading motions near the wall, and they could perform a kind of barrier to restrict the radial drift of the platelet from the lateral to the center. In the present

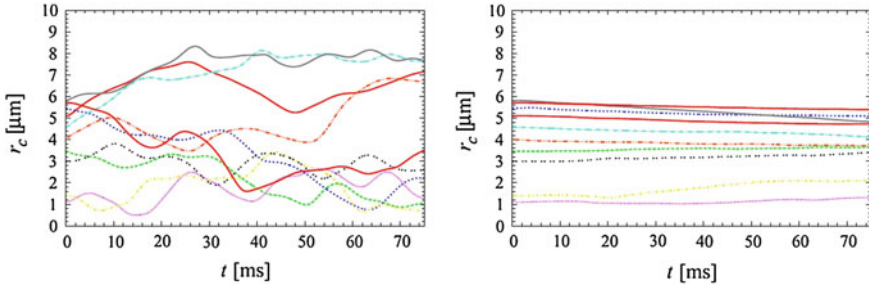


Fig. 14 Trajectories of the respective 10 platelets in a radial direction. *Left* figure shows the result with the suspension of the RBCs and *right* figure shows the result with the pure plasma. Reproduced with permission from Ii et al. (2012b)

simulation, it is not clear by what this separation is triggered because the number of platelets is only 10 and the simulation is run with 1 initial configuration. Nevertheless, it is considered that the radial fluctuation comes from the motions of the RBCs. To clarify it, we carry out a computation without taking account of the RBCs. The platelet trajectories are shown in Fig. 14(right). In a situation without the RBCs, the radial fluctuation of the platelet only comes from the platelet motion itself. Therefore, the platelets straightforwardly drift in the flow with less radial fluctuation for $t \leq 75$ ms. It therefore appears that the dynamic motions of the platelets are strongly affected by the motions of the RBCs.

5 Conclusion

A full Eulerian simulation method for solving fluid–structure interaction (FSI) problems has been developed. A volume-of-fluid formulation was applied to describing the multi-component geometry. The temporal change in both the solid deformation and membrane deformation were described in the Eulerian frame by updating a (surface) left Cauchy-Green deformation tensor, which was used to express the nonlinear hyperelastic constitutive law. The validity of the present simulation method was established through comparisons with the available simulation data. We confirmed that the present Eulerian approach can capture the reversibility in shape by introducing the grids with sufficiently high resolution.

The significance of the present full Eulerian simulation method may be that the approach showed a feasibility of reducing the FSI coupling problem to simple incompressible fluid flow solvers. Thus, the conventionally-used efficient computational techniques, such as the fast Fourier transform, and multi-grid method, are applicable. The present Eulerian method has been shown to be well-suited for using the voxel-based multi-component geometry on the fixed Cartesian system. Once the initial field of the solid volume fraction is given over the entire domain, the present Eulerian method enables one to carry out the FSI simulation without

mesh generation procedure. The method promises to extend the possibility of the FSI simulation to certain additional classes of problems in the medical field, owing to a facility in incorporating the voxel data directly converted from medical images.

Acknowledgments The authors would like to thank Shintaro Takeuchi, Huaxiong Huang, Xiaobo Gong, Jinbiao Wu, Feng Xiao, Shigenobu Okazawa and Shigeho Noda for fruitful discussions. K.S. is grateful to Tong Gao for providing the detailed simulation conditions in [Sect. 2.3.2](#). S.I. is grateful to Yasuhiro Kawashima for code development and wish to acknowledge that the run in [Sect. 4](#) was performed on RIKEN Integrated Cluster of Clusters (RICC) system.

References

- Amsden AA, Harlow FH (1970) A simplified MAC technique for incompressible fluid flow calculations. *J Comput Phys* 6:322–325
- Bagchi P (2007) Mesoscale simulation of blood flow in small vessels. *Biophys J* 92:1858–1877
- Barthés-Biesel D, Rallison JM (1981) The time-dependent deformation of a capsule freely suspended in a linear shear flow. *J Fluid Mech* 113:251–267
- Brackbill JU, Kothe DB, Zemach C (1992) A continuum method for modeling surface tension. *J Comput Phys* 100:335–354
- Belytschko T (1980) Fluid–Structure Interaction. *Comput Struct* 12:459–469
- Bonet J, Wood RD (2008) *Nonlinear continuum mechanics for finite element analysis*, 2nd edn. Cambridge University Press, Cambridge
- Cottet GH, Maitre E (2006) A level set method for fluid–structure interactions with immersed surfaces. *Math Model Meth Appl Sci* 16:415–438
- Cottet GH, Maitre E, Milcent T (2008) Eulerian formulation and level set models for incompressible fluid–structure interaction. *Math Model Numer Anal* 42:471–492
- Crowl LM, Fogelson AL (2010) Computational model of whole blood exhibiting lateral platelet motion induced by red blood cells. *Int J Numer Meth Biomed Eng* 26:471–487
- Crowl LM, Fogelson AL (2011) Analysis of mechanisms for platelet near-wall excess under arterial blood flow conditions. *J Fluid Mech* 676:348–375
- Doddi SK, Bagchi P (2009) Three-dimensional computational modeling of multiple deformable cells flowing in microvessels. *Phys Rev E* 79:046318
- Drew DA, Passman SL (1999) *Theory of multicomponent fluids*. Springer-Verlag, New York, Chap. 11
- Dunne T (2006) An Eulerian approach to fluid–structure interaction and goal-oriented mesh adaptation. *Int J Numer Meth Fluids* 51:1017–1039
- Eggleton CD, Popel AS (1998) Large deformation of red blood cell ghosts in a simple shear flow. *Phys Fluids* 10:1834–1845
- Evans E, Fung Y (1972) Improved measurement of the erythrocyte geometry. *Microvasc Res* 4:335–347
- Evans EA, Skalak R (1980) *Mechanics and thermodynamics of biomembranes*. CRC, Boca Raton
- Fåhræus R, Lindqvist T (1931) The viscosity of blood in narrow capillary tubes. *Am J Physiol* 96:562–568
- Gaetgens P, Duhresen C, Albrecht KH (1980) Motion, deformation, and interaction of blood cells and plasma during flow through narrow capillary tubes. *Blood Cells* 6:799–817
- Gao T, Hu HH (2009) Deformation of elastic particles in viscous shear flow. *J Comput Phys* 228:2132–2151

- Glowinski R, Pan T-W, Hesla TI, Joseph DD (1999) A distributed lagrange multiplier/fictitious domain method for particulate flows. *Int J Multiph Flow* 25:755–794
- Gong X, Sugiyama K, Takagi S, Matsumoto Y (2009) The deformation behavior of multiple red blood cells in a capillary vessel. *J Biomech Eng* 131:074504
- Guilkey JE, Weiss JA (2003) Implicit time integration for the material point method: quantitative and algorithmic comparisons with the finite element method. *Int J Numer Meth Engrg* 57:1323–1338
- Gurtin ME, Guidugli PP (1973) The thermodynamics of constrained materials. *Arch Ration Mech Anal* 51:192–208
- Harlow FH, Welch JE (1965) Numerical calculation of time-dependent viscous incompressible flow of fluid with free surface. *Phys Fluids* 8:2182–2189
- Harlow FH (1988) PIC and its progeny. *J Comput Phys* 48:1–10
- Hirt CW, Amsden AA, Cook JL (1974) An arbitrary Lagrangian-Eulerian computing method for all flow speeds. *J Comput Phys* 14:227–253
- Hirt CW, Nichols BD (1981) Volume of fluid (VOF) methods for the dynamics of free boundaries. *J Comput Phys* 39:201–225
- Hochmuth R, Waugh R (1987) Erythrocyte membrane elasticity and viscosity. *Annu Rev Physiol* 49:209–219
- Holzapfel G (2000) *Nonlinear solid mechanics*. John Wiley & Sons, Chichester
- Huang ZJ, Savage SB (1998) Particle-in-cell and finite difference approaches for the study of marginal ice zone problems. *Cold Reg Sci Tech* 28:1–28
- Huang H, Sugiyama K, Takagi S (2009) An immersed boundary method for restricted diffusion with permeable interfaces. *J Comput Phys* 228:5317–5322
- Hughes TJR, Liu WK, Zimmermann TK (1981) Lagrangian-Eulerian finite element formulation for incompressible viscous flows. *Comput Methods Appl Mech Eng* 29:329–349
- Ii S, Sugiyama K, Takeuchi S, Takagi S, Matsumoto Y (2011) An implicit full Eulerian method for the fluid-structure interaction problem. *Int J Numer Meth Fluids* 65:150–165
- Ii S, Gong X, Sugiyama K, Wu J, Huang H, Takagi S (2012a) A full Eulerian fluid-membrane coupling method with a smoothed volume-of-fluid approach. *Commun Comput Phys* 12:544–576
- Ii S, Sugiyama K, Takeuchi S, Takagi S, Matsumoto Y (2012b) A computational blood flow analysis in a capillary vessel including multiple red blood cells and platelets. *J Biomech Sci Engrg* 7:72–83
- Ii S, Sugiyama K, Takeuchi S, Takagi S, Matsumoto Y, Xiao F (2012c) An interface capturing method with a continuous function: the THINC method with multi-dimensional reconstruction. *J Comput Phys* 231:2328–2358
- Ikeno T, Kajishima T (2007) Finite-difference immersed boundary method consistent with wall conditions for incompressible turbulent flow simulations. *J Comput Phys* 226:1485–1508
- Jiang GS, Shu C-W (1996) Efficient implementation of WENO schemes. *J Comput Phys* 126:202–228
- Kajishima T (1994) Conservation properties of finite difference method for convection. *Trans Jpn Soc Mech Eng B* 60:2058–2063 (in Japanese)
- Kajishima T, Takiguchi S, Hamasaki H, Miyake Y (2001) Turbulence structure of particle-laden flow in a vertical plane channel due to vortex shedding. *JSME Int J Ser B* 44:526–535
- Kajishima T, Takiguchi S (2002) Interaction between particle clusters and particle-induced turbulence. *Int J Heat Fluid Flow* 23:639–646
- Lac E, Barthés-Biesel D, Pelekasis NA, Tsamopoulos J (2004) Spherical capsules in three-dimensional unbounded Stokes flows: effect of the membrane constitutive law and onset of buckling. *J Fluid Mech* 516:303–334
- LeVeque RJ, Li Z (1994) The immersed interface method for Elliptic equations with discontinuous coefficients and singular sources. *SIAM J Numer Anal* 31:1019–1044
- Li Z, Lai M-C (2001) The immersed interface method for the Navier-Stokes equations with singular forces. *J Comput Phys* 171:822–842

- Liu X-D, Osher S, Chan T (1994) Weighted essentially non-oscillatory schemes. *J Comput Phys* 115:200–212
- Liu C, Walkington NJ (2001) An Eulerian description of fluids containing visco-elastic particles. *Arch Rational Mech Anal* 159:229–252
- Mooney M (1940) A theory of large elastic deformation. *J Appl Phys* 11:582–592
- Mori Y, Peskin CS (2008) Implicit Second-order immersed boundary methods with boundary mass. *Comput Methods Appl Mech Eng* 197:2049–2067
- Nagano N, Sugiyama K, Takeuchi S, Ii S, Takagi S, Matsumoto Y (2010) Full-Eulerian finite-difference simulation of fluid flow in hyperelastic wavy channel. *J Fluid Sci Tech* 5:475–490
- Okazawa S, Kashiwayama K, Kaneko Y (2007) Eulerian formulation using stabilized finite element method for large deformation solid dynamics. *Int J Numer Methods Eng* 72:1544–1559
- Peskin CS (1972) Flow patterns around heart valves: a numerical method. *J Comput Phys* 10:252–271
- Peskin CS (2002) The immersed boundary method. *Acta Numer* 11:479–517
- Rivlin RS (1948) Large elastic deformations of isotropic materials IV, further development of general theory. *Phil Trans Royal Soc A* 241:379–397
- Pozrikidis C (1995) Finite deformation of liquid capsules enclosed by elastic membranes in simple shear flow. *J Fluid Mech* 297:123–152
- Pozrikidis C (2001) Effect of bending stiffness on the deformation of liquid capsules in simple shear flow. *J Fluid Mech* 440:269–291
- Pozrikidis C (2003) Modeling and simulations of capsules and biological cells. Chapman & Hall, Boca Raton
- Pries AR, Neuhaus D, Gaehtgens P (1992) Blood viscosity in tube flow: dependence on diameter and hematocrit. *Am J Physiol* 263:1770–1778
- Richter T, Wick T (2010) Finite elements for fluid–structure interaction in ALE and fully Eulerian coordinates. *Comput Methods Appl Mech Engrg* 199:2633–2642
- Simo JC, Taylor RL, Plesler KS (1985) Variational and projection methods for the volume constraint in finite deformation elasto-plasticity. *Comput Methods Appl Mech Eng* 51:177–208
- Skalak R, Tözeren A, Zarda PR, Chien S (1973) Strain energy function of red blood cell membranes. *Biophys J* 13:245–264
- Sugiyama K, Ii S, Takeuchi S, Takagi S, Matsumoto Y (2010a) Full Eulerian simulations of biconcave neo-Hookean particles in a Poiseuille flow. *Comput Mech* 46:147–157
- Sugiyama K, Nagano N, Takeuchi S, Ii S, Takagi S, Matsumoto Y (2010b) Particle-In-Cell Method for fluid–structure interaction simulations of Neo-Hookean tube flows. *Theor Appl Mech Japan* 59:245–256
- Sugiyama K, Ii S, Takeuchi S, Takagi S, Matsumoto Y (2011) A full Eulerian finite difference approach for solving fluid-structure coupling problems. *J Comput Phys* 230:596–627
- Sui Y, Chew YT, Roy P, Cheng YP, Low HT (2008) Dynamic motion of red blood cells in simple shear flow. *Phys Fluids* 20:112106
- Sulsky D, Zhou S-J, Schreyer HL (1995) Application of a particle-in-cell method to solid mechanics. *Comput Phys Comm* 87:236–252
- Takagi S, Oguz HN, Prosperetti A (2003) PHYSALIS: a new method for particle simulation: part II: Two-dimensional Navier-Stokes flow around cylinders. *J Comput Phys* 187:371–390
- Takagi S, Yamada T, Gong X, Matsumoto Y (2009) The deformation of a vesicle in a linear shear flow. *J Appl Mech* 76:021207
- Takagi S, Sugiyama K, Ii S, Matsumoto Y (2012) A review of full Eulerian methods for fluid structure interaction problems. *J Appl Mech* 79:010911
- Takeuchi S, Yuki Y, Ueyama A, Kajishima T (2010) A conservative momentum exchange algorithm for interaction problem between fluid and deformable particles. *Int J Numer Methods Fluids* 64:1084–1102
- Takizawa K, Tezduyar TE (2011) Multiscale space-time fluid–structure interaction techniques. *Comput Mech* 48:247–267

- Tezduyar TE, Behr M, Liou J (1992a) A new strategy for finite element computations involving moving boundaries and interfaces—The deforming-spatial-domain/space-time procedure: I. The concept and the preliminary numerical tests. *Comput Methods Appl Mech Eng* 94:339–351
- Tezduyar TE, Behr M, Mittal S, Liou J (1992b) A new strategy for finite element computations involving moving boundaries and interfaces—The deforming-spatial-domain/space-time procedure: II. Computations of free-surface flows, two-liquid flows, and flows with drifting cylinders. *Comput Methods Appl Mech Eng* 94:353–371
- Tezduyar TE, Sathe S (2007) Modeling of Fluid–structure interactions with the space-time finite elements: solution techniques. *Int J Numer Methods Fluids* 54:855–900
- Trapp JA (1971) Reinforced materials with thermo-mechanical constraints. *Int J Eng Sci* 9:757–773
- Tryggvason G, Sussman M, Hussaini MY (2007) Immersed boundary methods for fluid interfaces. In: Prosperetti A, Tryggvason G (eds) *Computational methods for multiphase flow*, Cambridge University Press, Cambridge (Chapter 3)
- Udaykumar HS, Tran L, Belk DM, Vanden KJ (2003) An Eulerian method for computation of multimaterial impact with ENO shock-capturing and sharp interfaces. *J Comput Phys* 186:136–177
- Van Hoogstraten PAA, Slaats PMA, Baaijens FPT (1991) A Eulerian approach to the finite element modelling of Neo-Hookean rubber material. *Appl Sci Res* 48:193–210
- Wallstedt PC, Guilkey JE (2008) An evaluation of explicit time integration schemes for use with the generalized interpolation material point method. *J Comput Phys* 227:9628–9642
- Xiao F, Yabe T (1999) Computation of complex flows containing rheological bodies. *Comput Fluid Dyn J* 8:43–49
- Xiao F, Honma Y, Kono K (2005) A simple algebraic interface capturing scheme using hyperbolic tangent function. *Int J Numer Methods Fluids* 48:1023–1040
- York AR II, Sulsky D, Schreyer HL (2000) Fluid-membrane interaction based on the material point method. *Int J Numer Meth Engrg* 48:901–924
- Yu Z (2005) A DLM/FD method for fluid/flexible-body interactions. *J Comput Phys* 207:1–27
- Yuki Y, Takeuchi S, Kajishima T (2007) Efficient immersed boundary method for strong interaction problem of arbitrary shape object with self-induced flow. *J Fluid Sci Technol* 2:1–11
- Zhang J, Johnson PC, Popel AS (2008) Effects of erythrocyte deformability and aggregation on the cell free layer and apparent viscosity of microscopic blood flows. *Microvasc Res* 77:265–272
- Zhang L, Gerstenbetger A, Wang X, Liu WK (2004) Immersed finite element method. *Comput Methods Appl Mech Eng* 193:2051–2067
- Zhao H, Freund JB, Moser RD (2008) A fixed-mesh method for incompressible flow-structure systems with finite solid deformation. *J Comput Phys* 227:3114–3140
- Zhao H, Isfahani AHG, Olson LN, Freund JB (2010) A spectral boundary integral method for flowing blood cells. *J Comput Phys* 229:3726–3744

Physiological Significance of Cell-Free Layer and Experimental Determination of its Width in Microcirculatory Vessels

Bumseok Namgung, Leo Hwa Liang and Sangho Kim

Abstract Formation of a cell-free layer (CFL) adjacent to the luminal surface of microvessels is a consequence of axial migration of red blood cells (RBCs) towards the flow centerline. The CFL formation is a prominent hemodynamic feature in the microcirculation and thus it can be a dynamic indicator for alteration of the microcirculatory system. Consequently, its dynamic characteristics (mean width and spatio-temporal variations) are important factors to better understand the microcirculatory functions under physiological and pathophysiological conditions. The CFL is known to play a lubricating role by reducing the friction between RBC core and vessel wall. As a result, a thicker CFL may attenuate wall shear stress by reducing the effective viscosity of blood which in turn leads to lower nitric oxide (NO) production by the endothelium, in particular in small arterioles. In addition, the CFL can be a diffusion barrier to NO scavenging by RBCs as well as oxygen delivery from the cells to tissue in the arterioles. Thus, due to the importance of the CFL formation in the microcirculation, there have been many attempts to experimentally quantify the CFL width in microcirculatory vessels. In this chapter, we will review currently available techniques for the CFL width measurements in microsystems and discuss about their limitations. For more detailed quantification on the spatio-temporal variations of the CFL, recently developed computer-based methods will be introduced.

B. Namgung · L. H. Liang · S. Kim (✉)

Department of Biomedical Engineering, Faculty of Engineering, National University of Singapore, 9 Engineering Drive 1, Block EA #03-12, Singapore 117576, Singapore
e-mail: bieks@nus.edu.sg

B. Namgung
e-mail: bienb@nus.edu.sg

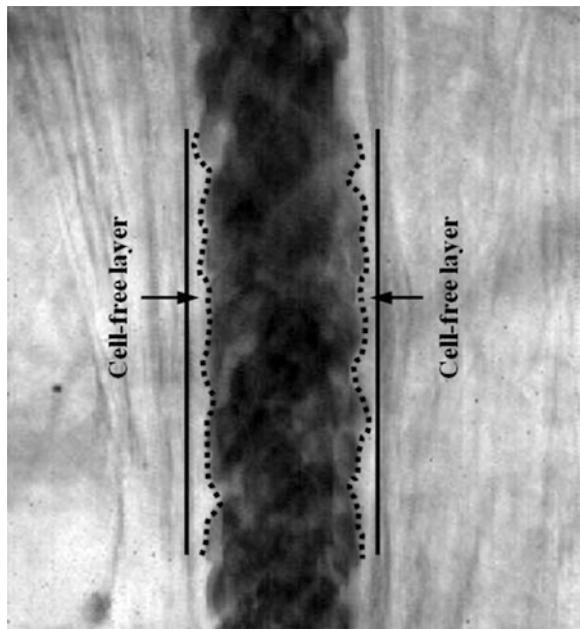
L. H. Liang
e-mail: bielhl@nus.edu.sg

S. Kim
Department of Surgery, National University of Singapore, Singapore, Singapore

1 Cell-Free Layer Formation in Microcirculation

Formation of a cell-free layer (CFL) is mainly attributed to axial migration of red blood cells (RBCs) toward the flow center (Goldsmith 1986; Kim et al. 2009; McHedlishvili and Maeda 2001). The axial migration is induced by “tank-treading” motion of the deformable cell membrane. The motion arises from both compressive and tensile forces acting on the cell membrane under shear flow (McHedlishvili and Maeda 2001). The deformable membrane of RBC is favorable towards tank-treading motion rather than tumbling which is commonly observed with solid particles under shear flow (Abkarian and Viallat 2008). The RBCs that migrate towards the centerline are subjected to relatively faster flow stream than at its initial lateral position adjacent to the wall. Consequently, the migrated RBCs maintain their individual lateral position in flow stream, which results in the development of blood phase separation to plasma and RBC core. This phase separation leads to formation of the CFL or cell-deplete zone near the wall (Goldsmith 1986; McHedlishvili and Maeda 2001). Therefore, the CFL width is defined as the distance between the outermost edge of RBC core and luminal surface of the endothelium in vessels (Fig. 1). The CFL width can be influenced by physical and rheological factors such as hematocrit, RBC deformability and aggregability, vessel diameter, and flow rate (Maeda 1996; McHedlishvili and Maeda 2001; Suzuki et al. 1998; Tateishi et al. 1994). In addition, the elasticity of vessels also influences the CFL width. A relatively thicker CFL can be formed in elastic vessels than in hardened vessels (Maeda et al. 1996).

Fig. 1 Typical example of the cell-free layer (CFL) formation in arteriole (ID = 55 μm). The solid and dashed lines indicate the inner vessel wall and outer edge of RBC core, respectively



2 Hemodynamic Aspect of Cell-Free Layer

It has long been established in micro-glass tube studies that the CFL plays a lubricating role in blood flow by reducing the friction between the RBC core and tube wall (Alonso et al. 1993; Cokelet and Goldsmith 1991). The CFL formed adjacent to the wall attenuates local viscosity, which in turn causes a reduction in apparent viscosity. The attenuation of apparent viscosity is mainly due to relatively lower viscosity of plasma near the wall than the viscosity of the core. Consequently, the apparent viscosity decrease results in reduction of blood flow resistance.

Alternatively, the CFL plays an important role in balancing nitric oxide (NO) production by the endothelium and NO scavenging by RBCs (Makena Hightower et al. 2011). NO is an important relaxation factor of smooth muscle cells, thus its bioavailability becomes a major concern of vasodilation (Horiuchi et al. 2002). The layer can be a diffusion barrier to NO scavenging by RBCs as well as oxygen delivery from the RBCs to tissue (Butler et al. 1998; Chen et al. 2006; El-Farra et al. 2003; Lamkin-Kennard et al. 2004; Vaughn et al. 1998). Many computational predictions have been performed to examine the effect of the CFL on the NO profiles by varying the layer width. These predictions showed that the CFL could inhibit the scavenging of NO by RBCs, which leads to higher tendency of NO diffusion to the tissue (Lamkin-Kennard et al. 2004). The inhibition effect of the CFL influences NO bioavailability greatly, and it can offset the increase in NO scavenging rate due to elevation of the core hematocrit by the thicker CFL formation (Lamkin-Kennard et al. 2004).

It should be noted that not only the diffusion barrier role of CFL but also its role in modulation of wall shear stress (WSS) is physiologically important. As the WSS is a dominant mechanical force triggering NO release from the endothelium (Chien 2007; Pittner et al. 2005; Resnick et al. 2003), its relation with the CFL has been of particular concern in many studies (Namgung et al. 2011; Sharan and Popel 2001; Yalcin et al. 2008). An *in vitro* study has reported that a thicker CFL formation may attenuate WSS by reducing effective viscosity of blood, which in turn leads to a lower NO production by the endothelium (Yalcin et al. 2008). A theoretical study (Sharan and Popel 2001) suggested that the WSS should be influenced by a dynamic change of the CFL width, which was examined later in an *in vivo* study (Namgung et al. 2011). The latter study highlighted potential enhancement of arteriolar WSS by the temporal variation of the CFL width. Subsequent computational studies reported that the CFL variation might potentially result in an augmentation of the NO bioavailability in tissue (Ong et al. 2011a, b). Therefore, not only the mean width of the CFL but also its spatio-temporal variations may have a significant impact on the NO transport in microcirculation.

3 Visualization of Cell-Free Layer Formation in Microcirculation

Figure 2 shows some examples for visualization of blood flow in the microcirculation, which is essential and a very first step for understanding of the microcirculatory system. Upon successful visualization, more detailed information can be obtained by employing appropriate image analysis techniques to further advance our knowledge of blood flow in the microcirculation. The surgical exposure of a particular muscle of rodents, e.g. cremaster or spinotrapezius muscle, allows us to directly visualize the microcirculation under an intravital microscopic system. In addition, advancement in optical technology has contributed in providing high quality images of blood flow in such small vessels. Especially, a high-speed video camera provides the capacity of digital recording of blood flow with better image contrast and sharpness. By merging the aforementioned technologies, now it becomes possible to visualize spatio-temporal variations of the CFL width in vivo.

The CFL width determination has relied mostly on transilluminated microscopic images. The CFL can be detected in distinct brighter region near the vessel wall than the RBC core region. Therefore, the light intensity difference (contrast) between the two regions is a key determinant in the layer measurement. By performing digital image processing (or manual measurement), the CFL width can be determined by measuring the distance between the inner vessel wall and outer edge of RBC core. For optical enhancement of the image contrast, a blue filter with wavelength for peak transmittance of ~ 400 nm can be used. The peak value corresponds to maximum wavelength of absorption of photons by hemoglobin in RBCs, which enhances the contrast between the CFL and RBC core.

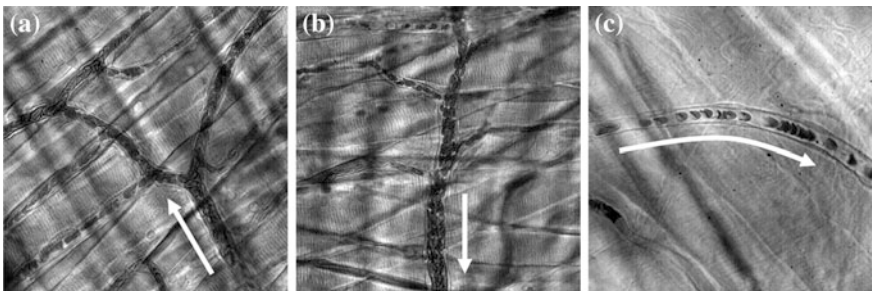


Fig. 2 Visualization of red cell flows in the rat cremaster muscle. **a**, **b** and **c** Show blood flows in arterioles, venules, and a capillary, respectively. The arrow indicates the flow direction

4 Quantification of Cell-Free Layer Width in Microcirculation

4.1 Conventional Manual Method

A number of studies have been carried out to quantify the CFL width in microvessels. The conventional method for the CFL width determination is the manual measurement on the analog video and/or digital image frames recorded through a microscopic system (Maeda et al. 1996; Soutani et al. 1995; Tateishi et al. 1994). In a recent study by Lima and coworkers, they visualized the layer by flowing labeled RBCs under a confocal microscopic system (Lima et al. 2009). In their study, the CFL widths were measured by manually tracking the trajectory of outermost cells of RBC core. This kind of manual measurement can be time-consuming and subjective, depending on performance. Thus, it may result in low reliability and repeatability of the measurement. Furthermore, it is not suitable to obtain detailed information on spatial and temporal variations of the CFL width.

4.2 Computer-Based Automated Method

4.2.1 Histogram-Based Thresholding Algorithm

To overcome the limitations of the manual measurement, a recent study proposed a simple but effective way for the CFL width determination by adopting a computer-based digital image processing technique (Kim et al. 2006). The key feature of the method is the image segmentation which is commonly used for separating the objective from background in an image. Its algorithm is based on light intensity values of the image. The method provides the consistency in measurement and automation of the process. Thus, it greatly minimizes the human measurement error and time consumption. In addition, the method is capable of providing information on spatio-temporal variations of the CFL width in more detail. Figure 3 shows a flow chart of the overall procedure for the computer-based CFL width determination (Kim et al. 2006), whereas the resulting digital images are represented in Fig. 4.

Firstly, an uncompressed-format footage recorded by a high-speed video camera is extracted into gray-scale images (*Image extraction*). Each image is then filtered with the median filter to reduce the ‘salt and pepper’ noise (Chan et al. 2005). After the image preparation, an analysis line is drawn across the vessel at a location of interest (Fig. 4a). To determine the vessel wall location (*Wall determination*, Fig. 4b), the light intensity profile along the analysis line is obtained and its initial peak that transits from dark to light over two pixels is considered as the location of the inner vessel wall. This criterion was suggested by previous studies for the determination of the endothelial surface (Gretz and Duling 1995; Kim et al.

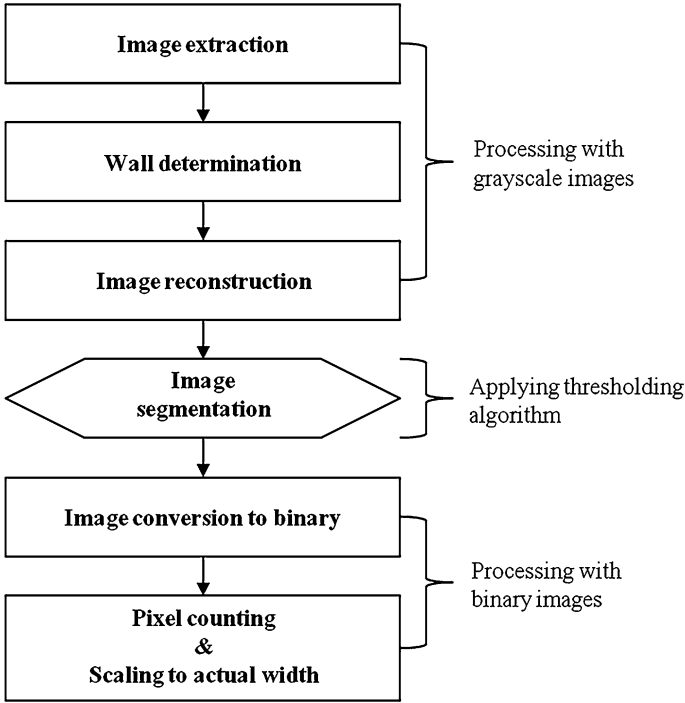


Fig. 3 Digital image processing for the cell-free layer (CFL) width determination from recorded images

2006; Smith et al. 2003). The error associated with this method is estimated to be $\pm 0.5 \mu\text{m}$ (Kim et al. 2006). After confirmation of the vessel wall location, the light intensity profile along the analysis line over all sequential images are accumulated into a single grayscale image (*Image reconstruction*, Fig. 4c). The reconstructed image then proceeds to '*Image segmentation*' to be converted into a binary image (Fig. 4d) by using a thresholding algorithm. During the segmentation process, any pixel of the image $f(x, y)$ with light intensity value greater than a certain threshold value (T) is considered as objective, whereas other pixels are considered as background. Therefore, the binary image $g(x, y)$ can be defined as follows:

$$g(x, y) = \begin{cases} 1 & \text{if } f(x, y) > T \\ 0 & \text{if } f(x, y) \leq T \end{cases} \quad (1)$$

Therefore, the CFL width can be obtained from the binary image by counting the number of white pixels from the vessel wall until the first black pixel is encountered (Fig. 4d).

In the above process, the thresholding algorithm is a crucial determinant in the CFL width measurement and thus several histogram-based thresholding algorithms

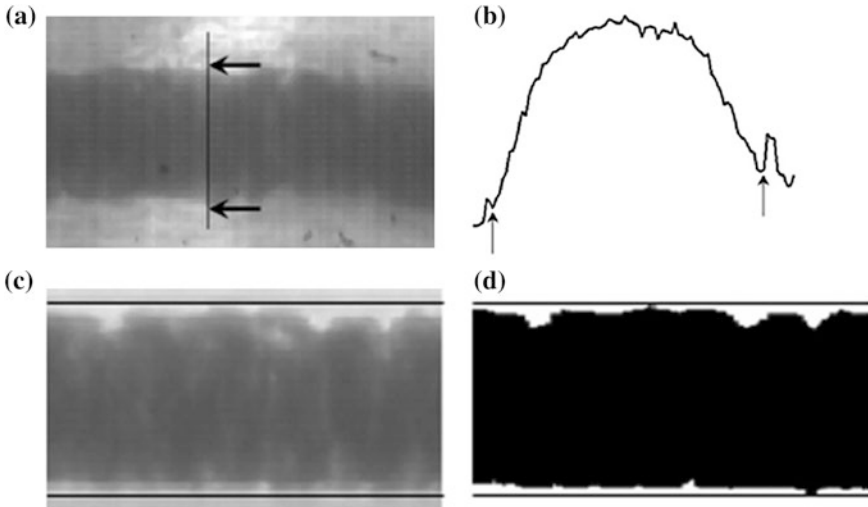


Fig. 4 Computer-based method for cell-free layer (CFL) measurement. **a** Grayscale image of red blood cell flow in a venule. **b** Light intensity profile along the analysis line (represented by solid line). **c** Grayscale image after reconstruction. **d** Binary image. Arrows in ‘a’ and ‘b’ and solid lines in ‘c’ and ‘d’ represent the location of vessel wall. (Reprinted with permission of Kim (Kim et al. 2006))

were examined in a subsequent study (Namgung et al. 2010). This study has highlighted that the Otsu’s algorithm used in the study by Kim and coworkers (Kim et al. 2006) has a drawback in the measurement accuracy when the sizes of object and background are significantly unequal as also pointed out in previous studies (Kittler and Illingworth 1985; Qiao et al. 2007). In this comparative study, four different histogram-based thresholding algorithms were tested, including the minimum (Prewitt and Mendelsohn 1966), intermodes (Prewitt and Mendelsohn 1966), 2nd peak detection (Sezan 1985), and Otsu’s methods (Kim et al. 2006; Otsu 1979). These algorithms have been widely used for their simplicity, ease of implementation, and high speed of processing (Qiao et al. 2007; Sezgin and Sankur 2004).

To better depict the histogram-based thresholding method, the probability distribution (normalized grayscale histogram) of image is described. The probability can be calculated as follows:

$$P_i = \frac{n_i}{N}, \quad P_i \geq 0, \quad \sum_{i=0}^L P_i = 1 \tag{2}$$

where L is the gray level (0–255), the number of pixels at the gray level i is denoted by n_i and the total number of pixels in an image is denoted by N . If an image has clear contrast between objective and background, the shape of probability distribution will have a bimodal (double-peaked) shape. Figure 5 shows a

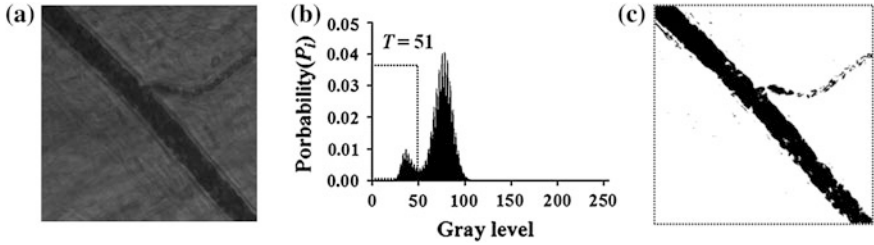


Fig. 5 Typical example of image segmentation by use of the minimum method. **a** Grayscale image, **b** Probability distribution of the image, **c** Binary image obtained by the minimum algorithm. T represents the threshold level determined by the minimum method

typical example of image segmentation based on the minimum thresholding method. The figure clearly shows that when the gray image (Fig. 5a) has good contrast between red cells and background, the probability distribution of the image can have a distinct bimodal shape (Fig. 5b). In the shape, each class (each unimodal distribution) represents an objective (blood core) and background (tissue). The gray level at which the probability has its minimum corresponding to the valley of the shape can be a most suitable threshold value for the segmentation (Fig. 5c). In this process, additional treatments can be performed such as digital image contrast enhancement to reduce imbalance between the two classes and iterative smoothing of the histogram to achieve the two unique local maxima (Glasbey 1993).

However, as mentioned above, if the image has unequal local maxima or a broad and flat valley of the class, it may not provide a proper threshold value. Especially, the Otsu's algorithm is highly sensitive to these unequal local maxima. Thus, an unequal variance of the classes may cause a tendency of the threshold level to be determined at a level closer to the peak with larger population of probability (Kittler and Illingworth 1985; Qiao et al. 2007).

4.2.2 Grayscale Method (Edge Detection)

The image contrast between RBCs and background can be significantly influenced by light intensity passing through the surrounding tissue. In particular, when the arteriole of interest is located in a deep tissue, faint shaded regions near the vessel wall may be observed, which causes possible breakdown of the histogram-based CFL width measurement. This limitation has been addressed in a study by Ong and coworkers (Ong et al. 2011c) In this study, an alternative way of determining the CFL width (grayscale method) was proposed to take into account the faint shaded region as part of the RBC core. This method provides local detections of the inner vessel wall as well as the boundary between the CFL and RBC column without binarization of the grayscale image (Ong et al. 2011c). A comparison between the previous histogram-based methods and the grayscale method is illustrated in

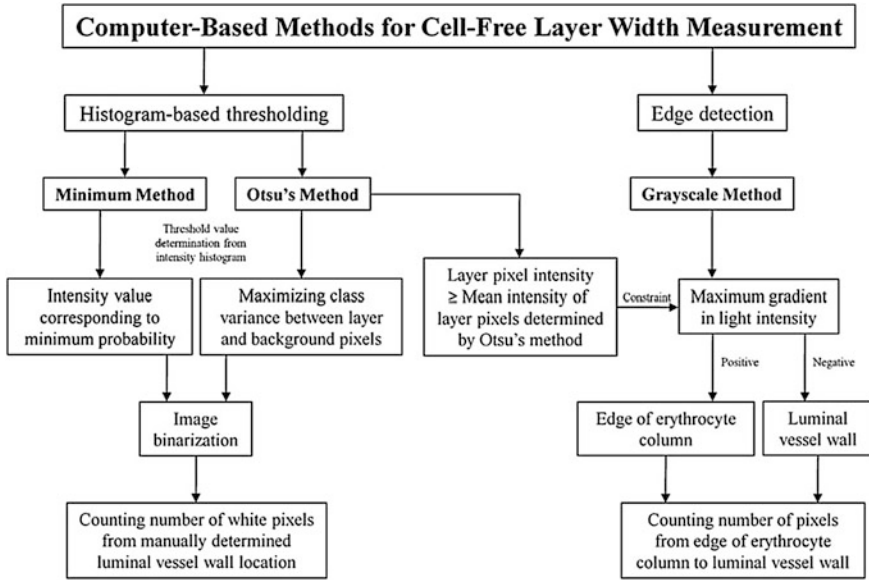


Fig. 6 A comparative description of the computer-based methods for cell-free layer width measurement. (Reprinted with permission of Ong (Ong et al. 2011c))

Fig. 6. The main feature of the grayscale method is the edge detection which relies on the local maximum gradient along the analysis line.

Firstly, the inner vessel wall is determined by comparing light intensities in two adjacent pixels along the analysis line. The local maximum light intensity decrease (negative gradient) determines the location of the inner vessel wall. After determination of the wall location, the reconstructed image is created (from *Image reconstruction* in Fig. 3). By performing the Otsu’s thresholding process, a prospective CFL region is predefined which possibly includes the shade region of RBC column in the CFL. The following equation defines the criterion used for the actual CFL region detection during the pixel scanning for light intensity comparison.

$$I(x, y) \geq \frac{\sum_{k=1}^{n_{CFL}} I_k}{n_{CFL}} \quad (x = 1, 2, \dots, N; y = 1, 2, \dots, R - 1) \quad (3)$$

where $I(x, y)$ refers to the gray level intensity value at a point in the reconstructed image. n_{CFL} denotes the total number of pixels in the CFL determined by the Otsu’s method. N and R are the width and height of the reconstructed image, respectively. The maximum increase in light intensity between two adjacent pixels along the analysis line satisfying the above criterion determines the edge location of the RBC column. The CFL width finally is obtained by counting the number of pixels from the light pixel to the inner vessel wall. Thus, the pixels (faint gray region) with lower intensity than the averaged intensity of the prospective CFL region determined by the Otsu’s method can be considered as part of RBC column.

5 Limitations of Current Methods and Future Prospects

All the measurement techniques discussed here are influenced by image quality that varies with microscopic systems. In addition, the spatial resolution of the measurement relies on the microscopic system including a digital video camera. Most recent studies have reported their spatial resolution to be $\sim 0.4 \mu\text{m}$ with use of high-speed framing rates $>3,000 \text{ f/s}$. The CFL measurement is sensitive to the image contrast, image resolution and frame rates of video recording. The resolution will become more significant in the layer measurement when small vessels (inner diameter $<20 \mu\text{m}$) are of particular interest.

A direct way to improve the spatial resolution is to use a higher magnification objective for the visualization. However, a smaller field of view with the higher magnification objective is inevitable. Especially for observation of the CFL formation in a microvascular network, the limited field of view may not allow us to obtain simultaneous measurements of the CFL width variations in the entire network. Therefore, if the CFL modulation inherited by upstream conditions is of interest, the enhancement of pixel resolution would be essential to secure the large enough field of view for network coverage. An alternative way of improving the pixel resolution is to adopt a camera with a high resolution CMOS (complementary metal-oxide-semiconductor) or CCD (charge-coupled device) sensor.

Another issue in the CFL width measurement will arise from the presence of glycocalyx layer on the endothelium. The thickness of the glycocalyx layer has been reported to be $\sim 0.5 \mu\text{m}$ in capillaries and venules and $\sim 0.4 \mu\text{m}$ in arterioles (Savery and Damiano 2008). The glycocalyx layer is not detectable under the transillumination microscopic system. Thus, the CFL width determined by such a system includes this transparent glycocalyx layer. In addition, when the thickness of the glycocalyx layer is smaller than the pixel resolution of the microscopic system, overestimation of the CFL width may be substantial. To overcome this limitation, the thickness of the glycocalyx layer should be predetermined before the CFL measurement. A previous study by Vink and Duling (1996) proposed a way of measuring the glycocalyx thickness by suspending FITC-dextran. They compared the anatomical diameter obtained from a bright field illumination image with the labeled plasma column from a fluorescent image. By subtracting the plasma column from the anatomical diameter, they visualized the existence of the glycocalyx layer (Pries et al. 2000). Thus, the estimation of the glycocalyx layer thickness for each flow condition can be made by using fluorescent plasma.

Lastly, as discussed in the *Grayscale method* section, considering the faint shaded region as part of RBC core may lead to an overestimation of the CFL width. The hematocrit distribution along the radial direction of the blood lumen is not homogenous in 3-D flow, but all the measurements described here are based on the 2-D images. Thus, if it is unclear whether the faint shaded region belongs to the same focal plane of interest, the CFL width measurement might be underestimated. Figure 7 shows typical examples of CFL width data measured with different image segmentation algorithms. As shown clearly in Fig. 7, the CFL width

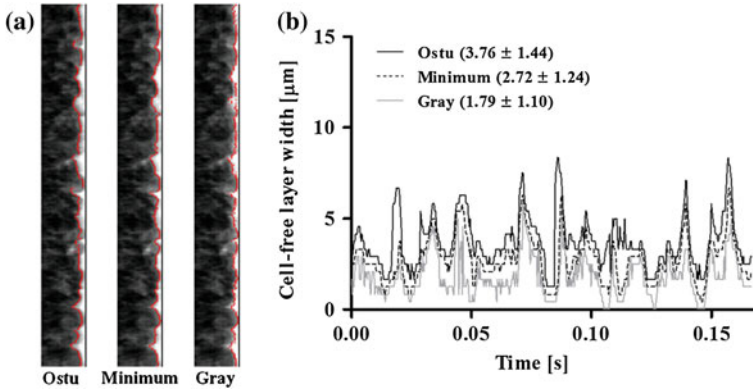


Fig. 7 **a** Cell-free layer width defined by the Otsu's, Minimum and Gray methods. **b** Corresponding cell-free layer width variations over 500 frames with 3,000 f/s. (Mean \pm SD)

measurement can be highly sensitive to determine whether or not the faint shaded region is considered as part of RBC core. A confocal microscopic system with suspending labeled RBCs may be used to address this issue. However, this method is limited to lower hematocrit RBC suspension and is only applicable when the labeled cells are positioned in outer most boundary of RBC core. Alternatively, the digital image enhancement techniques (Filtering, smoothing, and transformation) can be performed for improvement of image contrast. However, it should be noted that such image manipulations may result in image artifacts and thus selection of an appropriate digital image post-processing would be essential.

6 Conclusion and Outlook

As mentioned earlier in this chapter, the CFL is of great interest in microcirculatory studies as an important hemodynamic parameter. To accumulate further detailed knowledge of relationship between hemodynamic impairment and its corresponding response in CFL width, the limitations of the CFL width measurement discussed in this chapter are to be overcome by advancement of the measurement techniques. For the future clinical application of the CFL as a diagnostic indicator, many attempts still need to be extended. In addition, miniaturization and integration of the CFL width measurement system would be the essential part of those attempts.

Acknowledgments This work was supported by NUS FRC 397-000-134-112. The authors wish to thank Dr. Alvin Koh for his valuable discussion.

References

- Abkarian M, Viallat A (2008) Vesicles and red blood cells in shear flow. *Soft Matter* 4(4):653–657
- Alonso C, Pries AR, Gaetgens P (1993) Time-dependent rheological behavior of blood at low shear in narrow vertical tubes. *Am J Physiol* 265(2 Pt 2):H553–H561
- Butler AR, Megson IL, Wright PG (1998) Diffusion of nitric oxide and scavenging by blood in the vasculature. *Biochim Biophys Acta* 1425(1):168–176
- Chan RH, Ho C-W, Nikolova M (2005) Salt-and-pepper noise removal by median-type noise detectors and detail-preserving regularization. *IEEE Trans Image Process Publ IEEE Sig Proc Soc* 14(10):1479–1485
- Chen X, Jaron D, Barbee KA, Buerk DG (2006) The influence of radial RBC distribution, blood velocity profiles, and glycocalyx on coupled NO/O₂ transport. *J Appl Physiol* 100(2):482–492
- Chien S (2007) Mechanotransduction and endothelial cell homeostasis: the wisdom of the cell. *Am J Physiol Heart Circ Physiol* 292(3):H1209–H1224
- Cokelet GR, Goldsmith HL (1991) Decreased hydrodynamic resistance in the two-phase flow of blood through small vertical tubes at low flow rates. *Circ Res* 68(1):1–17
- El-Farra NH, Christofides PD, Liao JC (2003) Analysis of nitric oxide consumption by erythrocytes in blood vessels using a distributed multicellular model. *Ann Biomed Eng* 31(3):294–309
- Glasbey CA (1993) An analysis of histogram based thresholding algorithms. *CVGIP Graph Models Image process* 55(6):532–537
- Goldsmith HL (1986) The microcirculatory society eugene M. Landis award lecture. The micro rheology of human blood. *Microvasc Res* 31(2):121–142
- Gretz JE, Duling BR (1995) Measurement uncertainties associated with the use of bright-field and fluorescence microscopy in the microcirculation. *Microvasc Res* 49(1):134–140
- Horiuchi T, Dietrich HH, Hongo K, GOTO T, Dacey RG (2002) Role of endothelial nitric oxide and smooth muscle potassium channels in cerebral arteriolar dilation in response to acidosis. *Stroke* 33(3):844–849
- Kim S, Kong RL, Popel AS, Intaglietta M, Johnson PC (2006) A computer-based method for determination of the cell-free layer width in microcirculation. *Microcirculation* 13(3):199–207
- Kim S, Ong PK, Yalcin O, Intaglietta M, Johnson PC (2009) The cell-free layer in microvascular blood flow. *Biorheology* 46(3):181–189
- Kittler J, Illingworth J (1985) On threshold selection using clustering criteria. *IEEE Trans Syst Man Cybern* 15(5):652–654
- Lamkin-Kennard KA, Jaron D, Buerk DG (2004) Impact of the Fåhræus effect on NO and O₂ biotransport: a computer model. *Microcirculation* 11(4):337–349
- Lima R, Oliveira MS, Ishikawa T, Kaji H, Tanaka S, Nishizawa M, Yamaguchi T (2009) Axisymmetric polydimethylsiloxane microchannels for in vitro hemodynamic studies. *Biofabrication* 1(3):035005
- Maeda N (1996) Erythrocyte rheology in microcirculation. *Jpn J Physiol* 46(1):1–14
- Maeda N, Suzuki Y, Tanaka J, Tateishi N (1996) Erythrocyte flow and elasticity of microvessels evaluated by marginal cell-free layer and flow resistance. *Am J Physiol* 271(6 Pt 2):H2454–H2461
- Makena Hightower C, Salazar Vazquez BY, Woo Park S, Sriram K, Martini J, Yalcin O, Tsai AG, Cabrales P, Tartakovsky DM, Johnson PC, Intaglietta M (2011) Integration of cardiovascular regulation by the blood/endothelium cell-free layer. *Wiley Interdiscip Rev Syst Biol Med* 3(4):458–470
- McHedlishvili G, Maeda N (2001) Blood flow structure related to red cell flow: a determinant of blood fluidity in narrow microvessels. *Jpn J Physiol* 51(1):19–30
- Namgung B, Ong PK, Johnson PC, Kim S (2011) Effect of cell-free layer variation on arteriolar wall shear stress. *Ann Biomed Eng* 39(1):359–366

- Namung B, Ong PK, Wong YH, Lim D, Chun KJ, Kim S (2010) A comparative study of histogram-based thresholding methods for the determination of cell-free layer width in small blood vessels. *Physiol Meas* 31(9):N61–N70
- Ong PK, Jain S, Kim S (2011a) Modulation of NO bioavailability by temporal variation of the cell-free layer width in small arterioles. *Ann Biomed Eng* 39(3):1012–1023
- Ong PK, Jain S, Kim S (2011b) Temporal variations of the cell-free layer width may enhance NO bioavailability in small arterioles: effects of erythrocyte aggregation. *Microvasc Res* 81(3):303–312
- Ong PK, Jain S, Namung B, Woo YI, Sakai H, Lim D, Chun KJ, Kim S (2011c) An automated method for cell-free layer width determination in small arterioles. *Physiol Meas* 32(3):N1–N12
- Otsu N (1979) A threshold selection method from gray-level histograms. *IEEE Trans Syst Man Cybern* 9(1):62–66
- Pittner J, Wolgast M, Casellas D, Persson AEG (2005) Increased shear stress-released NO and decreased endothelial calcium in rat isolated perfused juxtamedullary nephrons. *Kidney Int* 67(1):227–236
- Prewitt JM, Mendelsohn ML (1966) The analysis of cell images. *Ann N Y Acad Sci* 128(3):1035–1053
- Pries AR, Secomb TW, Gaehtgens P (2000) The endothelial surface layer. *Pflugers Arch* 440(5):653–666
- Qiao Y, Hu Q, Qian G, Luo S, Nowinski WL (2007) Thresholding based on variance and intensity contrast. *Pattern Recognit* 40:596–608
- Resnick N, Yahav H, Shay-Salit A, Shushy M, Schubert S, Zilberman LCM, Wofovitz E (2003) Fluid shear stress and the vascular endothelium: for better and for worse. *Prog Biophys Mol Biol* 81(3):177–199
- Savery MD, Damiano ER (2008) The endothelial glycocalyx is hydrodynamically relevant in arterioles throughout the cardiac cycle. *Biophys J* 95(3):1439–1447
- Sezan MI (1985) A peak detection algorithm and its application to histogram-based image data reduction. *Comput Vision Graph Image Process* 29:47–59
- Sezgin M, Sankur B (2004) Survey over image thresholding techniques and qualitative performance evaluation. *J Electron Imaging* 13(1):146–165
- Sharan M, Popel AS (2001) A two-phase model for flow of blood in narrow tubes with increased effective viscosity near the wall. *Biorheology* 38(5–6):415–428
- Smith ML, Long DS, Damiano ER, Ley K (2003) Near-wall micro-PIV reveals a hydrodynamically relevant endothelial surface layer in venules in vivo. *Biophys J* 85(1):637–645
- Soutani M, Suzuki Y, Tateishi N, Maeda N (1995) Quantitative evaluation of flow dynamics of erythrocytes in microvessels: influence of erythrocyte aggregation. *Am J Physiol* 268(5 Pt 2):H1959–H1965
- Suzuki Y, Tateishi N, Maeda N (1998) Electrostatic repulsion among erythrocytes in tube flow, demonstrated by the thickness of marginal cell-free layer. *Biorheology* 35(2):155–170
- Tateishi N, Suzuki Y, Soutani M, Maeda N (1994) Flow dynamics of erythrocytes in microvessels of isolated rabbit mesentery: cell-free layer and flow resistance. *J Biomech* 27(9):1119–1125
- Vink H, Duling BR (1996) Identification of distinct luminal domains for macromolecules, erythrocytes, and leukocytes within mammalian capillaries. *Circ Res* 79(3):581–589
- Vaughn MW, Kuo L, Liao JC (1998). Effective diffusion distance of nitric oxide in the microcirculation. *Am J Physiol* 274(5 Pt 2):H1705–H1714
- Yalcin O, Ulker P, Yavuzer U, Meiselman HJ, Baskurt O K (2008). Nitric oxide generation by endothelial cells exposed to shear stress in glass tubes perfused with red blood cell suspensions: role of aggregation. *Am J Physiol Heart Circ Physiol* 294(5):H2098–H2105

Computational Simulation of NO/O₂ Transport in Arterioles: Role of Cell-Free Layer

Seungkwan Cho, Swe Soe Ye, Hwa Liang Leo and Sangho Kim

Abstract Nitric oxide (NO) is the primary signalling molecule that regulates blood flow and tissue oxygenation. NO diffuses into the vessel lumen and surrounding tissues after its production in the endothelium, where the NO production rate may be significantly affected by oxygen (O₂) bioavailability. Indeed, many studies have reported that abnormal changes in the bioavailability of these two gases are highly correlated with cardiovascular diseases such as hypertension, atherosclerosis and angiogenesis-associated disorders. However, despite a growing body of literature on the physiological role of NO and O₂, precise mechanisms of action remain largely unknown. Therefore, it is necessary to develop appropriate mathematical models of NO and O₂ biotransport to better understand such mechanisms. In addressing this purpose, a number of researchers have developed mathematical and computational models of varying sophistication to describe the gas transport in arterioles. In brief, early theoretical studies introduced numerical models capable of predicting only the NO transport in arterioles. Subsequent studies improved upon this methodology by developing transport models that simulate the interaction between NO and O₂ under steady-state conditions. Most recently, the coupled NO/O₂ computational models for gas transport in arterioles have been developed with the added dimension of time-dependency. These time-dependent models incorporate potential physiological responses to temporally varying cell-free (plasma) layer widths near the vessel wall. In this chapter, we

S. Cho · S. S. Ye · H. L. Leo · S. Kim (✉)

Department of Biomedical Engineering, Faculty of Engineering, National University of Singapore, 9 Engineering Drive 1, Block EA #03-12, Singapore 117576, Singapore
e-mail: bieks@nus.edu.sg

S. Cho

e-mail: biecsk@nus.edu.sg

S. S. Ye

e-mail: a0093837@nus.edu.sg

H. L. Leo

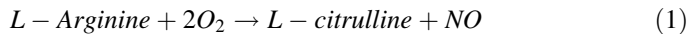
e-mail: bielhl@nus.edu.sg

will provide a historical review of the computational models employed for NO and O₂ transport in arterioles and lastly, we will discuss about the new developments for numerical models that study gas transport in detail.

1 General Principles

1.1 Biological and Chemical Systems of Nitric Oxide and Oxygen Synthesis

Nitric oxide (NO) is a principal signalling molecule associated with tissue oxygenation and vasodilation in the microvascular network. It is produced from the guanidine-nitrogen terminal of L-Arginine by the enzyme NO synthase (eNOS) in the endothelial cells. NO release by eNOS is initiated by the variation in shear stress on the endothelial cell surface, or by the activation of specific endothelial receptors by several hormones (Ballermann et al. 1998; Busse et al. 1998). In elaboration, the activation of eNOS depends on intracellular concentrations of Ca²⁺ and CaM, and this concentration can be enhanced by acute increases in shear stress (Kuchan et al. 1994). Therefore, changes in wall shear stress due to varying blood flow conditions can modulate NO release rate by eNOS. When eNOS is maximally activated, the co-substrates oxygen (O₂) and L-Arginine are required to synthesize NO. The general oxidation reaction that synthesizes NO can be summarized as follows (Chen and Popel 2006; Buerk 2001):



In this synthesis, O₂ availability is the primary factor that affects the production rate of NO. Accordingly, the general agreement in the literature is that an increase in O₂ enhances the NO production by eNOS. With regards to studying the NO/O₂ chemical relationship, the NO production rate can be represented by Michaelis–Menten kinetics. Michaelis and Menten first applied the concept of mass action kinetics developed for gas-phase reactions to biochemical reactions.

The Michaelis–Menten kinetics for NO/O₂ production can be summarized by the following equation:

$$R_{NO} = R_{NOmax}C_{O_2}/(C_{O_2} + K_m) \quad (2)$$

where R_{NOmax} is the maximum NO production rate and K_m is the Michaelis constant. The Michaelis constant represents the O₂ concentration (C_{O_2}) when the NO production rate R_{NO} is half of the maximum NO production rate R_{NOmax} (Buerk 2001).

The various values of K_m have been suggested from several experimental studies. Rengasamy and Johns (1996) investigated the effect of different concentrations of O₂ on NO synthase activity in bovine brain, cultured bovine aortic

Table 1 Biochemical reactions describing the sources/sinks for NO/O₂ in biotransport modelling (Buerk 2001)

Sources
1. $L\text{-Arginine} + O_2 \rightarrow L\text{-citrulline} + NO$
2. $2RSNO \rightarrow RSSR + 2NO$
3. $SNO\text{-Hb}(Fe^{2+})O_2 + GSH \rightarrow HS\text{-Hb}(Fe^{2+})O_2 + GSNO + O_2$
4. $GSNO + O_2^- \rightarrow GSH + O_2 + NO$
5. $NO_2^- + H^+ + NADH \rightarrow NO + H_2O$
Sinks
1. $4NO + O_2 + H_2O \rightarrow 4NO_2^- + 4H^+$
2. $NO + O_2^- \rightarrow ONOO^-$
3. $NO + ONOO^- \rightarrow NO_2^- + NO_3^-$
4. $NO + Hb(Fe^{2+}) \rightarrow Hb(Fe^{2+})NO$
5. $NO + Hb(Fe^{2+})O_2 \rightarrow Hb(Fe^{2+}) + NO_3^-$
6. $NO + Mb(Fe^{2+}) \rightarrow Mb(Fe^{2+})NO$
7. $NO + Mb(Fe^{2+})O_2 + H_2O \rightarrow Mb(Fe^{2+})OH + ONOO^- + H^+$
8. $2NO + RSH + O_2 \rightarrow RSNO + ONOO^-$

endothelial cells and macrophages. In their results, apparent K_m values for O₂ were reported to be 23.2 ± 2.8 , 7.7 ± 1.6 and 6.3 ± 0.9 μM for the brain, endothelial cells and macrophages respectively. Whorton et al. (1997) investigated the effect of varying O₂ concentrations on NO production by measuring nitrite (NO₂⁻) and nitrate (NO₃⁻) production by intact vascular endothelial cells. They found that the half-maximal NO production rate occurred at a PO₂ level of 38 Torr.

In addition to the O₂-L-Arginine biochemical reaction, there are several biochemical reactions that can be treated as sources or sinks for the NO/O₂ biotransport modelling (Buerk 2001). These reactions are summarized in Table 1.

However, despite a growing body of literature on the physiological role of NO/O₂, the precise mechanisms of action remain largely unknown. Thus, there is a need to develop appropriate mathematical models of NO/O₂ biotransport to better understand the different mechanisms. The use of mathematical models together with experimental data could help to elucidate the role of NO/O₂ and its related effects in the pathophysiological conditions.

1.2 Rheological Factors Affecting NO/O₂ Transport

1.2.1 Cell-Free Layer

The cell-free layer (CFL) is a plasma-rich layer present in the blood lumen adjacent to the endothelium. To be rigorous, the definition of the CFL width is the distance from the outer edge of the red blood cell (RBC) core to the luminal surface of the endothelium. The CFL formation may influence the local haematocrit, which in turn affects the NO/O₂ diffusion in the vessel. Several factors are

known to affect the width of CFL in microvessels, and these have been summarized by Tateishi and co-workers (1994): (1) decreasing the microvessel inner diameter increases the CFL width; (2) lowering the hematocrit increases the width; (3) increasing flow rate and shear stress increases the width, and (4) decreasing the deformability of RBCs reduces the width.

In addition, the CFL width also affects the NO/O₂ gas transport by serving as a diffusion barrier between the RBCs and the endothelium.

1.2.2 RBC Distribution and Blood Flow

Gas exchange between blood and the surrounding tissue primarily occurs in the microcirculation. Hence, the hemodynamics in microvessels will inevitably affect this exchange dynamics. Due to the comparable length scales between the RBC size and the microvessel size, the two phase nature of the blood mixture becomes apparent in the local hemodynamics. The key observations from the two phase nature of blood flow are that the distribution of RBCs in the bloodstream is non-uniform and that the RBCs tend to aggregate in the center of the blood vessel to form a core RBC flow. The resulting velocity profile from this non-uniform RBC distribution is a blunted velocity profile where variations in the edge of the core bulk flow may have significant influence on NO synthesis and transport. The discrete nature of RBCs along the edge of the RBC core engenders the likelihood of RBCs being present in the plasma layer between the core flow and the endothelium; variations in the location and spatial orientation of these discrete RBCs along the core edge directly affect the local CFL width and hence the NO dynamics. Experimental observations of RBCs in the plasma layer can be found in the literature (Kobayashi and Takizawa 2002), which indicate that the RBC distribution in the vessel lumen is uneven. They noted that the edge of the RBC core close to the wall occasionally contain RBCs. Their results agreed with the RBC distribution curve by Prakash and Singh (1995) who had obtained RBC distribution profiles for hematocrit values ranging from 10 to 60 % in a glass capillary with an internal diameter of 200 μm using axial tomographic and image velocimetry techniques. Their results confirmed that the RBC cell population is almost constant in the center of a glass tube and decreases to zero almost linearly near the wall when the tube hematocrit is high. Long et al. (2004) performed experiments in rat venules using fluorescent microparticle image velocimetry and estimated viscosity profiles in the vessel lumen. In their results, blood viscosity was constant in the core region of the venular flow, but decreased almost linearly near the vessel wall.

Until this point, we understand that the local wall shear stress in arterioles affects the NO synthesis by the endothelium cells. Wall shear stress is an entity that arises from the hemodynamics in the blood vessel and consequently this implies that the vessel geometry changes along the axial flow direction inherently affect the NO synthesis by affecting the wall shear stress. Particularly, curved vessels and bifurcations are essential geometric characteristics of the vascular network; the disturbed blood flow in these locations may affect the local

vasodilation. It has been suggested that in the long term, these disturbances might play a role in the development of vascular diseases, such as atherogenesis (Cooke and Dzau 1997; Malek et al. 1999).

In addition to affecting the NO production rate, hemodynamics in the microvessel also affects the O₂ transport and exchange dynamics. The blood flow provides a convective field velocity along which the O₂-carrying RBCs advect. In a review of the O₂ transport models, Hellums and co-workers (1996) proposed that the effect of intra-luminal blood flow velocities ought to be considered in order to sufficiently quantify the O₂ supply from blood to tissue. Due to the inherent coupling between NO and O₂, this convective effect of blood flow on O₂ transport may consequently affect the NO transport dynamics.

2 Development of Mathematical Models for NO/O₂ Transport

Mathematical modelling is a useful and powerful tool for investigating the simultaneous diffusion and reaction of NO/O₂. These models should be based on known mechanisms and employ physiologically relevant values of the production/decomposition rate. However, these rate values are neither well characterized, nor is it clear how the NO/O₂ production and decomposition rates affect the diffusion distance in the blood lumen, endothelium, and surrounding smooth muscle.

2.1 *Mathematical Models for NO/O₂ Transport with a Constant CFL Width*

2.1.1 NO Transport Models

Most mathematical models for NO transport have been developed to investigate local NO transport in the vessel and surrounding tissue by employing a constant CFL width. Lancaster (1994) developed the first mathematical model for describing the NO diffusion and reaction in a blood vessel. The NO production rate employed in the model was based on the maximum NO concentration from the measured data in Malinski and Taha's earlier study (1992), which have had significant impact on the development and calibration of mathematical models for studying NO diffusion. In similarity to the Lancaster model, Wood and Garthwaite (1994) have developed theoretical models for describing the kinetic and concentration profiles of NO generated from single or multiple sources in the brain. They modelled the neuron to be a point source of NO and expressed the decay of NO in the brain tissue as a first order reaction. Although several questions regarding NO diffusion and reaction have been well addressed by these initial studies, the early

models still suffer an inaccuracy due to their non-complete representation of physical reality. Furthermore, initial studies have not taken into account the finite size of the tissue region across which NO diffusion occurs.

Subsequent models were developed for more realistic cylindrical geometry, including other physiological factors that allow higher NO levels in the vascular wall to be simulated. For instance, Butler et al. (1998) have developed a mathematical model that simulates NO transport within an infinite-radius cylinder. This model is an improvement over the Lancaster model in that it specifies a RBC-rich region with a high NO scavenging rate and a CFL with zero NO scavenging rate. Vaughn et al. (1998a, b) developed a mathematical model to estimate the nitric oxide production and reaction rates in tissue. Their model provides a general analysis of NO reaction and diffusion in the lumen, endothelium, and abluminal regions. In addition, El-Farra et al. (2003) developed a two-dimensional multicellular model to evaluate the effect of the non-uniform RBC profiles on NO transport across the blood lumen and surrounding tissue for a 50 μm diameter vessel. Kavdia and Popel (2004) also studied the effect of wall shear stress on NO level in arterioles with diameters of 50 μm . In their analysis, a linear relation between eNOS production rate and wall shear stress was assumed. Their model predicted that a physiological wall shear stress of 24 dyn/cm^2 results in a NO concentration of about 100 nm in the smooth muscle.

2.1.2 O₂ Transport Models

The early investigators (Lagerlund and Low 1991; Lagerlund and Low 1987; Reneau et al. 1969) made a number of assumptions in their blood-to-tissue O₂ transport models, namely (1) that blood can be represented as a homogeneous hemoglobin solution; (2) that the vessel wall does not participate in the consumption of O₂, and (3) that O₂ does not react with other molecules in blood and tissue. Despite these oversimplifications, early investigators were able to set up a fairly reasonable framework for studying O₂ transport, and have made several discoveries of interesting phenomena through this basic framework.

A typical early model is the model constructed by Lagerlund and Low (1987, 1991). They modelled the O₂ transport in the capillaries and tissue surrounding rat nerves based on the work by Reneau et al. (1969). Their model coupled the O₂ transport across the two distinct regions (the vessel lumen and surrounding tissue). In addition, it was assumed in the model that the only sink for O₂ is the surrounding tissue, which consumes O₂ with a certain rate predicted by the Michaelis–Menten Kinetics. Interestingly, Lagerlund and Low found that Michaelis–Menten Kinetics could affect the overall O₂ distribution in the model. Popel et al. (1989) used a Fick's law diffusion model with the inclusion of an additional term representing capillary flow in analyzing the experimental data on O₂ flux from arterioles in the hamster cheek pouch retractor muscle. They pointed out that if mitochondrial respiration were the only sink for O₂ as assumed in earlier models, the available O₂ supply from blood would be more than the needs of the tissue.

Tsai et al. (1998) performed experiments combined with mathematical modelling to study O₂ transport around an arteriole in rat mesentery. They hypothesized that the excess O₂ is consumed by the vascular wall, which has a significantly higher O₂ consumption rate than the surrounding tissue. In their experiments, the phosphorescence quenching microscopy technique was used to measure PO₂ values inside the arteriolar lumen and surrounding tissues. Based on the data obtained from the direct measurements in the tissue, they established PO₂ profiles. Although the radial intravascular PO₂ profiles could not be obtained directly due to their experimental limitation, they managed to estimate the intravascular PO₂ values adjacent (about 4 μm from the blood-tissue interface) to the inner membrane of the vessel. They found a dramatic PO₂ drop inside the vessel wall. They also developed a two dimensional model to estimate the O₂ consumption rate using the O₂ profiles obtained from their experimental measurements. It was concluded that the O₂ consumption rate in small arterioles of the rat mesentery can be much higher (>200 times) than the mesenteric tissue O₂ consumption rate. In a recent review, Tsai et al. (2003) pointed out that the non-uniform distribution of RBCs in the bloodstream might be an important factor for O₂ delivery.

2.1.3 Coupled NO/O₂ Transport Models

Recently, several theoretical studies have introduced numerical models that simulate the NO/O₂ transport in the arteriolar blood flow with an inclusion of the role of the CFL. Lamkin-Kennard et al. (2004a) investigated how coupled O₂ and NO transport in arterioles is influenced by the plasma boundary layer that forms as a result of RBCs migrating towards the center of microvessel (Fåhræus-Lindqvist effect). In this study, they used a two-phase model which is composed of a RBC core region and a CFL region. From their results, two mechanisms by which NO bioavailability to the surrounding tissue can be affected were highlighted. In the first mechanism the increase in CFL width implicitly increases the core hematocrit which promotes a higher scavenging rate, resulting in reduction of NO bioavailability to the tissue. However, in the second mechanism, the increase in CFL width provides a larger diffusion barrier across the blood lumen, hence promoting the diffusion and bioavailability of NO into the surrounding tissue. It is clear that these two mechanisms work in opposing effects on the bioavailability of NO and O₂ to the tissue. They concluded that for a given rate of NO production by the eNOS, the second mechanism takes dominance in the NO transport dynamics of smaller arterioles. In another similar model developed by the same group (Lamkin-Kennard 2004b), the gas model complexity was enhanced to include the coupled physics between NO and O₂ by solving for both gas transport equations. The coupling comes from the interdependency that links the concentration of either molecule to the production or consumption of its partner in the binary relationship: the NO production from the NOS is O₂ concentration dependent, while the O₂ consumption at the tissue is mediated by the presence of NO. Their

results predicted that NO levels in the endothelium and vascular wall can be higher with additional NO production from iNOS or nNOS at locations near the vessel wall than with NO production from just purely eNOS alone. They also modelled the competition between superoxide and superoxide dismutase on NO bioavailability and their resulting impact on the coupled O₂ and NO transport in arterioles and surrounding tissue (Buerk et al. 2003). These modelling efforts were consistent with the majority of previous models for NO transport in the literature (Buerk 2001), which are based on a simplified one-dimensional radial mass transport model for NO by diffusion. Convective effects and axial diffusion could be ignored in these models since it is generally understood that the scavenging reaction for NO in the bloodstream is extremely rapid hence leading to a significantly higher radial diffusive flux than axial convective or diffusive flux.

2.2 Mathematical Models for NO/O₂ Transport with a Time-Dependent CFL Width

2.2.1 Time-Dependent Computational Model for NO Transport

NO transport in small arterioles is complicated by formation of the CFL which directly affects the diffusion dynamics across the blood lumen (Goldsmith et al. 1989). The CFL creates a physical diffusion barrier to NO transport by widening the separating distance from the NO source in the endothelium to RBCs in the flow stream. This phenomenon is likely to lower the exposure of NO to scavenging by RBCs in the blood lumen which in turn helps to improve the preservation of NO bioavailability in the arteriolar vessel (Liao et al. 1999; Vaughn 1998b). On the contrary, NO preservation can be attenuated by an increase in NO scavenging rate caused by a more compact RBC core in the blood lumen due to the CFL (Lamkin-Kennard et al. 2004b). Furthermore, it is also possible that NO production in the endothelium could be mitigated by a diminished wall shear stress due to reduction in effective viscosity near the vessel wall (Yalcin et al. 2008; Baskurt et al. 2004). The aforementioned computational studies that examined the effect of the CFL formation on NO transport in the arterioles are all based on steady-state models where the layer width is non-varying in the time domain. Consequently previous models have assumed constant NO scavenging rates by the RBCs and NO production rates in the endothelium.

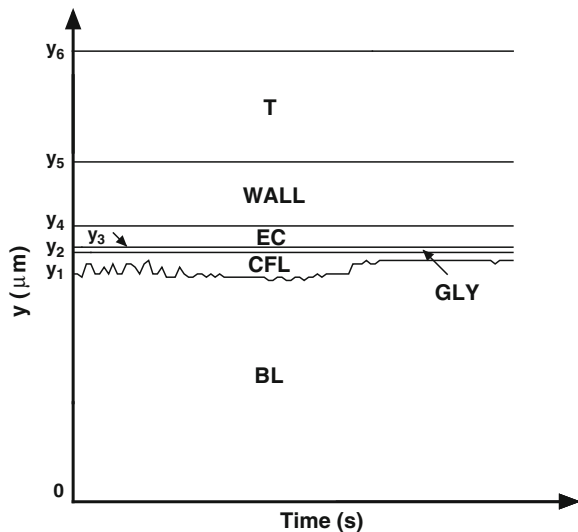
With regards to the transient gas transport phenomena, Ong et al. (2011) hypothesized that temporal variations in the CFL width would improve overall NO bioavailability in the arteriole predominantly through the transient modulation of wall shear stress and NO production. In their study, a time-dependent computational model on NO transport was implemented to test this hypothesis in relation to their measured temporal data of the CFL width in arterioles. They showed that transient changes in physiological responses accompanying the temporal variations in the CFL could significantly affect the NO bioavailability in the vessels.

2.2.2 Time-Dependent Computational Model for Coupled NO/O₂ Transport

Most recently, Ong et al. (2012) developed a new time-dependent computational model for coupled NO/O₂ transport in arterioles with consideration of temporal variations of the CFL width. This simulation study provides unique information on how the CFL changes induced by alteration of red cell aggregability, deformability, and hematocrit influence the gas transport in a single arteriole. In this study, for simplicity, the 1-Dimensional system was used for the gas diffusion in small arterioles. A six compartmental model of the arteriole was considered, which comprises of the blood lumen (BL), cell-free layer (CFL), glycocalyx (GLY), endothelium (EC), vascular wall (WALL) and tissue (T) (see Fig. 1). In their model, four assumptions were made; (1) only one-dimensional diffusion of NO and O₂ in the radial direction of the vessel (y-direction) is considered, (2) convective transport of NO and O₂ in the axial direction of the vessel is neglected, (3) the respective diffusion coefficients of NO and O₂ are constant in all compartments, and (4) O₂ solubility is the same in all compartments.

Unlike their previous model (Ong et al. 2011a, b), NO and O₂ transport in the arteriole were coupled in this model via two mechanisms: (1) NO production in the endothelium is dependent on O₂ bioavailability based on the Michealis-Menten kinetics and (2) O₂ consumption in the vascular wall and tissue can be inhibited by NO based on the modified Michealis-Menten kinetics. Time-dependent changes in the core hematocrit and wall shear stress due to the CFL variations were also considered in their simulation, which would simultaneously lead to variations in the NO scavenging rate and O₂ partial pressure (PO₂) in the blood lumen and the

Fig. 1 Six-compartment arteriolar diffusion model. (Reprinted with permission of Ong (Ong et al. 2012))



NO production rate in the endothelium, respectively. The influence of changes in wall shear stress on NO production was considered by modifying the maximum NO production rate term in the Michealis-Menten equation.

3 Future Developments for the Gas Transport Model

One common simplification in the models earlier discussed is the assumption that a one-dimensional diffusion model can sufficiently describe the overall dynamics of gas exchange and transport. The metastability of NO is well known, and this in addition to the considerable scavenging ability of hemoglobin in the RBC core dictates that NO produced by eNOS at the endothelium does not remain in the blood lumen for very long. These two factors are the usual argument given for the assumption that neither the axial diffusion nor convection by the bulk flow in the lumen affects the magnitude or direction of the NO diffusive flux. That is to say, in describing a system characterised by quasi-equilibrium states, the dominant transport direction remains in the radial direction. The radial diffusion model is certainly adequate in elucidating the role of each compartment in the microvessel and its surrounding tissue with regards to NO/O₂ exchange. As mentioned earlier, researchers can quantify or at least predict trends in how the radial placement of sources/sinks affects the bioavailability of these two important molecules in our smooth muscle and tissue. As such, these models are reasonably useful for describing a general picture of the microcirculation physiology.

The limitation however is that the location of NO/O₂ sources/sinks in microvessels is hardly ever constant, even in the mean sense. From experimental studies alone, researchers have found that key participants of the gas exchange system do in fact exhibit strong variation in both the axial direction and in the time domain (Ong et al. 2012). One participating element already highlighted is the CFL. The CFL can vary both temporally and spatially in the axial and azimuthal directions. RBCs along the edge of the core flow determine the CFL width. As the RBCs are free to tumble and interact with one another, the pattern of the CFL spatial (or temporal) variation can hardly be predicted and quantified.

The CFL variations may have two implications, the first being that because of the temporal variation, even the mean CFL is evolving with time. The second implication is that with a non-smooth CFL profile in space, the role of convection in the transport process across the lumen (and hence indirectly, the surrounding tissue) may be non-trivial after all. When the two are considered together, it may be arguable that the NO/O₂ dynamic can safely always be assumed to be quasi-steady state. Furthermore it is conceivable that the variation in wall shear stress due to both temporal and spatial variations of the flow field inevitably changes the rate of NO production at the endothelium. Without including at least the axial dimension, the effect of flow variation and NO production rate may not be treated as coupled parameters in the model as they truly are in reality for the arteriole. With regards to the varying hemodynamics that underlies the actual NO/O₂

exchange in a microvessel, it may be worthwhile to combine the current NO/O₂ diffusion models with existing hemodynamic models that incorporate two-dimensional or even three-dimensional flow modelling. A higher dimensioned diffusion-convection model would be particularly useful in analysing changes in NO/O₂ transport dynamics in relation to changing microvessel geometries.

Acknowledgments This work was supported by NUS FRC R-397-000-134-112.

References

- Ballermann B, Dardik A, Eng E, Liu A (1998) Shear stress and the endothelium. *Kidney Int Suppl* 67:S100–S108
- Baskurt O, Yalcin O, Ozdem S, Armstrong J, Meiselman H (2004) Modulation of endothelial nitric oxide synthase expression by red blood cell aggregation. *Am J Physiol Heart Circ Physiol* 286:H222–H229
- Buerk D (2001) Can we model nitric oxide biotransport? A survey of mathematical models for a simple diatomic molecule with surprisingly complex biological activities. *Annu Rev Biomed Eng* 3:109–143
- Buerk D, Lamkin-Kennard K, Jaron D (2003) Modeling the influence of superoxide dismutase on superoxide and nitric oxide interactions, including reversible inhibition of oxygen consumption. *Free Radic Biol Med* 34(11):1488–1503
- Butler A, Megson I, Wright P (1998) Diffusion of nitric oxide and scavenging by blood in vasculature. *Biochim Biophys Acta* 1425:168–176
- Busse R, Fleming I (1998) Pulsatile stretch and shear stress: physical stimuli determining the production of endothelium-derived relaxing factors. *J Vasc Res* 35(2):73–84
- Chen K, Popel A (2006) Theoretical analysis of biochemical pathways of nitric oxide release from vascular endothelial cells. *Free Radic Biol Med* 41(4):668–680
- Cooke J, Dzau V (1997) Nitric oxide synthase: role in the genesis of vascular disease. *Annu Rev Med* 48:489–509
- El-Farra N, Christofides P, Liao J (2003) Analysis of nitric oxide consumption by erythrocytes in blood vessels using a distributed multicellular model. *Ann Biomed Eng* 31(3):294–309
- Goldsmith H, Cokelet G, Gaehetgens P (1989) Robin Fahraeus: evolution of his concepts in cardiovascular physiology. *Am J Physiol* 257:H1005–H1015
- Hellums J, Nair P, Huang N, Ohshima N (1996) Simulation of intraluminal gas transport processes in the microcirculation. *Ann Biomed Eng* 24(1):1–24
- Kavdia M, Popel A (2004) Contribution of nNOS- and eNOS-derived NO to microvascular smooth muscle NO exposure. *J Appl Physiol* 97(1):293–301
- Kobayashi H, Takizawa N (2002) Imaging of oxygen transfer among microvessels of rat cremaster muscle. *Circulation* 105:1713–1719
- Kuchan M, Frangos J (1994) Role of calcium and calmodulin in flow-induced nitric oxide production in endothelial cells. *Am J Physiol* 266:C628–C636
- Lagerlund T, Low P (1987) A mathematical simulation of oxygen delivery in rat peripheral nerve. *Microvasc Res* 34:211–222
- Lagerlund T, Low P (1991) Axial diffusion and Michaelis-Menten kinetics in oxygen delivery in rat peripheral nerve. *Am J Physiol* 260:R430–R440
- Lamkin-Kennard K, Buerk D, Jaron D (2004a) Interactions between NO and O₂ in the microcirculation: a mathematical analysis. *Microvasc Res* 68:38–50
- Lamkin-Kennard K, Jaron D, Buerk D (2004b) Impact of the Fahraeus effect on NO and O₂ biotransport: a computer model. *Microcirculation* 11:337–349

- Lancaster J (1994) Simulation of the diffusion and reaction of endogenously produced nitric oxide. *Proc Natl Acad Sci USA* 91:8137–8141
- Liao J, Hejn T, Vaughn M, Huang K, Kuo L (1999) Intravascular flow decreases erythrocyte consumption of nitric oxide. *Proc Natl Acad Sci USA* 96:8757–8761
- Long D, Smith M, Pries A, Ley K, Damiano E (2004) Microviscometry reveals reduced blood viscosity and altered shear rate and shear stress profiles in microvessels after hemodilution. *Proc Natl Acad Sci USA* 101(27):10060–10065
- Malek A, Alper S, Izumo S (1999) Hemodynamic shear stress and its role in atherosclerosis. *JAMA* 282(21):2035–2042
- Malinski T, Taha Z (1992) Nitric oxide release from a single cell measured in situ by a porphyrinic-based microsensor. *Nature* 358:676–678
- Ong P, Jain S, Kim S (2011a) Modulation of NO bioavailability by temporal variation of the cell-free layer width in small arterioles. *Ann Biomed Eng* 39:1012–1023
- Ong P, Jain S, Kim S (2011b) Temporal variations of the cell-free layer width may enhance NO bioavailability in small arterioles: effects of erythrocyte aggregation. *Microvasc Res* 81:303–312
- Ong P, Cho S, Namgung B, Kim S (2012) Effects of cell-free layer formation on NO/O₂ bioavailability in small arterioles. *Microvas Res* 83:168–177
- Popel A, Pittman R, Ellsworth M (1989) Rate of oxygen loss from arterioles is an order of magnitude higher than expected. *Am J Physiol* 256:H921–H924
- Prakash B, Singh M (1995) Optimum kinetic energy dissipation to maintain blood flow in glass capillaries: an analysis based on flow field determination by axial tomographic and image velocimetry techniques. *J Biomech* 28(6):649–659
- Rengasamy A, Johns R (1996) Determination of K_m for oxygen of nitric oxide synthase isoforms. *J Pharmacol Exp Ther* 276:30–33
- Reneau D, Bruley D, Knisely M (1969) A digital simulation of transient oxygen transport in capillary-tissue systems (cerebral grey matter). Development of a numerical method for solution of transport equations describing coupled convection-diffusion systems. *AIChE J* 15:916–925
- Tateishi N, Suzuki Y, Soutani M, Maeda N (1994) Flow dynamics of erythrocytes in microvessels of isolated rabbit mesentery: cell-free layer and flow resistance. *J Biomech* 27(9):1119–1125
- Tsai A, Friesenecker B, Mazzoni M, Kerger H, Buerk D, Johnson P, Intaglietta M (1998) Microvascular and tissue oxygen gradients in the rat mesentery. *Proc Natl Acad Sci USA* 95:6590–6595
- Tsai A, Johnson P, Intaglietta M (2003) Oxygen gradients in the microcirculation. *Physiol Rev* 83:933–963
- Vaughn M, Kuo L, Liao J (1998a) Effective diffusion distance of nitric oxide in the microcirculation. *Am J Physiol* 274:H1705–H1714
- Vaughn M, Kuo L, Liao J (1998b) Estimation of nitric oxide production and reaction rates in tissue by use of a mathematical model. *Am J Physiol* 274:H2163–H2176
- Whorton A, Simonds D, Piantadosi C (1997) Regulation of nitric oxide synthesis by oxygen in vascular endothelial cells. *Am J Physiol* 272:L1161–L1166
- Wood J, Garthwaite J (1994) Models of the diffusional spread of nitric oxide: implications for neural nitric oxide signalling and its pharmacological properties. *Neuropharmacology* 33:1235–1244
- Yalcin O, Ulker P, Yavuzer U, Meiselman H, Baskurt O (2008) Nitric oxide generation by endothelial cells exposed to shear stress in glass tubes perfused with red blood cell suspensions: role of aggregation. *Am J Physiol Heart Circ Physiol* 294:H2098–H2105

Flow-Induced Deformation of a Capsule in Unbounded Stokes Flow

Toshihiro Omori, Takuji Ishikawa, Yohsuke Imai
and Takami Yamaguchi

Abstract Dynamics of deformable capsules in fluid flow is great interest in chemical engineering, bioengineering, and food industry. To investigate the motion and deformation of a capsule, both the fluid mechanics of the internal and external liquids and the solid mechanics of the membrane must be solved precisely. To express the elastic behaviours of the solid membrane, two different kinds of modelling are commonly used. One is a continuum constitutive law and the other is a discrete spring network model. This study first examines the correlations between the mechanical properties of the discrete spring network model and those of continuum constitutive laws. We also derive the relationships between the spring constant and continuum properties, such as Young modulus, Poisson ratio, area dilation modulus, and shear elastic modulus. Next, we investigate the motion and deformation of a capsule in simple shear flow. Especially, we analyze the dynamics of a non-spherical capsule in shear. In the absence of inertia effect of fluid motions, a boundary element method is used to compute the internal and external Stokes flow. The results show that the orientation of a non-spherical capsule is variant under time reversal, though that of a rigid particle is invariant. Interestingly, the alignment of a non-spherical capsule over a long time duration shows a transition depending on the shear rate.

T. Omori (✉) · T. Ishikawa · Y. Imai
School of Engineering, Tohoku University, 6-6-01 Aoba, Sendai 980-8579, Japan
e-mail: omori@pfs1.mech.tohoku.ac.jp

T. Ishikawa
e-mail: ishikawa@pfs1.mech.tohoku.ac.jp

Y. Imai
e-mail: yimai@pfs1.mech.tohoku.ac.jp

T. Yamaguchi
School of Biomedical Engineering, Tohoku University, 6-6-01 Aoba, Sendai 980-8579,
Japan
e-mail: takami@pfs1.mech.tohoku.ac.jp

1 Introduction

A capsule is a liquid drop enclosed by a thin membrane. Capsules can be found in nature, such as cells, eggs, etc., and artificial capsules are used in various engineering fields, including chemical engineering, bioengineering, and food industries. Since capsules are usually suspended in another liquid, a viscous stress is exerted on the membrane owing to the motion of both the internal and external liquids. Understanding the deformation of capsules is crucial to predict their risk of rupture, either to prevent or favor it depending on the application (Barthès-Biesel et al. 2006).

Capsule deformation is governed by the fluid–structure interaction between the motion of internal and external liquids and the deformation of the solid membrane. Thus, the model chosen to solve the solid mechanics of the capsule membrane plays a key role to predict capsule deformations (Barthès-Biesel et al. 2002). Since typical thickness of the membrane, which is about nano-meter order, is much smaller than the capsule size (typically micron order), only the deformation of its median surface is considered. Henceforth, the word *membrane* refers to the two-dimensional median surface. To model hyper-elastic behaviours of the capsule membrane, several continuum constitutive laws have been proposed. Neo-Hookean (NH) law has been used for isotropic volume-incompressible rubber-like materials (Green and Adkins 1970). To express the area incompressible property of biological membranes, Skalak et al. (1973) introduced the law (SK). Different constitutive laws allow us to predict quite different material properties under large deformation. For example, the NH law shows a strain-softening behaviour, whereas the SK law shows a strain-hardening property (Barthès-Biesel et al. 2002).

Discrete spring network model has also been used for modelling of capsule and biological cell membrane, because it can avoid the numerical implementation of the complicated solid mechanics of the continuous models. Especially, in bioengineering field, a spring network model has been used to model a red blood cell (RBC) membrane. The RBC membrane is primarily consists of the lipid bilayer and spectrin network. The lipid bilayer contributes area incompressibility of the membrane and the cytoskeleton of spectrin network enables the RBC to undergo large deformation while maintaining the structural integrity of the membrane. In Omori et al. (2011), we investigated the mechanical properties of a spring network model and clarified the relationship between the spring constant and continuum mechanical properties, such as the Young modulus, area dilation modulus, Poisson ratio, and shear elastic modulus. In this chapter, we explain how to compare the mechanical properties of discrete spring network model and those of continuum constitutive laws.

Fluid motions around the capsule are also important to simulate the deformation of capsules. In particular, discontinuity of the viscous stress across the thin membrane must be concerned. Due to the small size of the capsule, the inertia effect of both internal and external fluid motions can be neglected. The fluid velocity field is thus governed by the Stokes equations and can be expressed in

terms of surface integrals defined on the capsule membrane. This method, known as a boundary element method, can treat the discontinuity of the viscous traction across the membrane explicitly. Therefore, it is one of the most accurate numerical methods to simulate flow-induced capsule deformation. In Sect. 4, we numerically investigate motion and deformation of a capsule in simple shear flow. The fluid mechanics of liquid motions is solved by a boundary element method, while the large deformation of hyper-elastic membrane is solved by a finite element method (Foessel et al. 2011; Walter et al. 2010). We then analyze the effect of different membrane models on the deformation of a spherical capsule in shear flow. Next, we show the motion and deformation of an oblate ellipsoidal capsule in shear, including an RBC type biconcave disk.

2 Governing Equations

In this section, we present the governing equations of a capsule deforming under viscous flow. Since details of capsule mechanics can be found in the book of Barthès-Biesel et al. (2010) and Pozrikidis (1992, 2003), we only describe the brief outline here. Throughout this chapter, summation is performed over repeated indices. Greek indices take values 1 or 2, whereas Latin indices refer to 1, 2, or 3.

2.1 Fluid Mechanics

Consider a capsule is freely suspended in a Newtonian liquid undergoing viscous flow with velocity \mathbf{v}^∞ . We assume a capsule is filled with an incompressible Newtonian liquid with viscosity $\lambda\mu$ and density ρ . Outer liquid is also assumed as an incompressible Newtonian liquid with viscosity μ but density ρ . Gravitational effects thus can be omitted and the capsule is neutrally buoyant.

Due to the small size of a capsule, typical Reynolds number of the flow based on the capsule dimension $\text{Re} = \rho a |\mathbf{v}^\infty| / \mu$ is much smaller than unity, where a is the characteristic length of the capsule. The inertia effect of the fluid flow can be neglected, and both the motions of internal and external liquids are governed by the Stokes equations. In the Stokes regime, the velocity field can be evaluated in terms of surface integral defined on the deformed membrane S (Pozrikidis 1992):

$$\begin{aligned} \frac{1+\lambda}{2}\mathbf{v}(\mathbf{x}) &= \mathbf{v}^\infty(\mathbf{x}) - \frac{1}{8\pi\mu} \int \mathbf{J}(\mathbf{x}, \mathbf{y}) \cdot \mathbf{q}(\mathbf{y}) dS(\mathbf{y}) \\ &+ \frac{1-\lambda}{8\pi} \int \mathbf{v}(\mathbf{y}) \cdot \mathbf{K}(\mathbf{x}, \mathbf{y}) \cdot \mathbf{n}(\mathbf{y}) dS(\mathbf{y}), \end{aligned} \quad (1)$$

where λ is the viscosity ratio of the internal and external liquids, \mathbf{n} is the unit outward normal vector, \mathbf{q} is the viscous load on the membrane, and \mathbf{J} and \mathbf{K} are the single- and double-layer potential of Green's function, respectively. Dynamic condition requires the load \mathbf{q} must be equal to the discontinuity of the stress tensor across the membrane

$$\mathbf{q} = [\boldsymbol{\sigma}^{out} - \boldsymbol{\sigma}^{in}] \cdot \mathbf{n}, \quad (2)$$

where $\boldsymbol{\sigma}^{out}$ and $\boldsymbol{\sigma}^{in}$ are the stress tensor of the outer and inner liquids, respectively. Single- and double-layer potentials \mathbf{J} and \mathbf{K} are defined as:

$$J_{ij} = \frac{\delta_{ij}}{r} + \frac{r_i r_j}{r^3}, \quad K_{ijk} = -6 \frac{r_i r_j r_k}{r^3}, \quad (3)$$

where $\mathbf{r} = \mathbf{y} - \mathbf{x}$, and $r = |\mathbf{r}|$.

2.2 Membrane Mechanics

We next describe the governing equations of the solid mechanics of the thin membrane. The local curvilinear coordinate (ξ^1, ξ^2) is introduced as depicted in Fig. 1.

Let $\mathbf{X}(\xi^1, \xi^2)$ and $\mathbf{x}(\xi^1, \xi^2)$ be a position of the material point in the reference and deformed state, respectively. The covariant bases in each state thus can be written as

$$\mathbf{G}_\alpha = \frac{\partial \mathbf{X}}{\partial \xi^\alpha}, \quad \mathbf{g}_\alpha = \frac{\partial \mathbf{x}}{\partial \xi^\alpha}. \quad (4)$$

For simplicity of the description, we only describe the bases in the deformed state, hereafter. The unit normal outward vector \mathbf{n} is also given by

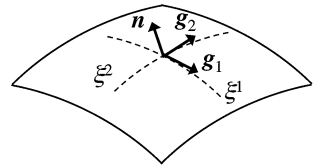
$$\mathbf{n} = \frac{\mathbf{g}_1 \wedge \mathbf{g}_2}{|\mathbf{g}_1 \wedge \mathbf{g}_2|}. \quad (5)$$

The associated contravariant bases are defined as

$$\mathbf{g}^\alpha \cdot \mathbf{g}_\beta = \delta_\beta^\alpha. \quad (6)$$

The covariant and contravariant metric tensor can be written as

Fig. 1 Illustration of the curvilinear coordinate and covariant vectors



$$g_{\alpha\beta} = \mathbf{g}_\alpha \cdot \mathbf{g}_\beta, \quad g^{\alpha\beta} = \mathbf{g}^\alpha \cdot \mathbf{g}^\beta. \quad (7)$$

Since the covariant and contravariant bases have the relation of

$$\mathbf{g}_\alpha = g_{\alpha\beta} \mathbf{g}^\beta, \quad \mathbf{g}^\alpha = g^{\alpha\beta} \mathbf{g}_\beta, \quad (8)$$

the metric tensor of contravariant bases can be rewritten as

$$g^{11} = \frac{g_{22}}{|g_{\alpha\beta}|}, \quad g^{22} = \frac{g_{11}}{|g_{\alpha\beta}|}, \quad g^{12} = g^{21} = -\frac{g_{12}}{|g_{\alpha\beta}|}, \quad (9)$$

where $|g_{\alpha\beta}| = g_{11}g_{22} - g_{12}^2$.

Assuming negligible bending rigidity, deformations occur only in the plane of the membrane. Let $d\mathbf{X}$ and $d\mathbf{x}$ be the infinitesimal in the reference state and deformed state, respectively. The surface deformation gradient tensor \mathbf{F}_s is given by

$$\mathbf{F}_s = \frac{\partial \mathbf{x}}{\partial \mathbf{X}}, \quad (10)$$

or

$$\mathbf{F}_s = \mathbf{g}_\alpha \otimes \mathbf{G}^\alpha, \quad (11)$$

where \otimes represents the tensor product over two vector spaces. The local deformation of the membrane can be measured by the right Cauchy-Green tensor

$$\begin{aligned} \mathbf{C} &= \mathbf{F}_s^T \cdot \mathbf{F}_s \\ &= (\mathbf{G}^\alpha \otimes \mathbf{g}_\alpha) \cdot (\mathbf{g}_\beta \otimes \mathbf{G}^\beta) \\ &= g_{\alpha\beta} \mathbf{G}^\alpha \otimes \mathbf{G}^\beta. \end{aligned} \quad (12)$$

The Green–Lagrange strain tensor \mathbf{E} is also given by

$$\begin{aligned} \mathbf{E} &= \frac{1}{2}(\mathbf{C} - \mathbf{I}_s) \\ &= \frac{1}{2}(g_{\alpha\beta} - G_{\alpha\beta}) \mathbf{G}^\alpha \otimes \mathbf{G}^\beta. \end{aligned} \quad (13)$$

where \mathbf{I}_s is the two-dimensional identity tensor. Two invariants of the strain tensor I_1 and I_2 can be written as a function of the principal extension ratios λ_1 and λ_2 (Skalak et al. 1973):

$$I_1 = 2tr\mathbf{E} = g_{\alpha\beta} G^{\alpha\beta} - 2 = \lambda_1^2 + \lambda_2^2 - 2, \quad (14)$$

$$I_2 = 4 \det \mathbf{E} + 2tr\mathbf{E} = |g_{\alpha\beta}| |G^{\alpha\beta}| - 1 = \lambda_1^2 \lambda_2^2 - 1. \quad (15)$$

In the membrane model, the stresses are integrated towards the thickness direction and replaced by tensions, which have the dimension of force per unit

length. In the case of isotropic hyper-elastic materials, the Cauchy tension is given by the strain energy function W :

$$\boldsymbol{\tau} = \frac{1}{J_s} \mathbf{F}_s \cdot \frac{\partial W}{\partial \mathbf{E}} \cdot \mathbf{F}_s^T, \quad (16)$$

where $J_s = \lambda_1 \lambda_2$ expresses the ratio between the deformed and the reference surface area. When the strain energy W is a function of I_1 and I_2 , the chain-rule is applied to the above equation, and the contravariant expression of the Cauchy tension is given by

$$\tau^{\alpha\beta} = \frac{2}{J_s} \frac{\partial W}{\partial I_1} G^{\alpha\beta} + 2J_s \frac{\partial W}{\partial I_2} g^{\alpha\beta}. \quad (17)$$

2.2.1 Two-Dimensional Continuum Constitutive Laws

A number of constitutive laws are now available for modelling thin hyper-elastic membrane. Different laws allow us to describe quite different material behaviours, including strain-softening behaviours of a gelled membrane or strain-hardening behaviours of a polymerized membrane. In this section, we introduce three different constitutive laws.

In the small deformation limit, all laws reduce to the 2D Hooke's law (H) (Barthès-Biesel et al. 2010):

$$W^H = G_s \left(tr(\mathbf{e}^2) + \frac{\nu_s}{1 - \nu_s} (tre)^2 \right), \quad (18)$$

where G_s is the shear elastic modulus, ν_s is the Poisson ratio and \mathbf{e} is the linearized Green–Lagrange strain tensor. The area dilation modulus K_s of the Hooke's law is given by $K_s = G_s (1 + \nu_s)/(1 - \nu_s)$, and the Young modulus is given by $E_s = 2 G_s (1 + \nu_s)$.

The Neo-Hookean (NH) law (Green and Adkins 1970) is widely used for modelling of capsule membrane. The NH law can describe the behaviour of volume incompressible rubber-like material. The strain energy function of the NH law is defined as

$$W^{NH} = \frac{G_s^{NH}}{2} \left(I_1 - 1 + \frac{1}{I_2 + 1} \right), \quad (19)$$

where G_s^{NH} is the shear elastic modulus of the NH membrane. In small deformation limit, the continuum material properties of the NH law have the relation of

$$G_s = G_s^{NH}, \quad E_s = 3G_s, \quad \nu_s = \frac{1}{2}, \quad K_s = 3G_s. \quad (20)$$

To model the large deformation of an RBC membrane, Skalak et al. (1973) introduced the law (SK):

$$W^{Sk} = \frac{G_s^{SK}}{4} (I_1^2 + 2I_1 - 2I_2 + CI_2^2), \quad (21)$$

where G_s^{SK} is the shear elastic modulus of the SK membrane. For small deformation, the correspondence between material properties and the law parameter is

$$G_s = G_s^{SK}, \quad E_s = 2G_s \frac{2C+1}{C+1}, \quad \nu_s = \frac{C}{C+1}, \quad K_s = G_s(2C+1). \quad (22)$$

To model the area incompressible material of a biological membrane, the law parameter C must be large enough. For example, the area dilation modulus of the RBC membrane is much larger than the shear modulus, and the parameter C is estimated as the order of 10^5 – 10^6 (Pozrikidis 2003; Skalak et al. 1973). For a numerical simulation, however, such high C may not be needed to discuss the effect of area incompressible property of the membrane, because the Poisson ratio ν_s rapidly converges to 1 by substituting large number of C into equation 22 (Note: in the case of a 2D area incompressible material, the Poisson ratio corresponds to 1). Actually, the areal change $J_s - 1$ of a biconcave disk in shear flow with $C = 10$ is less than 2 % (capillary number is 2, the viscosity ratio $\lambda = 1$).

2.2.2 Discrete Spring Network Model

Next, we derive a spring network to model the capsule membrane. A 2D sheet is discretized by a network of springs. Assume that all springs have the same elastic resistance, which is proportional to the length change of the springs. In a Cartesian frame (x_1, x_2) , the spring force between the node i and j is defined as

$$\mathbf{f}_{ij} = k \left(|\mathbf{r}_{ij}| - |\mathbf{r}_{ij}^0| \right) \frac{\mathbf{r}_{ij}}{|\mathbf{r}_{ij}|}, \quad \mathbf{f}_{ji} = -\mathbf{f}_{ij}, \quad (23)$$

where k is the spring constant, $\mathbf{r}_{ij} = \mathbf{r}_j - \mathbf{r}_i$, and \mathbf{r}_j and \mathbf{r}_i are the position vector of node i and j , respectively. $|\mathbf{r}_{ij}^0|$ is the equilibrium length between the points i and j . To investigate how influence the mesh topology to the mechanical properties of the spring network, four kinds of triangular mesh are used (Fig. 2). The cross mesh is constructed by squares with diagonal line. Nodal points are added at the intersections of the diagonal line, refers as the cross-centre mesh. In the regular triangle, the mesh is based on regular hexagons associated with a central node. The unstructured mesh is generated by the Delaunay triangulation.

To compare the mechanical properties of spring network and those of continuum constitutive laws, the tension-strain relationship of the spring network model must be taken into account. Consider deformation of a 2D sheet of length L_1 and width L_2 . The initial boundary grid spacing ΔL_1 and ΔL_2 are also given by

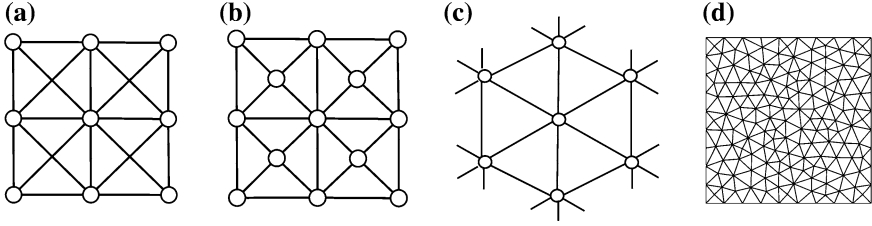


Fig. 2 Mesh configuration of spring network model (Omori et al. 2011) **a** Cross. **b** Cross centre. **c** Regular triangle. **d** Unstructured

$\Delta L_1 = L_1/n$ and $\Delta L_2 = L_2/m$, where n and m are the number of boundary segmentation towards the x_1 and x_2 directions, respectively. When the 2D sheet is deformed to $\lambda_1 L_1$ and $\lambda_2 L_2$ in the x_1 and x_2 directions, respectively, the principal tension τ_1 and τ_2 of the spring network model is defined as

$$\tau_1 = \frac{\sum_i F_{i,1} \big|_{x_1=\lambda_1 L_1}}{\lambda_2 L_2}, \quad \tau_2 = \frac{\sum_j F_{j,2} \big|_{x_2=\lambda_2 L_2}}{\lambda_1 L_1}, \quad (24)$$

where $F_{i,1}$ is the x_1 component of the total spring force \mathbf{F}_i acting on the node i and $F_{j,2}$ its x_2 component. For simplicity of the discussion, L_1 and L_2 correspond to 1, and we use $\Delta L_1 = \Delta L_2$ in this study. The principal strain is also defined as

$$\varepsilon_x = \frac{1}{2} (\lambda_x^2 - 1). \quad (25)$$

3 Comparison Between Continuum Model and Spring Network

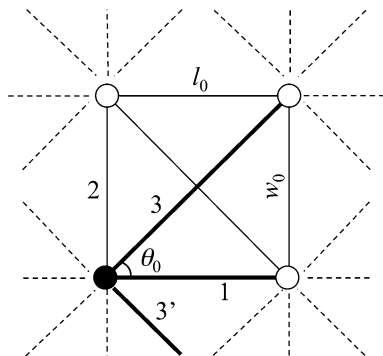
3.1 Small Deformation Limit

In this section, we analytically investigate small deformation of the spring network model. Especially, the Young modulus, Poisson ratio, area dilation modulus, and shear elastic modulus of the spring network are derived. Next, we compare these parameters to those of the continuum constitutive model.

3.1.1 Analytical Solution for Infinitely Fine Mesh

We consider an infinitely fine spring network, assuming that all the mesh elements are identically deformed so that the forces acting on the nodes are symmetric. For the sake of simplicity, we only detail here the derivation of the elastic constant for a cross mesh element under uniaxial deformation.

Fig. 3 Numbering of the spring network



Configuration of the spring network is shown in Fig. 3. Spring 1 has the initial length l_0 and oriented to the x_1 direction. Spring 2 has the initial length w_0 and oriented to the x_2 direction. Spring 3 is along with the cross direction and its initial length L_0 is calculated as $L_0^2 = l_0^2 + w_0^2$. The initial angle between the spring 1 and 3 is defined as θ_0 . The counterpart of spring 3 is also defined as spring 3'. Consider the spring network is deformed from l_0 to $l_0 + \Delta l_0$ in the x_1 direction and from w_0 to $w_0 + \Delta w_0$ in the x_2 direction, respectively. In the small deformation limit ($\Delta l_0 \ll l_0$, and $\Delta w_0 \ll w_0$), the three springs has the relation of

$$(L_0 + \Delta L_0)^2 \approx (l_0 + \Delta l_0)^2 + (w_0 + \Delta w_0)^2, \quad (26)$$

where ΔL_0 is the length change of spring 3. Neglecting the second order term of ΔL_0 , Δl_0 , and Δw_0 , we have the following equation:

$$\Delta L_0 = \frac{l_0 \Delta l_0 + w_0 \Delta w_0}{L_0}. \quad (27)$$

The x_1 components of total spring force acting on a node is contributed from spring 1, 3, 3':

$$F_1 = k \Delta l_0 + 2k \Delta L_0 \cos(\theta_0 + \Delta \theta_0), \quad (28)$$

where $\Delta \theta_0$ is the angle change. Apply similar manner to the x_2 component of the spring force, we have

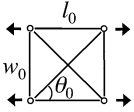
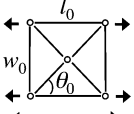
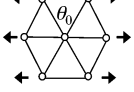
$$F_2 = k \Delta w_0 + 2k \Delta L_0 \sin(\theta_0 + \Delta \theta_0). \quad (29)$$

The local tension τ_1 and τ_2 on a mesh are given by

$$\tau_1 = \frac{F_1}{w_0 + \Delta w_0}, \quad \tau_2 = \frac{F_2}{l_0 + \Delta l_0}. \quad (30)$$

In uniaxial deformation ($\tau_2 = 0$), we can determine the Poisson ratio and Young modulus of the spring network model. The transverse displacement Δw_0 can be deduced from Eq. (29) with $\tau_2 = 0$ condition

Table 1 Young modulus and Poisson ratio of the spring network model (Omori et al. 2011). A 2D sheet is discretized by cross mesh, cross centre mesh, and regular triangles

Mesh type	k as a function of E_s	ν_s
	$k = \frac{L_0 + 2w_0 \sin \theta_0}{L_0 + 2(w_0 \sin \theta_0 + l_0 \cos \theta_0)} \frac{w_0}{l_0} E_s$ Isotropic mesh: $k = 2/3 E_s$	$\nu_s = \frac{2l_0 \sin \theta_0}{L_0 + 2w_0 \sin \theta_0} \frac{l_0}{w_0}$ Isotropic mesh: $\nu_s = 1/2$
	$k = \frac{L_0 + w_0 \sin \theta_0}{L_0 + w_0 \sin \theta_0 + l_0 \cos \theta_0} \frac{w_0}{l_0} E_s$ Isotropic mesh: $k = 3/4 E_s$	$\nu_s = \frac{l_0 \sin \theta_0}{L_0 + w_0 \sin \theta_0} \frac{l_0}{w_0}$ Isotropic mesh: $\nu_s = 1/3$
	Isotropic mesh: $k = \frac{\sqrt{3}}{2} E_s$	Isotropic mesh: $\nu_s = 1/3$

$$\frac{\Delta w_0}{\Delta l_0} = - \frac{2l_0 \sin \theta_0}{L_0 + 2w_0 \sin \theta_0}. \quad (31)$$

In the small deformation limit, the Poisson ratio is thus given by

$$\nu_s = \frac{|\Delta w_0/w_0|}{|\Delta l_0/l_0|} = \frac{2l_0 \sin \theta_0}{L_0 + 2w_0 \sin \theta_0} \frac{l_0}{w_0}. \quad (32)$$

Substituting Eq. (31) into (28), we obtain the expression of F_1 as a function of Δl_0 , from which the small deformation Young modulus follows

$$E_s = \frac{\tau_1}{\Delta l_0/l_0} = \frac{L_0 + 2w_0 \sin \theta_0 + 2l_0 \cos \theta_0}{L_0 + 2w_0 \sin \theta_0} \frac{l_0}{w_0} k. \quad (33)$$

In the isotropic deformation ($\tau_1 = \tau_2$), we can also have the relation between area dilation modulus K_s and the spring constant k by using a similar manner with uniaxial deformation (Omori et al. 2011). In Table 1, the results of the uniaxial deformation of cross mesh, cross centre mesh, and regular triangle are shown. These results clearly show the geometrical dependency of the spring network model. To express isotropic elasticity using a spring network model, the mesh must therefore be isotropic.

3.1.2 Comparison of Spring Network and Continuum Model

We compare the small deformation mechanical properties of spring network models with an isotropic mesh and the constitutive laws NH and SK. The Poisson ratio of a spring network model is determined only by the mesh configuration and is independent of k . For the isotropic cross mesh, the Poisson ratio can be estimated as $1/2$, which corresponds to the NH law and the SK law with $C = 1$. In the

case of two-dimensional isotropic elastic material, two mechanical module are independent as related by the conventional relations of elasticity:

$$K_s = G_s \frac{1 + \nu_s}{1 - \nu_s}, \quad E_s = 2G_s(1 + \nu_s). \tag{34}$$

If the spring constant is further set to $k/G_s = 2$, the small deformation mechanical properties E_s , G_s , and K_s of the isotropic cross mesh model are identical to those of a MR or of SK ($C = 1$) membrane. Similarly, by adjusting $k/G_s = 2$ for isotropic cross-centre mesh and $k/G_s = 4/\sqrt{3}$ for regular triangles, the mechanical properties of the spring network coincide with those of the SK law with $C = 1/2$.

3.2 Large Deformation

Next, we present mechanical properties of the spring network model under large uniaxial and isotropic deformation. In large deformation, we numerically compare the tension-strain relationship of the spring network discretized with isotropic cross mesh, cross centre mesh, and unstructured mesh and those of the continuum model. The tension-strain relationship under large uniaxial extension is shown in Fig. 4. The cross mesh exhibits a strain-hardening behaviour similar to the SK law, whereas the cross centre and unstructured mesh show a quasi-linear behaviour even for large deformation. The results of isotropic deformation are also shown in Fig. 5. In this case, all three spring network models show a strain-softening behaviour. This result suggests that the spring model is not appropriate to express the area incompressible membrane property of the material.

Fig. 4 Tension-strain relationship under uniaxial extension ($\tau_2 = 0$)

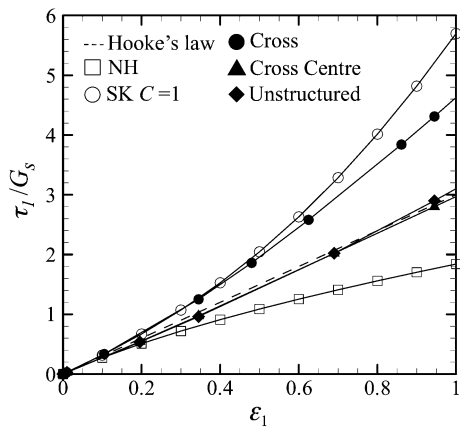
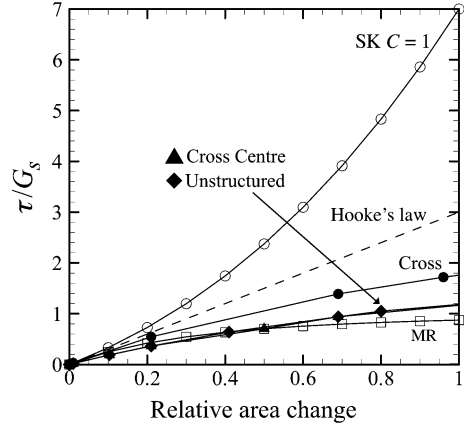


Fig. 5 Tension-strain relationship under isotropic extension ($\tau = \tau_1 = \tau_2$)



4 Capsule in Shear Flow

We next describe motion and deformation of a capsule in simple shear flow. Due to small size of a capsule, we assume the flow is Stokesian and the flow field is solved by a boundary element method. A finite element method is employed to solve the solid mechanics of continuum thin membrane. Since we use the same numerical method of Foessel et al. (2011), and Walter et al. (2010), only brief numerical procedures are described here.

We track the Lagrangian position of the membrane material points over time. Thus, we can explicitly compute local membrane deformations. Once, the strain is given, the membrane tension can be computed depending on the constitutive law. The static local equilibrium equation of the membrane is given by

$$\nabla_s \cdot \boldsymbol{\tau} + \mathbf{q} = \mathbf{0}, \quad (35)$$

where ∇_s is the surface divergence operator. Based on the virtual work principle, the above equilibrium equation can be written as the weak form:

$$\int \hat{\mathbf{u}} \cdot \mathbf{q} dS = \int \hat{\mathbf{e}} : \boldsymbol{\tau} dS, \quad (36)$$

where $\hat{\mathbf{u}}$ and $\hat{\mathbf{e}} = \frac{1}{2}(\nabla_s \hat{\mathbf{u}} + \nabla_s \hat{\mathbf{u}}^T)$ are the virtual displacement and strain, respectively. A finite element method is used to solve Eq. (36) with respect to the load \mathbf{q} . Once, the load is given, the velocity field is calculated from Eq. (1). The membrane material point \mathbf{x} is updated by means of the kinematic condition $\partial \mathbf{x} / \partial t = \mathbf{v}$. This equation is solved by an explicit second order Runge–Kutta method. The whole procedure is repeated while we get sufficient long computation time.

In a Cartesian reference frame with the capsule centre as the origin, the undisturbed linear flow \mathbf{v}^∞ can be defined as $\mathbf{v}^\infty = (\mathbf{E} + \boldsymbol{\Omega}) \cdot \mathbf{x}$, where \mathbf{E} and $\boldsymbol{\Omega}$ are the rate of strain and rotation tensors, respectively. In the case of a simple shear

flow, \mathbf{E} and $\mathbf{\Omega}$ are defined as $E_{12} = E_{21} = W_{12} = -\Omega_{21} = \dot{\gamma}/2$ and all the other components equal zero, where $\dot{\gamma}$ is the shear rate. The capillary number Ca represents the ratio of the fluid viscous forces and the membrane elastic forces:

$$Ca = \frac{\mu a \dot{\gamma}}{G_s} \tag{37}$$

where a is the characteristic length, which is defined as the radius of the spherical capsule with the same volume of an ellipsoidal capsule and a biconcave disk. To ensure reliable results with high numerical accuracy, the membrane is discretized by 5,120 linear triangle meshes, and non-dimensional time step $\dot{\gamma}\Delta t$ is ranged from 10^{-5} to 10^{-3} .

4.1 Deformation of a Spherical Capsule

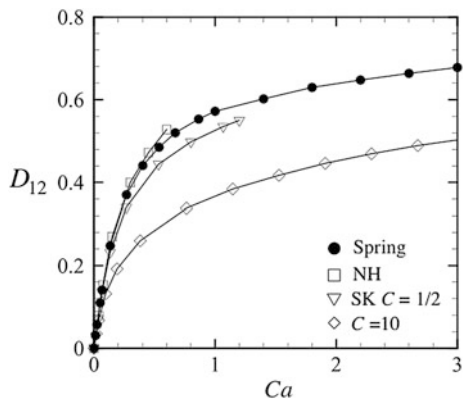
We first investigate deformation of a spherical capsule in shear flow. The deformation of a capsule can be measured by the Taylor parameter, which is defined as:

$$D_{12} = \frac{|L_1 - L_2|}{L_1 + L_2}, \tag{38}$$

where L_1 and L_2 are the semi-axis length of the ellipsoid inertia of the deformed capsule in the shear plane.

Figure 6 shows the results of D_{12} with several membrane models. In all cases, the viscosity ratio is 1. For the spring network with triangle meshes, the spring constant of the capsule membrane is adjusted, so that it coincides, in the small deformation limit, with the value of E_s/G_s of the SK law with $C = 1/2$. This figure shows deformation of the spring network is larger than that of a capsule enclosed with the SK $C = 1/2$ membrane, although the two membranes have the same

Fig. 6 Taylor parameter of a spherical capsule in shear flow



mechanical properties in the small deformation limit. This is due to the fact that the spring network is strain-softening under large deformation, whereas the SK $C = 1/2$ membrane is strain-hardening.

4.2 Off-plane Motion of a Non-Spherical Capsule

Last, we present kinematic motions of a non-spherical capsule in simple shear flow. Since capsules are often initially oriented to random directions in some experimental situations, the revolution axis of the spheroid capsule is initially out of the shear plane.

To explain the orientation of a capsule efficiently, we define the orientation vector \mathbf{d} as a unit vector extending from the centre of gravity and pointing to material point located at the revolution axis of the spheroidal capsule. The angle θ is also defined as the angle between the vector \mathbf{d} and the vorticity direction, i.e. the x_3 -axis.

In Fig. 7, the results of an oblate spheroidal capsule with $Ca = 0.3$ and 1 are shown. The membrane is modelled by the NH law and the aspect ratio of the minor and major axes is 0.6. For both Ca cases, the viscosity ratio of internal and external liquid is equal to 1. The initial orientation of the capsule is set to $\theta^0 = \pi/4$. Time history of the angle θ is also shown in Fig. 7c. Since we assume the reference shape coincides with the initial shape, θ oscillates two times during one period (rim of the oblate capsule passes through the x_1 axis in twice during a period). In addition to the short-time oscillation, θ tends to approach towards 0 or $\pi/2$, depending on Ca , over a long time duration. This tendency also can be found in a prolate capsule and biconcave disk (Omori et al. 2012). For comparison, the result of a rigid oblate with the same aspect ratio is also drawn in Fig. 7c. In the case of the rigid body, the angle θ periodically oscillates around the mean angle and does not show the transition. These results clearly illustrate that a deformable capsule becomes reoriented, even in simple shear flow, and the time reversibility of rigid particles can be destroyed by introducing particle deformability.

We also compare the numerical results and former experimental studies of an RBC in shear flow. In the numerical simulation, the RBC membrane is modelled by the SK law with $C = 10$ to express the area incompressible property of a biological membrane. As the same for the oblate capsule, orientation of the RBC converges to $\theta = 0$ in high Ca regime, whereas it converges to $\theta = \pi/2$ in low Ca regime. When $\theta = 0$, the membrane property becomes symmetric towards the flow and vorticity directions, and the RBC shows a steady deformation with a tank-treading motion. This motion is called as a steady tank-treading motion, in this study. When $\theta = \pi/2$, on the other hand, the membrane property becomes anisotropic towards the flow direction, and the RBC shows a swinging motion. In Fig. 8b, critical capillary number Ca_0 and $Ca_{\pi/2}$ are shown. In $Ca \leq Ca_{\pi/2}$ conditions, the angle θ converges to $\pi/2$, whereas it converges to 0 in $Ca \geq Ca_0$. The criterion of the transition is defined as $|\theta_{30} - \theta_f| \leq 0.05$, where θ_{30} is the mean

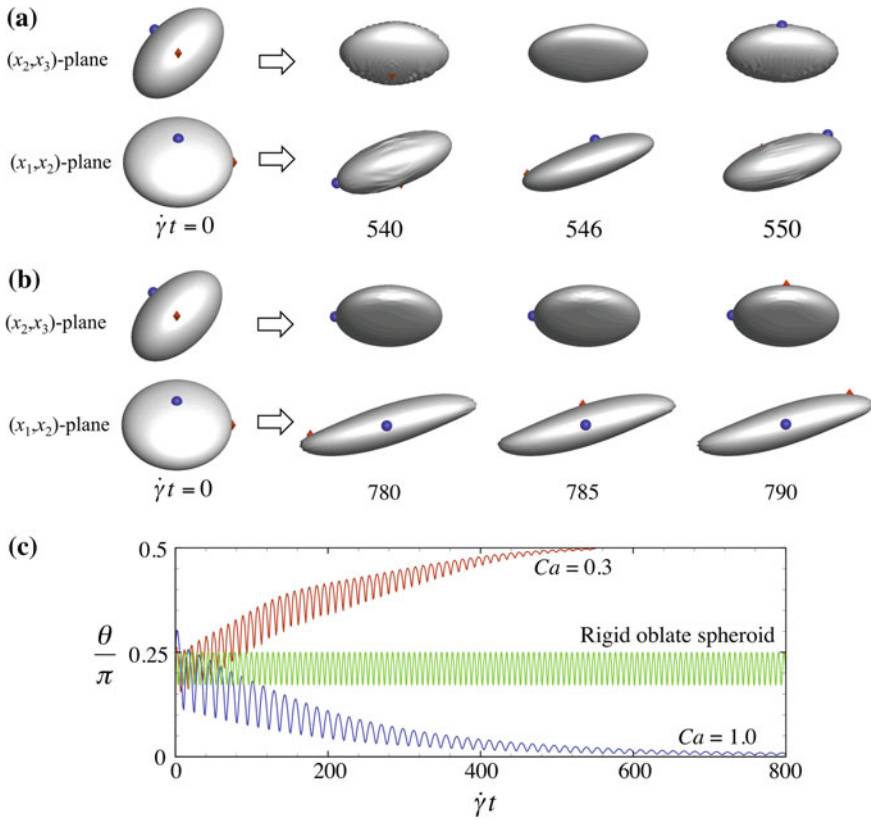


Fig. 7 Oblate capsule in simple shear flow with **a** $Ca = 0.3$, and **b** $Ca = 1.0$. The viscosity ratio is 1 and the aspect ratio is 0.6. The membrane is modelled by the NH law. The *dot* and *octahedron* represented in the figure are the material point on the membrane. **c** Time change of the angle θ . For comparison, the result of a rigid oblate is also plotted in this figure

angle at the 30th rotation, and $\theta = 0$ or $\pi/2$. The experimental conditions of former studies (Abkarian et al. 2007; Fischer et al. 1978) are also plotted in this figure. In Abkarian et al. (2007), the swinging motion of an RBC was reported, while an RBC show the steady tank-treading motion in Fischer et al. (1978). The parameter range of Abkarian et al. is below $Ca_{\pi/2}$, and our numerical results also show the swinging motion. Whereas the range of Fischer et al. is above Ca_0 , and the results show the steady tank-treading. Thus, the present results can nicely explain the difference of two former experimental observations, even without introducing any inertial effect.

The reorientation transition appears in a wide variety of artificial and biological capsules. Given that the transition can be controlled by adjusting the background flow, the results obtained here can be utilized for particle-alignment techniques in engineering applications.

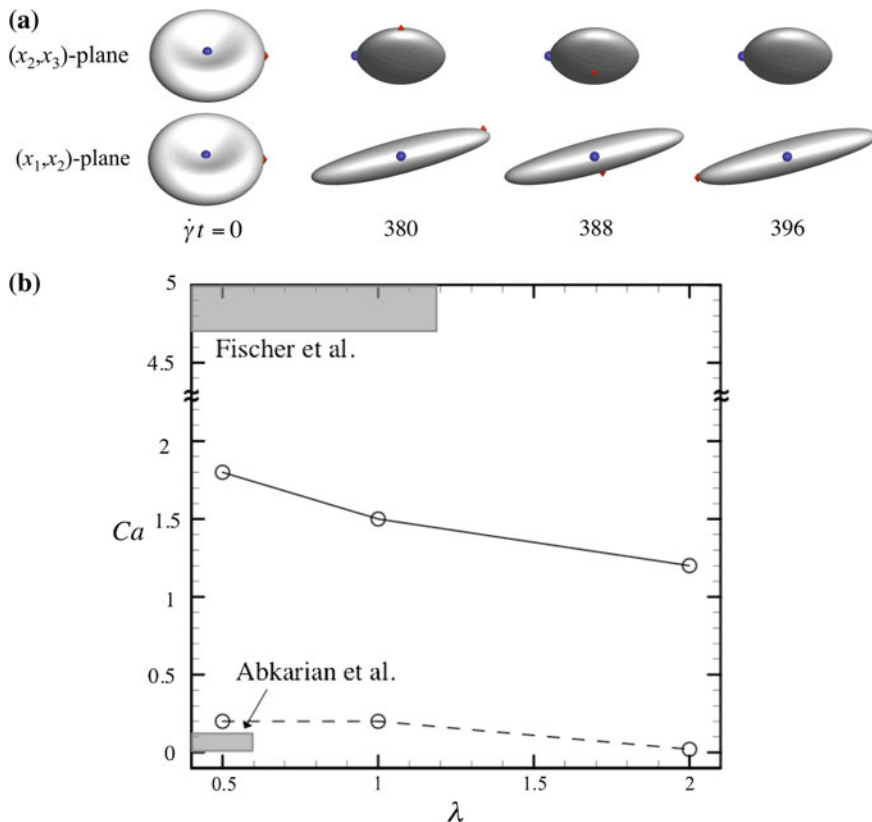


Fig. 8 **a** Motion of an RBC in simple shear flow. The capillary number is 2 and the viscosity ratio is 1. **b** Comparison with former experimental study of Abkarian et al. (2007), and Fischer et al. (1978). The solid line indicates Ca_0 and the broken line is $Ca_{\pi/2}$

References

Abkarian M, Faivre M, Viallat A (2007) Swinging of red blood cells under shear flow. *Phys Rev Lett* 98:188302

Barthès-Biesel D, Walter J, Salsac AV (2010) Computational hydrodynamics of capsules and biological cells. In: C. Pozrikidis (ed) *Flow-induced deformation of artificial capsules*. Taylor & Francis, Boca Raton

Barthès-Biesel D, Yamaguchi T, Ishikawa T, Lac E (2006) From passive motion of capsules to active motion of cells. *J Biomech Sci Eng* 1:51–68

Barthès-Biesel D, Diaz A, Dhenin E (2002) Effect of constitutive laws for two-dimensional membranes on flow-induced capsule deformation. *J Fluid Mech* 460:211–222

Fischer TM, Stöhr-Liesen M, Schmid-Shönbein H (1978) The red cell as a fluid droplet: tank tread-like motion of the human erythrocyte membrane in shear flow. *Science* 202:894–896

Foessel E, Walter J, Salsac AV, Barthès-Biesel D (2011) Influence of internal viscosity on the large deformation and buckling of a spherical capsule in a simple shear flow. *J Fluid Mech* 672:477–486

- Green AE and Adkins JE (1970) *Large elastic deformations*, 2nd edn. Oxford University Press, Oxford
- Pozrikidis C (2003) *Modeling and simulation of capsules and biological cells*. Chapman and Hall/CRC, Boca Raton
- Pozrikidis C (1992) *Boundary integral and singularity methods for linearized viscous flow*. Cambridge University Press, Cambridge
- Omori T, Imai Y, Yamaguchi T, Ishikawa T (2012) Reorientation of a nonspherical capsule in creeping shear flow. *Phys Rev Lett* 108:138102
- Omori T, Ishikawa T, Barthès-Biesel D, Salsac AV, Walter J, Imai Y, Yamaguchi T (2011) Comparison between spring network models and continuum constitutive laws: application to the large deformation of a capsule in shear flow. *Phys Rev E* 83:0419818
- Skalak R, Tozeren A, Zarda RP, Chien S (1973) Strain energy function of red blood cell membranes. *Biophys J* 13:245–264
- Walter J, Salsac AV, Barthès-Biesel D, Tallec PL (2010) Coupling of finite element and boundary integral methods for a capsule in a Stokes flow. *Int J Numer Meth Eng* 83:829–850

Cell-Free Layer (CFL) Measurements in Complex Geometries: Contractions and Bifurcations

Susana Novais, Diana Pinho, David Bento, Elmano Pinto, Tomoko Yaginuma, Carla S. Fernandes, Valdemar Garcia, Ana I. Pereira, José Lima, Maite Mujika, Ricardo Dias, Sergio Arana and Rui Lima

Abstract In this chapter we discuss the cell-free layer (CFL) developed adjacent to the wall of microgeometries containing complex features representative of the microcirculation, such as contractions, expansions, bifurcations and confluences. The microchannels with the different geometries were made of polydimethylsiloxane (PDMS) and we use optical techniques to evaluate the cell-free layer for red blood cells (RBCs) suspensions with different hematocrit (Hct). The

S. Novais (✉) · D. Pinho · D. Bento · E. Pinto · T. Yaginuma · C. S. Fernandes · V. Garcia · A. I. Pereira · J. Lima · R. Dias · R. Lima
Polytechnic Institute of Bragança, ESTiG/IPB, C. Sta. Apolónia 5301-857 Bragança, Portugal
e-mail: sc2005@sapo.pt

D. Pinho
e-mail: diana@ipb.pt

D. Bento
e-mail: davidbento@ipb.pt

E. Pinto
e-mail: elmanopinto@ipb.pt

T. Yaginuma
e-mail: tyaginuma09@gmail.com

C. S. Fernandes
e-mail: cveiga@ipb.pt

V. Garcia
e-mail: Valdemar@ipb.pt

A. I. Pereira
e-mail: apereira@ipb.pt

J. Lima
e-mail: jllima@ipb.pt

R. Dias
e-mail: ricardod@ipb.pt

images are captured using a high-speed video microscopy system and the thickness of the cell-free layer was measured using both manual and automatic image analysis techniques. The results show that in *in vitro* microcirculation, the hematocrit and the geometrical configuration have a major impact on the CFL thickness. In particular, the thickness of the cell-free layer increases as the fluid flows through a contraction–expansion sequence and that this increase is enhanced for lower hematocrit. In contrast, the flow rates tested in these studies did not show a clear influence on the CFL thickness.

1 Introduction

Human blood is a complex fluid composed mainly of suspended deformable red blood cells (RBCs) within plasma. The RBCs are responsible for the supply of oxygen and nutrients to the body and removal of carbon dioxide and metabolic wastes from tissues. Blood flow behaviour in microcirculation depends on several combined effects such as cell deformability, flow shear rates and geometry of the microvessel, as well as biochemical and biophysical factors which may also affect the rheological characteristics of blood.

A well known hemodynamic phenomenon, known as Fahraeus-Lindqvist effect, observed in both *in vivo* and *in vitro* studies states that for narrow microtubes ($<300\ \mu\text{m}$) both hematocrit and apparent blood viscosity decreases as the tube diameter is reduced (Pires et al. 1992, Goldsmith et al. 1989). The physical reason behind this phenomenon is related to the tendency of the RBCs to undergo axial migration induced by the tank treading motion of its deformable cell membrane as a result of the high shear stresses developed around the wall, and the parabolic velocity profile which forces the RBCs to move towards the center of the vessel (Caro et al. 1978, Garcia et al. 2012, Maeda 1996a, Lima et al. 2012a),

R. Lima
e-mail: ruimec@ipb.pt

D. Pinho · D. Bento · E. Pinto · R. Dias · R. Lima
CEFT, Faculdade de Engenharia da Universidade do Porto (FEUP), 4200-465 Porto,
Portugal

A. I. Pereira
Algoritmi University of Minho, Braga, Portugal

J. Lima
INESC, Faculdade de Engenharia da Universidade do Porto (FEUP), Porto, Portugal

M. Mujika · S. Arana
CEIT and Tecnun, University of Navarra, Paseo de Manuel Lardizábal No 15 20.018
Donostia-San Sebastián, Spain
e-mail: mmujika@ceit.es

S. Arana
e-mail: sarana@ceit.es

consequently leading to the formation of two phases, i. e., a flow core with mainly RBCs and a cell-free layer (CFL) (Lima et al. 2009a, Fujiwara et al. 2009, Lima et al. 2009b). The CFL formation in microvessels reduces the apparent viscosity of blood and by increasing the CFL thickness the blood viscosity decreases in both microchannels and microvessels. Hence, it is extremely important to understand the behavior of the CFL in microcirculation as it contributes to the rheological properties of blood flowing in microvessels, it modulates the nitric oxide scavenging effects by RBCs and it may lead to heterogeneous distribution of blood cells in microvascular networks (Fedosov et al. 2010, Kim et al. 2009).

The cell-free layer width or thickness can be defined as the distance between the wall of the microchannel and the boundary region of the RBCs core. Although the formation of the CFL *in vivo* (Maeda et al. 1996b, Tateishi et al. 1994) has been of great interest over many years, little information is available about this phenomena due to the limitations of the measurement techniques and the complexity of the vascular network. Various researchers have attempted to replicate this behaviour *in vitro* using microfluidic systems in order to better understand this phenomena and explore its potential as a new diagnostic tool (Fujiwara et al. 2009, Lima et al. 2009b). Shevkoplyas et al. (2005) developed a microdevice to isolate WBCs from a blood sample by using the margination effect, whereas Hou et al. (2010) have proposed, very recently, a biomimetic separation device to separate normal and malaria infected RBCs. Other researchers have found several advantages to control and manipulate blood flow in microfluidic devices. Fujiwara et al. (2009) have found evidence that not only it is possible to create an artificial CFL under appropriate hemodynamic and geometrical conditions but also the CFL thickness is strongly influenced by the RBC deformability.

According to Kim et al. (2009) the width of the CFL generally decreases with increasing hematocrit (Hct). The physiological conditions of the working fluid have also a significant influence on the CFL (Maeda 1996, Lima et al. 2012a), and the geometry of the microchannel is another factor that influences the CFL thickness (Sollier et al. 2010, Faivre et al. 2006).

Manual tracking methods have been used extensively to study the blood flow behaviour in microchannels. Examples are the tracking of individual RBCs flowing through glass capillaries (Lima et al. 2007, 2008, 2009a, 2012b, Suzuki et al. 1996), straight polydimethylsiloxane (PDMS) microchannels with rectangular cross-section (Fujiwara et al. 2009), stenosis (Lima et al. 2009a), hyperbolic contractions (Yaginuma et al. 2011, 2013) and bifurcations (Leble et al. 2011, Lima et al. 2011). Manual methods can be highly reliable but they are relatively time consuming and are more subject to user errors. As a result, it is essential to develop image analysis methods able to process the data automatically. Some researchers have already proposed automatic methods to obtain automatically the trajectories of labelled RBCs (Pinho et al. 2012, 2013) or to measure the CFL thickness in microvessels (Kim et al. 2006, Namgung et al. 2010).

In this paper we present an automatic method based in a sequence of simple steps such as the noise reduction by applying pre-processing filters and images binarization by applying threshold levels (Eddins et al. 2002, Bovik 2009). The

main purpose is to examine the effect of different artificial contractions, bifurcations and confluences, different hematocrits (Hct) and different velocities in the CFL thickness. In this study, we expect to improve our understanding about the effect of both geometries and Hct on the CFL thickness and that will be crucial to optimize the design of a microfluidic device able to perform in a single step blood separation and cell deformability measurements.

The current chapter is divided in two main parts: in the first part we use a manual tracking plugin from Image J (Abramoff et al. 2004) to study the effect of sudden contraction followed by a sudden expansion on the CFL thickness whereas in the second part we discuss an automatic method for image analysis using MatLab (2010), to obtain the CFL thickness along a microchannel containing several diverging and converging bifurcations.

2 Materials and Methods

2.1 Microchannels Fabrication and Geometry

The microchannels fabricated for the proposed assays have been produced in PDMS by softlithography from a photo-resist mold. An overview of the fabrication procedure is illustrated in Fig. 1. First, the mold was fabricated by photolithographic technique on a silicon (Si) wafer with an ultra-thick photoresist (SU-8). In this process, a layer of SU-8 photoresist was spin-coated onto the Si wafer and patterned by UV exposure through a photomask. After various curing steps, a SU-8 developer was then used to obtain the final mold master containing the inverse of the desired microchannels.

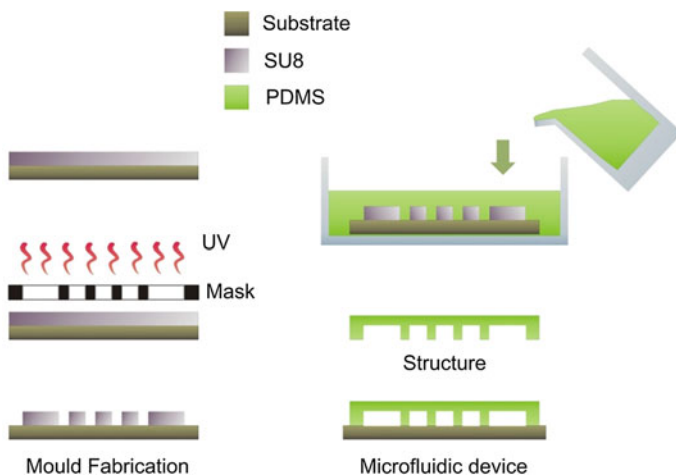


Fig. 1 Main steps of the PDMS microfluidic devices fabrication procedure

The PDMS was prepared by mixing a base and curing agent at a weight ratio of 10:1 for the channels, and 20:1 for the glass slide. After removing the bubbles created during the mixing steps, the mixture was poured over the mold master and baked in the oven for about 20 min at 80 °C. The PDMS is then removed from the mold, cooled to room temperature and the input/output ports were made with an appropriate punching.

Finally, the three-dimensional PDMS microchannel structure was sealed with a glass slide previously spin-coated with PDMS and baked in the oven for 20 min at 80 °C. After this procedure the microfluidic device returns to the oven for further 24 h for a strong seal.

For the first study, the geometry used was a straight channel 400 μm wide containing a sudden contraction 20 μm in width followed by a sudden expansion (see Fig. 2a). The expansion ratio of the geometries, r_e , is given by:

$$r_e = \frac{w_1}{w_2} \tag{1}$$

where w_1 is the dimension of the large channel and w_2 is the dimension of the narrow channel (see Fig. 2) in the contraction region.

In the second study the geometry used is more complex, containing several bifurcations and confluences (see Fig. 2b). Figure 2 illustrate the configuration and relevant dimensions of the geometries used in both studies.

2.2 Experimental Set-up and Working Fluids

The blood samples used were collected from a healthy adult sheep, and ethylenediaminetetraacetic acid (EDTA) was added to prevent coagulation. The RBCs were separated from the blood by centrifugation and washed twice with physiological saline (PS). The washed RBCs were suspended in Dextran 40 (Dx 40) to make up the required RBCs concentration by volume. All blood samples were

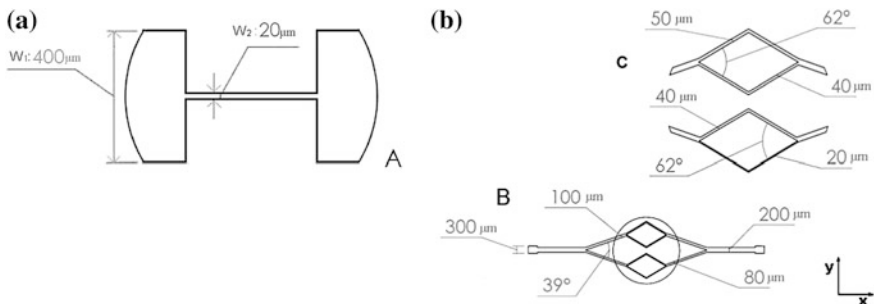
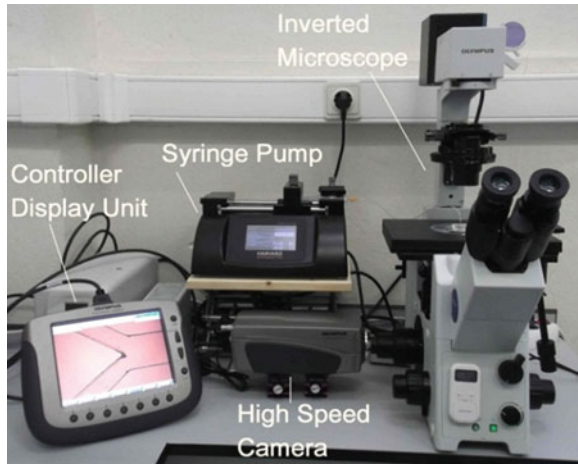


Fig. 2 Geometry and dimensions of the microchannels; **a** contraction–expansion geometry used in the first study, A (scale 50:1); **b** bifurcation–confluence geometry used for the second study, B (scale 6:1) and a detail view C (scale 15:1)

Fig. 3 Micro-PTV experimental set-up



stored hermetically at 4 °C until the experiment was performed at an ambient temperature of about 22 °C.

The micro-particle tracking velocimetry (PTV) system used in the present study consists of an inverted microscope (IX71, Olympus) combined with a high-speed camera (*i*-SPEED LT, Olympus) (see Fig. 3). The PDMS microchannel was placed on the stage of the microscope where the flow rate of the working fluids was kept constant by means of a syringe pump (PHD ULTRA) with a 5 ml syringe (TERUMO[®] SYRING).

The series of x - y images were captured with a resolution of 600×800 pixels. All images were recorded at the center plane of the microchannels at a rate of 600 frames/sec for the first experiment and of 200 frames/sec for the second experiment and were transferred to the computer and then evaluated using image analysis.

2.3 Image Analysis

2.3.1 Manual Method

MTrackJ plugin (Meijering et al. 2006), available for ImageJ was used to automatically computed the centroid of the selected RBC. After obtaining x and y positions, the data were exported for the determination of each individual RBC trajectory, Fig. 4.

This method was used in both studies to obtain the data. In the first study the manual data was used to measure the CFL thickness and in the second study the manual data was used for comparison with the measurements obtained by the proposed automatic method.

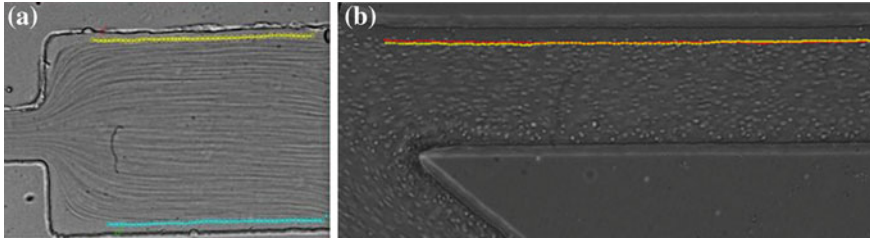


Fig. 4 Manual method showing the trajectories of labeled RBC: **a** for an expansion geometry; **b** for a bifurcation geometry

2.3.2 Automatic Method

All image sequences were processed using Image Processing toolbox available in MatLab (Abramoff et al. 2004) and an automatic method is developed and tested, Automatic Method.

Firstly a median filter with a 3×3 pixel mask was applied to each frame to reduce the noise of the images. Then, the intensity of each pixel in the frame sequence was evaluated to obtain an image with the maximum intensity, with this step is possible identified the region of biggest concentration of blood cells and the region where blood cells don't exist, the plasma layer. As a final step, the image was converted into a binary image, (Fig. 5b). Finally, the region of interest is selected and the upper CFL trajectories are automatically measured. Figure 5 shows the image processing result for the developed method.

2.3.3 Procedures to Measure the CFL Thickness

To analyze the CFL thickness, measurements were taken upstream (before) and downstream (after) the artificial contraction region, as show in Fig. 6: CFL_u corresponds to the thickness of the CFL upstream the contraction, and the CFL_d to the thickness downstream the contraction. The difference of the CFL upstream and downstream of the contraction is given by:

$$\Delta_{CFL} = CFL_d - CFL_u \quad (2)$$

A positive difference indicates an expansion of the CFL.

3 Results and Discussion

In this section the data obtained from both studies is analysed and discussed.

Fig. 5 Results from the automatic method: **a** Original image; **b** Binary image obtained by Automatic Method

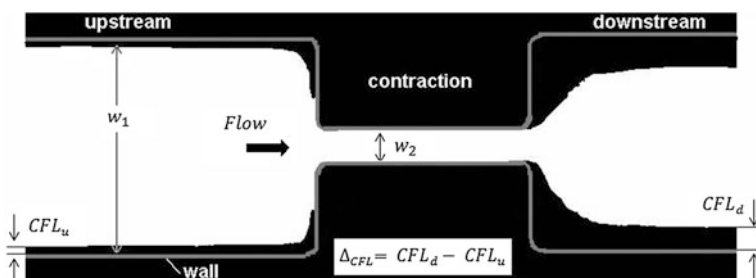
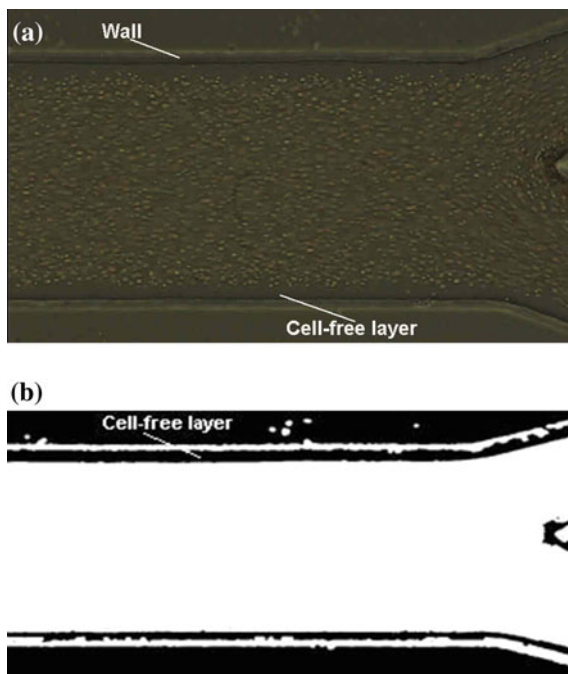


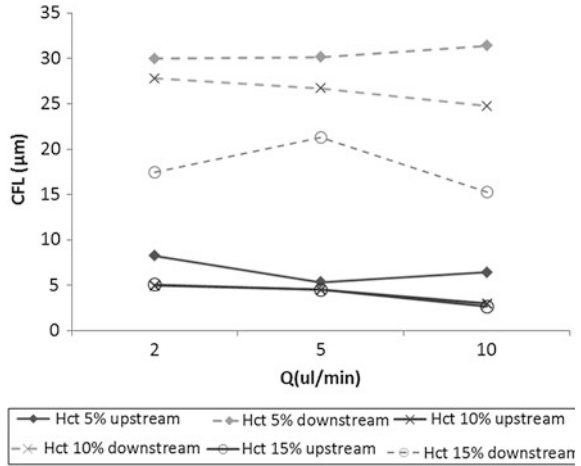
Fig. 6 Schematic view of the contraction–expansion geometry, identifying the relevant variables

In the first study, the geometry used is presented in (Fig. 3a). This geometry has an expansion ratio of 20 and experiments with three distinct hematocrits, 5, 10 and 15 %, and three different flow rates, 2, 5 and 10 $\mu\text{l}/\text{min}$ have been performed.

The results of the CFL represented in the diagrams below show the effect of hematocrit at different flow rates, and the effect of contraction on the CFL thickness. To analyse the influence of the contraction on CFL thickness the CFL difference between upstream (CFL_u) and downstream (CFL_d) the contraction was calculated (see Fig. 6).

In Fig. 7, one can analyze the effect of the Hct and flow rate on the thickness of the CFL.

Fig. 7 CFL thickness upstream and downstream for 5, 10 and 15 % Hct



The results suggest that, for a 5 % of Hct, the cell-free layer has significantly higher values downstream of the contraction. In general terms, nothing can be concluded regarding the influence that flow rate may have on the thickness of the CFL, but comparing the CFL before and after the contraction, the results suggest that the CFL is about 4.6 times bigger after the contraction than before the contraction.

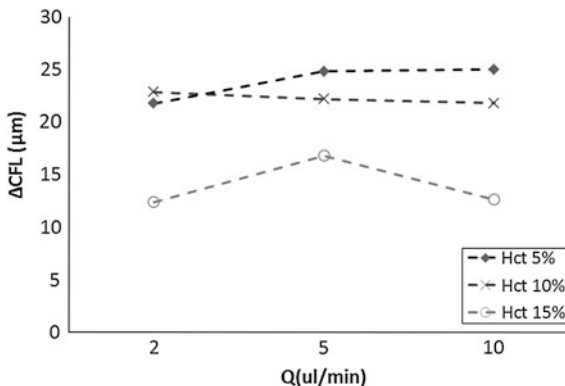
In addition to the considerations made previously, for a 10 % Hct again it is visible the increase in CFL thickness after the contraction, and this sustained an average increase of about 5.9 times. The data from the 15 % Hct, it is concluded again that the CFL, as for 5 and 10 % of hematocrit, is higher than upstream of the contraction, and this contraction downstream of the CFL thickness is about 4.4 times larger than the upstream of contraction.

These results suggest that the contraction provides an increased thickness of the CFL. Moreover, the results of the CFL obtained from downstream of the contraction suggest that increasing the Hct promotes a slight decrease in the CFL.

Figure 8 shows an analysis for all Hcts in relation to the CFL difference, Δ_{CFL} , of the CFL upstream and downstream of the contraction as a function of the flow rates 2, 5 and 10 µl/min. Generally, the results suggest that an increase in Hct involves a reduction in the difference of the CFL. Taking as an example, for the second flow rate (5 µl/min), the previous conclusion is strengthened, since it is found that for a 5 % Hct there is a Δ_{CFL} of 22.8 µm, then with a Hct 10 % there is a reduction of 7.21 µm for Δ_{CFL} . Finally, for the Hct 15 %, Δ_{CFL} has the smallest of 12.4 µm, i.e. the increase in Hct implies a reduction in Δ_{CFL} and therefore a reduction in the formation of the CFL.

For the second study we have used the geometry presented in the (Fig. 2 b) and the results were taken in the sections represented in the Fig. 9, i.e., sections CFL_{A,B,C} represents the results obtained upstream of the middle of the geometry and section CFL_{D,E,F} the results obtained downstream of the middle of the

Fig. 8 CFL difference (Δ_{CFL}) of the contractions for all Hcts as a function of the flow rate of 2, 5 and 10 $\mu\text{l}/\text{min}$



geometry. In this study it was applied the manual method used in the first study and then was applied the automatic method already described in the Sect. 2.

In this study we used two different hematocrits, 5 and 10 % and the same velocity for both, 500 nl/min , and the results obtained by the automatic method were compared with manual results obtained by using a manual tracking method (MtrackJ) from Image J.

As we can see in Table 1, the data obtained from the automatic method, in different regions of geometry analysis, present some discrepancy compared with results obtained manually. This discrepancy occurs because, when performing the binarization of the image with the maximum intensity, parts of the walls of the channels are added to CFL, this is because the intensity of the CFL and the walls are very close. To minimize some of the errors in automatic method we can apply different levels of thresholding and obtain data more close to those obtained manually. However, it is possible to observe in the Fig. 10, there is a similar behaviour between the results obtained by automatic method and manual method for both hematocrits. As example in the case of the hematocrit 5 %, the both methods have a different data, separated for more or less 10 μm , though both have the same behaviour along the channel.

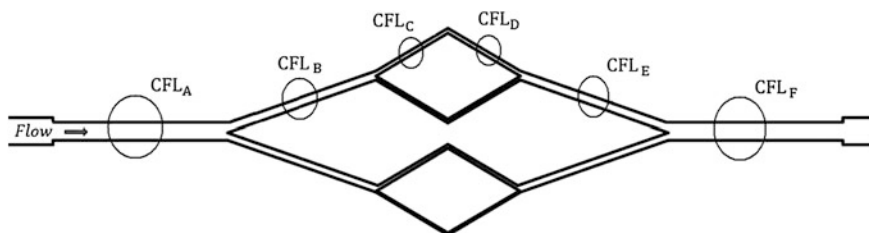


Fig. 9 Visualization the regions where the data was taken

Table 1 - Comparison between the manual and automatic data for CFL (μm)

<i>Hct</i> (%)		<i>CFL_A</i>	<i>CFL_B</i>	<i>CFL_C</i>	<i>CFL_D</i>	<i>CFL_E</i>	<i>CFL_F</i>
5	Manual	15.377	15.564	10.668	10.481	11.755	12.409
	Automatic	22.582	25.431	18.689	17.996	22.487	21.321
10	Manual	9.917	9.184	7.623	8.179	9.448	9.875
	Automatic	12.218	12.694	8.0146	10.867	16.301	15.201

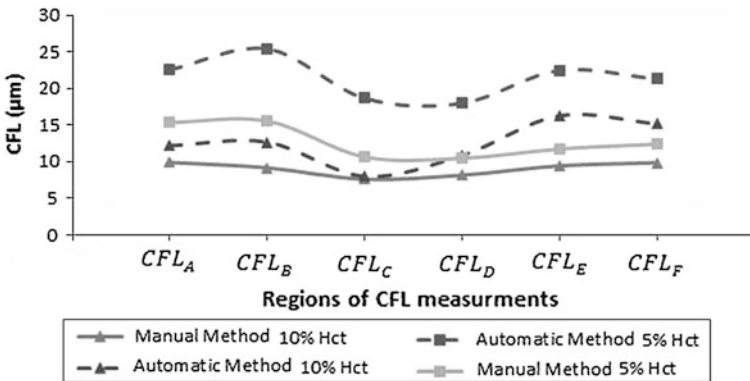


Fig. 10 Comparison between the data obtained manually and automatically

Other visible influence is a decrease in the CFL when Hct increase, and it is verified a tendency to reduce the CFL comparing the *CFL_A* with the *CFL_F* for both hematocrits.

4 Conclusions and Future Directions

Regarding the analysis of the variation of CFL thickness, it can be stated that the geometry created with an expansion ratio of 20, led to a series of obstacles, such as clogging of microchannels due to the very small size of the contraction. However, it should be noted that with this geometry, high values been obtained for the CFL, then it can be concluded that the expansion ratio influences the thickness of the CFL. Additionally, the results also demonstrate that the CFL is always higher in the downstream than the upstream of the contraction. When comparing the values of the difference of thickness of the CFL (upstream–downstream), it is evident that the fluid with a 5 % Hct is the one having greater values, followed by the fluid with a Hct of 10 % and finally the fluid with an Hct of 15 %. Note that for the second study, where we used two different methods (one manual and one automatic) the results corroborate the data obtained from the first study, i.e., the CFL decreases as the Hct increases.

Image analysis plays an important role in this kind of studies but the image quality and the conditions of the recorded videos are also important steps for a reliable image processing. Although the proposed automatic method presents satisfactory results, in the near future we plan to improve the quality and resolution of the images and also the processing steps to obtain results closer to the reality. Additionally, for the first study we also plan in the near future to optimize the geometry in order to achieve one biomedical microdevice with the capability of in one single step, to separate the blood cells that exist in the CFL and measure the deformability of these cells. According to some researchers a microdevice with this skill will be interesting for a direct and rapid diagnosis of some diseases since it will allow studies with different blood cells in the presence of some diseases and separate a specific constituent from blood.

Acknowledgments The authors acknowledge the financial support provided by: PTDC/SAU-BEB/108728/2008, PTDC/SAU-BEB/105650/2008, PTDC/EME-MFE/099109/2008 and PTDC/SAU-ENB/116929/2010 from FCT (Science and Technology Foundation), COMPETE, QREN and European Union (FEDER). The authors are grateful to Mónica Oliveira for many valuable comments on this study.

References

- Abramoff M, Magelhaes P, Ram S (2004) Image processing with image. *J Int Biophotonics* 11:36–42
- Bovik A (2009) *The essential guide to image processing*. Elsevier, Burlington
- Caro C, Pedley T, Schroter R, Seed W (1978). *The mechanics of the circulation*. Oxford University Press, USA
- Eddins SL, Gonzalez RC, Woods RE (2002). *Digital image processing using matlab*. Prentice Hall, NJ
- Faivre M, Abkarian M, Bickraj K, Stone H (2006) Geometrical focusing of cells in a microfluidic device: an approach to separate blood plasma. *Biorheology* 43:147
- Fedosov DA, Caswell B, Popel AS, Karniadakis G (2010) Blood flow and cell-free layer in microvessels. *Microcirculation* 17(8):615–628
- Fujiwara H, Ishikawa T, Lima R, Matsuki N, Imai Y, Kaji H, Nishizawa M, Yamaguchi T (2009) Red blood cell motions in high-hematocrit blood flowing through a stenosed microchannel. *J Biomech* 42:838–843
- Garcia V, Dias R, Lima R (2012). In vitro blood flow behaviour in microchannels with simple and complex geometries. In: Dr. Ganesh R.N (ed) *Applied biological engineering—principles and practice*, ISBN: 978-953-51-0412-4. InTech, 393–416
- Goldsmith H, Cokelet G, Gahtgens P (1989) Robin Fahraeus: evolution of his concepts in cardiovascular physiology. *Am J Physiol* 257:H1005–H10015
- Hou HW, Bhagat AA, Chong AG, Mao P, Tan KS, Han J, Lim CT (2010) Deformability based cell margination—a simple microfluidic design for malaria-infected erythrocyte separation. *Lab Chip* 10:2605–2613
- Kim S, Kong RL, Popel AS, Intaglietta M, Johnson PC (2006) A computer—based for determination of cell-free layer width in microcirculation. *Microcirculation* 13:199–207
- Kim S, Kai Ong P, Yalcin O, Intaglietta M, Johnson PC (2009). The cell-free layer in microvascular blood flow. *Biorheology* 46(3): 181–189

- Leble V, Lima R, Dias R, Fernandes C, Ishikawa T, Imai Y, Yamaguchi T (2011) Asymmetry of red blood cell motions in a microchannel with a diverging and converging bifurcation. *Biomicrofluidics* 5:044120
- Lima R, Wada S, Takeda M, Tsubota K, Yamaguchi T (2007) In vitro confocal micro-PIV measurements of blood flow in a square microchannel: the effect of the hematocrit on instantaneous velocity profiles. *J Biomech* 40:2752–2757
- Lima R, Ishikawa T, Imai Y, Takeda M, Wada S, Yamaguchi T (2008) Radial dispersion of red blood cells in blood flowing through glass capillaries: role of hematocrit and geometry. *J Biomech* 44:2188–2196
- Lima R, Ishikawa T, Imai Y, Takeda M, Wada S, Yamaguchi T (2009a) Measurement of individual red blood cell motions under high hematocrit conditions using a confocal micro-PTV system. *Ann Biomed Eng* 37:1546–1559
- Lima R, Oliveira MSN, Ishikawa T, Kaji H, Tanaka S, Nishizawa M, Yamaguchi T (2009b) Axisymmetric polydimethylsiloxane microchannels for in vitro hemodynamic studies. *Biofabrication* 1:1–7
- Lima R, Fernandes C, Dias R, Ishikawa T, Imai Y, Yamaguchi T (2011). Microscale flow dynamics of red blood cells in microchannels: an experimental and numerical analysis. In: Tavares J (ed) *Computational vision and medical image processing: recent trends*, vol 19. Springer 297–309
- Lima R, Ishikawa T, Imai Y, Yamaguchi T (2012a). Blood flow behavior in microchannels: advances and future trends. In: Ricardo D.M, Rui L, Antonio A, Teresa M.M (eds) *Single and two-phase flows on chemical and biomedical engineering*. Bentham Sci 513–547
- Lima R, Ishikawa T, Imai Y, Yamaguchi T (2012b). Confocal micro-PIV/PTV measurements of the blood flow in micro-channels. In: Collins M.W, Koening C.S (eds), *Nano and micro flow systems for bioanalysis*. Springer, New York, 131–152
- Maeda N (1996) Erythrocyte rheology in microcirculation. *Jpn J Physiol* 46:1–14
- Maeda N, Suzuki Y, Tanaka J, Tateishi N (1996) Erythrocyte flow and elasticity of microvessels evaluated by marginal cell-free layer and flow resistance. *Am J Physiol* 271 Heart Circ Physiol 40:H2454–H2461
- MatLab (2010). The mathworks, Inc., version 7.11. Image processing toolbox version 7.1 user's guide
- Meijering E, Smal I, Danuser G (2006) Tracking in molecular bioimaging. *IEEE Signal Process Mag* 23:46–53
- Namgung B, Ong PK, Wong YH, Lim D, Chun KC, Kim S (2010) A comparative study of histogram-based thresholding of cell-free layer width in small blood vessels. *Physiol Meas* 31:N61–N70
- Pinho D, Lima R, Pereira AI, Gayubo F (2012) Automatic tracking of labeled red blood cells in microchannels. *Int J for Numer Methods Biomed Eng*. doi:[10.1002/cnm.2526](https://doi.org/10.1002/cnm.2526)
- Pinho D, Lima R, Pereira AI, Gayubo F (2013). Tracking red blood cells in microchannels: a comparative study between an automatic and a manual method. In Tavares JMRS, Natal Jorge RM (eds), *Topics in medical image processing and computational vision*, vol 8. Springer, Heidelberg. doi [10.1007/978-94-007-0726-9_9](https://doi.org/10.1007/978-94-007-0726-9_9)
- Pries AR, Neuhaus D, Gaehtgens P (1992) Blood viscosity in tube flow-dependence on diameter and hematocrit. *Am J Physiol* 263:H1770–H1778
- Shevkopylas SS, Yoshida T, Munn LL, Bitensky MW (2005) Biomimetic autoseparation of leukocytes from whole blood in a microfluidic device. *Anal Chem* 77:933–937
- Sollier E, Cubizolles M, Fouillet Y, Achard JL (2010) Fast and continuous plasma extraction from whole human blood based on expanding cell-free layer devices. *Biomed Microdevices* 12:485–497
- Suzuki Y, Tateishi N, Soutan M, Maeda N (1996) Deformation of erythrocytes in microvessels and glass capillaries: effects of erythrocyte deformability. *Microcirculation* 3:49–57
- Tateishi N, Suzuki Y, Soutani M, Maeda N (1994) Flow dynamics of erythrocytes in microvessels of isolated rabbit mesentery: cell-free layer and flow resistance. *J Biomech* 27:1119–1125

- Yaginuma T, Oliveira MSN, Lima R, Ishikawa T, Yamaguchi T (2011). Red blood cell deformation in flows through a PDMS hyperbolic microchannel. In: Proceedings of TechConnect World 2011—Microtech Conference and Expo, vol 2. Boston, USA, p 505
- Yaginuma T, Oliveira MSN, Lima R, Ishikawa T, Yamaguchi T (2013). Human red blood cell behavior under homogeneous extensional flow in a hyperbolic-shaped microchannel. *Biomicrofluidics* 7:054110

Image Processing in the Tracking and Analysis of Red Blood Cell Motion in Micro-Circulation Experiments

Ana João and Alberto Gambaruto

Abstract Red blood cells constitute about 45 % of the blood cells and contain haemoglobin which facilitates transportation of oxygen. Even though RBCs usually present shapes similar to circular cushions with a dimple on the side, they can, sometimes, deform into an asymmetrical slipper shape. As RBCs are required to flow through thin capillaries to deliver oxygen to the human body, deformability is crucial when studying microcirculation. By studying their behaviour in blood vessels one can analyse the normal state of these cells and the diseased states. The insights can help to understand the mechanisms involved in arterial disease and other blood flow related conditions. The aim of this work is to analyse RBC behaviour in experimental conduits using image-based techniques. Images were acquired from a micro-channel with a contraction, where the red blood cells experience shear flow near the center-line. RBCs are tracked throughout a digital video sequence and analysed in terms of shape and deformation index at different time frames. Results show that under strong flows, RBC present an extremely deformable behaviour. RBC tracking and image processing techniques are implemented and analysed.

1 Introduction

The cardiovascular system is vitally important, responsible largely for the transport of nutrients and waste products, but also in the transport of heat, chemical triggers and also responsible for protection, such as healing wounds through thrombus formation, the transport of white blood cells and many other phenomena. The blood acts as the medium for the transport, and is composed largely of plasma,

A. João (✉) · A. Gambaruto
Departamento de Matemática and CEMAT/IST, Instituto Superior Técnico,
Technical University of Lisbon, Av. Rovisco Pais 1, 1049-001 Lisbon, Portugal
e-mail: ana.joao@ist.utl.pt

with a suspension mainly of red blood cells (RBCs), white blood cells and platelets. The state of the blood is therefore an important indicator to the health of an individual (Fung et al. 1970). During the past years, the rapid growth of biomedical technology, mainly of cardiovascular devices and blood-analysis devices has stimulated research on blood degradation and thrombosis associated with their use. The importance of checking the health state of whole blood has stimulated for faster, cheaper and more compact devices for analysis. Great part of the research performed has been focused on red blood cells, which have high concentrations in blood ($\sim 45\%$) and carry high concentrations of oxygen.

Discoveries that normal erythrocytes are nucleus free deformable liquid capsules, enclosed by a biological membrane, which are almost incompressible and show quasi-elastic response to shear and bending deformation, have led to numerous experimental and computational studies. The majority of these studies focus on two goals: firstly, explain the biconcave shape of healthy red blood cells (RBCs) and evaluate whether its membrane is stressed while in resting configuration; secondly, to describe the RBCs behavior in large scale and capillary blood flow (Mohandas and Evans 1994).

RBCs typically have an average diameter of $7\text{--}9\ \mu\text{m}$ at rest, but undergo large deformability when submitted to certain flow conditions. RBC deformation is an important property of oxygen delivery to the body and the passage in small vessels such as capillaries. The deformation of RBCs is also responsible for the non-Newtonian rheology of blood. A decrease in RBC deformation (as is caused by malaria infection) will have serious consequences and may lead to serious health problems (Hou et al. 2010).

Studies have suggested that a minimum RBC deformability may be connected to certain diseases and therefore analysis of RBC deformation can be a crucial tool for medical diagnosis (Hou et al. 2010). The majority of research on human RBC deformation has been performed using a variety of techniques, such as optical tweezers or micro-pipeting. Even though these techniques involve both shear and extension, most of the works usually focus on shear effects on RBCs (Musielak 2009).

Here we study the deformation of RBCs in an experimental setup, of a micro-channel with a sudden change in cross-sectional area in the geometry, through image processing and tracking. The experimental data has been kindly made available from Prof Rui Lima and Prof. Takami Yamaguchi, and their research teams at Instituto Politécnico de Bragança and Tohoku University, respectively. The data obtained from the experiments is a digital video sequences captured with the following characteristics: sample rate of 8,000 pps, exposure time $6\ \mu\text{s}$, image interval $125\ \mu\text{s}$, and magnification $60\times$, equivalent to a pixel size of $2.7\ \mu\text{m}$. For image analysis purposes, the captured video was converted to a stack of images, with resolution of 208×800 . The micro-channel used was produced in polydimethylsiloxane (PDMS) using standard soft-lithography techniques from a SU-8 photoresist mold.

The different stages of the study of the images are, in order: filtering, contrast enhancement, segmentation and finally tracking and analysis. These stages are detailed in the following sections. For simplicity, selected representative images

from the stack are used in order to highlight the processing stage, with the intention that the discussion carries naturally to the entire set of images used. As a initial step, the stack of images was averaged and removed from each individual image; removing therefore some impurity (such as spots due to dirt) and especially the channel geometry, in this manner giving emphasis to the RBCs.

2 Image Preprocessing

2.1 Image Filtering

Prior to segmentation of the RBCs and the analysis of their motion and shape, the images are processed in order to improve their interpretation. Common procedures consist of filtering (de-noising) the images, followed by contrast enhancement to recapture smoothed features. In certain occasions optimal results are seen in procedures to first improve the contrast and them perform filtering, however this is not the common practice.

Images are often diminished by noise and artefact. In microscopy, noise can be seen as the systematic or random corruption of single or small cluster of pixels. Artefacts include RBCs moving in and out of the focal plane that results in a fading and smearing of the RBC definition as well as reduction in cross-sectional area, and partial volume effects. Noise can be understood as an undesired signal that affects the communication or measurement of another signal. Artefacts, on the other hand, are errors in representation of visual information caused by the imaging equipments and modalities. By reducing the noise intensity in the image a clearer and more robust interpretation is possible. A number of approaches have been proposed for image de-noising, such as low-pass filtering using a Fourier (or wavelet) expansion or simply a convolution to a Gaussian (hence, the solution to the heat equation). Here we briefly discuss the background and motivation for adopting a partial differential equation based diffusion, that is in essence an anisotropic diffusion equation, such that the diffusion will occur in rather homogeneous regions and not across boundaries (Perona and Malik 1990).

Let us consider each image of the stack as 2-dimensional orthogonal domain $\Omega = (1, N_1) \times (1, N_2)$. Considering $I_0(x, y, 0)$ to be the original image, we denote as the image $I(x, y, t)$ at a moment during the processing phase. The non-linear anisotropic diffusion process proposed by Perona and Malik in (Perona and Malik 1990) looks for the solution of

$$\frac{\partial I(x, y, t)}{\partial t} = \nabla \cdot (c(x, y, t) \nabla I(x, y, t)) \quad (1)$$

where the diffusion coefficient is commonly a decreasing function of the image gradient $c(x, y, t) = g(|\nabla I(x, y, t)|)$; $\nabla \cdot$ and ∇ are the divergence and the gradient operator, respectively. The anisotropic diffusion coefficient is a chosen to estimate

edges in the object, since these will have the largest gradient in the image. A popular choice is

$$g(|\nabla I(x, y, t)|) = \frac{1}{1 + |\nabla I|^2/K^2} \quad (2)$$

hence at edges the diffusion coefficient is small and large in region of rather homogeneous intensity. This form of the equation is denoted by *PM* [from the work of Perona and Malik (Perona and Malik 1990)] in the following discussion of the filtering performance.

If in Eq. (1) the diffusion coefficient is made constant, it reduces to the well known heat equation $\frac{\partial I(x, y, t)}{\partial t} = c \nabla^2 I(x, y, t)$. Expanding Eq. (1) with $c = g(|\nabla I|)$ we obtain

$$I_t = g(|\nabla I|) \partial_{\tau\tau} I + [g(|\nabla I|) + 2|\nabla I|^2 g'(|\nabla I|)] \partial_{\nu\nu} I \quad (3)$$

where τ and ν are orthogonal direction tangential and normal to an edge. Hence the diffusion process is decomposed into a process tangential to an edge and normal to it. The coefficient of the derivative in the direction normal to the level set of I becomes negative for large values of the image gradient (“edges” in an image) and popular choice of g mentioned above (Guidotti 2012). This leads to a regime where diffusion can reverse its sign at least in one direction, and hence a forward–backward diffusion process is obtained. The Perona-Malik equation given in Eq. (1) is ill-posed and several approaches have been proposed to regularise the equations (Guidotti 2012). In practice however the approach work well and observed problems are occasional staircasing effects after long time evolution, and in other words a mild gradient region evolves into piece-wise almost linear segments separated by jumps. The original image used through out the analysis can be seen in Fig. 1.

An alternative approach is to define the image edge not by the gradient of the image but the Laplacian of the image. This can be seen to be appropriate in the case of a slowly varying edge with a constant gradient along it: the edge will have the same gradient and hence no sharpening effect will be produced, while using a diffusion coefficient based on the Laplacian will provide a more appropriate edge detection criterion. This is the case in RBCs visualisation using confocal microscopy as the light distortion due to the membrane covers several pixels, hence indicating that the edge is represented by a uniform change in the image (constant image gradient) over a spatial extent of a few pixels. Gilboa et al. (Gilboa et al. 2004) combined the diffusion equation with the Schrödinger equation such that the non-linear complex diffusion process is given by

$$\frac{\partial}{\partial t} I = \nabla \cdot (d(\text{Im}(I)) \nabla I) \quad (4)$$

where $\text{Im}(\cdot)$ denotes the imaginary value and the diffusion coefficient is defined as

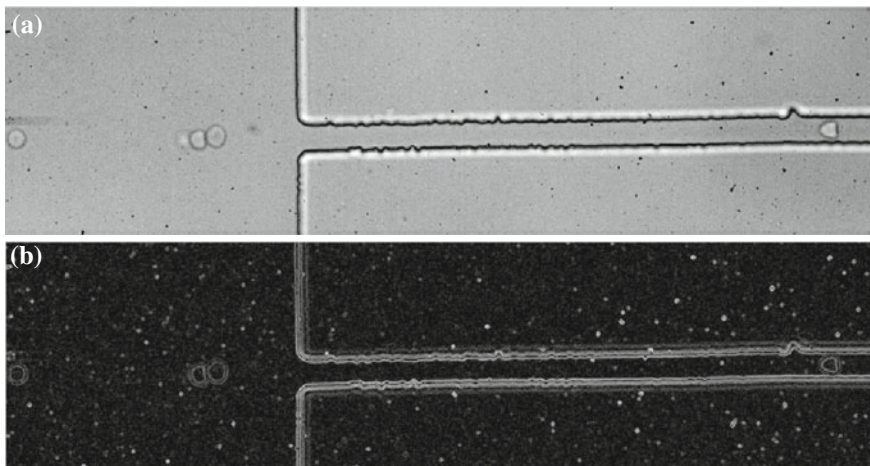


Fig. 1 **a** Original image (frame 50)—PMDS hyperbolic microchannel, **b** Image gradient

$$d(\text{Im}(I)) = \frac{\exp(i\theta)}{1 + \left(\frac{\text{Im}(I)}{k\theta}\right)^2} \approx \frac{1}{1 + \left(\frac{\Delta I}{\kappa}\right)^2} \quad (5)$$

It has been reported in (Gilboa et al. 2004) that $\text{Im}(I)$ approximates a smoothed second order derivative of the image (Salinas and Fernandez 2007). This avoids the discretisation errors and sensitive nature of using finite differences for the calculation of the Laplacian (Araujo et al. 2012). Overall this non-linear complex diffusion filter (NCDF) has been reported to give improved despeckling and denoising properties (Bernardes et al. 2010).

The NCDF method has been improved by (Bernardes et al. 2010) in their use for optical coherence tomography data for the human eye, by introducing an adaptive time step and adaptive coefficient k in Eq. (5). The reason behind an adaptive time step is due to the fact that the diffusion coefficient (Eq. 5) depends on the second order derivative of the image, which is greater during the initial steps of the diffusion process due to a greater presence of noise that is then progressively reduced; hence more emphasis has to be given to small image features during the initial iteration steps by use of small time steps initially. Choosing the correct parameter k in Eq. (5) modulates the spread of the diffusion coefficient in the vicinity of its maximum, hence at edges and homogeneous areas, where the image Laplacian disappears.

$$k = k_{MAX} + (k_{MAX} - k_{MIN}) \frac{g - \min(g)}{\max(g) - \min(g)} \quad (6)$$

where $\max(g)$ and $\min(g)$ are the maximum and minimum of g , with $g = G_{N,\sigma} * \text{Re}(I)$, where $*$ is the convolution operator, $G_{N,\sigma}$ is a local Gaussian

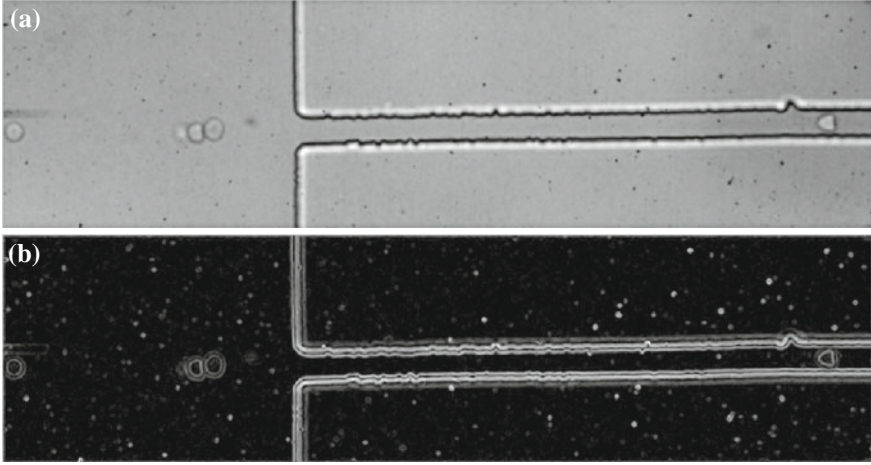


Fig. 2 Frame 50 with **a** image filtered using adaptive NCDF, **b** filtered image gradient

kernel of size $N \times N$ and standard deviation σ , and $\text{Re}(I)$ denotes the real part of the image.

The adaptive time step is given by

$$\Delta t = \frac{1}{\alpha} [a + b \exp\{-\max(|\text{Re}(\partial I/\partial t)|/\text{Re}(I))\}], \quad (7)$$

where $|\text{Re}(\partial I/\partial t)|/\text{Re}(I)$ is the fraction of change of the image at a certain iteration step and a, b are constants and control the time step with $a + b \leq 1$. For this study $\alpha = 4$, $a = 0.25$ and $b = 0.75$ (Bernardes et al. 2010) and the result of filtering Frame 50 can be seen in Fig. 2 .

2.2 Contrast Enhancement

Even though the results obtained using the adaptive NCDF method are satisfactory due to low blurring effects (small diffusion) on the RBC edges, contrast enhancement is performed to intensify feature edges that may have been mitigated at high intensity of denoising. Here, the images have been enhanced using the *unsharp masking* method and the results are presented in Fig. 3 .

In the unsharp masking method, the enhanced image $I_{enhanced}(x, y)$ is obtained from the input image $I(x, y)$ and given by:

$$I_{enhanced}(x, y) = I(x, y) + \lambda(I(x, y) - G_{\sigma} * I(x, y)) = I(x, y) + \lambda F(x, y) \quad (8)$$

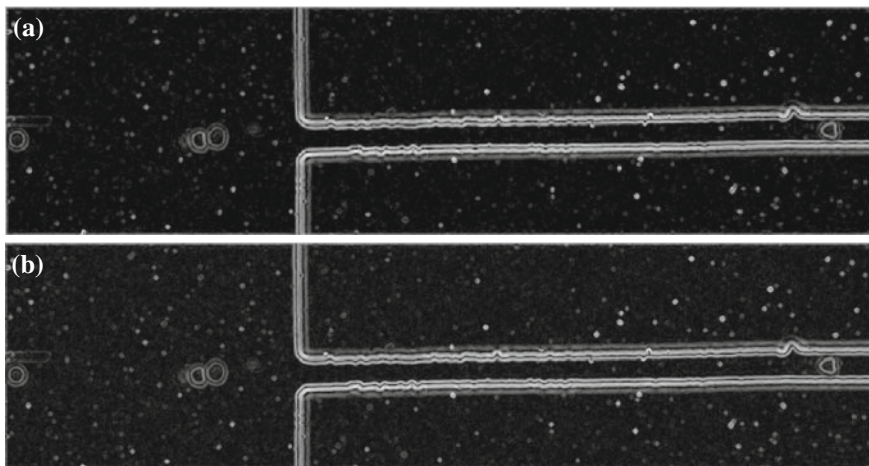


Fig. 3 Frame 50 **a** image gradient after filtering with adaptive NCDF, **b** image gradient after filtering and enhancement

where $F(x, y)$ is the correction signal computed as the output of the linear high-pass filter, and λ is the scaling factor which controls the contrast enhancement level acquired as the output image ($0 \leq \lambda \leq 1$, with $\lambda = 0.5$ throughout these results) (Polesel et al. 2000).

3 Image Quality Measures

We can now briefly compare the performance of both methods using performance metrics measures: the variance of the image pixel intensities measured locally and denoted by σ_{local} , defined by Eq. (9); and the contrast to noise ratio (CNR), defined in Eq. (10).

The local variance at a given pixel of an image is defined as

$$\sigma_{local}^2(I(x, y)) = \frac{1}{n^2} \sum_{X=-\frac{n-1}{2}}^{\frac{n-1}{2}} \sum_{Y=-\frac{n-1}{2}}^{\frac{n-1}{2}} (I(x + X, y + Y) - \mu)^2 \quad (9)$$

where μ is the mean of local region of interest of size $n \times n$, and for this work $n = 3$ was chosen. We can analyse the local variance of an image as a measure of image noise intensity, since for a binary image high values of variance are seen only at feature edges.

The CNR gives an objective measure of contrast (the difference of means) between a region of background noise (reference) and an image feature (object in study).

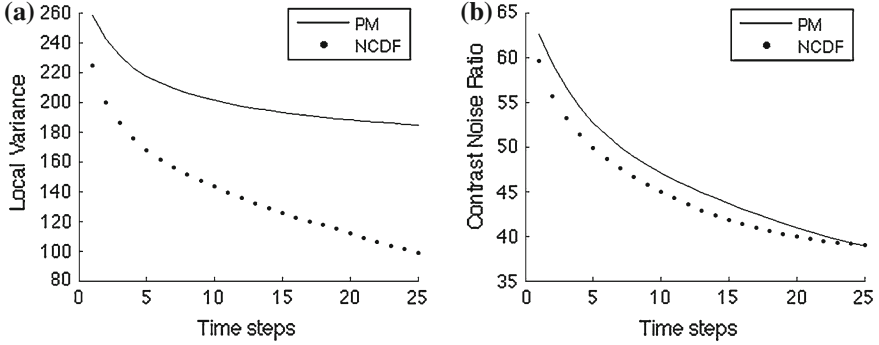


Fig. 4 Frame 50 performance metrics for filtering with: **a** average local variance of the image, **b** contrast to noise ratio

$$CNR = \frac{\mu_t - \mu_r}{\sqrt{\sigma_t^2 + \sigma_r^2}} \quad (10)$$

where μ_r and σ_r are the pixel mean and standard deviation of a reference area of the image, while μ_t and σ_t are the mean and standard deviation of the region of the object.

Fig. 4 presents the performance metrics at different levels of filtering, denoted by time evolution of Eq. (1). The mean σ_{local}^2 for the image is seen to be less for the adaptive NCDF method compared to the PM method, while the CNR is comparable for both methods. Based on these results, it is apparent that the adaptive NCDF not only retain all the advantages of PM but also achieves a superior performance. A significant advantage furthermore in the adaptive NCDF method over the PM, is that the diffusion parameter need not to be defined a priori, but instead it adapts to the image in study and during the filtering process.

4 Detecting and Tracking Red Blood Cells

When tracking the RBCs in the video sequence it is often pertinent to provide information about the shape of the object. Due to the fact that cell shapes are restricted, the analysis of the image sequence can exploit the prior known information about the cells geometry in order to increase the robustness of the method and the computation time. This is moreover the case in a high frame rate video sequence, where the analysis of the previous image can be used as a starting point for the current frame.

Here two methods are presented: the Hough transform (Ballard 1981) and the Active Contours (Snakes) (Kass et al. 1988). The Hough transform is used to identify predefined shapes in a given image, here circles of integer variable radius are matched to the RBCs. The Snakes method allows for a deformable curve to

align image features, with the deformation of the curve given by a minimisation of internal (tension and bending) and external forces (image-inferred and imposed).

In the case of segmenting and tracking the RBCs, the Hough transform will only be able to provide best-fit circles, while the Snakes will be able to capture the cell deformation. The Hough transform tends to be more robust and faster as the shape is given, while the location and radius are free parameters. For the Snakes method however, there is no global structure imposed and the shape of the object is computed by local constraints of continuity and smoothness. We can argue that this makes the method more sensitive to noise and image irregularities. For both methods, the preprocessing steps of filtering and contrast enhancement considerably improve the robustness of the methods.

In this work the Hough transform is used on the first image in the sequence, and the contours provided are used to initiate the Snakes method. For the following frames in the video sequence, the RBC velocity is estimated in order to improve robustness and speed of the algorithms. Both methods are now briefly presented.

4.1 Hough Transform Method

The Hough transform method allows for object detection of a specific shape within an image that has been transformed into edge representation. In that kind of representation, sample pixels in the image do not contain the grey level information, but the magnitude and direction of the local grey level change. A commonly used edge representation is the gradient operator which provides the local grey level change as a ramp, while another possibility is the Hueckel operator which gives a step representation instead (Ballard 1981).

The basis of the general Hough algorithm used in this study is presented here concisely following the work in (Ballard 1981), and only a brief conceptual outline of the method is reported here. The gradient of the image is to infer information about object edges in the image. A threshold value for the image gradient magnitude is chosen such that pixels above this value will be considered as part of object edges. For these pixels, the gradient direction provides additional information to the edge representation. In the case of identifying circles in the image, the gradient direction will indicate the line on which the circle centre lies. An *accumulator array* is used to identify possible circle matches, and based on a scoring system the local maxima once all edge pixels have been considered, defines the circle centre and radius.

The method is robust and works well in the case of incomplete edge representations and noise, that can be handled by introducing uncertainties in the scoring system in the accumulator array. Figure 5 shows the results of RBC segmentation using Hough transform. This segmentation is used to initiate the Snakes method, by initially maintaining the centre of the identified circles but reducing the radius in order that the perimeter lies within the RBCs. The Snakes method is now briefly outlined.

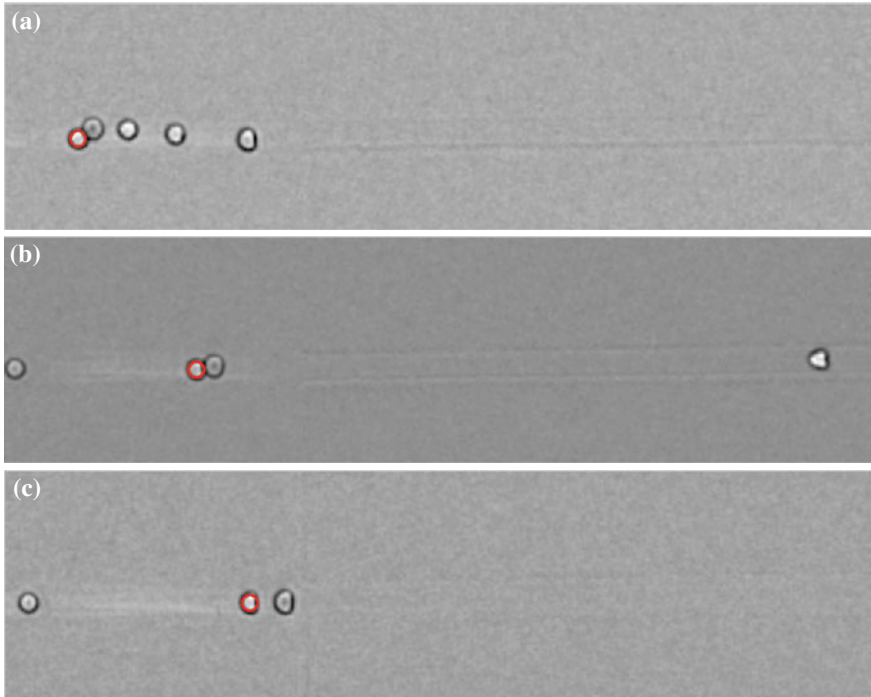


Fig. 5 Detection of one RBC in different frames using Hough transform method

4.2 Active Contours Method (Snakes)

Snakes are active contour models, which localise edges adaptively. The snake model is controlled by a continuity spline under the influence of image forces and external constraint forces, as well as internal regularising forces. The image forces push the snake toward salient image features, while the external forces are responsible for putting the snake closer to the desired local minimum (Kass et al. 1988). Here we use the slightly shrunken contour obtained using the Hough transform as the initial snake position, and allow the Snakes to adapt to the deformed RBC shape.

Considering $p(s) = (x(s), y(s))$ as the position of a Snake represented parametrically, we can write its energy functional as

$$\begin{aligned}
 E_{snake}^* &= \int_0^1 E_{snake}(p(s)) ds \\
 &= \int_0^1 E_{internal}(p(s)) + E_{external}(p(s)) ds
 \end{aligned}
 \tag{11}$$

where $E_{internal}$ is the internal energy due to tension and bending, and $E_{external}$ is given by the summation of the image forces E_{image} with the constraint forces E_{constr} (Kass et al. 1988), hence $E_{external} = E_{image} + E_{constr}$.

The internal spline energy of the Snake is given by a first-order term controlled by $\alpha(s)$, and second-order term controlled by $\beta(s)$ and can be written as

$$E_{internal} = \frac{1}{2}(\alpha(s)|p_s(s)|^2 + \beta(s)|p_{ss}(s)|^2) \quad (12)$$

The first-order term weighted by $\alpha(s)$ regulates the membrane behaviour (tension), while the second-order term weighted by $\beta(s)$ regulates the thin-plate behaviour (bending).

To make sure that the external energy attracts the snakes to salient features of the image, three different energy functions are used for E_{image} , given by a weighted combination of the functionals that attract the Snake to lines, edges and terminations:

$$E_{image} = w_{line}E_{line} + w_{edge}E_{edge} + w_{ter}E_{ter} \quad (13)$$

The different behaviours of the snake are adjusted by the weights w_{line} , w_{edge} and w_{ter} . The most commonly used image functional is the image intensity, hence $E_{line} = I(x, y)$. Depending on the sign of w_{line} . The Snake is attracted either to light or dark lines. The edge functional allows the Snake to be attracted to contours with large image gradients and is commonly given by $E_{edge} = -|\nabla I(x, y)|^2$. The termination functional E_{ter} permits the Snake to be attracted to terminations (corners) by using the curvature of level lines. The curvature of a contour in a two-dimension image is given by:

$$E_{ter} = \frac{C_{yy}C_x^2 - 2C_{xy}C_xC_y + C_{xx}C_y^2}{(C_x^2 + C_y^2)^{3/2}} \quad (14)$$

where $C(x, y) = G_\sigma(x, y) * I(x, y)$, and $G_\sigma(x, y)$ is a Gaussian of standard deviation σ . The constraint forces E_{constr} is used to define attractive (or repulsive) forces, that can be denied manually or automatically. Here $E_{constr} = k/(|\mathbf{q} - \mathbf{x}|^2)$, as a repulsive force located at position \mathbf{q} , which is the centre of the closed contour from the previous frame that has been shrunk to fit inside the RBC. In this way E_{constr} serves as an inflation force to push the Snake out.

Different weights in the energy functionals give different properties to the Snake and the interpretation of the image information. Figure 6 shows the results for different images in the stack, tracking a single RBC.

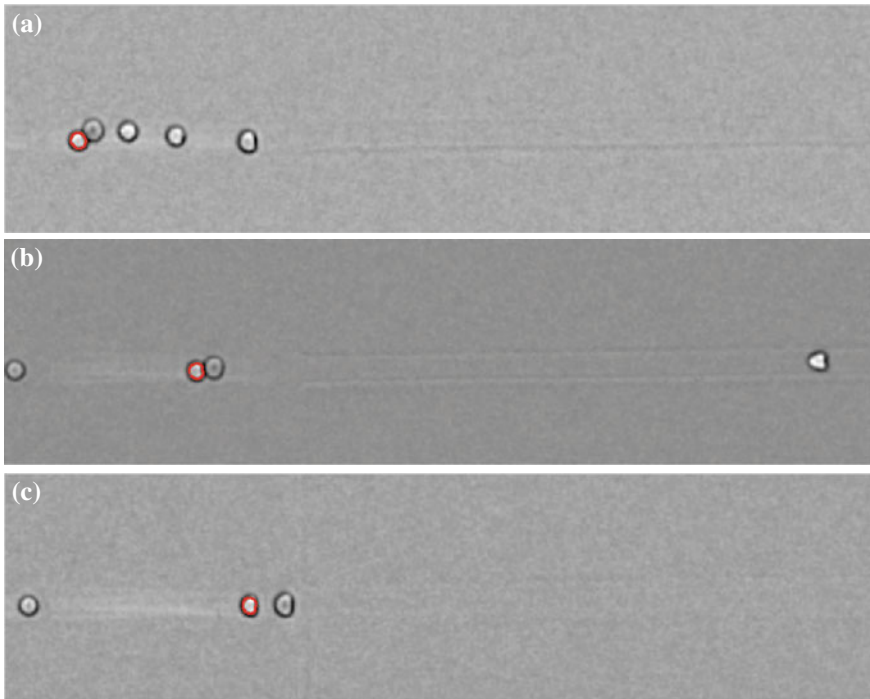


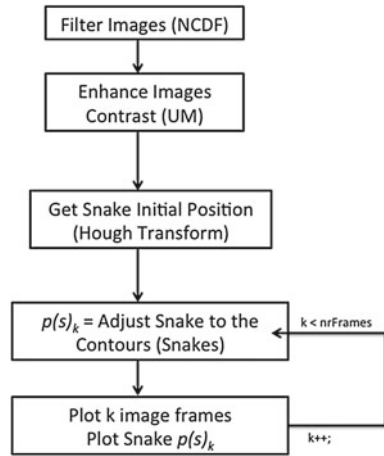
Fig. 6 Detection of one RBC in different frames using our algorithm

4.3 Outline of Algorithm

The algorithm is concisely presented in Fig. 1. The image processing steps are in order: (1) subtract the image stack average from each image; (2) perform filtering using the adaptive NCDF method; (3) perform contrast enhancement using the unsharp masking method. From here the first frame in the sequence is taken and the Hough transform is used to identify the best-fit circles to the RBCs. These are shrunk to fit entirely within each RBC and then the Snakes method is used to capture the RBC shape more accurately. For subsequent frames, each RBC velocity is estimated, the contour from the previous frame is translated accordingly and shrunk slightly to ensure that the contour lies within the RBC, and the Snakes method is used again to identify delineate the RBCs. This is continues until all frames in the video sequence have been analysed.

In the experimental data studied, the micro-channel is not deep such that RBCs will not move entirely out of the focusing plane. This signifies that no RBC will appear or disappear within the domain but only enter or leave through the inflow and outflow edges, respectively. In the case of different setups where the channel height is greater to allow RBC to move in and out of the focal plane, and in the case of tracking newly entering RBCs, the Hough transform can be used more

Fig. 7 RBC detection algorithm



regularly in the image stack to identify the RBCs and not track them, as mentioned above, with an added computational cost.

Tracking is possible by considering the centre and radius of each RBC, detecting the closest ones in adjacent frames in the image stack. The RBC perimeter is discretised parametrically in the Snakes method into straight line segments. The contour thus represented, is used to calculate the centroid of the polygon and its area. Let us consider our contour as a non-self-intersecting closed polygon defined by M vertices $(x_0, y_0), (x_1, y_1), \dots, (x_M, y_M)$, the centroid is the pixel C_x, C_y where

$$\begin{aligned}
 C_x &= \frac{1}{6A} \sum_{i=0}^{M-1} (x_i + x_{i+1})(x_i y_{i+1} - x_{i+1} y_i) \\
 C_y &= \frac{1}{6A} \sum_{i=0}^{M-1} (y_i + y_{i+1})(x_i y_{i+1} - x_{i+1} y_i)
 \end{aligned} \tag{15}$$

where A is the contour area given by $A = \frac{1}{2} \sum_{i=0}^{M-1} (x_i y_{i+1} - x_{i+1} y_i)$. The vertices are numbered in order of their occurrence along the contour's perimeter, and the last vertex (x_M, y_M) is assumed to be the same as the first one (x_0, y_0) . We should note that if the vertices are numbered clockwise the area A will have a negative value, but the centre coordinates will still be correct.

The method is fully automatic, robust, fast and accurate enough for the purpose of identifying, tracking and analysing the shapes of the RBCs. An example of tracking a RBC is shown in Fig. 8.

Results are shown in Fig. 9 for the tracking of a RBC undergoing large deformations (Table 1). From this figure it is evident that the outlined method proves to be sufficiently robust in the cases of: a rounded shape RBC, slightly deformed, and severely deformed by the channel.

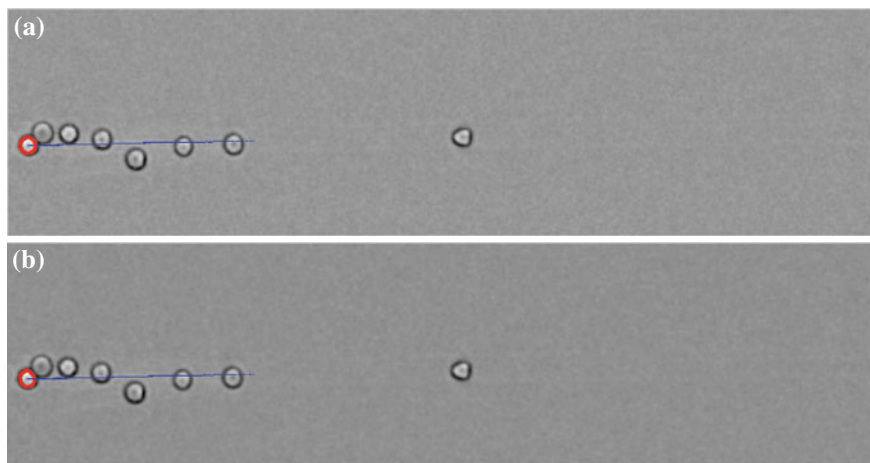


Fig. 8 Tracking an RBC using the **a** Hough transform and **b** Snakes

Table 1 RBC deformation at different regions of the PDMS micro-channel (in pixels)

	RBC perimeter			RBC area		
	Region 1	Region 2	Region 3	Region 1	Region 2	Region 3
Hough	43.9823			153.9380		
Hough + Snakes	46.1460	45.0526	47.4106	179.2320	175.4701	178.2284

5 Results and Discussion

A method for identifying and tracking red blood cells from experimental data has been put forward. The analysis of the translation and deformation of the RBCs is now discussed in terms of basic measures such as the perimeter length and the area. Comparison is performed on the filtering methods (PM and adaptive NCDF) as well as the segmentation methods (Hough transform and Snakes) in order to investigate suitability and give an indication of errors or variability that the analysis is susceptible to.

Initially we focus on testing the filtering method used, hence the anisotropic diffusion presented in Eq. (1) for both diffusivity coefficients: the gradient based function in Eq. (2) (Perona and Malik 1990), and the Laplacian based coefficient from Eq. (5) together with the adaptivity methods of Eqs. (6, 7) (Bernardes et al. 2010). Results are shown in Fig. 4 for measures of the mean local variance (Eq. 9) and contrast to noise ration (CNR) (Eq. 10). As noted above, this result indicates that improved noise removal is obtained with no effective loss in the CNR, leading to the proposition that adaptive NCDF performs better than PM methods for the data case used in this work.

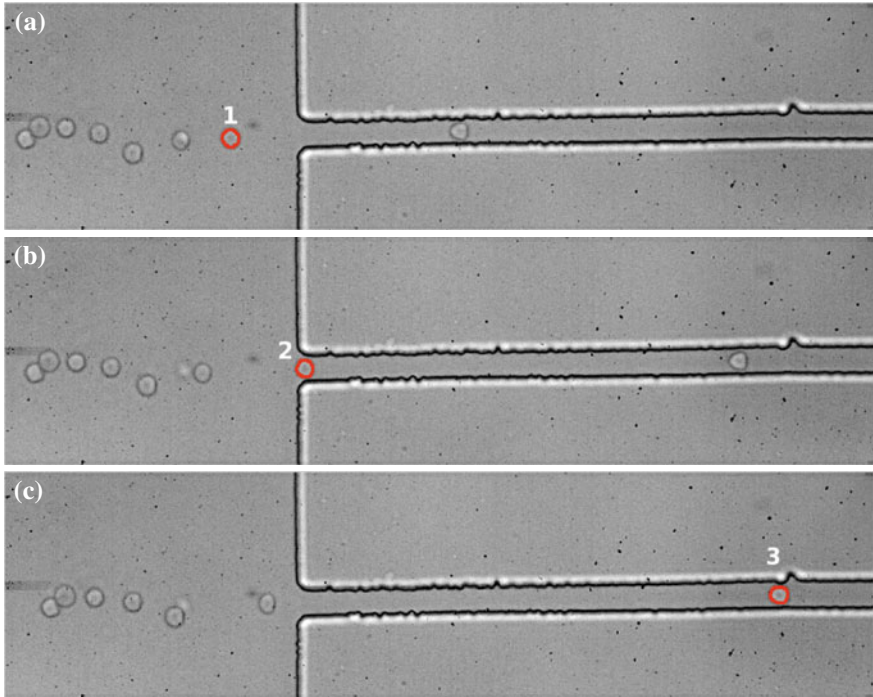


Fig. 9 RBC deformation in different regions of the PDMS micro-channel **a** region with no contraction, **b** beginning of the micro-channel, **c** narrow region of the micro-channel

The effect of filtering and enhancing the contrast is complemented with results presented in (Fig. 10). These show the variation of image intensity and intensity gradient along a line. As expected, filtering the image alters significantly the quality by reducing noise, and subsequently leading to a more accurate and robust segmentation and subsequent analysis.

We now observe the effects of the segmentation methods with respect to basic shape measures. The RBCs were analysed in three frames of the sequence, indicated by (1), (2) and (3) in Fig. 9. Location (1) is in a region of free flow before the contraction, (2) is at the beginning of the micro-channel constriction, and (3) is within the constriction. Results are presented in Table 1. Far from the contraction region, the red blood cells are effectively circular, resulting in a bigger area as it lies largely in the focus plane. The deformation index (ratio between the major and minor axes of an ellipse that best fits the RBC) will hence give values close to unity. As the cells approach the contraction, location (2), and during the contraction itself, location (3), they become deformed with an elongated shape. Due to the RBC deformation in the contraction, the RBC perimeter increases as well as the deformation index. This occurs since the cells are being submitted to strong shear flow.

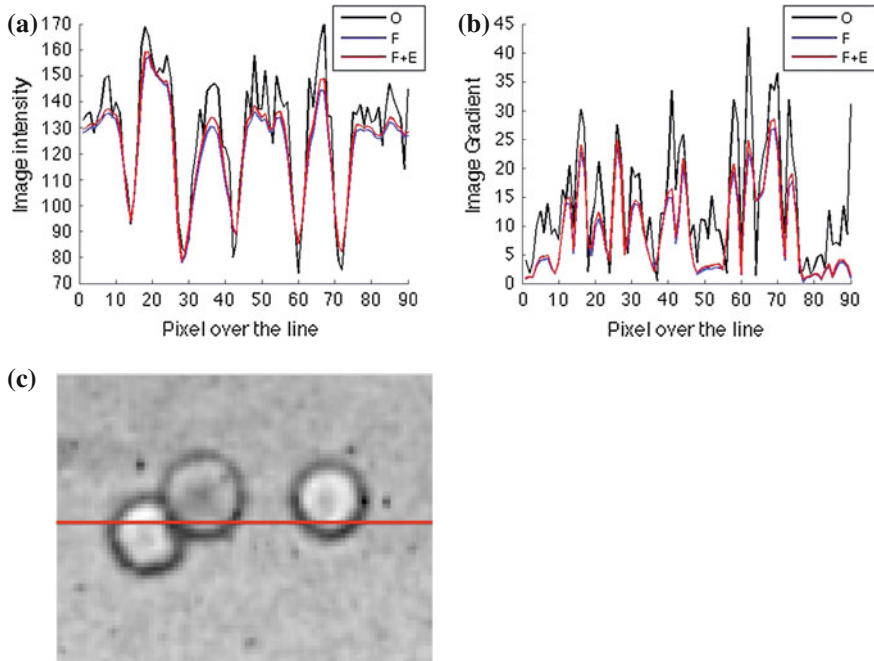


Fig. 10 Variation of image intensity (a) and intensity gradient (b), along a *red line* (from left to right) shown in (c). Key: *O* Original; *F* Filtered (using adaptive NCDF); *F + E* Filtered and Enhanced (using unsharp masking)

Results have shown the potential advantage of using preprocessing techniques in image segmentation, which was one of our goals during this study. When considering RBC deformation, in order to deeply understand the findings, tests have to be done with different concentration of RBCs (hematocrit) and flow rates as well as different geometries of the micro-channel. The results show that the RBCs are highly deformable under strong shear flows. Different hematocrit levels or flow rates will provide further results, such as the influence and size of the cell-depleted regions near the stationary walls, and effects non-Newtonian rheology in small vessels.

Acknowledgments The authors kindly acknowledge the support provided by CEMAT/IST and funding support by the FCT project BIOMIMETIC—PTDC/SAU-ENB/116929/2010. We kindly thank Prof. Rui Lima and his research team from Instituto Politécnico de Bragança, and Prof. Takami Yamaguchi and his research team from Tohoku University, for providing the experimental data.

References

- Araujo A, Barbeiro A, Serranho P (2012) Stability of finite difference schemes for complex diffusion processes. *SIAM J Numer Anal* 50(30):1284–1296
- Ballard DH (1981) Generalizing the Hough transform to detect arbitrary shapes. *Pattern Recogn* 13(2):111–112
- Bernardes R, Maduro C, Serranho P, Araujo A, Barbeiro S, Cunha-Vaz J (2010) Improved adaptive complex diffusion despeckling filter. *Opt Express* 18(23):24048–24059
- Fung Y, Perrone N, Anliker M (1970) *Biomechanics: its foundation and objectives*. Prentice-Hall, Englewood Cliffs
- Gilboa G, Sochen N, Zeevi YY (2004) Image enhancement and denoising by complex diffusion processes. *IEEE Trans Pattern Anal Mach Intell* 26(8):1020–1036
- Guidotti P (2012) A family of nonlinear diffusions connecting perona-malik to standard diffusion. *Discrete Contin Dyn Syst Ser S* 5(3):581–590
- Hou, Han Wei, Bhagat, ALI Aqar S, Lin Chong, AlvinGuo, Mao, Pan, Wei Tan, Kevin Shyong, Han, Jongyoon Lim, Chwee Teck (2010) Deformability based cell margination-a simple microfluidic design for malaria-infected erythrocyte separation. *Lab Chip* 10:2605–2613
- Kass M, Witkin A, Terzopoulos D (1988) Snakes: active contour models. *Int J Comput Vision* 1(4):321–331
- Mohandas N, Evans E (1994) Mechanical properties of the red cell membrane in relation to molecular structure and genetic defects. *Annu Rev Biophys Biomol Struct* 23:787–818
- Musielak M (2009) Red blood cell-deformability measurement: review of techniques. *Clin Hemorheol Microcirc* 42(1):47–64
- Perona P, Malik J (1990) Scale-space and edge detection using anisotropic diffusion. *IEEE Trans Pattern Anal Mach Intell* 12(7):629–639
- Polesel A, Ramponi G, Mathews VJ (2000) Image enhancement via adaptive unsharp masking. *IEEE Trans Image Process* 9(3):505–510
- Salinas HM, Fernandez DC (2007) Comparison of pde-based nonlinear diffusion approaches for image, enhancement and denoising in optical coherence tomography. *IEEE Trans Med Imag* 26(6):761–771

Flow of Red Blood Cells Suspensions Through Hyperbolic Microcontractions

Vera Faustino, Diana Pinho, Tomoko Yaginuma,
Ricardo C. Calhelha, Geyong M. Kim, Sergio Arana,
Isabel C. F. R. Ferreira, Mónica S. N. Oliveira and Rui Lima

Abstract The present study uses a hyperbolic microchannel with a low aspect ratio (AR) to investigate how the red blood cells (RBCs) deform under conditions of both extensional and shear induced flows. The deformability is presented by the

V. Faustino (✉) · D. Pinho · T. Yaginuma · R. Lima
ESTiG, Polytechnic Institute of Bragança, C. Sta. Apolónia 5301-857 Bragança, Portugal
e-mail: verafaustino@ipb.pt

D. Pinho
e-mail: diana@ipb.pt

T. Yaginuma
e-mail: tomoko@ipb.pt

R. Lima
e-mail: ruimec@ipb.pt

G. M. Kim · S. Arana
CEIT and Tecnum, University of Navarra, Paseo de Manuel Lardizábal N 1520.018
Donostia, San Sebastián, Spain
e-mail: gmkim@ceit.es

S. Arana
e-mail: sarana@ceit.es

M. S. N. Oliveira
James Weir Fluids Lab, Department of Mechanical and Aerospace Engineering,
University of Strathclyde, Glasgow G1 1XJ, UK
e-mail: monica.oliveira@strath.ac.uk

V. Faustino · D. Pinho · R. Lima
CEFT, Faculdade de Engenharia da Universidade do Porto (FEUP),
R. Dr. Roberto Frias 4200-465 Porto, Portugal

R. C. Calhelha · I. C. F. R. Ferreira
CIMO-ESA, Polytechnic Institute of Bragança, C. Sta. Apolónia 5301-857,
Bragança, Portugal
e-mail: calhelha@ipb.pt

I. C. F. R. Ferreira
e-mail: iferreira@ipb.pt

degree of the deformation index (DI) of the flowing RBCs throughout the microchannel at its centerline. A suitable image analysis technique is used for semi-automatic measurements of average DIs, velocity and strain rate of the RBCs travelling in the regions of interest. The results reveal a strong deformation of RBCs under both extensional and shear stress dominated flow conditions.

1 Introduction

It is known that red blood cells (RBCs) at rest exhibit a biconcave disk shape 8 μm in diameter and 2 μm thick and comprise 40–50 % of whole blood volume (Caro et al. 1979; Lima et al. 2012). An RCB at rest has a shape close to a circle but when subjected to certain flow conditions it has also the ability to deform and consequently evolve to other shapes (Dobbe et al. 2002). For example, the RBCs change to an ellipsoidal shape when submitted to shear stress and elongate significantly to pass through the smallest capillaries of the microcirculation (3–7 μm) (Hardeman and Ince 1999, Dobbe et al. 2002). The RBC deformability plays a major role for oxygen delivery in the microcirculation and reduced RBC deformability is found to be linked to certain diseases such as diabetes and sickle cell anemia (Mokken et al. 1992; Hardeman and Ince 1999; Shin et al. 2007).

The clinical relevance of RBC deformability has been prompting the development of methods for measuring this phenomenon. Some examples are: the RBC filtration—a simple method that measures the ability of RBC to pass a filter by calculating the transit time required for the passage of a certain RBC (Gueguen et al. 1984); laser diffraction ellipsometry (ektacytometry)—based on laser diffraction analysis of RBCs under different stress levels (Mokken et al. 1992; Shin et al. 2004); rheoscopy—RBCs are deformed by simple shear flow and image analysis techniques allow a direct measurement of the RBC deformability (Dobbe et al. 2002); micropipette aspiration—RBCs are aspirated into glass capillaries with diameters of 1–5 μm and the RBC deformability is calculated by using the measured negative pressure needed to aspirate the RBC (Mokken et al. 1992).

The recent developments in microfabrication make it possible to fabricate transparent micrometer-sized channels, and as a result several studies have proposed microfluidic devices able to measure the motion and dynamical deformation of cells flowing through the microchannels (Abkarian et al. 2006; Shevkoplyas et al. 2006; Zhao et al. 2006, Abkarian et al. 2008; Fujiwara et al. 2009, Kang et al. 2008; Lima et al. 2009, Tomaiuolo et al. 2011; Leble et al. 2011). Most of the proposed biomedical microdevices focus on the effect of shear flow alone. Shear flow in this context results from the flow induced by shear stress caused by the velocity gradient that develops adjacent to the neighbouring walls of the microdevice (Fig. 1b). Some examples of shear flow studies from the literature are the measurement of the RBC cellular trajectories and deformation under a transient high shear stress in a narrow channel (Zhao et al. 2006) and the determination of

cell deformability through a single RBC flowing in a microfluidic device with a microchannel thickness comparable to RBC size (Tomaiuolo et al. 2011). Besides the effect of shear flow, extensional flow [in which stretching flow is generated as a consequence of a velocity gradient in the flow direction (Fig. 1b), and the combination of both can be encountered in the human body. Relevant examples include micro-stenosis, which can be generated at a retinal arteriole by foam cell formation due to low-density lipoprotein (LDL) migration (Kang et al. 2008); in microvascular networks composed of small irregular vessel segments; in prosthetic blood contacting devices, such as blood pumps and other medical instrumentation, e.g. syringes. Despite the importance of the study of RBC deformation under extensional flow, only a few studies have been reported in the literature. Hence, it is crucial not only to understand the motion and RBC mechanical properties under the effect of simple shear flow but also to quantify the influence of extensional flow and/or the combination of both on the RBCs deformation and orientation.

Flows through contractions generate complex flows despite their simple geometries. The flow of single phase Newtonian and non-Newtonian fluids through contractions is well studied both experimentally and numerically, both at the macro and micro-scale. The flow involves a reduction in the cross-sectional area, which generates strongly converging flows as the fluid goes through the contraction. With complex fluids, the flow has been shown to exhibit a variety of flow structures, such as Moffatt vortices, lip vortices, and corner vortices, that depend on the rheological characteristics of the fluid and the geometric configuration of the contraction, including its shape (Fig. 1a–c) and configuration

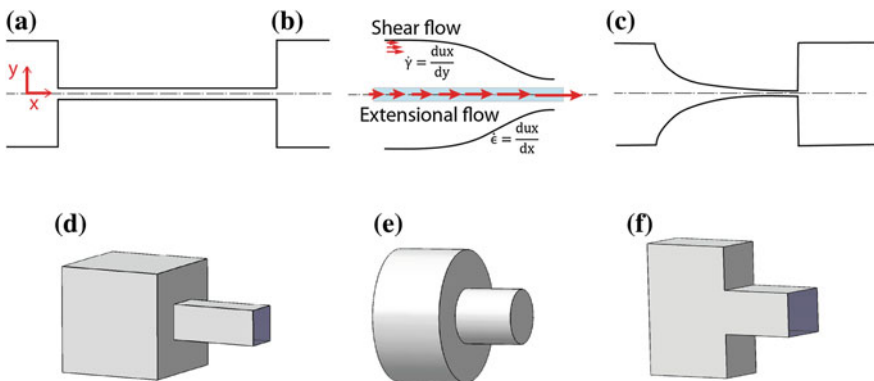
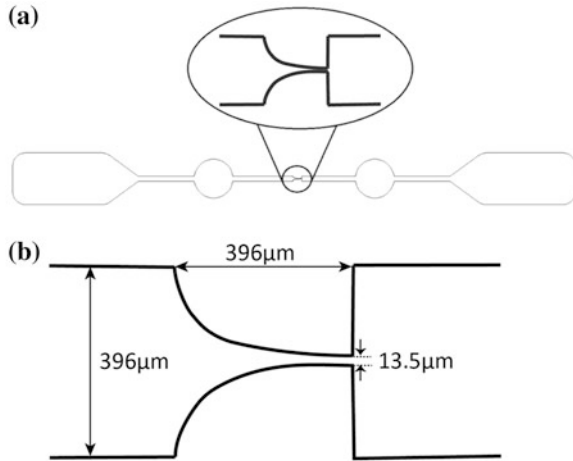


Fig. 1 Fluid flow in contractions with different shapes: **a** Sudden contraction **b** Smooth contraction **c** Hyperbolic contraction; and configurations: **d** Square–square, **e** Axisymmetric, **f** Planar 2D (if AR is high), planar 3D (if AR is moderate or low). The aspect ratio (AR) is defined as h/w where h refers to the depth and w refers to the width of the microchannel. An illustration of the velocity gradients expected in different regions dominated by shear and extensional flow is shown in panel **b**

Fig. 2 **a** Illustration of the entire microchannel view. **b** Schematic geometry and dimensions of the hyperbolic contraction region of the microchannel



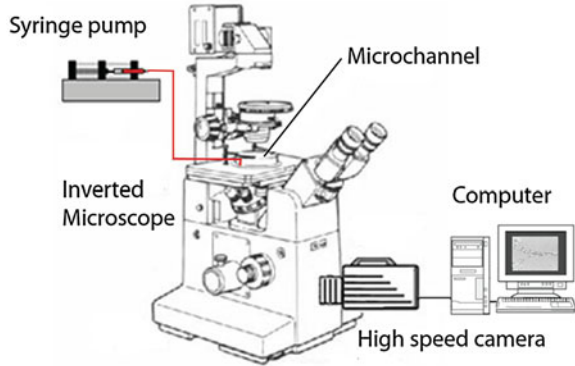
(Fig. 1d–f). The flow exhibits mixed kinematics with strong extensional flow along the centreline (stretching flow as the fluid accelerates as it is going through the contraction, Fig. 1c), and shear flow close to the walls (Fig. 1a).

Blood is an extremely complex fluid due to a suspension of different deformable cells of varying in size, such as red blood cells, white blood cells and platelets. Although the flow of single phase Newtonian and non-Newtonian fluids through contractions has been well studied, this is not the case for blood flow. Among the few are the microscopic studies performed by Zhao et al. (2006) and by Kang et al. (2008) where the authors investigated the mechanical behaviour of RBCs when they pass through sudden and smooth contraction, respectively. Others such as Lee et al. (2009), Yaginuma et al. (2011a, b, 2013) and Sousa et al. (2011) studied the effect of the extensional flow in a hyperbolic converging microchannel for animal blood, human blood and blood analogue fluids, respectively. In this study, we use a microchannel having a hyperbolic shape (cf. Fig. 2) with a very low aspect ratio ($AR = 0.035$) in which the RBCs experiences a strong extensional flow but in addition shear flow effects are not negligible due to the low AR of the microchannel geometry. The RBC deformation flowing throughout this microchannel is measured along the centerline and the degree of their deformability is presented by the deformation index (DI).

2 Materials and Methods

2.1 Working Fluids and Microchannel Geometry

The working fluid used in this study was hank's balanced salt solution (HBSS) containing 2 % Hct of Human RBCs. The blood was collected from a healthy adult

Fig. 3 Experimental set-up

volunteer, and ethylenediaminetetraacetic acid (EDTA) was added to prevent coagulation. The RBCs were separated from the plasma and buffy coat by centrifugation (1,000 rpm for 10 min). The RBCs were then washed and centrifuged with HBSS twice. Washed RBCs were diluted with HBSS to make several samples with hematocrit levels of $\sim 2\%$ by volume. All blood samples were stored hermetically at 4°C until the labelling.

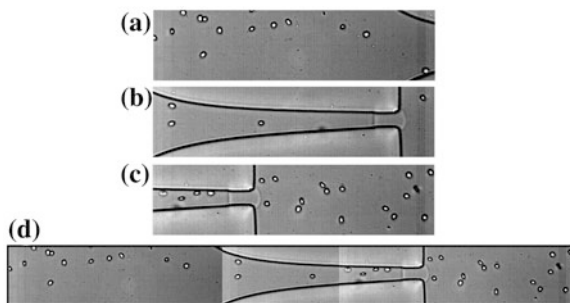
The confocal system used in the present study consists of an inverted microscope (Diaphot 300, Nikon) combined with a high-speed camera (FASTCAM SA3, Photron). By using a soft-lithography technique we were able to manufacture a polydimethylsiloxane (PDMS) microchannel having a hyperbolic shape. As described in Fig. 2, the dimensions of the microchannel are $396\ \mu\text{m}$ (w) \times $396\ \mu\text{m}$ (l) \times $14\ \mu\text{m}$ (h) where w , l and h refer to the width of the inlet microchannel, the length of the hyperbolic contraction region and the depth of the microchannel. From this, the aspect ratio $AR = h/w$ can be obtained as 0.035. The PDMS microchannel was placed on the stage of the microscope where the flow rate Q of the working fluids was kept constant ($0.5\ \mu\text{l}/\text{min}$) by means of a syringe pump (PHD ULTRA) with a 1 mL syringe (TERUMO[®] SYRING).

The images of the flowing RBCs were captured using the high speed camera at a frame rate of 7,500 frames/s and were then transferred to the computer to be analyzed. An illustration of the experimental set-up is shown in Fig. 3.

2.2 Image Analysis

High magnification was used to obtain better quality images so that the accuracy of RBC measurements is maximized during image analysis. As can be seen in Fig. 4a–c, the original data consists of three sets of video sequences focusing in different regions of the channel. These sets of images can be combined to obtain the required information the entire hyperbolic contraction region of the microchannel as shown in Fig. 4d.

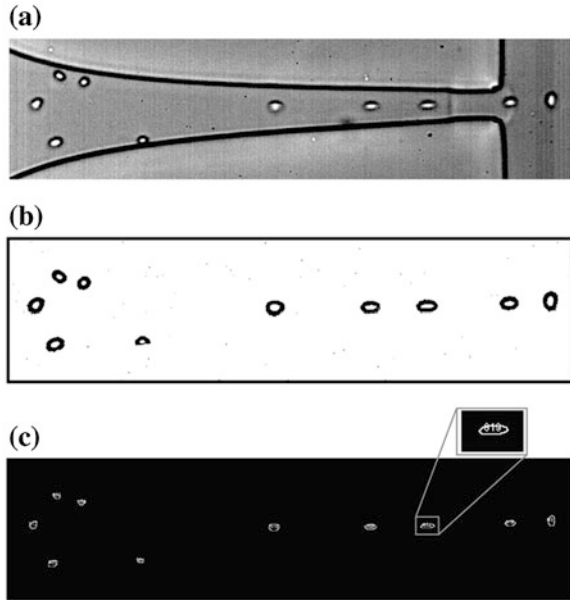
Fig. 4 Original video images (a), (b), and (c) focusing on different regions of the channel, and a combined image (d) that presents the centreline region ($y = 0$) at the hyperbolic microchannel



The following image handling was carried out. First, the captured video data was converted to JPEG image sequences. Each image has $1,024 \times 256$ pixels size and in total 4,072 frames were obtained for one video with a frame interval of $133 \mu\text{s}$. The sequences of static images (known as a stack) were processed using the image handling software ImageJ (Abramoff et al. 2004). For measuring flowing RBC particles, the following pre-processing was executed on the stack. First, an averaged image (background) was created from the original stack images by averaging each pixel over the sequence of static images, and then subtracted from the stack images. This process eliminates all the static objects, for example, the microchannel walls and other static artefacts, leaving only RBCs visible. Next, the images were filtered by replacing each pixel with the median of the neighbouring pixel values with a mask size of 3×3 pixels, in order to reduce the artefacts and enhance the image quality. Then the brightness and contrast of the resulting images were manually adjusted. Finally, the grey scale images were converted to binary images adjusting the threshold level. The well-known Otsu threshold method was used in this case (Otsu 1979). The final images contain regions of interest (RBCs) as black ellipsoidal objects against a white background. After this segmentation process, the flowing RBCs were measured frame by frame automatically by *Analyze Particles* function in ImageJ. This function counts and measures the objects in binary images, by detecting the edge of the objects and outlining them. Various parameters, such as area and circularity of the cells, were appropriately pre-set so that the values outside the range specified were ignored. For instance, we set the range of area as $17\text{--}150 \mu\text{m}^2$ such that the objects smaller than $17 \mu\text{m}^2$ and larger than $150 \mu\text{m}^2$ were eliminated from the results table. Likewise, the circularity range was set to be $0.5\text{--}1.0$. Here the circularity is defined as $4\pi \times (\text{area})/(\text{perimeter})^2$. This way, most of the apparent deviant objects (e.g. out-of-focus cells, aggregated cells, etc.) were ignored in the measurements. The most important steps of image handling described above are illustrated in Fig. 5.

The major output results of this measurement are the *major* (primary) and *minor* (secondary) axis lengths of the ellipse that can be best fitted to the RBCs and the $x - y$ coordinates of their centroid. Using this set of data, the deformation index (DI) of all the measured cells was calculated using Matlab and stored together with the cell positions (centroid) given by their $x - y$ coordinates. In this

Fig. 5 Steps of image analysis. **a** Original image, **b** Binary image, **c** A view of cells automatically measured by ImageJ function *Analyze Particles*



study, DI is defined by the formula shown in Fig. 6, where X and Y refer to the *major* and *minor* axis lengths of the cell, respectively. RBC deformability is the ability of the erythrocytes to deform when submitted to certain flow conditions in both in vivo and in vitro environments, and the deformation index can display the degree of their deformability with values between 0 and 1, where 0 indicates a perfect circle and higher values represent more elongated cells.

In addition to the DI measurement, the trajectories of several flowing RBCs at a flow rate of 0.5 $\mu\text{l}/\text{min}$ were measured manually using MTrackJ plug-in installed in ImageJ (Meijering et al. 2012). MTrackJ provides useful functions for tracking objects in motion. By placing the target RBC within the snap window, it computes automatically the centroid of the RBC based on Otsu threshold method. We manually follow the identified RBC frame by frame recording the centroid trajectory, and finally get the velocity of the RBC. By using real velocity of the RBCs the strain rate was also calculated.

3 Results and Discussion

3.1 Deformation Index (DI) of RBCs in Extensional Flow

In this work, the deformation of the RBCs travelling through the microchannel centerline ($y = 0$) region was observed. As stated in the previous section, the original data consists of three video sequences. Therefore, the DI values are the

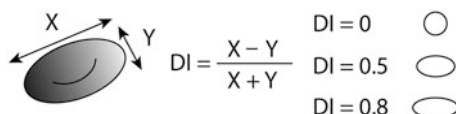


Fig. 6 Definition of deformation index. X and Y refer to the *major* and *minor* axis lengths of the cell. Note that the length of major axis (X) oriented to the flow direction considers the cell's travel length caused by the camera's exposure time

average of pre-defined regions of interest along the centreline at each image. Each region of interest is defined as $36\ \mu\text{m}$ long and $20\ \mu\text{m}$ high and located consecutively from far upstream to far downstream of the contraction part of the microchannel (see Fig. 7a). All the cells captured in each region were measured and the averaged DI was calculated. Fig. 7b presents average DI through the microchannel for an inlet flow rate of $0.5\ \mu\text{l}/\text{min}$. The horizontal axis corresponds to the microchannel x axis where $x = 0$ is set to be at the beginning of the hyperbolic curve and $x = 1$ is set to be at the end of the contraction region. It is possible to observe that the DI values at the centreline far upstream of the contraction are around 0.13 and fairly constant. After entering the contraction region, RBCs start elongating and their DI values start increasing. At the region right before the exit of contraction part ($x = 1$), the DI reaches the maximum value of 0.33 (see Figs. 7b, 8). Just downstream of the expansion plane DI drops dramatically and the

Fig. 7 Evaluation of the deformation of the flowing RBCs around the centerline of the hyperbolic microchannel. **a** Illustration of the regions of interest to analyze the RBCs deformation index (DI). Note that each region is $36\ \mu\text{m}$ long and $20\ \mu\text{m}$ high. **b** Average DI in each region throughout the microchannel at a flow rate of $0.5\ \mu\text{l}/\text{min}$

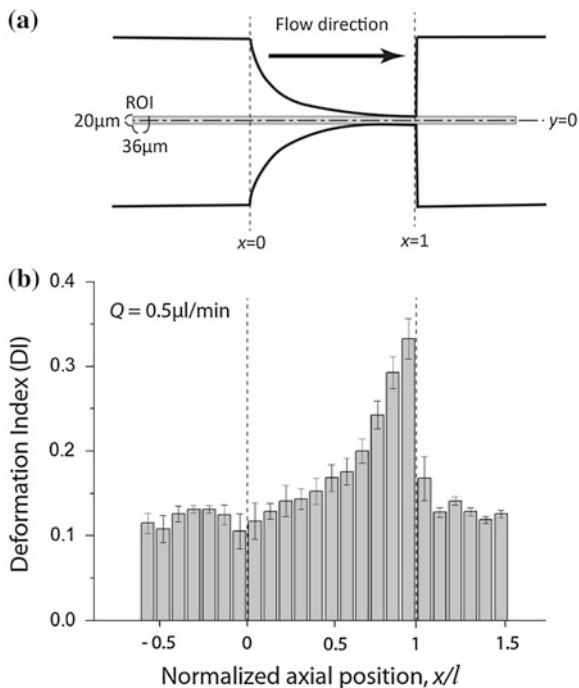
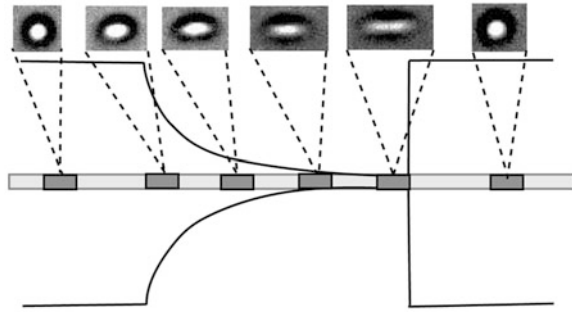


Fig. 8 Evolution of RBC deformation throughout the hyperbolic microchannel



RBCs start returning to their original shape. It can be seen that the DI value far downstream in this plane is almost the same as the one at the upstream of the channel.

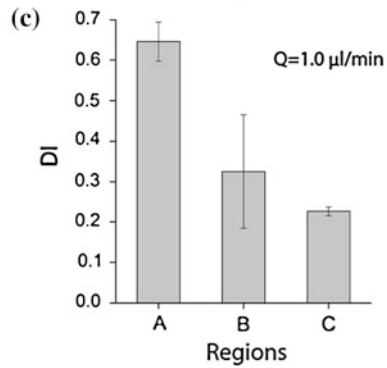
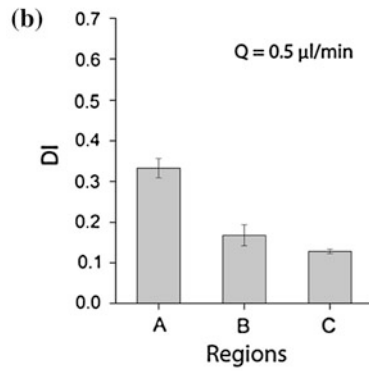
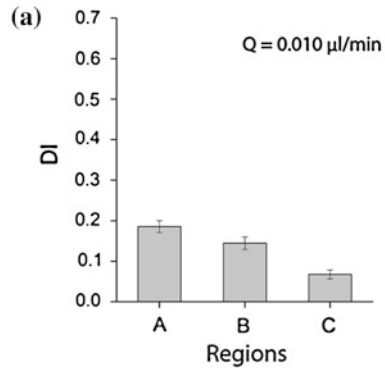
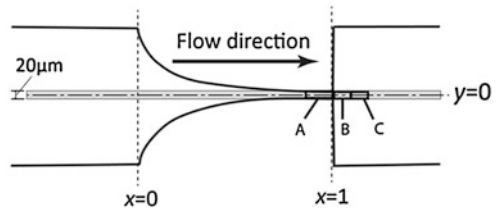
3.2 Flow Rate Effect on RBCs Deformation Index (DI)

Figure 9 shows the RBCs DI in the expansion region for three different flow rates, i. e., 0.010, 0.5 and 1.0 $\mu\text{l}/\text{min}$ in the same microchannel. Following the same measurement procedures used before, these results (see Fig. 9) shows that for all the flow rates studied the DI has a maximum value at the region right before the exit of the contraction. After that, the RBCs tend to recover their initial shape which corresponds to a minimal value of the DI attained when they are no longer exposed to extensional flow. Another additional result is that the RBCs have a tendency to increase the DI as the flow rate increases (Yaginuma et al. 2013). In contrast, in the work performed by Zhao et al. (2006), where shear flow dominates (see Fig. 1), the DI reaches a maximum value at a shear rate of $1,760 \text{ s}^{-1}$ and the cells could not deform any further, regardless the increase of the flow rate. These qualitative comparisons suggest that the flow rate strongly affects the response of RBCs when exposed to an extensional flow field. Nevertheless, to confirm it, further careful studies should be necessarily employed with higher flow rates and with different dimensions of the microchannels.

3.3 Axial Velocity and Strain Rate

To measure the actual RBC velocity, the cells traveling along the centerline of the microchannel were manually tracked using ImageJ plug-in, MTrackJ. Along with the velocity for each tracking point, the strain rate was also calculated from $d\nu/dx$, where $d\nu$ refers to differential cell velocity and dx refers to the distance between two tracking points.

Fig. 9 DI recovery in the expansion region for different flow rates: **a** $Q = 0.010 \mu\text{l}/\text{min}$, **b** $Q = 0.5 \mu\text{l}/\text{min}$, **c** $Q = 1.0 \mu\text{l}/\text{min}$



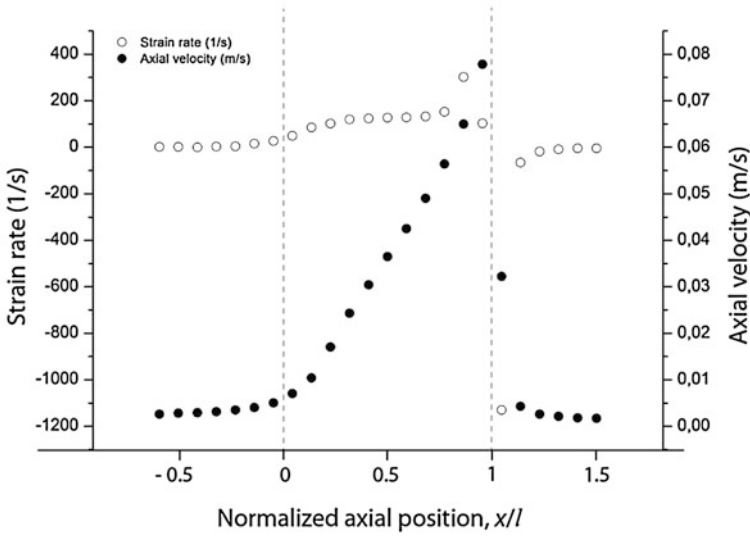


Fig. 10 Average axial velocity at the centreline and corresponding strain rate for RBCs flowing at the flow rate of 0.5 $\mu\text{l}/\text{min}$

Figure 10 shows the average cell velocity and average strain rate for every 36 μm axial region throughout the central region of the microchannel at a flow rate of 0.5 $\mu\text{l}/\text{min}$. The velocity of the cells far upstream is initially constant and then starts slightly increasing when the cells approach the entrance of the hyperbolic region. After the entrance ($x = 0$), the velocity increases almost linearly, corresponding to a constant strain-rate, and reaches the maximum value at the end part of the contraction region. After the cells are released from the contraction region, their velocity decreases and eventually recovers the upstream velocity value. The fact that we are able to obtain a wide region of constant strain-rate confirms the potential of hyperbolic channels for generating a controlled and strong homogeneous extensional flow field.

4 Conclusions and Future Directions

The current study evaluated the RBC deformability in the relatively low aspect ratio hyperbolic contraction microchannel, where the RBCs experience a strong extensional and shear flow. The results show that when the RBCs enter the hyperbolic contraction region they tend to elongate up to a maximum value indicating their high deformability in a strong extensional flow. For a flow rate of 0.5 $\mu\text{l}/\text{min}$ RBC deformation index increases from about 0.12 to 0.33 with a maximum strain rate up to 320 s^{-1} . Qualitative comparison between DIs of sudden

contraction and hyperbolic contraction microchannels indicated that for latter case the flow rate strongly affects the response of RBCs under extensional flow induced deformation. These results support the use of hyperbolic converging microchannels as a new promising approach for RBC deformability assessment for clinical applications. We recognize that the working fluid used in the current study (HBSS with 2 % Hct of human blood) is not close to in vivo environment. However, our purpose is to develop an alternative diagnostic microfluidic system. Therefore, it is important to notice these differences might affect the RBC deformability but the efficiency of deformability measurements have to be considered. For example, low Hct is necessary for better image analysis results. HBSS (physiological saline) is used as it is closer to plasma than the other possible solutions such as Dextran 40.

Acknowledgments The authors acknowledge the financial support provided by: International Doctoral Program in Engineering, from the Ministry of Education, Culture, Sports, Science and Technology of Japan (MEXT), 2007 Global COE Program “Global Nano-Biomedical Engineering Education and Research Network”, Japan. Grant-in-Aid for Science and Technology (PTDC/SAU-BEB/108728/2008, PTDC/SAU-BEB/105650/2008 and PTDC/EME-MFE/099109/2008) from the Science and Technology Foundation (FCT), FEDER and COMPETE, Portugal.

References

- Abkarian M, Faivre M, Stone H (2006) High-speed microfluidic differential manometer for cellular-scale hydrodynamics. *PNAS* 103(3):538–542
- Abkarian M, Faivre M, Horton R, Smistrup K, Best-Popescu CA, Stone HA (2008) Cellular-scale hydrodynamics. *Biomed Mater* 3:034011
- Abramoff MD, Magalhães PJ, Ram SJ (2004) Image processing with ImageJ. *Biophotonics Int* 11:36–42
- Caro C, Pedley T, Schroter R, Seed W (1979) *The mechanics of the circulation*. Oxford University Press, Oxford
- Dobbe JGG, Hardeman MR, Streekstra GJ, Strackee J, Ince C, Grimbergen CA (2002) Analyzing red blood cell-deformability distributions. *Blood Cells Mol Dis* 28:373–384
- Fujiwara H, Ishikawa T, Lima R, Matsuki N, Imai Y, Kaji H, Nishizawa M, Yamaguchi T (2009) Red blood cell motions in a high hematocrit blood flowing through a stenosed micro-channel. *J Biomech* 42:838–843
- Gueguen M, Bidet JM, Durand F, Driss F, Joffre A, Genetet B (1984) Filtration pressure and red blood cell de-formability: evaluation of a new device: erythrometre. *Bio-rheol Suppl* 1:261–265
- Hardeman MR, Ince C (1999) Clinical potential of in vitro measured red cell deformability, a myth? *Clin Hemorheol Microcirc* 21:277–284
- Kang M, Ji HS, Kim KC (2008) An in-vitro investigation of RBCs flow characteristics and hemodynamic feature through a microchannel with a micro-stenosis. *Int J Biol Biomed Eng* 1(2):1–8
- Leble V, Lima R, Dias R, Fernandes C, Ishikawa T, Imai Y, Yamaguchi T (2011) Asymmetry of red blood cell motions in a microchannel with a diverging and converging bifurcation. *Biomicrofluidics* 5:044120
- Lee SS, Yim Y, Ahn KH, Lee SJ (2009) Extensional flow-based assessment of red blood cell deformability using hyperbolic converging microchannel. *Biomed Microdevices* 11:1021–1027

- Lima R, Oliveira MSN, Ishikawa T, Kaji H, Tanaka S, Nishizawa M, Yamaguchi T (2009) Axisymmetric PDMS microchannels for in vitro haemodynamics studies. *Biofabrication* 1(3):035005
- Lima R, Ishikawa T, Imai Y, Yamaguchi T (2012) Blood flow behavior in microchannels: past, current and future trends. In: Dias R, Martins AA, Lima R et al (eds) *Single and two-phase flows on chemical and biomedical engineering*. Bentham, Oak Park, pp 513–554
- Meijering E, Dzyubachyk O, Smal I (2012) Methods for Cell and Particle Tracking. *Methods Enzymol* 504:183–200
- Mokken FC, Kedaria M, Henny CP, Hardeman MR, Gelb AW (1992) The clinical importance of erythrocyte deformability, a hemorheological parameter. *Ann Hematol* 64:113–122
- Otsu N (1979) A threshold selection method from gray-level histograms. *IEEE Trans Sys Man Cyber* 9(1):62–66
- Shevkopyas SS, Yoshida T, Gifford SC, Bitensky MW (2006) Direct measurement of the impact of impaired erythrocyte deformability on microvascular network perfusion in a microfluidic device. *Lab Chip* 6(7):914–920
- Shin S, Ku Y, Park MS, Suh JS (2004) Measurement of red cell deformability and whole blood viscosity using laser-diffraction slit rheometer. *Korea-Australia Rheol J* 16:85–90
- Shin S, Ku Y, Ho J, Kim Y, Suh J, Singh M (2007) Progressive impairment of erythrocyte deformability as indicator of microangiopathy in type 2 diabetes mellitus. *Clin Hemorheol Micro* 36:253–261
- Sousa PC, Pinho FT, Oliveira MSN, Alves M (2011) Extensional flow of blood analog solutions in microfluidic devices. *Biomicrofluidics* 5:014108
- Tomaiuolo G, Barra M, Preziosi V, Cassinese A, Rotoli B, Guido S (2011) Microfluidics analysis of red blood cell membrane viscoelasticity. *Lab Chip* 11:449–454
- Yaginuma T, Lima R, Oliveira MSN, Ishikawa T, Yamaguchi T (2011a) Flow of red blood cells through a microfluidic extensional device: an image analysis assessment. In: *Proceedings of the III ECCOMAS thematic conference on computational vision and medical image processing: VipIMAGE*, pp 217–220
- Yaginuma T, Oliveira MSN, Lima R, Ishikawa T, Yamaguchi T (2011b) Red blood cell deformation in flows through a PDMS hyperbolic microchannel. *Proc NSTI-Nanotech* 2:505–507
- Yaginuma T, Oliveira MSN, Lima R, Ishikawa T, Yamaguchi T (2013). Human red blood cell behavior under homogeneous extensional flow in a hyperbolic-shaped microchannel. *Biomicrofluidics* 7:054110
- Zhao R, Antaki JF, Naik T, Bachman TN, Kameneva MV, Wu ZJ (2006) Microscopic investigation of erythrocyte deformation dynamics. *Biorheology* 43(6):747–765

Responses of Living Cells to Hydrodynamic Stimuli Due to Fluid Flow

Naoya Sakamoto

Abstract Cells, the basic units of our body, are constantly exposed to fluid-dynamic stimuli. Typical examples are the epithelial cells of tubular organs, including blood and lymphatic vessels and renal tubes, which are in direct contact with flowing fluid. In addition, other cell types such as smooth muscle cells, fibroblasts, articular chondrocytes, and bone cells are subjected to interstitial fluid flow, which is the movement of fluid through the extracellular matrix of tissues elicited by differences in hydrostatic pressure and deformation of tissues. Fluid-dynamic stimuli can modulate cell alignment, proliferation, differentiation, migration, and cytokine secretion. These morphological and functional responses of cells play important roles not only in the maintenance of physiological functions of tissues but also in the development and progression of disease. Many attempts have been made to understand the effect of fluid-dynamic stimuli on cells. This chapter summarizes cellular responses induced by such stimuli, mainly focusing on the effect of shear stress on vascular cells, which have been extensively investigated in vitro over the last three decades. In addition, the possible mechanisms by which cells sense shear stress are also introduced briefly.

1 Introduction

The most abundant molecular compounds in the human body are fluids, including blood, lymph, and urine. The total amount of water in a human is approximately 60 % of the body weight; extracellular and intracellular water comprises 26 and 34 % of the body weight, respectively (Wang et al. 1992). Flow of these fluids in the body results from pressure created by organs and differences in pressure due to

N. Sakamoto (✉)

Department of Medical Engineering, Kawasaki University of Medical Welfare, 288
Matsushima, Kurashiki, Okayama 701-0193, Japan
e-mail: sakan@me.kawasaki-m.ac.jp

body movements. Fluid flow is known to play important roles in homeostasis of the living body by inducing morphological and functional changes in cells, which are the basic components of tissues.

In addition to experimental and computational analyses of the hydrodynamic conditions in the body, numerous attempts have been made to understand how the living body responds to fluid flow, its importance in maintaining healthy physiological function, and its role in disease development. It is difficult to control hydrodynamic conditions and reproducibility in *in vivo* studies with animal models. Therefore, extensive research has focused on investigating the responses of cultured cells isolated from the living body to hydrodynamic stimuli under well-defined conditions. This chapter introduces cellular responses to fluid flow stimuli, mainly focusing on the relationship between shear stress due to flow, and cultured cell responses. The mechanisms by which cells sense flow stimuli have also been discussed briefly.

2 Responses of Epithelial Cells to Flow

In general, the lumens of organs, particularly tubular organs such as blood vessels, bronchial tubes, and renal tubules, are covered with epithelium composed of a layer of epithelial cells. Epithelial cells are in direct contact with fluid flowing through the tubular organs and are subjected to hydrodynamic stimuli due to fluid flow (Fig. 1). Vascular endothelial cells (ECs) are the most well-known and well-studied epithelial cells, although other types of epithelial cells have recently received attention.

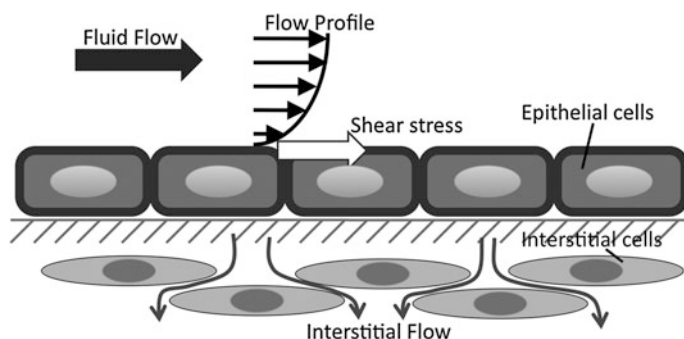


Fig. 1 Schematic illustration of hydrodynamic conditions of epithelial and interstitial cells. Epithelial cells directly come in contact with fluid flowing in organs. Interstitial cells embedded in the extracellular matrix also experience flow through the tissues (interstitial flow)

2.1 *Vascular ECs*

Although the ECs lining the intima of the blood vessels have been traditionally considered as a simple static barrier between tissues and blood, they are now recognized as key regulators for not only vessel functions including regulation of vascular tone, provision of an antithrombotic interface of blood, transport of nutrients to tissue, angiogenesis, and vasculogenesis but also formation and development of vascular diseases such as atherosclerosis and aneurysms. Hydrodynamic stimuli generated by blood flow, especially shear stress, play crucial roles in the morphology and functions of ECs.

Since animal model studies have revealed correlations between patterns of blood flow and morphology of ECs in atherosclerosis-prone sites of vessels, EC responses to blood flow have become the focus of many researchers. Atherosclerotic lesions do not occur randomly in the arterial vasculature but tend to be localized to curvature sites and bifurcations. Hydrodynamic stimuli resulting from the complex blood flow that atherosclerosis-prone sites may experience, such as turbulent flow (Wesolowski et al. 1965), high shear (Fry 1968), low shear (Caro et al. 1978), and oscillatory flow (Ku et al. 1985), have been thought to be implicated in the pathogenesis of atherosclerosis.

Flaherty et al. (1972) studied the relationship between the orientation of EC nuclei and the blood flow pattern in the canine artery. In straight vessel regions, *e.g.*, the middle and lower descending thoracic aorta through which flow seems to be stable, the nuclei were elongated and oriented parallel to the longitudinal axis of the blood vessels. However, in the ascending aorta, a less ordered arrangement of nuclei orientation and elongation was observed. Nerem et al. (1981) conducted a quantitative study of EC size and shape using a vascular cast of rabbit aorta and suggested that EC morphology is an indicator of the detailed feature of blood flow. Based on these results, morphological and functional responses of ECs to blood flow stimuli have been thought to correlate with atherogenesis. ECs are now one of the most well-studied cell types, and research conducted over the past three decades has revealed that responses by ECs are crucial not only to the pathogenesis of atherosclerosis but also to vascular homeostasis and other types of vascular diseases.

2.1.1 Morphological and Mechanical Responses of ECs to Laminar Flow

ECs are known to exhibit elongated shapes and orient in the direction of flow applied. To the best of the author's knowledge, such morphological responses by ECs were first reported by *in vivo* experiments performed by Flaherty et al. (1972). In these studies, a segment of canine thoracic aorta was excised, opened longitudinally, and re-implanted so as to expose the segments to blood flow perpendicular to the original flow direction. Examination of the nuclei orientation in ECs

lining the lumen of the segment revealed that the nuclear pattern realigned in the direction of flow. Since then, detailed morphological responses of ECs have been examined by *in vitro* experiments performed under well-defined flow conditions. Dewey et al. (1981) demonstrated that bovine ECs showed elongation and orientation in the direction of flow after exposure to unidirectional steady flow; however, they adopted a polygonal shape under static culture conditions. Levesque and Nerem (1985) reported that elongation and orientation of bovine ECs in the flow direction were dependent on the flow exposure time and magnitude of shear stress. These results indicated that ECs sensed the direction and magnitude of shear stress exerted on them.

Concomitant with morphological changes, the surface topography, intracellular structure, and mechanical properties of ECs can also change. A study using atomic force microscopy revealed that in ECs aligned in the flow direction by exposure to shear stress, height differences between the nucleus and intercellular junctions decreased compared with statistically cultured cells (Barbee et al. 1994). Computational analysis revealed that the spatial gradient of shear stress on the cell surface was significantly reduced by the topographic changes in ECs. With regard to intracellular structures, the nuclei of ECs align in the direction of flow when cells are exposed to chronic shear stress (Flaherty et al. 1972), and the microtubule organizing center (MTOC), associated with the determination of cell polarity, orients to a position on the downstream side of the nucleus relative to the direction of flow (Tzima et al. 2003). Actin filaments, one of the major components of the cytoskeleton, exhibit dynamic structural remodeling in response to shear stress. In ECs under static conditions, actin filaments are generally located at cell peripheries, referred to as dense peripheral bands, whereas the application of shear stress induces reorganization of the actin structure to create thick actin bundles and stress fibers aligned in the direction of flow (Kataoka et al. 1998; Sakamoto et al. 2010b) (Fig. 2). Actin filaments are known to play crucial roles in the determination of cell shape and mechanical properties. Indeed, after exposure to shear stress, both whole and local mechanical stiffness of ECs increase compared that of cells maintained under static conditions. This is thought to correspond to reorganization of the actin cytoskeletal structure (Sato et al. 1987; Sato et al. 2000). In addition, mechanical stiffness of the nucleus is greater in ECs exposed to shear stress than in control cells, suggesting that the nucleus *per se* remodels in response to shear stress (Deguchi et al. 2005).

2.1.2 Functional Responses of ECs to Laminar Flow

In addition to morphological responses, ECs show many flow-induced functional changes associated with vascular biology and pathology. ECs line the entire inner surface of the body's blood vessels and serve as a semiselective barrier regulating the transport of fluid and macromolecules between the blood and interstitial tissues (referred to as permeability). The effect of fluid shear stress on cultured EC permeability was studied by Jo et al. (1991). The permeability of bovine ECs

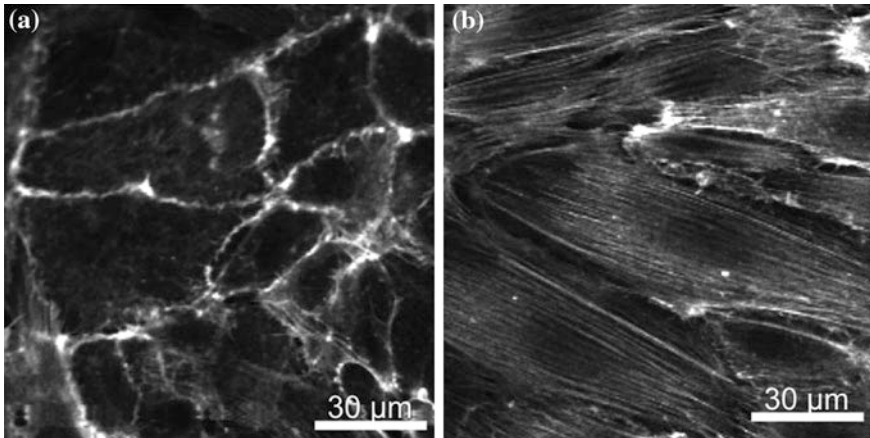


Fig. 2 Typical fluorescence images of actin filaments in vascular endothelial cells under static conditions **a** and after exposure to fluid shear stress **b** (2 Pa, 24 h). The direction of flow is *left to right*

increased during exposure to shear stress and returned to the preshear level after withdrawal of the shear stress, indicating that EC permeability *in vitro* is acutely sensitive to shear stress. When part of the EC monolayer is denuded, ECs from intact areas of the monolayer migrate into the denuded region, proliferate, and eventually repair the injury to maintain the barrier function (wound closure). Vyalov et al. (1996) examined the effect of shear conditions on wound closure in the rabbit common carotid artery *in vivo* and revealed that in response to a decrease in blood flow rates and shear stresses, the cells at the wound edge spread lesser than those in normal vessels 12 h after wounding. The cells were randomly oriented and polygonal in shape, indicating that low shear stress reduces the migration of ECs into wounds. Furthermore, in cell culture experiments, physiological levels of shear stress enhanced wound closure by stimulating the spread and migration of ECs (Albuquerque et al. 2000). On the other hand, proliferation of ECs was decreased by physiological shear stress (Levesque et al. 1990) but stimulated by lower levels of shear stress (Ando et al. 1987).

ECs express leukocyte adhesion molecules, which play important roles in the invasion of leukocytes into vessel walls at sites of inflammation and atherosclerotic lesions. Nagel et al. (1994) studied the effect of shear stress on the expression of leukocyte adhesion molecules in ECs. Expression of intercellular adhesion molecule-1 (ICAM-1) was increased by shear stress, while expression of E-selectin and vascular adhesion molecule-1 (VCAM-1) was not affected. This result is consistent with the suggestion that selective upregulation of leukocyte adhesion molecules by shear stress may play an important role in the generation of atherosclerosis.

It is well known that ECs produce a wide variety of biologically active substances, which act on ECs themselves and neighboring cells such as smooth

muscle cells (SMCs) and fibroblasts. Production of substances by ECs is also affected by shear stress. For example, ECs secrete nitric oxide (NO), which is known to be a multifunctional effector molecule that plays a central role in the regulation of vascular homeostasis, including vasodilatation, by inhibiting SMC constriction. Exposure to shear stress increases NO release by ECs in a biphasic manner, with an initial rapid production consequent to the onset of flow followed by a sustained production. The release of NO and expression of the associated synthase mRNA, *i.e.*, endothelial NO synthase (eNOS), are dependent on physiological levels of shear stress and show dose-dependent induction (Kuchan and Frangos 1993; Malek et al. 1999; Uematsu et al. 1995). In contrast, ECs also release a vasoconstrictor protein, endothelin-1 (ET-1), and shear stress regulates its release in an inverse manner; sustained exposure to lower levels of shear stress results in stimulation of ET-1 release and higher shear stress downregulates ET-1 release by ECs (Kuchan and Frangos 1993; Morawietz et al. 2000).

2.1.3 Response of ECs to Flow Stimuli with Spatiotemporal Changes

Many of the EC responses to shear stress, including those described above, have been evident after exposure to steady shear stress, which could be considered a simplified condition for investigating a “pure” effect of shear stress magnitude. Because blood flow in the vasculature *in vivo* is pulsatile rather than steady under normal physiological conditions, the effects of additional parameters of flow pulsation, including frequency, pulse amplitude, and mean magnitude of shear stress, on ECs have also been studied. ECs exhibit elongated shapes under sinusoidal flow conditions when the mean shear stress is not equal to zero; however, the changes are less rapid compared with those observed under steady flow conditions. Furthermore, ECs retain their polygonal shape as observed in static culture and do not exhibit actin stress fibers when they are exposed to oscillatory flow with a mean shear stress equal to zero (Helmlinger et al. 1991). The effect of pulsatile flow on the syntheses of vascular tone regulators by ECs has also been investigated extensively. Although it was reported that pulsatile shear stress of equal time-average magnitude elicited the same decrease in ET-1 mRNA as steady laminar shear (Malek and Izumo, 1992), production of the vasodilator prostacyclin by ECs subjected to pulsatile shear stress was more than twice that by cells exposed to steady shear stress and 16 times greater than that by cells in static culture (Frangos et al. 1985). Production of prostacyclin and NO are sensitive to flow frequency, and NOS activity and prostacyclin production in ECs reach maximum levels at 1 Hz, which corresponds to the physiological value of heart rate (Balcells et al. 2005). In addition to vasodilators, pulsatile shear stress induces different responses in ECs compared with steady shear (Brooks et al. 2002), including EC proliferation (Balcells et al. 2005), activation of the transcription factor NF- κ B (Mohan et al. 1997), and expression of VCAM-1 (Himburg et al. 2007). Studies aimed at the endothelialization of artificial and tissue-engineered organs to understand the detailed responses of ECs *in vivo* focused extensively on the responses of ECs to

temporal changes in shear stress (Jimenez-Vergara et al. 2010; Lichtenberg et al. 2006; Mall et al. 2004).

Spatial changes in the magnitude of shear stress have recently been recognized as a regulator of EC morphology and functions. As mentioned above, ECs exposed to uniform shear stress elongate and align in the direction of flow. In contrast, in studies using a T-shaped flow chamber created to produce spatial variations in the magnitude of shear stress (spatial shear stress gradient; SSG), ECs did not elongate or orient in the flow direction (Sakamoto et al. 2010a; Szymanski et al. 2008). In experiments using a step-flow chamber, which has a sudden-expansion step in the flow channel and can elicit disturbed flow producing SSG, activities of the transcription factors NF- κ B, Egr-1, c-Jun, and c-Fos in ECs were higher than those in cells maintained under uniform shear stress (Nagel et al. 1999). LaMack and Friedman (2007) applied SSG to ECs using a converging width flow chamber and used real-time quantitative PCR analysis to reveal that expression of eNOS is positively dependent on the magnitude of shear stress but not insensitive to SSG and that the expression of c-jun and monocyte chemoattractant protein-1 (MCP-1) is affected by the magnitude and gradient of shear stress. Dolan et al. (2011) examined the effect of positive and negative SSG on ECs using a chamber with a converging and diverging height channel and reported that positive SSG stimulates proliferation and apoptosis of ECs, whereas negative SSG suppresses these activities. The shear stress gradient is believed to be a hemodynamic factor underlying the development of atherosclerosis and intracranial aneurysms (Farmakis et al. 2004; Kolega et al. 2011; Meng et al. 2007; Metaxa et al. 2010).

2.1.4 Roles of EC Responses to Flow in Peripheral Cells in Vessel Walls

Bioactive substances secreted by ECs in response to flow conditions diffuse through the vessel walls and can indirectly transmit information of hemodynamic conditions to peripheral cells such as SMCs and fibroblasts, thereby inducing functional changes in such cells. In other words, ECs act as an interface between blood flow and peripheral cells that are not in contact with blood. In animal model experiments, changes in arterial diameter and wall thickness are induced by alteration of the blood flow rate and the resulting change in shear stress magnitude acting on ECs. These do not occur when the artery is denuded of endothelium (Langille et al. 1989; Langille and O'Donnell 1986). Because many factors are involved in the relationship between ECs and peripheral cells in vivo, the effect of shear stress has been investigated in detail using in vitro experiments.

Shear stress applied to ECs co-cultured with SMCs induced G-protein (GTP-binding protein) activation in unsheared SMCs, which triggered a number of signal transduction cascades (Redmond et al. 1998). When ECs are exposed to physiological levels of shear stress, they suppress the migration of underlying SMCs (Sakamoto et al. 2006; Wang et al. 2006). It was revealed that NO secreted from ECs under shearing conditions caused migration of co-cultured SMCs (Sakamoto

et al. 2006). Chiu et al. (2004) have developed a system for using PET transwell-based EC/SMC co-cultures under shear conditions. They found that when the EC surface of the co-culture was exposed to shear stress, the ECs oriented parallel to the flow, whereas SMCs oriented perpendicular to the flow. Exposure of ECs co-cultured with SMCs to shear stress modulated the SMC phenotype from a synthetic to a contractile state, with upregulation of contractile markers including alpha-smooth muscle actin (α -SMA) and smooth muscle-myosin heavy chain (SM-HMC), downregulation of proinflammatory genes, and decrease in the percentage of cells in the synthetic phase (Li et al. 2009; Tsai et al. 2009). These changes in SMC behavior were induced by prostacyclin released from ECs under shear stress (Tsai et al. 2009). Increased expression of contractile proteins in SMCs gradually decreased under static cultivation in the presence or absence of co-cultured ECs; however, physiological shear stress applied to ECs can maintain the expression levels of contractile proteins in co-cultured SMCs (Sakamoto et al. 2011). Although this section introduces the roles of ECs in SMC behaviors and functions under flow conditions, the interaction between ECs and SMCs is bidirectional. Studies have demonstrated that EC functions are affected by co-culture with SMCs (Cao et al. 2011; Chiu et al. 2005; Wang et al. 2010).

2.2 Responses of Other Types of Epithelial Cells to Flow

The epithelium of the renal system has been investigated as another example of epithelial cells in tubular organs, which respond to hydrodynamic stimuli. In the 1960s, Schnermann et al. (1968) demonstrated that fluid reabsorption by rat proximal tubules is nearly proportional to variations in glomerular filtration rates. This was termed the “Glomerulo-Tubular Balance”. This study indicated that mechanical forces due to fluid flow are sensed by renal epithelial cells, which are key regulators of the renal system. Detailed responses of renal epithelial cells have been demonstrated by in vitro studies showing that shear stress modulates fibrinolytic activity of proximal cells (Essig et al. 2001b) and production of NO and prostaglandin E2 in the collecting duct cells (Cai et al. 2000; Flores et al. 2012). Shear stress response elements, which modulate gene expression in ECs, are also active in renal epithelial cells. Rotating wall culture of renal cells changes expression of selected gene products, including the giant glycoprotein scavenger receptors and the classic shear stress response genes ICAM, VCAM, and MnSOD (Kaysen et al. 1999). Cytoskeletal reorganization induced by shear stress has also been reported using proximal tubular epithelial cells. Under static conditions, actin stress fibers are observed on the basal membrane of proximal tubule epithelial cells; however, shear stress induces the disappearance of actin stress fibers and formation of a lateral actin network at cell–cell junctions (Duan et al. 2008; Essig et al. 2001a). Interestingly, although the magnitude of shear stress required for induction of actin cytoskeletal reorganization is approximately 10-fold higher

than that for ECs, these cytoskeletal responses are nearly opposite to that of ECs exposed to shear stress as stated above.

Several studies have demonstrated that corneal epithelial cells, although not epithelia of tubular organs, are exposed to shear stress during lid blinking. Karuri et al. (2004) showed that corneal epithelial cells are elongated and align in the direction of flow after exposure to higher levels of shear stress. Ren and Wilson (1997) reported that although they did not quantify the extent, shear stress applied to corneal epithelial cells significantly increased the cell shedding rate from the corneal surface, suggesting that shear stress due to blinking may play a role in the induction of apoptosis.

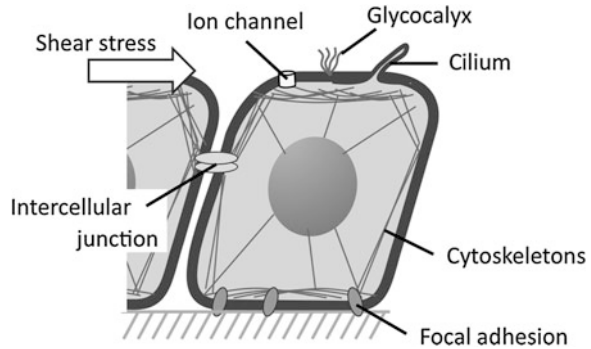
3 Responses of Interstitial Cells to Flow

Unlike epithelial cells, interstitial cells such as medial SMCs and adventitial fibroblasts of blood vessels are not in direct contact with flowing fluid. However, they are exposed to fluid movement through the extracellular matrix of tissues (interstitial flow) elicited by differences in hydrostatic pressure and deformation of tissues and can sense and respond to flow stimuli (refer to Fig. 1). For example, it has been estimated that vascular SMCs could be exposed to a maximum interstitial shear stress of 0.1 Pa (Tada and Tarbell; 2000, 2001, 2002) and that this level of shear stress leads to increase in the production of prostaglandins PGE2 and PGI2 (Alshihabi et al. 1996). Shear stress also induces NO production via inducible NOS (Gosgnach et al. 2000) and growth factor release (Rhoads et al. 2000; Sterpetti et al. 1993). SMCs exhibit different morphological responses to shear stress compared to ECs. Lee et al. (2002) reported that application of shear stress of 2 Pa for 48 h causes perpendicular orientation of SMCs in the direction of flow and that cell orientations are dependent on the magnitude of shear stress and the exposure time. Rice et al. (2010) showed that after exposure to shear stress of less than 1 Pa for 24 h, SMCs align at approximately 45° relative to the direction of flow. The effects of shear stress due to interstitial flow have also been demonstrated on other cell types. Interstitial flow modulates phenotypes and cell alignment in fibroblasts (Ng et al. 2005; Ng and Swartz, 2003), production of NO and PGE2 in bone cells (Ajubi et al. 1996; Johnson et al. 1996), and cell metabolic activity and collagen synthesis in articular chondrocytes (Chen et al. 2012; Raimondi et al. 2008).

4 Flow Sensing Mechanisms in Cells

This section introduces candidate sensor molecules (mechanosensors) expressed on or in cells for shear stress detection and a better understanding of cellular responses to flow (Fig. 3).

Fig. 3 Schematic illustration of mechanosensors for shear stress expressed on or in cells



External forces applied to the apical membranes of epithelial cells may directly act on molecules expressed on the cytoplasmic membrane. Some of these molecules might be mechanosensors. Ion channels are well-known mechano-sensitive molecules. Shear stress has been shown to increase Ca^{2+} influx in ECs mediated by P2X4 ATP-driven Ca^{2+} ion channels within 1 min of shear stress application (Ando et al. 1993; Yamamoto et al. 2000; Yamamoto et al. 2006), indicating that the P2X4 ion channel functions as a mechanosensor. Membrane G-proteins serve as molecular switches, which change the activity of GTP, and are known to be activated by G-protein-coupled receptors (GPCR). It was demonstrated that conformational changes in GPCR and G-protein activation are induced by exposure to shear stress within 1 s (Chachisvilis et al. 2006; Gudi et al. 1996). These results raise the possibility that G-proteins also act as shear stress sensors.

Focal adhesions are protein complexes through which the cytoskeleton connects to the extracellular matrix. Focal adhesions consist of integrin, a receptor mediating cell attachment to the extracellular matrix, and focal adhesion-associated proteins. Shear stress induces activation and clustering of intergrins (Chen et al. 1999; Wang et al. 2002), phosphorylation of associated proteins (Zaidel-Bar et al. 2005a), and activation of signaling cascades mediated by focal adhesion proteins (Shikata et al. 2005). Since focal adhesions serve as a mechanical linkage between the extracellular matrix and cytoskeleton and shear stress does not directly act on focal adhesions, the latter are thought to be stimulated by forces transmitted through the cytoskeleton from the apical surface on which shear stress is exerted.

Cells generally form adhesions with neighboring cells, which are termed intercellular junctions. Several types of transmembrane proteins form molecular complexes and mediate adhesions between cells (Dejana 2004). One of these, the cadherin complex, is thought to function as a mechanosensor. Cadherin complexes contain molecules such as α -catenin (Lecuit 2010) and vinculin (le Duc et al. 2010). These are believed to be mechano-sensitive and bind to the actin cytoskeleton, which can transmit external forces exerted to E-cadherin complexes. The detailed role of cadherin in sensing hydrodynamic stimuli has not been demonstrated directly. However, since vascular endothelial cadherin (VE-cadherin) has been reported to be one of the necessary proteins for producing a morphological

response by cells (Tzima et al. 2005), cadherin complexes are thought to be mechanosensors for shear stress stimuli. The role of platelet endothelial adhesion molecule-1 (PECAM-1) has also been investigated in ECs. Osawa et al. (2002) reported that application of shear stress to ECs resulted in phosphorylation of PECAM-1, which then activated an intracellular signaling cascade. They also demonstrated that tensile forces directly exerted on PECAM-1 induced its phosphorylation, suggesting that PECAM-1 senses tension at intercellular junctions caused by shear stress.

Glycocalyx is a surface layer primarily consisting of proteoglycans and glycoproteins bound to the cytoplasmic membrane of cells. It is thought to be a sensor for shear stress by transmitting shear stress to the cortical cytoskeleton or remote regions of the cells, such as intercellular junctions and focal adhesions (Tarbell et al. 2005). Shear stress sensed by glycocalyx has been reported to cause functional changes in several types of cells (Ainslie et al. 2005; Florian et al. 2003). Cilia are membrane-enveloped microtubule-based projections on the apical surface of cells and are also believed to have mechanosensory function in certain cell types such as ECs (Egorova et al. 2012) and kidney epithelial cells (Schwartz et al. 1997). Cilia play an important role in shear stress-induced intracellular Ca^{2+} signaling and NO synthesis in ECs (Nauli et al. 2008).

5 Concluding Remarks

This chapter provides an overview of the cellular responses to shear stress due to fluid flow and the mechanisms underlying mechanosensing in cells. The majority of related literature over the last three decades has addressed the effect of shear stress on vascular cells, particularly on EC morphology and function. Based on the results obtained from vascular cells, flow-induced responses of other cell types have also been investigated recently. Flow of biological fluid can be observed all over the living body, and an understanding of the cellular responses to flow undoubtedly provides critical insight into the physiological functions of tissues as well as mechanisms of pathogenesis. Further research is required to gain an understanding of the detailed responses by cells and the underlying mechanisms at both the cellular and molecular levels. Moreover, because a tissue is composed of multiple cells that interact directly and indirectly (via soluble bioactive substances), future research should include interactions between neighboring cells and interactions among the different cell types that constitute a tissue. It will be important to conduct these studies under flow conditions in order to elucidate how physiological systems of living tissues cooperate.

Acknowledgments This work was partially supported by Grants-in-Aid for Scientific Research from the Ministry of Education, Culture, Sports, Science and Technology (MEXT) of Japan (Nos. 20001007 and 21700457).

References

- Ainslie KM, Garanich JS, Dull RO, Tarbell JM (2005) Vascular smooth muscle cell glycocalyx influences shear stress-mediated contractile response. *J Appl Physiol* 98(1):242–249
- Ajubi NE, Klein-Nulend J, Nijweide PJ, Vrijheid-Lammers T, Alblas MJ, Burger EH (1996) Pulsating fluid flow increases prostaglandin production by cultured chicken osteocytes—a cytoskeleton-dependent process. *Biochem Biophys Res Commun* 225(1):62–68
- Albuquerque ML, Waters CM, Savla U, Schnaper HW, Flozak AS (2000) Shear stress enhances human endothelial cell wound closure in vitro. *Am J Physiol Heart Circ Physiol* 279(1):H293–H302
- Alshihabi SN, Chang YS, Frangos JA, Tarbell JM (1996) Shear stress-induced release of PGE2 and PGI2 by vascular smooth muscle cells. *Biochem Biophys Res Commun* 224(3):808–814
- Ando J, Nomura H, Kamiya A (1987) The effect of fluid shear stress on the migration and proliferation of cultured endothelial cells. *Microvasc Res* 33(1):62–70
- Ando J, Ohtsuka A, Korenaga R, Sakuma I, Kamiya A (1993) Flow-induced calcium transients and release of endothelium-derived relaxing factor in cultured vascular endothelial cells. *Front Med Biol Eng* 5(1):17–21
- Balcells M, Fernandez Suarez M, Vazquez M, Edelman ER (2005) Cells in fluidic environments are sensitive to flow frequency. *J Cell Physiol* 204(1):329–335
- Barbee KA, Davies PF, Lal R (1994) Shear stress-induced reorganization of the surface topography of living endothelial cells imaged by atomic force microscopy. *Circ Res* 74(1):163–171
- Brooks AR, Lelkes PI, Rubanyi GM (2002) Gene expression profiling of human aortic endothelial cells exposed to disturbed flow and steady laminar flow. *Physiol Genomics* 9(1):27–41
- Cai Z, Xin J, Pollock DM, Pollock JS (2000) Shear stress-mediated NO production in inner medullary collecting duct cells. *Am J Physiol Renal Physiol* 279(2):F270–F274
- Cao L, Wu A, Truskey GA (2011) Biomechanical effects of flow and coculture on human aortic and cord blood-derived endothelial cells. *J Biomech* 44(11):2150–2157. DOI: [10.1016/j.jbiomech.2011.05.024](https://doi.org/10.1016/j.jbiomech.2011.05.024)
- Caro CG, Pedly TJ, Schroter RC, Seed WA (1978) The mechanics of the circulation
- Chachisvilis M, Zhang YL, Frangos JA (2006) G protein-coupled receptors sense fluid shear stress in endothelial cells. *Proc Natl Acad Sci U S A* 103(42):15463–15468
- Chen KD, Li YS, Kim M, Li S, Yuan S, Chien S, Shyy JY (1999) Mechanotransduction in response to shear stress. Roles of receptor tyrosine kinases, integrins, and Shc. *J Biol Chem* 274(26):18393–18400
- Chen T, Buckley M, Cohen I, Bonassar L, Awad HA (2012) Insights into interstitial flow, shear stress, and mass transport effects on ECM heterogeneity in bioreactor-cultivated engineered cartilage hydrogels. *Biomech Model Mechanobiol* 11(5):689–702
- Chiu JJ, Chen LJ, Chang SF, Lee PL, Lee CI, Tsai MC, Lee DY, Hsieh HP, Usami S, Chien S (2005) Shear stress inhibits smooth muscle cell-induced inflammatory gene expression in endothelial cells: role of NF- κ B. *Arterioscler Thromb Vasc Biol* 25(5):963–969
- Chiu JJ, Chen LJ, Chen CN, Lee PL, Lee CI (2004) A model for studying the effect of shear stress on interactions between vascular endothelial cells and smooth muscle cells. *J Biomech* 37(4):531–539
- Deguchi S, Maeda K, Ohashi T, Sato M (2005) Flow-induced hardening of endothelial nucleus as an intracellular stress-bearing organelle. *J Biomech* 38(9):1751–1759
- Dejana E (2004) Endothelial cell-cell junctions: happy together. *Nat Rev Mol Cell Biol* 5(4):261–270
- Dewey CF Jr, Bussolari SR, Gimbrone MA Jr, Davies PF (1981) The dynamic response of vascular endothelial cells to fluid shear stress. *J Biomech Eng* 103(3):177–185
- Dolan JM, Meng H, Singh S, Paluch R, Kolega J (2011) High fluid shear stress and spatial shear stress gradients affect endothelial proliferation, survival, and alignment. *Ann Biomed Eng* 39(6):1620–1631

- Duan Y, Gotoh N, Yan Q, Du Z, Weinstein AM, Wang T, Weinbaum S (2008) Shear-induced reorganization of renal proximal tubule cell actin cytoskeleton and apical junctional complexes. *Proc Natl Acad Sci U S A* 105(32):11418–11423. DOI: [10.1073/pnas.0804954105](https://doi.org/10.1073/pnas.0804954105)
- Egorova AD, van der Heiden K, Poelmann RE, Hierck BP (2012) Primary cilia as biomechanical sensors in regulating endothelial function. *Differentiation* 83(2):S56–S61
- Essig M, Terzi F, Burtin M, Friedlander G (2001a) Mechanical strains induced by tubular flow affect the phenotype of proximal tubular cells. *Am J Physiol Renal Physiol* 281(4):F751–F762
- Essig M, Terzi F, Burtin M, Friedlander G (2001b) Mechanical strains induced by tubular flow affect the phenotype of proximal tubular cells. *Am J Physiol Renal Physiol* 281(4):F751–F762
- Farmakis TM, Soulis JV, Giannoglou GD, Zioupos GJ, Louridas GE (2004) Wall shear stress gradient topography in the normal left coronary arterial tree: possible implications for atherogenesis. *Curr Med Res Opin* 20(5):587–596
- Flaherty JT, Pierce JE, Ferrans VJ, Patel DJ, Tucker WK, Fry DL (1972) Endothelial nuclear patterns in the canine arterial tree with particular reference to hemodynamic events. *Circ Res* 30(1):23–33
- Flores D, Liu Y, Liu W, Satlin LM, Rohatgi R (2012) Flow-induced prostaglandin E2 release regulates Na and K transport in the collecting duct. *Am J Physiol Renal Physiol* 303(5):F632–F638
- Florian JA, Kosky JR, Ainslie K, Pang Z, Dull RO, Tarbell JM (2003) Heparan sulfate proteoglycan is a mechanosensor on endothelial cells. *Circ Res* 93(10):e136–e142
- Frangos JA, Eskin SG, McIntire LV, Ives CL (1985) Flow effects on prostacyclin production by cultured human endothelial cells. *Science* 227(4693):1477–1479
- Fry DL (1968) Acute vascular endothelial changes associated with increased blood velocity gradients. *Circ Res* 22(2):165–197
- Gosgnach W, Messika-Zeitoun D, Gonzalez W, Philippe M, Michel JB (2000) Shear stress induces iNOS expression in cultured smooth muscle cells: role of oxidative stress. *Am J Physiol Cell Physiol* 279(6):C1880–C1888
- Gudi SR, Clark CB, Frangos JA (1996) Fluid flow rapidly activates G proteins in human endothelial cells. Involvement of G proteins in mechanochemical signal transduction. *Circ Res* 79(4):834–839
- Helmlinger G, Geiger RV, Schreck S, Nerem RM (1991) Effects of pulsatile flow on cultured vascular endothelial cell morphology. *J Biomech Eng* 113(2):123–131
- Himburg HA, Dowd SE, Friedman MH (2007) Frequency-dependent response of the vascular endothelium to pulsatile shear stress. *Am J Physiol Heart Circ Physiol* 293(1):H645–H653
- Jimenez-Vergara AC, Guiza-Arguello V, Becerra-Bayona S, Munoz-Pinto DJ, McMahon RE, Morales A, Cubero-Ponce L, Hahn MS (2010) Approach for fabricating tissue engineered vascular grafts with stable endothelialization. *Ann Biomed Eng* 38(9):2885–2895
- Jo H, Dull RO, Hollis TM, Tarbell JM (1991) Endothelial albumin permeability is shear dependent, time dependent, and reversible. *Am J Physiol* 260(6 Pt 2):H1992–H1996
- Johnson DL, McAllister TN, Frangos JA (1996) Fluid flow stimulates rapid and continuous release of nitric oxide in osteoblasts. *Am J Physiol* 271(1 Pt 1):E205–E208
- Karuri NW, Liliensiek S, Teixeira AI, Abrams G, Campbell S, Nealey PF, Murphy CJ (2004) Biological length scale topography enhances cell-substratum adhesion of human corneal epithelial cells. *J Cell Sci* 117(Pt 15):3153–3164
- Kataoka N, Ujita S, Sato M (1998) Effect of flow direction on the morphological responses of cultured bovine aortic endothelial cells. *Med Biol Eng Comput* 36(1):122–128
- Kaysen JH, Campbell WC, Majewski RR, Goda FO, Navar GL, Lewis FC, Goodwin TJ, Hammond TG (1999) Select de novo gene and protein expression during renal epithelial cell culture in rotating wall vessels is shear stress dependent. *J Membr Biol* 168(1):77–89
- Kolega J, Gao L, Mandelbaum M, Mocco J, Siddiqui AH, Natarajan SK, Meng H (2011) Cellular and molecular responses of the basilar terminus to hemodynamics during intracranial aneurysm initiation in a rabbit model. *J Vasc Res* 48(5):429–442

- Ku DN, Giddens DP, Zarins CK, Glagov S (1985) Pulsatile flow and atherosclerosis in the human carotid bifurcation. Positive correlation between plaque location and low oscillating shear stress. *Arteriosclerosis* 5(3):293–302
- Kuchan MJ, Frangos JA (1993) Shear stress regulates endothelin-1 release via protein kinase C and cGMP in cultured endothelial cells. *Am J Physiol* 264(1 Pt 2):H150–H156
- LaMack JA, Friedman MH (2007) Individual and combined effects of shear stress magnitude and spatial gradient on endothelial cell gene expression. *Am J Physiol Heart Circ Physiol* 293(5):H2853–H2859
- Langille BL, Bendeck MP, Keeley FW (1989) Adaptations of carotid arteries of young and mature rabbits to reduced carotid blood flow. *Am J Physiol* 256(4 Pt 2):H931–H939
- Langille BL, O'Donnell F (1986) Reductions in arterial diameter produced by chronic decreases in blood flow are endothelium-dependent. *Science* 231(4736):405–407
- le Duc Q, Shi Q, Blonk I, Sonnenberg A, Wang N, Leckband D, de Rooij J (2010) Vinculin potentiates E-cadherin mechanosensing and is recruited to actin-anchored sites within adherens junctions in a myosin II-dependent manner. *J Cell Biol* 189(7):1107–1115
- Lecuit T (2010) alpha-catenin mechanosensing for adherens junctions. *Nat Cell Biol* 12(6):522–524
- Lee AA, Graham DA, Dela Cruz S, Ratcliffe A, Karlon WJ (2002) Fluid shear stress-induced alignment of cultured vascular smooth muscle cells. *J Biomech Eng* 124(1):37–43
- Levesque MJ, Nerem RM (1985) The elongation and orientation of cultured endothelial cells in response to shear stress. *J Biomech Eng* 107(4):341–347
- Levesque MJ, Nerem RM, Sprague EA (1990) Vascular endothelial cell proliferation in culture and the influence of flow. *Biomaterials* 11(9):702–707
- Li M, Stenmark KR, Shandas R, Tan W (2009) Effects of pathological flow on pulmonary artery endothelial production of vasoactive mediators and growth factors. *J Vasc Res* 46(6):561–571
- Lichtenberg A, Tudorache I, Cebotari S, Suprunov M, Tudorache G, Goerler H, Park JK, Hilfiker-Kleiner D, Ringes-Lichtenberg S, Karck M, Brandes G, Hilfiker A, Haverich A (2006) Preclinical testing of tissue-engineered heart valves re-endothelialized under simulated physiological conditions. *Circulation* 114(1 Suppl):I559–I565
- Malek A, Izumo S (1992) Physiological fluid shear stress causes downregulation of endothelin-1 mRNA in bovine aortic endothelium. *Am J Physiol* 263(2 Pt 1):C389–C396
- Malek AM, Izumo S, Alper SL (1999) Modulation by pathophysiological stimuli of the shear stress-induced up-regulation of endothelial nitric oxide synthase expression in endothelial cells. *Neurosurgery* 45(2):334–344; discussion 344–335
- Mall JW, Philipp AW, Rademacher A, Paulitschke M, Buttemeyer R (2004) Re-endothelialization of punctured ePTFE graft: an in vitro study under pulsed perfusion conditions. *Nephrol Dial Transplant* 19(1):61–67
- Meng H, Wang Z, Hoi Y, Gao L, Metaxa E, Swartz DD, Kolega J (2007) Complex hemodynamics at the apex of an arterial bifurcation induces vascular remodeling resembling cerebral aneurysm initiation. *Stroke* 38(6):1924–1931
- Metaxa E, Tremmel M, Natarajan SK, Xiang J, Paluch RA, Mandelbaum M, Siddiqui AH, Kolega J, Mocco J, Meng H (2010) Characterization of critical hemodynamics contributing to aneurysmal remodeling at the basilar terminus in a rabbit model. *Stroke* 41(8):1774–1782
- Mohan S, Mohan N, Sprague EA (1997) Differential activation of NF-kappa B in human aortic endothelial cells conditioned to specific flow environments. *Am J Physiol* 273(2 Pt 1):C572–C578
- Morawietz H, Talanow R, Szibor M, Rueckschloss U, Schubert A, Bartling B, Darmer D, Holtz J (2000) Regulation of the endothelin system by shear stress in human endothelial cells. *J Physiol* 525(Pt 3):761–770
- Nagel T, Resnick N, Atkinson WJ, Dewey CF Jr, Gimbrone MA Jr (1994) Shear stress selectively upregulates intercellular adhesion molecule-1 expression in cultured human vascular endothelial cells. *J Clin Invest* 94(2):885–891

- Nagel T, Resnick N, Dewey CF Jr, Gimbrone MA Jr (1999) Vascular endothelial cells respond to spatial gradients in fluid shear stress by enhanced activation of transcription factors. *Arterioscler Thromb Vasc Biol* 19(8):1825–1834
- Nauli SM, Kawanabe Y, Kaminski JJ, Pearce WJ, Ingber DE, Zhou J (2008) Endothelial cilia are fluid shear sensors that regulate calcium signaling and nitric oxide production through polycystin-1. *Circulation* 117(9):1161–1171
- Nerem RM, Levesque MJ, Cornhill JF (1981) Vascular endothelial morphology as an indicator of the pattern of blood flow. *J Biomech Eng* 103(3):172–176
- Ng CP, Hinz B, Swartz MA (2005) Interstitial fluid flow induces myofibroblast differentiation and collagen alignment in vitro. *J Cell Sci* 118(Pt 20):4731–4739
- Ng CP, Swartz MA (2003) Fibroblast alignment under interstitial fluid flow using a novel 3-D tissue culture model. *Am J Physiol Heart Circ Physiol* 284(5):H1771–H1777
- Osawa M, Masuda M, Kusano K, Fujiwara K (2002) Evidence for a role of platelet endothelial cell adhesion molecule-1 in endothelial cell mechanosignal transduction: is it a mechanoresponsive molecule? *J Cell Biol* 158(4):773–785
- Raimondi MT, Candiani G, Cabras M, Cioffi M, Lagana K, Moretti M, Pietrabissa R (2008) Engineered cartilage constructs subject to very low regimens of interstitial perfusion. *Biorheology* 45(3–4):471–478
- Redmond EM, Cahill PA, Sitzmann JV (1998) Flow-mediated regulation of G-protein expression in cocultured vascular smooth muscle and endothelial cells. *Arterioscler Thromb Vasc Biol* 18(1):75–83
- Ren H, Wilson G (1997) The effect of a shear force on the cell shedding rate of the corneal epithelium. *Acta Ophthalmol Scand* 75(4):383–387
- Rhoads DN, Eskin SG, McIntire LV (2000) Fluid flow releases fibroblast growth factor-2 from human aortic smooth muscle cells. *Arterioscler Thromb Vasc Biol* 20(2):416–421
- Rice KM, Kakarla SK, Mupparaju SP, Paturi S, Katta A, Wu M, Harris RT, Blough ER (2010) Shear stress activates Akt during vascular smooth muscle cell reorientation. *Biotechnol Appl Biochem* 55(2):85–90
- Sakamoto N, Kiuchi T, Sato M (2011) Development of an endothelial-smooth muscle cell coculture model using phenotype-controlled smooth muscle cells. *Ann Biomed Eng* 39(11):2750–2758
- Sakamoto N, Ohashi T, Sato M (2006) Effect of fluid shear stress on migration of vascular smooth muscle cells in cocultured model. *Ann Biomed Eng* 34(3):408–415
- Sakamoto N, Saito N, Han X, Ohashi T, Sato M (2010a) Effect of spatial gradient in fluid shear stress on morphological changes in endothelial cells in response to flow. *Biochem Biophys Res Commun* 395(2):264–269
- Sakamoto N, Segawa K, Kanzaki M, Ohashi T, Sato M (2010b) Role of p120-catenin in the morphological changes of endothelial cells exposed to fluid shear stress. *Biochem Biophys Res Commun* 398(3):426–432
- Sato M, Levesque MJ, Nerem RM (1987) An application of the micropipette technique to the measurement of the mechanical properties of cultured bovine aortic endothelial cells. *J Biomech Eng* 109(1):27–34
- Sato M, Nagayama K, Kataoka N, Sasaki M, Hane K (2000) Local mechanical properties measured by atomic force microscopy for cultured bovine endothelial cells exposed to shear stress. *J Biomech* 33(1):127–135
- Schnermann J, Wahl M, Liebau G, Fischbach H (1968) Balance between tubular flow rate and net fluid reabsorption in the proximal convolution of the rat kidney. I. Dependency of reabsorptive net fluid flux upon proximal tubular surface area at spontaneous variations of filtration rate. *Pflugers Archiv: European journal of physiology* 304(1):90–103
- Schwartz EA, Leonard ML, Bizios R, Bowser SS (1997) Analysis and modeling of the primary cilium bending response to fluid shear. *Am J Physiol* 272 (1 Pt 2):F132–138
- Shikata Y, Rios A, Kawkitinarong K, DePaola N, Garcia JG, Birukov KG (2005) Differential effects of shear stress and cyclic stretch on focal adhesion remodeling, site-specific FAK

- phosphorylation, and small GTPases in human lung endothelial cells. *Exp Cell Res* 304(1):40–49
- Sterpetti AV, Cucina A, D'Angelo LS, Cardillo B, Cavallaro A (1993) Shear stress modulates the proliferation rate, protein synthesis, and mitogenic activity of arterial smooth muscle cells. *Surgery* 113(6):691–699
- Szymanski MP, Metaxa E, Meng H, Kolega J (2008) Endothelial cell layer subjected to impinging flow mimicking the apex of an arterial bifurcation. *Ann Biomed Eng* 36(10):1681–1689
- Tada S, Tarbell JM (2000) Interstitial flow through the internal elastic lamina affects shear stress on arterial smooth muscle cells. *Am J Physiol Heart Circ Physiol* 278(5):H1589–H1597
- Tada S, Tarbell JM (2001) Fenestral pore size in the internal elastic lamina affects transmural flow distribution in the artery wall. *Ann Biomed Eng* 29(6):456–466
- Tada S, Tarbell JM (2002) Flow through internal elastic lamina affects shear stress on smooth muscle cells (3D simulations). *Am J Physiol Heart Circ Physiol* 282(2):H576–H584
- Tarbell JM, Weinbaum S, Kamm RD (2005) Cellular fluid mechanics and mechanotransduction. *Ann Biomed Eng* 33(12):1719–1723
- Tsai MC, Chen L, Zhou J, Tang Z, Hsu TF, Wang Y, Shih YT, Peng HH, Wang N, Guan Y, Chien S, Chiu JJ (2009) Shear stress induces synthetic-to-contractile phenotypic modulation in smooth muscle cells via peroxisome proliferator-activated receptor alpha/delta activations by prostacyclin released by sheared endothelial cells. *Circ Res* 105(5):471–480
- Tzima E, Irani-Tehrani M, Kiosses WB, Dejana E, Schultz DA, Engelhardt B, Cao G, DeLisser H, Schwartz MA (2005) A mechanosensory complex that mediates the endothelial cell response to fluid shear stress. *Nature* 437(7057):426–431
- Tzima E, Kiosses WB, del Pozo MA, Schwartz MA (2003) Localized cdc42 activation, detected using a novel assay, mediates microtubule organizing center positioning in endothelial cells in response to fluid shear stress. *J Biol Chem* 278(33):31020–31023
- Uematsu M, Ohara Y, Navas JP, Nishida K, Murphy TJ, Alexander RW, Nerem RM, Harrison DG (1995) Regulation of endothelial cell nitric oxide synthase mRNA expression by shear stress. *Am J Physiol* 1269 (6 Pt 1):C1371–C1378
- Vyalov S, Langille BL, Gotlieb AI (1996) Decreased blood flow rate disrupts endothelial repair in vivo. *Am J Pathol* 149(6):2107–2118
- Wang HQ, Huang LX, Qu MJ, Yan ZQ, Liu B, Shen BR, Jiang ZL (2006) Shear stress protects against endothelial regulation of vascular smooth muscle cell migration in a coculture system. *Endothelium* 13(3):171–180
- Wang Y, Miao H, Li S, Chen KD, Li YS, Yuan S, Shyy JY, Chien S (2002) Interplay between integrins and FLK-1 in shear stress-induced signaling. *Am J Physiol Cell Physiol* 283(5):C1540–C1547
- Wang YH, Yan ZQ, Qi YX, Cheng BB, Wang XD, Zhao D, Shen BR, Jiang ZL (2010) Normal shear stress and vascular smooth muscle cells modulate migration of endothelial cells through histone deacetylase 6 activation and tubulin acetylation. *Ann Biomed Eng* 38(3):729–737
- Wang ZM, Pierson RN Jr, Heymsfield SB (1992) The five-level model: a new approach to organizing body-composition research. *Am J Clin Nutr* 56(1):19–28
- Wesolowski SA, Fries CC, Sabini AM, Sawyer PN (1965) The Significance of Turbulence in Hemic Systems and in the Distribution of the Atherosclerotic Lesion. *Surgery* 57:155–162
- Yamamoto K, Korenaga R, Kamiya A, Qi Z, Sokabe M, Ando J (2000) P2X(4) receptors mediate ATP-induced calcium influx in human vascular endothelial cells. *Am J Physiol Heart Circ Physiol* 279(1):H285–H292
- Yamamoto K, Sokabe T, Matsumoto T, Yoshimura K, Shibata M, Ohura N, Fukuda T, Sato T, Sekine K, Kato S, Isshiki M, Fujita T, Kobayashi M, Kawamura K, Masuda H, Kamiya A, Ando J (2006) Impaired flow-dependent control of vascular tone and remodeling in P2X4-deficient mice. *Nat Med* 12(1):133–137
- Zaidel-Bar R, Kam Z, Geiger B (2005) Polarized downregulation of the paxillin-p130CAS-Rac1 pathway induced by shear flow. *J Cell Sci* 118(Pt 17):3997–4007

The Effect of a Static Magnetic Field on the Flow of Iron Oxide Magnetic Nanoparticles Through Glass Capillaries

N. Pereira, M. Mujika, S. Arana, T. Correia, A. M. T. Silva,
H. T. Gomes, P. J. Rodrigues and R. Lima

Abstract Iron oxide nanoparticles were developed using solvothermal synthesis and suspended in a physiological fluid constituted by erythrocytes in order to perform studies of flow behaviour in glass microchannels. The main purpose of this work was to study the influence of different iron oxide nanoparticles and magnetic fields in the plasma layer thickness and also the influence of the magnetic field in the area composed of nanoparticles attracted to the wall of the microchannel. The results obtained show that nanoparticles with magnetic characteristics promote the thinning of the plasma layer, in contrast to the behaviour observed with nanoparticles without magnetic characteristics. It was also observed upon application of magnetic fields with different intensities, the plasma layer tend to disappear in some areas depending on the type of particles. Moreover, the area of nanoparticles attracted to the microchannel wall increases with the increase of the magnetic field intensity.

N. Pereira · T. Correia · H. T. Gomes · P. J. Rodrigues · R. Lima (✉)
Instituto Politécnico de Bragança (IPB), Campus de Santa Apolónia, 5301-857,
Bragança, Portugal
e-mail: ruimec@ipb.pt

M. Mujika · S. Arana
CEIT, Universidade de Navarra, Parque Tecnológico de San Sebastian, Paseo
de Manuel Lardizábal, N 1520.018 Donostia, San Sebastián, Spain

T. Correia
CIMO, Instituto Politécnico de Bragança (IPB), Campus de Santa Apolónia, 5301-857
Bragança, Portugal

A. M. T. Silva · H. T. Gomes
LCM—Laboratório de Catálise e Materiais—Laboratório Associado LSRE/LCM, Faculdade
de Engenharia, Universidade do Porto, Rua Dr. Roberto Frias, 4200-465 Porto, Portugal

R. Lima
CEFT, Faculdade de Engenharia da Universidade do Porto (FEUP),
Rua Dr. Roberto Frias, 4200-465 Porto, Portugal

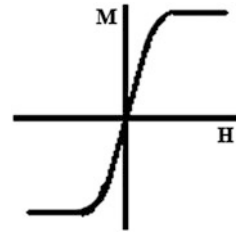
1 Introduction

There are various types of magnetic nanoparticles, such as metal nanoparticles, bimetallic nanoparticles and nanoparticles of iron oxide. Iron oxides, in particular, have an important role in different fields, such as chemical industry, medicine, biology, geology, among others, and their performance is affected either by the particle size or by the crystal structure (Sun et al. 2008, Schwertmann and Cornell. 2000, Cornell and Schwertmann 2003). Among the existing iron oxides, hematite (α -Fe₂O₃), magnetite (Fe₃O₄) and maghemite (γ -Fe₂O₃) are the most commonly studied forms in the reported applications. While hematite is a weak ferromagnetic material, magnetite is ferromagnetic at room temperature and above T_C (Curie temperature) is paramagnetic, presenting black colour. It is a mixture of Fe₂O₃ and FeO and the magnetization that appears by the presence of an external magnetic field disappears when the field is removed. As magnetite is very sensitive to environmental conditions, it easily undergoes oxidation forming maghemite. In turn, maghemite is ferromagnetic at 25 °C and their susceptibility decreases with time. Maghemite has the crystal structure and the magnetic nature of magnetite, but the composition is the same as that of hematite, showing brown colour, maghemite being transformed into hematite under temperatures between 370 and 600 °C (Cornell and Schwertmann 2003; Sidhu et al. 1978; Finotelli 2006; Wiesner and Bottero 2007; Trinchi et al. 2008; Teja and Koh 2009).

Currently, due to their physical and chemical properties, magnetic nanoparticles are of great interest in the fields of biomedical and bioengineering. They can be used in controlled drug delivery and drug targeting systems, as contrast agents in magnetic resonance imaging (MRI) and in hyperthermia. For these applications, the nanoparticles should be superparamagnetic, smaller than 100 nm with a narrow size distribution, and characterized by uniform chemical and physical properties, exposing high values of magnetization (Sun et al. 2008; Guo et al. 2009; Jain 2008). The ferromagnetic and ferrimagnetic nanoparticles undergo a change of behaviour when are smaller than a certain critical diameter (D_c), ceasing to submit ferrimagnetic and ferromagnetic behaviour when their temperature is below T_c, becoming superparamagnetic nanoparticles. The superparamagnetic behaviour arises in monodomain nanoparticles, where the magnetization is seen as a large and single magnetic moment. The consistency of magnetization can be achieved within a short period of time and under certain experimental temperatures, verifying values of high magnetic susceptibility (Schwertmann and Cornell 2000; Cullity 1972; Earnshaw 1968; Pankhurst et al. 2003). There is no hysteresis for superparamagnetic particles because the magnetic moments of particles orient themselves in one parallel direction, causing the residual magnetization (M_r) and coercive field (H_c) to be null, as can be seen in Fig. 1 (Pankhurst et al. 2003).

Hyperthermia is a therapy for the treatment of cancer, which is based on a deliberate rise of temperature in the affected area, in order to cause lysis of cancer cells. These cells, compared to normal cells, are poorly resistant to a sudden

Fig. 1 Hysteresis curve of a superparamagnetic particle, showing the absence of residual magnetization and coercive field



increase in temperature, thereby causing their destruction at a temperature of 41–42 °C. This sudden increase of temperature is achieved, for example, through the use of magnetic nanoparticles with sizes below 50 nm, which warm up when subjected to the action of an external magnetic field of alternating frequencies (Tartaj et al. 2003; Wen et al. 2011).

In recent years much research has been undertaken aiming to produce stable, biocompatible and monodisperse iron oxide nanoparticles. The most common methods include co-precipitation, thermal decomposition, hydrothermal/solvothermal synthesis and sonochemical synthesis (Wu et al. 2008). Hydrothermal/solvothermal methods allow the synthesis of iron oxide particles with specific sizes and shapes, which is technologically important because there is a strong connection between these parameters and their magnetic properties. This type of synthesis can be performed using various technologies (including those implementing sealed vessels), but the main fundamental mechanism consists in the crystallization of the desired species using aqueous solutions (hydrothermal), or other suitable solvents (solvothermal), at high temperatures (between 130 and 250 °C) and high steam pressures (among 0.3 and 4 MPa). With these processes it is possible to obtain highly crystalline iron oxides (Wu et al. 2008).

In this work, the first objective was the synthesis of magnetic nanoparticles by a solvothermal process, studying the influence of some synthesis parameters in the final characteristics of the materials, in particular the amount of precursor ($\text{FeCl}_3 \cdot 6\text{H}_2\text{O}$), the amount of NaOH and the synthesis temperature. In a second step, the flow of blood containing nanoparticles in suspension was studied, in order to investigate their influence on the cell-free layer (CFL). The CFL, also known as plasma layer, is a physiological phenomenon that occurs in the microcirculation of blood, either in vivo or in vitro environments. This phenomenon is due to the tendency of red blood cells to migrate through the flow of blood to the center of the microvessel (axial migration). The CFL is an area with very low concentration of cells (Kim et al. 2006; Lima et al. 2008). In the flow studies, different magnetic fields have been applied to examine the CFL behaviour and the area of particles which agglomerate along the wall of the microchannel.

2 Materials and Methods

2.1 Preparation of Iron Oxide Magnetic Nanoparticles

The iron oxide magnetic nanoparticles used in this study were synthesized by a solvothermal method, adapting procedures described in the literature (Liu et al. 2010). In a typical procedure, 5 mmol of precursor ($\text{FeCl}_3 \cdot 6\text{H}_2\text{O}$) is dissolved in 20 mL of ethyleneglycol (EG) and then 20 mmol of sodium hydroxide (NaOH) is added to the resultant mixture. Thereafter, the mixture obtained is placed in a Teflon vessel inside a stainless steel reactor (Parr Acid Digestion Vessel, Model 4748 see Fig. 2) and heated at 180 °C for 6 h. After the heat exposure time, the mixture is allowed to cool down to room temperature and withdrawn from the reactor. The synthesized solid materials are recovered by vacuum filtration, followed by washing with water and drying at 40 °C for 24 h. This procedure was repeated for each synthesized sample, yielding ultimately six different types of nanoparticles, by varying the amount of precursor (between 2.5 mmol and 10 mmol of $\text{FeCl}_3 \cdot 6\text{H}_2\text{O}$), the amount of NaOH (between 10 and 30 mmol) and the synthesis temperature (180 or 200 °C), as summarized in Table 1. The six types of nanoparticles obtained were labeled as: NP1 and NP6 (composed only by magnetite with mean diameters of 22.8 and 21.9 nm, respectively), NP2 and NP5 (composed by a mixture of magnetite and maghemite with mean diameters of 25.7 and 16.0 nm, respectively), and NP3 and NP4 (non-magnetic particles with a mean diameter of 21.6 nm). Besides these synthesized samples, two types of commercial nanoparticles were also considered in the studies: maghemite nanoparticles (Aldrich, Madrid) and encapsulated Fe_3O_4 nanoparticles, structured with a core of magnetite surrounded with a shell matrix composed by citric acid and sodium salt (chemicell GmbH, Berlin), which were named NPC and NPCE, respectively.

Fig. 2 Reactor parr acid digestion vessel, model 4748



Table 1 Conditions for synthesis of nanoparticles

Sample	FeCl ₃ (mmol)	NaOH (mmol)	Time (h)	T (°C)
NP1	5	20	6	180
NP2	2.5	20	6	180
NP3	10	20	6	180
NP4	5	10	6	180
NP5	5	30	6	180
NP6	5	20	6	200

2.2 Working Fluids, Microchannels and Magnetic Fields

All studies were performed in circular microchannels of borosilicate glass with a diameter of 300 μm (Vitrocom, USA). Initially, the CFL status was studied in physiological fluid (*in vitro* blood) with 5 % Hematocrit (Hct). Then the blood was mixed with the various types of nanoparticles (commercial—NPC and NPCE, and synthesized—NP1, NP2, NP3, NP4, NP5 and NP6), and suspended in physiological saline with 1 % concentration, to study their impacts on the CFL. To separate the red blood cells (RBCs) from the other blood components, it is necessary to perform two washes with physiological saline and centrifugate (Centrifuge MPW-260R) at a speed of 2,000 rpm for 15 min. Finally, it is necessary to join dextran 40 (DX40) with RBCs. For example, to prepare 5 ml of RBCs with 5 % Hct, 4.75 ml of DX40 is mixed with 0.25 ml of RBCs. Another study was based on the approximation of a needle with multiple magnets, thus creating a magnetic field to study the effect of this field in the area of nanoparticles attracted to the microchannel wall and also the effect on the CFL. The magnetic field varies with the number of magnets used and may be measured using the Hall Effect Sensor. With the described experimental arrangement, magnetic fields of 61.5 G (two magnets applied), 123.1 G (five magnets) and 138.5 G (eight magnets) were obtained. The flow studies were performed in an experimental set-up consisting on a syringe pump (Harvard Apparatus PHD ULTRATM), for pumping the fluids within microchannels and controlling the flow rate, and an inverted microscope (IX71, Olympus) combined with a high speed camera (i-SPEED LT, Olympus), to make the visualization of the flows (see Fig. 3).

In the visualization experiments without applied magnetic field, only the central area of the microchannel was examined, as shown in Fig. 4, while in the visualization experiments with an applied magnetic field four separate zones were considered: the zone where the magnetic field (MF) is applied—“center region (C)”, the zones immediately preceding and following the zone where MF is applied—“upstream of MF (UM)” and “downstream of MF (DM)”, respectively—and the zone upstream farthest from the magnetic field, about 650 μm far back—“more upstream of MF (MUM)” as shown in Fig. 5.

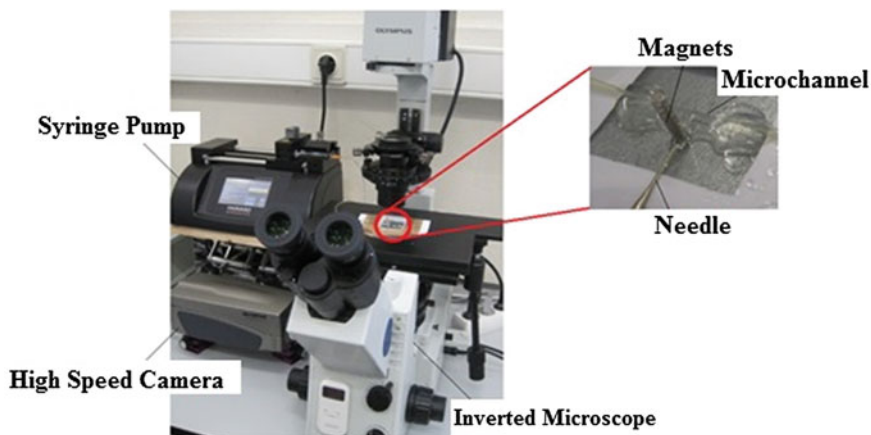


Fig. 3 Microvisualization high speed system to visualize the flow within the capillary

Fig. 4 Region of study (C) to visualize flow behaviour without applied magnetic field

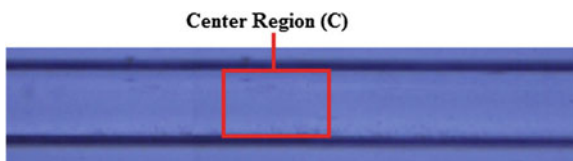
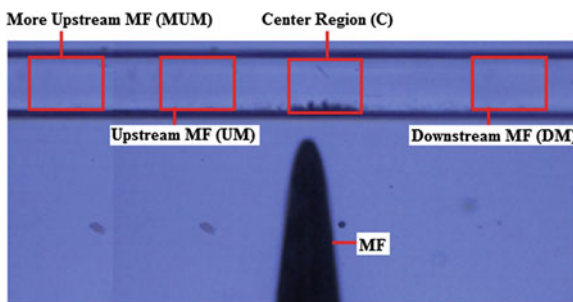


Fig. 5 Regions selected to study the flow behaviour with an applied magnetic field



3 Results and Discussion

3.1 Effect of Nanoparticles in the CFL in the Absence of a MF

This study was carried out with a flow rate of 2 $\mu\text{L}/\text{min}$, where the images were obtained with a 20 \times objective lens with a resolution of 800 \times 600 pixels and a frame rate of 1,000 frames/s. The images were transferred to the computer and

evaluated with the software Image J (NIH). In this section, the results obtained with two of the synthesized nanoparticles, NP4 and NP6 are presented, where the NP4 is a representative sample of the non-magnetic particles and NP6 is a representative sample of the magnetic particles. The images obtained with the samples NP4 and NP6 can be observed, respectively, in Fig. 6, where (a) and (c) are the original images and (b) and (d) are the images processed by Image J where the CFL is clearly visible.

Figure 7 shows the thickness of both bottom and top CFL observed with NP4 and NP6, and with the commercial nanoparticles aforementioned, all mixed with 5 % Hct of RBCs.

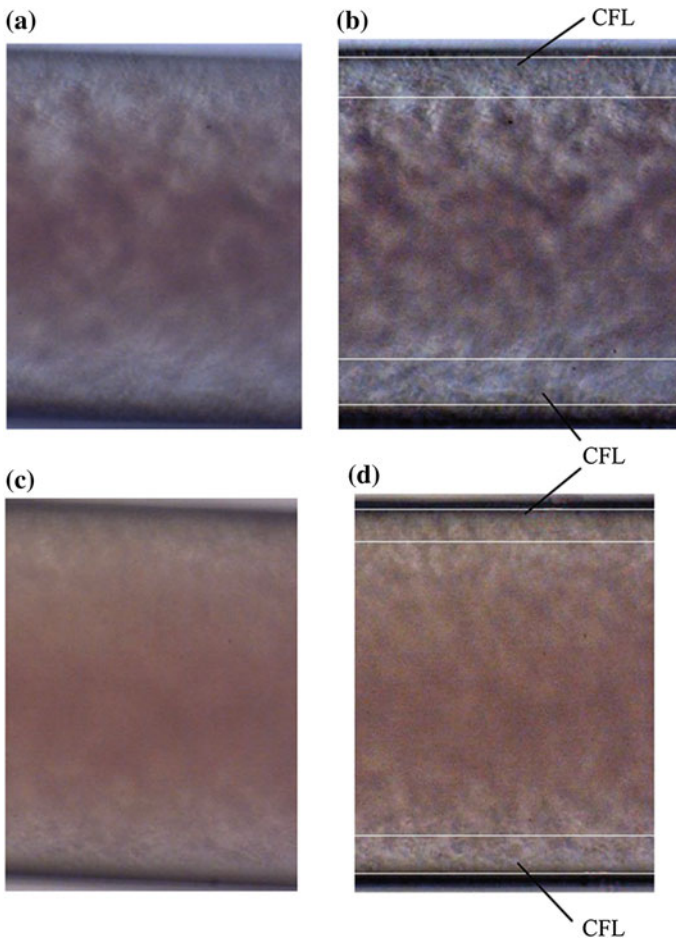
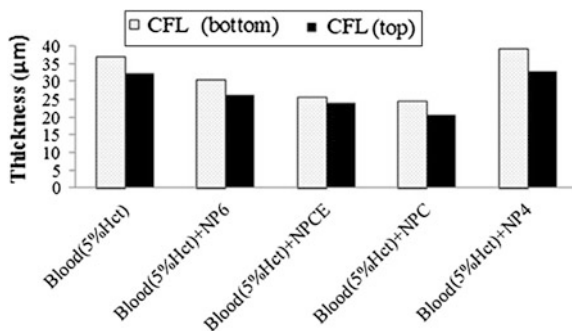


Fig. 6 Flow visualization of the samples, NP4 and NP6; **a** the original image of NP4 sample, **b** the NP4 sample image treated by image J, **c** the original image of NP6 sample, **d** the NP6 sample image treated by image J

Fig. 7 CFL thickness of in vitro blood with 5 % Hct and in vitro blood mixed with four distinct types of nanoparticles



The results in Fig. 7 reveal that the presence of magnetic nanoparticles (NP6, NPCE and NPC) promotes a decrease in the CFL thickness. It can be suggested that the presence of nanoparticles within the plasma decreases somehow the tendency of RBCs to migrate axially. In contrast, the presence of non-magnetic nanoparticles (NP4) tends to slightly increase the CFL thickness. The presence of NP4 within the plasma may induce RBC aggregation (darker parts in Fig. 6a, b), consequently increasing the CFL thickness. This latter result corroborates past studies (Bishop et al. 2001, Reinke et al. 1987) where it was shown that aggregation tends to increase the axial migration of RBCs, leading to an increase of the CFL thickness.

3.2 Effect of Nanoparticles in the CFL with the Presence of a Magnetic Field

In this study, a MF was applied to the in vitro blood flow (5 % Hct) containing in suspension each of the nanoparticles referred in the previous section. MF was different in each visualization experiment, increasing in the order 61.5, 123.1 and 138.5 G (designated as G1, G2 and G3 respectively) and capturing images after 1 min at each MF. The only exception was the case conducted with the sample NPCE, in the central zone (C), where a longer video was recorded, resulting in an increased time between each MF.

Figures 8, 9 and 10 show the CFL thickness obtained in the experiments carried out with three different nanoparticles (NPCE, NP6 and NPC) in four different zones (MUM, UM, C and DM) with different MF intensities (61.5, 123.1 and 138.5 G).

Considering the CFL (bottom) results in Fig. 8 for the studies conducted with the sample NPCE, it is observed that, regardless of the applied MF intensity, the CFL existing in the zone “MUM”, decreases its thickness in the following zone “UM”, and disappears almost completely in zones “C” and “DM”. In zone “C”, where the MF is stronger, it is observed that the nanoparticles begin to agglomerate, creating a

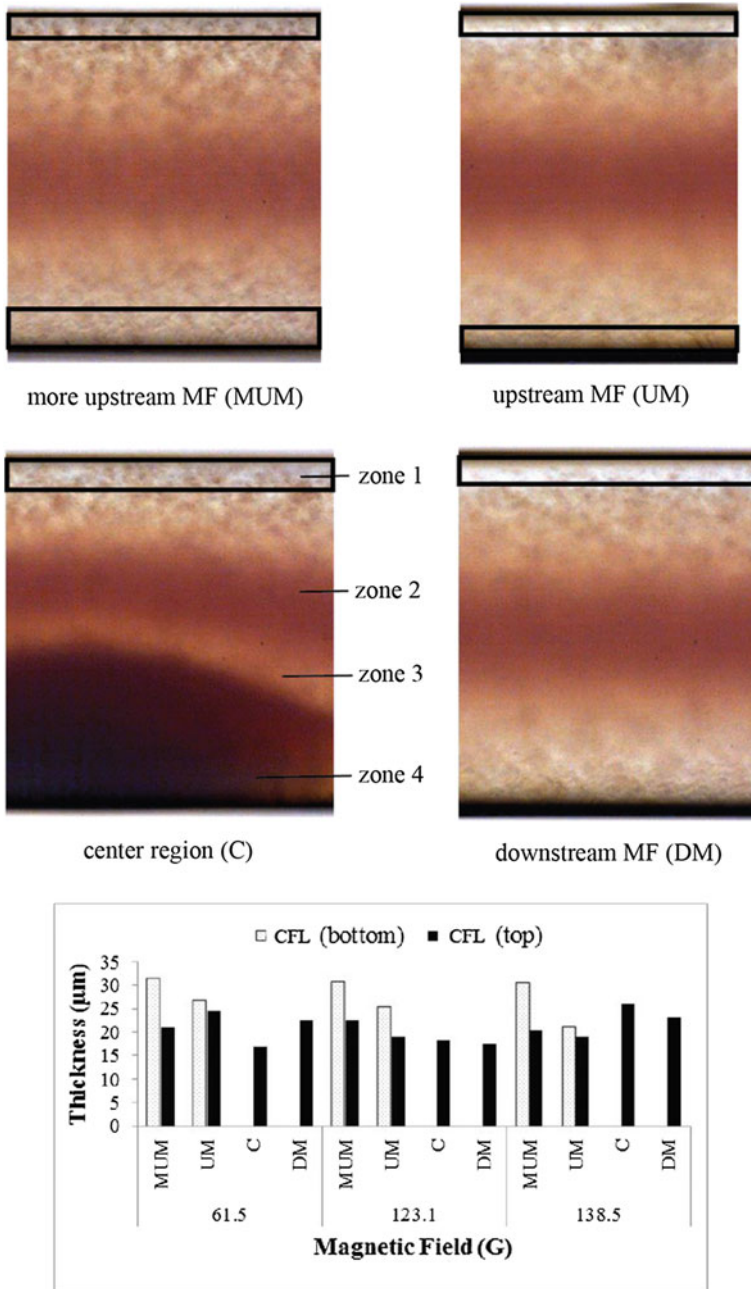


Fig. 8 Treated images of in vitro blood with NPCE nanoparticles in different zones when subjected to a magnetic field of 138.5 G. The *grayish regions* (indicated in *rectangular boxes*) correspond to the zones considered to measure the CFL thickness. The graph shows the thickness of the CFLs observed in the flow studies performed with the nanoparticles NPCE, in different zones and with different magnetic field forces. Note that the CFL at bottom disappeared in zone “C” and “DM”

three-phase flow, as visible in Fig. 8 (center region, C). The first phase corresponds to the CFL (top) a zone with practically no cells (zone 1). The second phase is more evident (zone 2) and corresponds to the central zone where a high concentration of RBCs occurs, since these cells tend to migrate to the center of the microchannel. The third phase (zone 3) corresponds to a zone with a lower concentration of RBCs, which is a mixture of plasma coupled with the magnetic nanoparticles that are migrating in the direction of the magnetic field located in the bottom wall. Additionally, there is another darker zone (zone 4) with respect to agglomeration of the nanoparticles due to magnetic forces generated by an externally applied magnetic field. It is worth mentioning that at the top region the CFL tends to increase as the MF increases. Further research is needed to completely understand this phenomenon.

Observing the results presented in Figs. 8, 9 and 10, it appears that, in opposition to that observed in the studies with the nanoparticles NPCE, the CFL existing in the bottom zone “MUM” tends to disappear in the following two zones “UM” and “C” since the particles NP6 and NPC soon begin to agglomerate in the upstream zone where the MF is applied (“UM”). However, the CFL is formed again after the zone where the MF is applied (“DM”), since, in contrast to the observed with NPCE, there aren't possibly micro-turbulences which cause increased mixing of the various elements constituting the fluid. Regarding the CFL at the top region, in all three cases, the thickness tends to increase with the increase of the MF intensity in zone “C”.

3.3 Agglomeration of Nanoparticles Under an Applied MF

In order to study the characteristics of agglomeration of the magnetic nanoparticles under the applied magnetic fields, flow experiments were performed considering the synthesized nanoparticles with magnetic characteristics (NP1, NP2, NP5 and NP6) and the commercial nanoparticles (NPC and NPCE) in physiological saline and in vitro blood with 5 % Hct. For the nanoparticles mixed with RBCs the same parameters as mentioned above were used (flow rate of 2 $\mu\text{L}/\text{min}$, 20 \times objective lens with a resolution of 800 \times 600 pixels and a frame rate of 1,000 frames/s). Only the study with the nanoparticles mixed in saline was observed using a 10 \times lens with a 1.6 zoom, a resolution of 800 \times 600 pixels and a flow rate of 10 $\mu\text{L}/\text{min}$.

To assess the magnitude of agglomeration of the different magnetic particles under an applied MF, the images were captured every minute and 2D areas were calculated as shown in Fig. 11. This figure shows the boundaries of the areas defined by the agglomerated NP6 nanoparticles in physiological saline (a) and in vitro blood (b), when subjected to a MF of 138.5 G. Upon these boundaries are defined, by simple integration, the 2D areas of agglomerated nanoparticles were calculated. The results obtained are shown in Fig. 12.

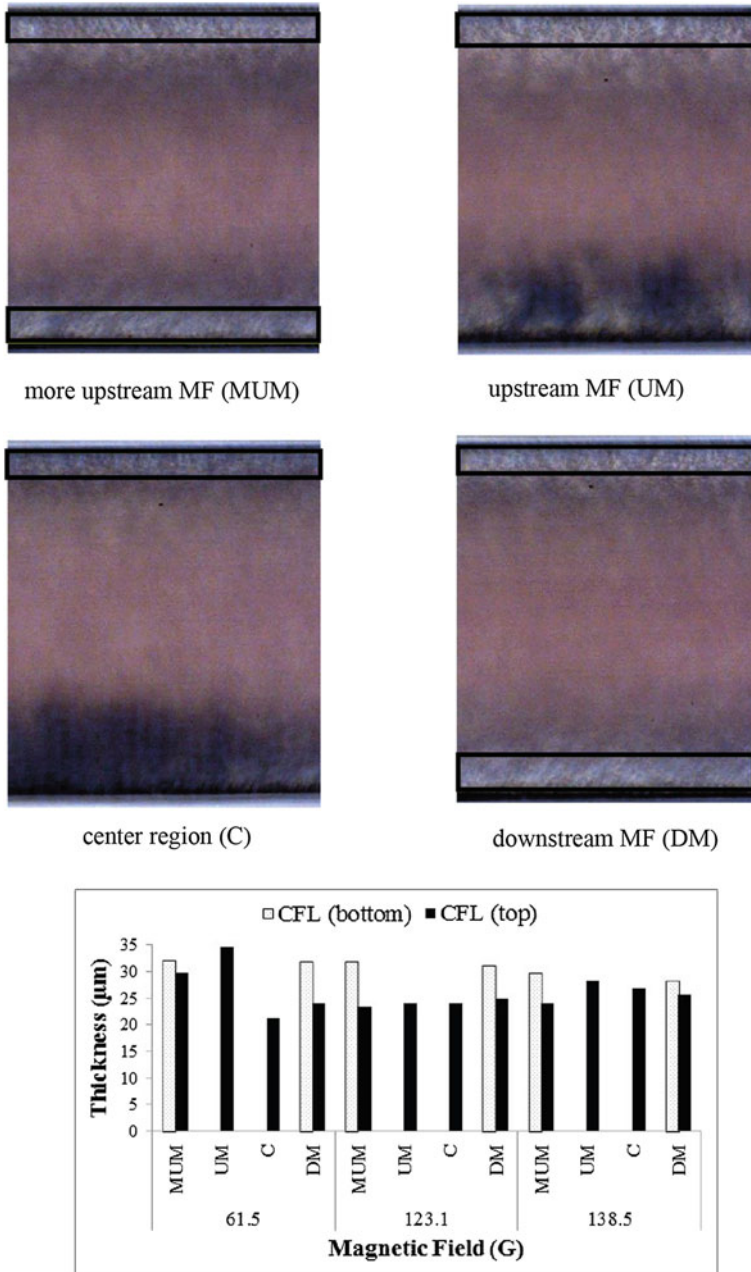
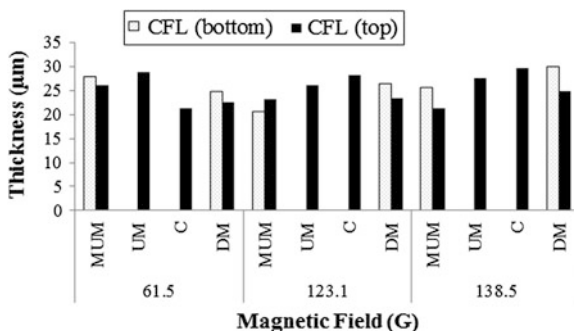


Fig. 9 Treated images of in vitro blood with NP6 nanoparticles in different zones when subjected to a magnetic field of 138.5 G. The *grayish regions* (indicated in *rectangular boxes*) correspond to the zones considered to measure the CFL thickness. The graph shows the thickness of the CFLs observed in the flow studies performed with the nanoparticles NP6, in different zones and with different magnetic field forces. Note that the CFL at bottom disappeared in zones “UM” and “C”

Fig. 10 Thickness of the CFL observed in the flow studies performed with the nanoparticles NPC, in different zones and with applied magnetic fields



From the analysis of Fig. 12 it can be seen that, in general, the increase of the MF intensity results in an increase of the agglomerated nanoparticle area, and this is an expected consequence of higher magnetic interaction forces between the magnet and the nanoparticles. An exception to this behaviour was the study with NPC, which shows no significant increase of the agglomerated area with the increase of the magnetic field intensity. The lowest agglomerated areas were observed in the studies with NPCE, under an applied magnetic field of 61.5 G, and with NPC at 123.1 G and 138.5 G. On the other hand, the nanoparticles that have an area of higher agglomeration are NP2 (at 61.5 G and 123.1 G) and NP6 (at 138.5 G). Among the synthesized particles, NP5 is the case which formed the lowest cluster of nanoparticles. In order to better understand and discriminate other possible effects, rather than the applied magnetic field intensity, on the obtained agglomerated areas, the areas of the synthesized nanoparticles were plotted against their diameter and against applied MF and composition, Figs. 13 and 14, respectively.

From the analysis of Fig. 13 it is concluded that, in general, the area of the nanoparticles agglomerated against the wall increases with the increase of the size of the nanoparticles, and this may be related to a better packaging effect (higher agglomerate density) when nanoparticles with lower sizes are considered. However, the observation of Fig. 14 also reveals that the composition of the nanoparticles has an influence on the agglomerated areas, i.e., in the studied carried out with nanoparticles composed only by magnetite (NP1 and NP6), there is a very marked increase of the area with the increase of the magnetic field. This increase is not so pronounced in the tests performed with the nanoparticles consisting of a mixture of magnetite and maghemite (NP2 and NP5). Such behaviour may be related to the magnetic characteristics of the pure magnetite materials, which are intensified upon increase of the applied magnetic field intensity, a behaviour that don't occur with the same intensity with the materials composed by magnetite and maghemite.

Figure 15 displays the agglomerated areas obtained in the studies carried out with the different nanoparticles suspended in 5 % Hct of RBCs, from where it can be observed that, as in the studies performed in physiological saline, the area of

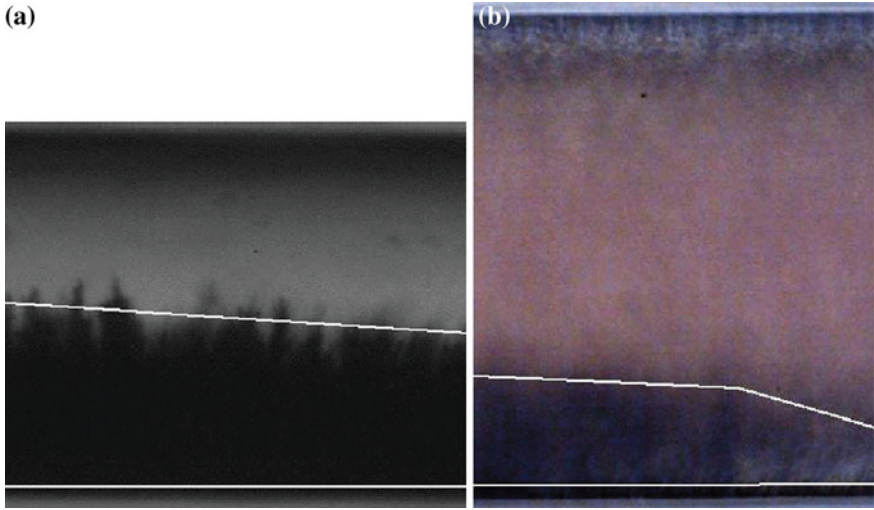


Fig. 11 Boundaries of the areas defined by the agglomerated NP6 nanoparticles in **a** physiological saline and **b** in vitro blood when subjected to a MF of 138.5 G

Fig. 12 Areas corresponding to the agglomeration of the nanoparticles in flow studies conducted in physiological saline under different magnetic field intensities

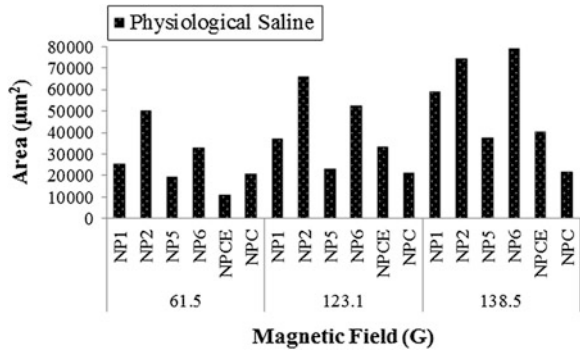


Fig. 13 Influence of the nanoparticles size on the agglomerated areas of the synthesized nanoparticles

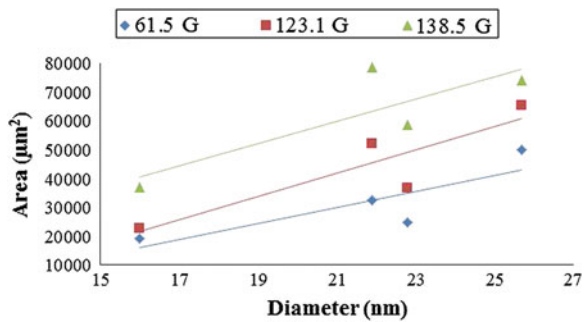


Fig. 14 Influence of the applied magnetic field on the agglomerated areas of synthesized nanoparticles

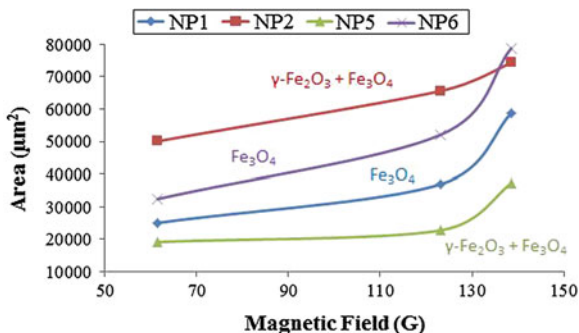
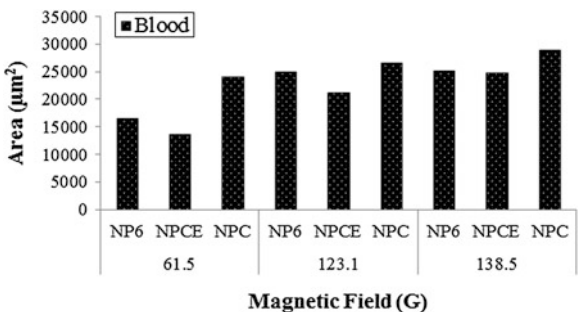


Fig. 15 Areas corresponding to the agglomeration of nanoparticles in flow studies conducted with NP6, NPC and NPCE in blood under different magnetic field intensities



agglomerated nanoparticles increases with the increase of the MF intensity. Curiously, the largest agglomerated area was obtained in the studies with the NPC nanoparticles (which is the opposite to that observed in the studies in physiological saline), while the smaller agglomerated area was obtained in the studies carried out with the NPCE nanoparticles.

4 Conclusions and Future Directions

From the studies carried out in this work it is possible to conclude that iron oxide nanoparticles, either magnetic and non-magnetic, have influence on the CFL thickness. While the magnetic nanoparticles promote a decrease of the thickness, the non-magnetic nanoparticles promote the increase of the thickness of the CFL. It is also concluded that, depending on the type of nanoparticles and the zones being analyzed, the fluid exhibits different behaviours. The CFL in fluids with the NPCE nanoparticles ceases just before the zone of magnetic field application, while in fluids with NPC and NP6 nanoparticles the CFL disappears just before and at the zone of MF application, but reappears later downstream. Regarding the area of nanoparticles agglomerated against the wall under applied MF, it is concluded that it increases with the increase of MF intensity and with the particle size.

It is also concluded that the composition of the magnetic nanoparticles influence their agglomeration, with those composed only by magnetite revealing intensified agglomeration upon increase of the applied MF intensity.

Further work is planned to strengthen the conclusions obtained and to study the influence of other parameters on the CFL, such as the influence of different hematocrits, different flow configurations and microchannels with different diameters. After these tests under constant MF, similar studies will be performed under an alternating MF in order to generate and measure the increase of temperature caused by the nanoparticles at the applied region, which will allow to assess the characteristics of the synthesized nanoparticles to generate enough heat to be applied in magnetic hyperthermia.

Acknowledgments The authors acknowledge FCT, COMPETE, NSRF and the European Union (FEDER) for funding through the following projects: PTDC/SAU-BEB/105650/2008, PTDC/SAU-BEB/108728/2008, PTDC/EME-MFE/099109/2008, PTDC/SAU-ENB/116929/2010 and PEst-C/EQB/LA0020/2011.

References

- Bishop JJ, Nance PR, Popel AS, Intaglietta M, Johnson PC (2001) Effect of erythrocyte aggregation on velocity profiles in venules. *Am J Physiol Heart Circ Physiol* 280(1):222–236
- Cornell RM, Schwertmann U (2003) *The iron oxides: structure, properties, reactions occurrence and uses*. Wiley-VCH, Weinheim
- Cullity BD (1972) *Introduction to magnetic materials*. Addison Wesley Publishing Company, London
- Earnshaw A (1968). *Introduction to magnetochemistry*. Academic Press Inc, New York
- Finotelli PV (2006). PhD Thesis. Microcápsulas de alginato contendo nanopartículas magnéticas para liberação controlada de insulina. UFRJ, Institute of Chemistry, Brasil
- Guo D, Song W, Wang X, Chen B (2009). Enhanced cytotoxicity suppression of arsenic trioxide to leukemia cancer cells by using magnetic nanoparticles. In: *Proceedings of 2nd International Conference on Biomedical Engineering and Informatics, China*, p 1–5
- Jain KK (2008) *Handbook of nanomedicine in: nanomolar diagnostic and nano-oncology*. Ed. Humana Press, EUA
- Kim S, Kong RL, Popel AS, Intaglietta M, Johnson PC (2006) A computer-based method for determination of the cell-free layer width in microcirculation. *Microcirculation* 13(3):199–207
- Lima R, Ishikawa T, Imai Y, Takeda M, Wada S, Yamaguchi T (2008) Radial dispersion of red blood cells in blood flowing through glass capillaries: role of hematocrit and geometry. *J Biomech* 41(10):2188–2196
- Liu R, Zhao Y, Huang R, Zhao Y, Zhou H (2010) Shape evolution and tunable properties of monodisperse magnetite crystals synthesized by a facile surfactant-free hydrothermal method. *Eur J Inorg Chem* 2010(28):4499–4505
- Pankhurst QA, Connolly J, Jones SK, Dobson J (2003) Applications of magnetic nanoparticles in biomedicine. *J Phys D Appl Phys* 36:167–181
- Reinke W, Gaetgens P, Johnson PC (1987) Blood viscosity in small tubes: effect of shear rate, aggregation, and sedimentation. *Am J Physiol Heart Circ Physiol* 253(3):540–547
- Schwertmann U, Cornell RM (2000) *Iron Oxides in the laboratory: preparation and characterization*. Wiley-VCH, Weinheim

- Sidhu PS, Gilkes RJ, Posner AM (1978) The synthesis and some properties of Co, Ni, Zn, Cu, Mn and Cd substituted magnetites. *J Inorg Nucl Chem* 40:429–435
- Sun C, Lee JSH, Zhang M (2008) Magnetic nanoparticles in MR imaging and drug delivery. *Adv Drug Deliv Rev* 60(11):1252–1265
- Tartaj P, Morales MP, Veintemillas-Verdaguer S, Gonzales-Carreño T, Serna JC (2003) The preparation of magnetic nanoparticles for applications in biomedicine. *J Phys D Appl Phys* 36:182–197
- Teja AS, Koh PY (2009) Synthesis, properties, and applications of magnetic iron oxide nanoparticles. *Prog Cryst Growth* 55:22–45
- Trinchi A, Muster TH, Dunlop JB, Collocott SJ (2008). Aging of magnetite nanoparticles in aqueous solutions of differing pH. In: *Proceedings of international conference on nanoscience and nanotechnology (ICONN 2008)*, Melbourne, Australia, p 83–85
- Wen B, Li J, Lin Y, Liu X, Fu J, Miao H, Zhang Q (2011) A novel preparation method for Fe_2O_3 nanoparticles and their characterization. *Mater Chem Phys* 128:35–38
- Wiesner MR, Bottero J-Y (2007) *Environmental nanotechnology: applications and impacts of nanomaterials*. McGraw-Hill, New York, p 40
- Wu W, He Q, Jiang C (2008) Magnetic iron oxide nanoparticles: synthesis and surface functionalization strategies. *Nanoscale Res Lett* 3(11):397–415

Three-Dimensional Simulations of Ciliary Flow

Raymond Quek, Kian Meng Lim and Keng Hwee Chiam

Abstract In many physiological scenarios such as the respiratory epithelium, fluid propulsion is achieved through the coordinated beating of an array of organelles called cilia. However, how these cilia couple to one another hydrodynamically to achieve coordinated beating is still unclear. In this chapter, we describe a three-dimensional numerical method to show how these cilia-fluid interactions may lead to the spontaneous generation of metachronal waves, a type of traveling wave produced by the sequential movement of the cilia. Our numerical method is based on the Immersed boundary method, which we have implemented and solved by massively parallel computing methods. By exploiting such massive parallelism, we are able to systematically investigate how changes in cilia stiffness and number density affect the properties of metachronal wave propagation. We also illustrate the use of our numerical method to simulate realistic experiments, such as how the localized reversal of the cilia stroke induced by the photorelease of caged calcium ions destabilizes the metachronal wave and how it can be reestablished. We also study fluid transport along the substrate and conclude that there exists an optimum cilia number density that gives a maximum slip velocity at the plane of the cilia tips. Finally we show that passive tracers in the vicinity of the cilia can display both diffusive and advective trajectories, depending on their distance from the cilia tips.

R. Quek · K. H. Chiam

A*STAR Institute of High Performance Computing, 1 Fusionopolis Way,
#16-16Singapore 138632, Singapore
e-mail: quekyl@ihpc.a-star.edu.sg

K. M. Lim

Department of Mechanical Engineering, National University of Singapore,
9 Engineering Drive 1, Singapore 117576, Singapore
e-mail: limkm@nus.edu.sg

K. H. Chiam (✉)

Mechanobiology Institute, National University of Singapore, T-Lab,
5A Engineering Drive 1, #05-01Singapore 117411, Singapore
e-mail: chiamkh@bii.a-star.edu.sg

1 Introduction

In many systems of biological interest, fluid propulsion at the micrometer scale is accomplished through the use of organelles known as cilia or flagella. These organelles are either active, comprising beating axonemes as their internal structure, or passive, being rotated by motors at their bases (Berg 1975), or are completely non-motile and devoid of autonomous movement. Motile cilia and flagella are made up of nine microtubule doublets arranged cylindrically around a central pair of microtubules, commonly referred to as the “9 + 2” axoneme (Fauci and Dillion 2006). The axoneme is powered by dynein motors arranged along the lengths of microtubule doublets, giving rise to a distinctive beat pattern. On the other hand, passive cilia and flagella lack the central pair of microtubules, leading to a “9 + 0” structure. Passive flagella are being driven by motors at their bases. These motors are powered by movement of hydrogen ions through the cell membrane caused by electrochemical gradients set up by cell metabolism. Passive non-motile cilia, or primary cilia as they are commonly known, do not possess autonomous movement.

There have been various experimental (Guasto et al. 2011, Gao et al. 2010) and numerical (Dillion et al. 1996, Hsu and Dillion, 2009) studies on flagellated propulsion. Guasto et al. have shown that spermatozoa can spontaneously alter their flagella beat to alter their swimming trajectories. Using artificial micro-swimmers, Gao et al. have shown how changing the micro-swimmer geometry enables it to change from a “pusher” to a “puller”. Dillion et al. have used the Immersed Boundary Method (IBM) to simulate accumulation of bacteria to form bio-films. Hsu and Dillion have further shown how the Immersed Boundary Method can be applied to simulate free-swimming bacteria.

Similarly, there have been numerous efforts to understand the cilia beat cycle. One early attempt by Sugina and Naitoh (1982) found the activation sequence of dynein motors required to give a cilium the shapes observed in experiments. However, while the dynein activation sequence is now known, the underlying mechanism giving rise to the sequence is still largely a mystery (Brokaw 2001).

Cilia are known to perform various biological functions. An early attempt to study the effect of cilia beat on mucus transport was undertaken by Sanderson and Sleight (1981). The authors describe the existence of short-range metachronal waves across small cilia patches. In addition, a two-layer transport mechanism is observed. During the effective stroke, cilia tips extend into the mucus layer to push the mucus forward, while during the recovery stroke, the cilia return to their initial positions beneath the mucus layer. This difference between forward and recovery strokes results in driving of the fluid.

Breuning et al. (2010) have described how cilia serve to maintain homeostasis in the brain. Neural precursor cilia have been shown to regulate sonic hedgehog (shh) signaling (Breuning et al. 2008). An example of hydrodynamic interactions with cilia formation in the brain is described by Guirao et al. (2010), where the

authors study the effects of cerebral-spinal fluid flow on the orientation of cilia from ependymal cells.

Cilia are also used for propulsion in swimming micro-organisms, an example of which is *Paramecium*. Iwadate and Nakaoka (2008) have shown that when caged calcium introduced into the environment of a swimming *Paramecium* is broken down by ultra-violet light, the released calcium ions cause a reversal in the direction of cilia forward stroke. This is accompanied by a contraction of the entire *Paramecium*. The authors suggest that this release of calcium ions is a mechanism which the *Paramecium* uses to change its trajectory while swimming.

Another micro-swimmer that makes use of cilia for propulsion is *Volvox*. Drescher et al. (2009) have studied the hydrodynamical interactions of mating *Volvox* pairs. To model the effect of the numerous surface flagella, resistive force theory is applied to the *Volvox* surface while lubrication theory is applied to the narrow gap between the *Volvox* pairs. The authors then study the different trajectories formed and suggest that the spiraling action helps in increasing the frequency of *Volvox* contacts, greatly helping in reproduction processes.

In addition to these biological systems, there have also been interests in artificial cilia for the purpose of exploiting their numerous naturally occurring properties, examples of which include enhanced diffusion and improved mixing. For example, magnetic cilia arrays driven by external magnets have been fabricated and studied by Shields et al. (2010). The sweeping motion of each cilium forms a cone which mimics the cilium motion in a mouse embryo node. By observing nanoparticles suspended in the fluid, the authors describe two flow regions. The first flow region is occupied by bulk flow above the cilia tips. Here a Poiseuille-Couette flow with a recirculation region is established. The second flow region takes place below the cilia tips. Here the motions of particles are rapid but nondirectional. This region offers improved effective diffusivity.

Similar experiments using artificial cilia have been conducted by Barataheri et al. (2011). A carpet of cilia is created and is similarly subjected to oscillating magnetic fields. The shapes from the experiments are shown to be in good agreement with shapes predicted from resistive force theory.

An example of a numerical simulation involving cilia is done by Alexeev et al. (2008). The authors describe how a net flow volume reversal is possible when the cilia bending stiffness, beat frequency, length and fluid viscosity are varied in some intermediate range.

The effect of metachronal waves in cilia beds have been numerically studied by Khaderi et al. (2011). The authors find that when cilia densities are low, metachronal wave speeds do not result in a significant difference in net flux. However when cilia densities are high, there is significantly greater net flux in presence of antiplectic waves compared to symplectic waves. The authors conclude that antiplectic metachrony should therefore be favored in nature, but note that there are many organisms that exhibit symplectic metachrony. This suggests symplectic metachronal waves may be optimized for some other as yet unknown property.

Realistic two-dimensional simulations of cilia using the Immersed Boundary Method have been presented by Dillion et al. (2003). The cilia are modelled as a pair

of microtubules, each represented by spring filaments with diagonal cross-links. Curvature between the two microtubules is used to determine if the dynein springs are in the forward or reverse stroke. The authors show that the spring model can be used to model a beating cilium or the flagellum on a swimming organism. Further discussions on dynein activation models are given by Murase (1992).

Mitran (2007) constructed a highly realistic cilia model by modeling the microtubules of the “9 + 2” axoneme as beams. The cilia are immersed in a Newtonian fluid beneath a viscoelastic fluid. These fluids correspond to the periciliary layer and the mucus layer respectively. By adjusting the dynein phase difference between adjacent microtubules to minimize work done, cilia arrays are shown to synchronize.

An alternative to explicit modelling of cilia is offered by Vilfan and Julicher (2006). Here, a pair of cilia are simplified into point forces moving in elliptical trajectories. By solving the incompressible Stokes equations, solutions to the flow-field can be obtained. The authors present solutions to show the regions in space where cilia beat in synchrony or asynchrony.

Osterman and Vilfan (2011) have used a series of beads to represent individual cilium within large beds of cilia. By solving the motion of the cilia as an optimization problem, the authors report that antiplectic metachronal waves give maximum pumping efficiency. The authors also report that initial pumping efficiency increases with increasing cilia number density, but as the cilia bed becomes overcrowded beyond an optimum, pumping efficiency is reduced.

Although these examples show that there has been a lot of work done to understand the workings and dynamics of cilia and flagella, much remains to be studied. The mechanics of formation of metachronal waves are still not well understood. Most numerical studies in this aspect remain two-dimensional, while in nature the transmission of metachronal waves, for example over the body surface of *Paramecium*, takes place in three dimensions.

In this chapter, we use numerical methods to investigate formation and effects of metachronal waves on a cilia bed. This arrangement mimics the cilia lining the respiratory or intestinal tracts, as well as the cilia on multi-ciliated or multi-flagellated swimmers such as *Paramecium* and *Volvox*. Our objective is to simulate realistically the beating of such cilia and how they couple to the hydrodynamics to generate metachronal waves. We also attempt to investigate wave properties such as wave speed and frequency as well as transport properties of fluid over the cilia bed.

2 Numerical Method

We simulate the beating of individual cilium, each of length L , arranged periodically in an array. These cilia are driven independently, but are all immersed in a viscous fluid that also serves to couple the cilia hydrodynamically. Our simulation is based on the Immersed Boundary Method (IBM). It is first described by Peskin

(2002) as a way to simulate moving membranes immersed in fluid. One of its first applications is to model the pumping movements of the human heart (McQueen and Peskin 2001). Since then, it has been applied to a multitude of problems that are biological in nature.

In our model, each cilium in the array is treated as a one-dimensional elastic structure immersed in a Newtonian fluid. The fluid is regarded as viscous and incompressible. The governing equations for the fluid is thus the momentum equation,

$$\rho \left(\frac{\partial \vec{u}}{\partial t} + (\vec{u} \cdot \nabla) \vec{u} \right) = -\nabla p + \mu \nabla^2 \vec{u} + \vec{F}(\vec{x}, t), \tag{1}$$

and the continuity equation,

$$\nabla \cdot \vec{u} = 0. \tag{2}$$

Here, ρ is the fluid density, μ the fluid dynamic viscosity, $\vec{u} = [u \ v \ w]^T$ the fluid velocity, p the pressure, and $\vec{F}(\vec{x}, t) = [F_x \ F_y \ F_z]^T$ the force per unit volume on the fluid.

The force acting on the cilium is given as $\vec{f}(\vec{X}, t) = [f_x \ f_y \ f_z]^T$, where $\vec{X} = \vec{X}(s, t)$ denotes the coordinates of the cilium control point and s is the Lagrangian coordinates of that cilium control point.

The force on the cilium is transferred to the fluid using

$$\vec{F}(\vec{x}, t) = \int \frac{\partial \vec{f}}{\partial s}(\vec{X}, t) \delta(\vec{x} - \vec{X}(s, t)) ds, \tag{3}$$

where $\frac{\partial \vec{f}}{\partial s}$ is the force per unit length along the cilium and $\delta(\vec{x} - \vec{X})$ is a three-dimensional Dirac delta function that serves to transfer the forces on the cilium control points onto the fluid grid points. In our implementation Eq. 3 is approximated as

$$\vec{F}(\vec{x}, t) \approx \sum_{m=1}^N \vec{f}_m(\vec{X}, t) \hat{\delta}(\vec{x} - \vec{X}_m(s, t)), \tag{4}$$

where N is the number of control points making up the cilium. As shown by Peskin (2002), the delta function $\delta(\vec{x} - \vec{X})$ in Eq. 3 can be approximated as

$$\hat{\delta}(\vec{x} - \vec{X}(s, t)) = \begin{cases} \prod_{i=1}^3 \frac{1}{4h} \left[1 - \cos\left(\frac{(x_i - X_i(s, t))\pi}{2h}\right) \right] & \text{for } 0 \leq |\vec{x}_i - \vec{X}_i(s, t)| \leq 2h \\ 0 & \text{for } 2h < lt; |\vec{x}_i - \vec{X}_i(s, t)| \end{cases}, \tag{5}$$

where h is the distance between fluid grid points and i denotes the three principal orthogonal directions in Cartesian coordinates.

Both the non-linear convective term $(\vec{u} \cdot \vec{\nabla})\vec{u}$ and the forcing term $\vec{F}(\vec{x}, t)$ in Eq. 1 are treated explicitly and discretized using the second-order Adam-Bashforth method. The linear viscous term $\mu \nabla^2 \vec{u}$ is treated implicitly and discretized using the second-order Crank–Nicholson method. In our implementation, the pressure field is solved at half time steps in between solving for the velocity field. The discretized momentum equation is therefore

$$\rho \left[\frac{\vec{u}^* - \vec{u}^n}{\Delta t} + \frac{3}{2} \left((\vec{u} \cdot \vec{\nabla})\vec{u} \right)^n - \frac{1}{2} \left((\vec{u} \cdot \vec{\nabla})\vec{u} \right)^{n-1} \right] = - \left(\vec{\nabla} p \right)^{n-1/2} + \mu \frac{1}{2} \left[(\nabla^2 \vec{u})^* + (\nabla^2 \vec{u})^n \right] + \left[\frac{3}{2} (\vec{F}(\vec{x}, t))^n - \frac{1}{2} (\vec{F}(\vec{x}, t))^{n-1} \right], \quad (6)$$

where intermediate velocities \vec{u}^* are solved. Following, a pressure correction term φ is solved using

$$\frac{\vec{\nabla} \cdot \vec{u}^*}{\Delta t} = \nabla^2 \varphi. \quad (7)$$

The velocities are updated to the $(n + 1)$ th time step using

$$\vec{u}^{n+1} = \vec{u}^* - \Delta t \left(\vec{\nabla} \varphi \right), \quad (8)$$

and finally the pressure is updated to the $(n + 1/2)$ th time step using

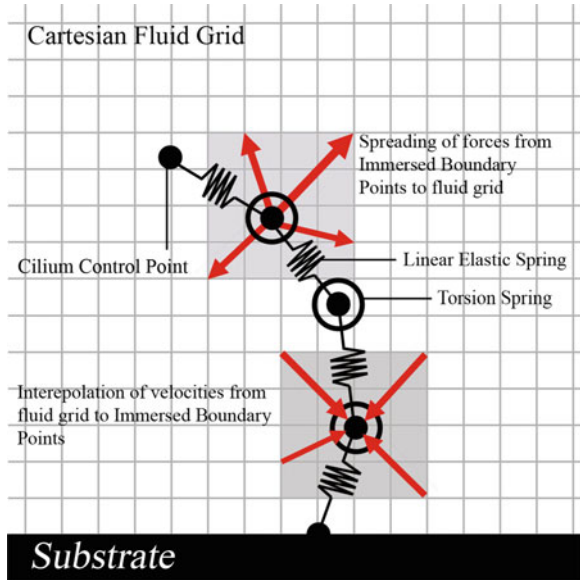
$$p^{n+1/2} = p^{n-1/2} + \varphi - \frac{\Delta t}{2} \left(\vec{\nabla} \cdot \vec{u}^* \right). \quad (9)$$

This concludes the advancement of the Navier–Stokes equation by one time step.

The spatial derivatives are discretized with a second-order central-difference scheme. The above equations are solved on a Marker-and-Cell (MAC) (Tannehill et al. 1997) grid. In our implementation, the velocity variables are solved at locations staggered from regular grid points: u is staggered half grid points in the y - and z - directions, v is staggered half grid points in the x - and z - directions, and w is staggered half grid points in the x - and y - directions. The pressure p and pressure correction variable φ are solved at cell centers and $\vec{F}(\vec{x}, t)$ is defined on cell grid points.

Each cilium is assumed to be neutrally buoyant and massless. Figure 1 shows a schematic of the IBM as applied to a cilium. A series of control points representing the discretized cilium is superimposed over a Cartesian fluid grid. The cilium is modeled using a rod-and-spring model. Due to the nature of the IBM, the fluid grid points and the cilium control points need not coincide. Linear elastic springs imposed between the cilium control points provide resistance to stretching and torsion springs imposed at each cilium control point provide resistance to bending.

Fig. 1 Schematic of a cilium in the context of the Immersed Boundary Method (IBM). The cilium is discretized as a series of control points connected by linear elastic springs. The inclusion of torsion springs at control points provides bending resistance. Forces are spread to the fluid grid for the solving of the Navier–Stokes equations. After the Navier–Stokes equations are solved, velocities are interpolated from the fluid grid to advect the cilium control points



The force $\vec{f}(\vec{X}, t)$ at each cilium control point is the sum of the stretching, bending, and driving forces, and is calculated as

$$\vec{f} = \vec{f}_{elastic} + \vec{f}_{moment} + \vec{f}_{active}. \quad (10)$$

Here, $\vec{f}_{elastic}$ is the restoring force from a linear spring, given by

$$\begin{aligned} \vec{f}_{elastic}(\vec{X}_i, t) = & -k(|\vec{X}_{i+1} - \vec{X}_i| - \Delta s_0) \frac{\vec{X}_i - \vec{X}_{i+1}}{|\vec{X}_i - \vec{X}_{i+1}|}, \\ & -k(|\vec{X}_{i-1} - \vec{X}_i| - \Delta s_0) \frac{\vec{X}_i - \vec{X}_{i-1}}{|\vec{X}_i - \vec{X}_{i-1}|} \end{aligned} \quad (11)$$

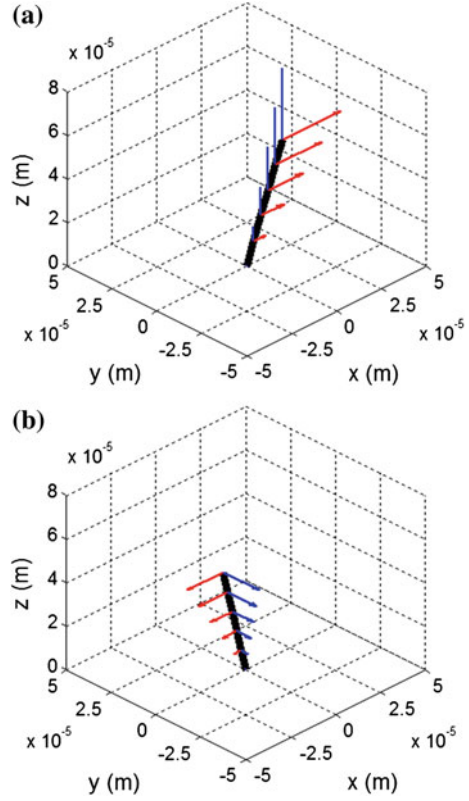
where k is a spring constant and $\Delta s_0 = L/(N - 1)$ is the natural length of the linear elastic spring connecting two adjacent points.

The second term in Eq. 10, \vec{f}_{moment} , is the force at each discretized cilium control point arising from moments in the cilium. It is given by

$$\begin{aligned} \vec{f}_{moment}(\vec{X}_i, t) = & -\frac{\vec{X}_{i+1} - \vec{X}_i}{|\vec{X}_i - \vec{X}_{i+1}|^2} \times \vec{M}_{i+1} + \frac{\vec{X}_{i-1} - \vec{X}_i}{|\vec{X}_i - \vec{X}_{i-1}|^2} \times \vec{M}_{i-1}, \\ & + \frac{\vec{X}_{i+1} - \vec{X}_i}{|\vec{X}_i - \vec{X}_{i+1}|^2} \times \vec{M}_i - \frac{\vec{X}_{i-1} - \vec{X}_i}{|\vec{X}_i - \vec{X}_{i-1}|^2} \times \vec{M}_i \end{aligned} \quad (12)$$

where \vec{M} is the moment at each cilium point,

Fig. 2 **a** Forces of the forward stroke $\vec{f}_{forward}$. Triangular loads are applied in the positive x -direction (red arrows) and in the positive z -direction (blue arrows). **b**. Forces of the reverse stroke $\vec{f}_{reverse}$. Triangular loads are applied in the negative x -direction (red arrows) and in the negative y -direction (blue arrows)



$$\vec{M} = -T(\vec{\theta} - \vec{\theta}_0), \quad (13)$$

with T a torsional spring constant. This torsional restoring force arises when adjacent cilium control points form angular deviations from $\vec{\theta}_0$, which is the natural angle defined between the control points. In our simulations, each cilium is a straight filament in its natural state, hence $\vec{\theta}_0 = 0$. In the regime where k is high, the rod-and-spring model can be used to represent an Euler–Bernoulli beam where the bending modulus EI is obtained as

$$EI = T\Delta s_0. \quad (14)$$

In our simulations, k is set stiff enough to render cilia stretch largely negligible.

The cilium is also modeled as being driven by an active force, \vec{f}_{active} , which is applied in two steps, $\vec{f}_{forward}$ and $\vec{f}_{reverse}$. The first step $\vec{f}_{forward}$ causes the cilium to undergo a forward stroke (Fig. 2a) while the second step $\vec{f}_{reverse}$ causes the cilium to undergo a reverse stroke (Fig. 2b). We implement $\vec{f}_{forward}$ as distributed

triangular loads in the positive x - and z - directions while $\vec{f}_{reverse}$ consists of distributed triangular loads in the negative x - and y - directions. At each control point,

$$\vec{f}_{forward}(\vec{X}, t) = f_x(\vec{X}, t) (\vec{i} + \alpha \vec{k}), \quad (15)$$

$$\vec{f}_{reverse}(\vec{X}, t) = -f_x(\vec{X}, t) (\vec{i} + \beta \vec{j}). \quad (16)$$

where

$$f_x(\vec{X}(s, t), t) = f_0 s, \quad (17)$$

with f_0 a force per unit length that determines the strength of the active strokes and α and β are parameters used to modify the cilium motion in the forward and reverse directions respectively. In our simulations, we choose $\alpha = 4$ and $\beta = 2$.

The energy expended by the cilium as it transverses in the x -direction is given by

$$E(t) = \iint \begin{bmatrix} u \\ 0 \\ 0 \end{bmatrix} \cdot \frac{\partial \vec{f}_{active}}{\partial s} ds dt, \quad (18)$$

In order to determine if the cilium is in the forward or reverse stroke, we apply the following switching criterion

$$\vec{f}_{active}(\vec{X}, t) = \begin{cases} \vec{f}_{forward}(\vec{X}, t) & \text{if } E(t) = E_0 \text{ and cilium is in reverse stroke} \\ \vec{f}_{reverse}(\vec{X}, t) & \text{if } E(t) = E_0 \text{ and cilium is in forward stroke} \end{cases}, \quad (19)$$

where E_0 is a predefined energy level.

Equations 18 and 19 can be viewed as a mechanism whereby the cilium switches from a forward stroke to a reverse stroke when the cilium has expended energy E_0 transversing in the positive x direction, and subsequently switches from a reverse stroke to a forward stroke when the cilium has expended energy E_0 transversing in the negative x direction.

Since the length and velocity scales in our problem are small, we can assume that the flow generated by our cilia takes place at zero Reynolds numbers. It is well known that reciprocal movements at zero Reynolds numbers cannot produce a net fluid flux (Purcell 1977). However, the cilia movements in our simulations are not reciprocal. The forward stroke is designed to be different from the reverse stroke, as can be seen in Eqs. 15–17. As such, net fluid propulsion is achieved in our system. In addition, the presence of cilia undergoing large, non-linear deformations renders the flow field non-reversible.

It should also be noted that by imposing the energy expended by the active force \vec{f}_{active} , the cilium oscillates with an intrinsic amplitude and frequency. This amplitude and frequency depend on the stiffness of the cilium and its interaction with surrounding cilia and fluid.

The force $\vec{f}(\vec{X}, t)$ in Eq. 10 exerted by the cilium is then transmitted to the fluid and the Navier–Stokes equations are solved. Solving the Navier–Stokes equations provides us with the fluid velocities and pressure. The velocities are then used to advect the cilium control points by interpolating velocities from the fluid grid using

$$\left(\frac{\partial \vec{X}_m(s, t)}{\partial t}\right)^{n+1} = \sum_{r=1}^{N_z} \sum_{q=1}^{N_y} \sum_{p=1}^{N_x} \vec{u}_{p,q,r}(x, t) \hat{\delta}(\vec{x}_{p,q,r} - \vec{X}_m(s, t)), \quad (20)$$

where $\left(\frac{\partial \vec{X}_m(s, t)}{\partial t}\right)^{n+1}$ is the velocity of cilium control point m at time $n + 1$. The variables p, q, r , and N_x, N_y, N_z are the fluid grid indices and the total number of fluid grid points in the x, y and z - directions, respectively. The positions of the cilium points are next updated implicitly using the second-order Crank-Nicolson method by

$$\vec{X}^{n+1}(s, t) = \frac{1}{2} \left[\left(\frac{\partial \vec{X}(s, t)}{\partial t}\right)^{n+1} + \left(\frac{\partial \vec{X}(s, t)}{\partial t}\right)^n \right] \Delta t + \vec{X}^n(s, t). \quad (21)$$

The IBM implemented for our ciliary flow simulations can thus be summarized as follows: assuming the fluid velocity \vec{u}^n and the position of the cilium \vec{X}^n at time step n are known, the IBM advances the system by Δt using the following procedure:

1. Calculate $\vec{f}(\vec{X}, t)$ on the cilium due to its present position $\vec{X}^n(s, t)$ using Eqs. 10, 11, 12 and 19
2. Spread the force $\vec{f}(\vec{X}, t)$ to the fluid grid points to obtain $\vec{F}(x, t)$ at all fluid grid points as described in Eqs. 4 and 5.
3. Solve the momentum equations (Eq. 6) for the intermediate velocities \vec{u}^* .
4. Solve Eq. 7 for the pressure correction φ .
5. Obtain updated velocities \vec{u}^{n+1} and pressure $p^{n+1/2}$ at the next time step using Eqs. 8 and 9.
6. Interpolate the fluid velocities to the cilium to obtain the position of the cilium at the next time step $\vec{X}^{n+1}(s, t)$ using Eqs. 20 and 21.
7. Advance $t \rightarrow t + \Delta t$ and repeat from Step 1.

The parameters used in our simulations are listed in Table 1.

In our implementation, the intermediate velocities \vec{u}^* in Eq. 6 are cast as Helmholtz equations and the pressure correction term φ in Eq. 7 is cast as a Poisson equation. These equations are solved in parallel using the Generalized minimal residual method (GMRES). We implement this method using the Hypre library (Center for Applied Scientific Computing, Lawrence Livermore National Laboratory 2006). Hypre is an open source library that uses Message Passing Interface (MPI) for solving large linear systems of equations. The advantage of Hypre lies in its provision of parallel high-performance preconditioners. Solving

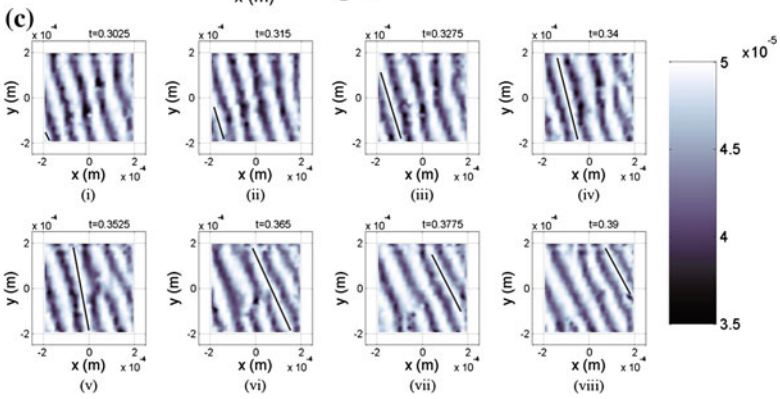
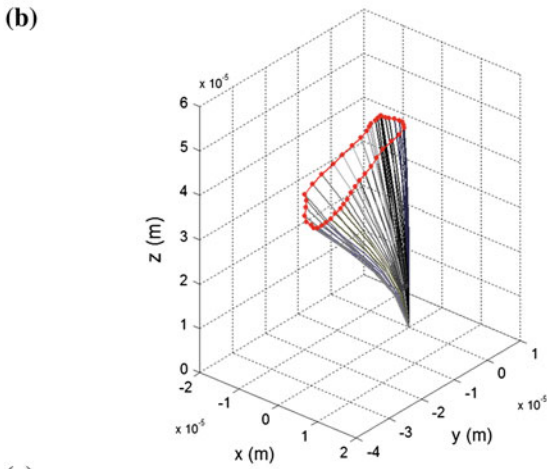
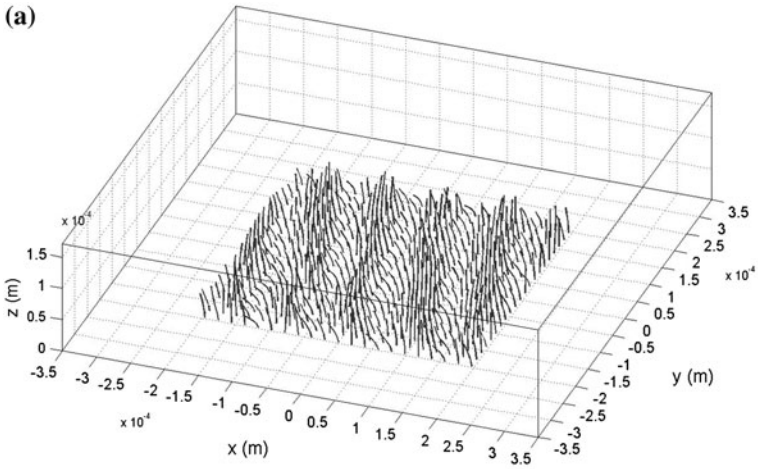
Table 1 Summary of parameters and their values used in the simulations

	Description	Symbol	Units	Value
Cilia parameters	Cilia length	L	m	4.91×10^{-5}
	Cilia bending stiffness	EI	Nm^2	$6.90 \times 10^{-23} - 1.38 \times 10^{-18}$
	Cilia stretching stiffness	k	N/m	1.2×10^{-2}
	Energy expanded by cilia per stroke	E_0	J	6.4×10^{-10}
	Forcing magnitude on cilia	f_0	N/m	6.6
	Cilia number density	d^{-2}	m^{-2}	$1.15 \times 10^9 - 4.06 \times 10^9$
Fluid parameters	Fluid density	ρ	kgm^{-3}	1000
	Fluid dynamic viscosity	μ	$kgm^{-1}s^{-1}$	1.0×10^{-3}
Fluid domain dimensions	Chamber length	L_Ω	m	$5.6 \times 10^{-4} - 1.05 \times 10^{-3}$
	Chamber width	W_Ω	m	$5.6 \times 10^{-4} - 1.05 \times 10^{-3}$
	Chamber height	H_Ω	m	1.72×10^{-4}
Numerical parameters	Number of cilia control points	N_c	–	6
	Time step size	Δt	s	5.0×10^{-6}
	Fluid grid size	h	m	4.40×10^{-6}

our equations in parallel gives us tremendous time savings. For example, simulating 40,000 time steps with a total of 1,024,000 fluid grid points and 2,646 cilia control points from a bed of 21 by 21 cilia require approximately 2.2 days on 32 cores and approximately 1.0 days on 64 cores, a reduction in computational time by about 50 %. Our simulations are run on a Fujitsu BX900 with Intel Xeon 5570 2.93 GHz processors.

3 Results and Discussion

We construct a cilia bed consisting of 21 by 21 equally spaced cilia each with bending stiffness $EI = 3.45 \times 10^{-19} Nm^2$. This value is chosen such that EI is large enough to have an effect on cilia dynamics. In comparison, the bending stiffness of singular microtubules have been shown experimentally to vary from $EI \sim 10^{-24} - 10^{-23} Nm^2$ (Gittes et al. 2003, Felgner et al. 1996). The cilia are arranged in a square lattice of side $1.96 \times 10^{-4} m$ (Fig. 3a). Each cilium is of length $4.91 \times 10^{-5} m$. This length is similar to that of artificial cilia investigated by Barataheri et al. (2011). Figure 3b shows a representation of the deformations of a representative cilium as it evolves through a single cycle. The forcing functions described in Eqs. 15–19 cause the cilia to sweep through a conical path. It is observed that although minor variations occur between cycles, the oscillatory motion is distinct and appear stable throughout the duration of our simulations. We



◀ **Fig. 3** **a** Arrangement of the cilia bed of 21 by 21 equally spaced cilia. The bed measures $1.96 \times 10^{-5} m$ by $1.96 \times 10^{-5} m$ and a cilium bending stiffness of $EI = 3.45 \times 10^{-19} Nm^2$ is used. **b** Deformation of a cilium as it evolves through a representative cycle. **c** Snapshots in time of contour plots formed by the heights of cilia tips above the substrate. Light colors denote locations where cilia are in the power stroke. This is when the cilia are mostly upright and the height of their tips are maximum, i.e., a wave crest. Dark colors denote locations where cilia are in their reverse stroke. This is when the cilia are bent and their tips are closer to the substrate, i.e., a wave trough. The black line marks a wave crest as it travels across the cilia bed

suggest the forward stroke serves to generate waves traveling in the x -direction while the reverse stroke, which takes place mostly in the y -direction, serves to couple adjacent cilia to form a wave front.

We establish that metachronal waves are formed spontaneously over the cilia bed. Figure 3c shows snapshots of contour plots obtained by the height of cilia tips above the substrate. Light contours therefore represent cilia that are in the forward stroke while dark contours represent cilia in the reverse stroke.

It is observed that metachronal waves form quickly within the first 0.02 s. This corresponds to approximately the first cycle of cilia oscillations. By $t = 0.07$ s, the metachronal waves are fully formed and translate across the cilia bed at constant velocity. We observe that most of the waves formed are symplectic in nature, i.e., the direction of wave travel is in the direction of the forward stroke.

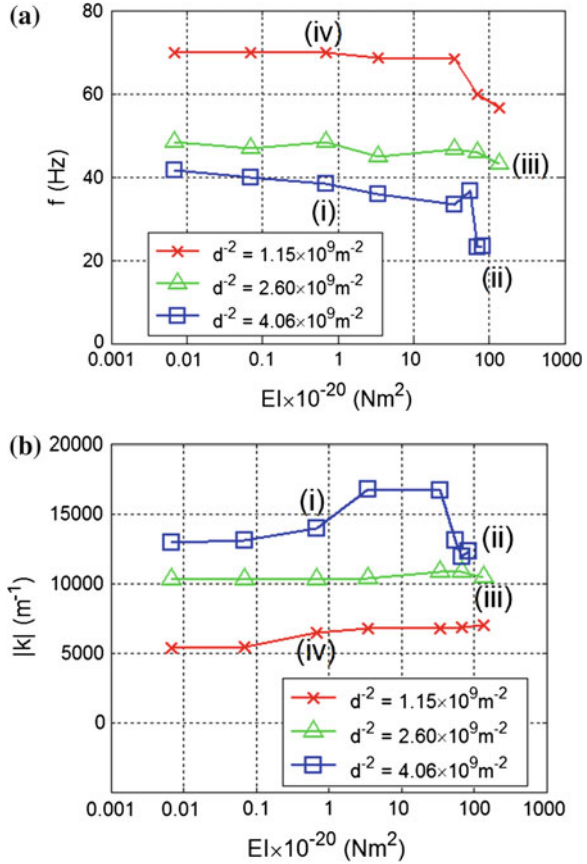
3.1 Characteristics of Metachronal Waves

To study what governs the speed of the metachronal waves, we systematically vary several parameters in our simulations: the bending stiffness of cilia from $EI = 6.90 \times 10^{-23} Nm^2$ to $EI = 1.38 \times 10^{-18} Nm^2$ and the cilia number density from $d^{-2} = 1.15 \times 10^9 m^{-2}$ to $d^{-2} = 4.06 \times 10^9 m^{-2}$, where d is the distance between adjacent cilia. We observe that for bending stiffness below $EI = 6.90 \times 10^{-21} Nm^2$, bending rigidity has little effect on cilia motion as both the viscous stresses and the active stresses acting on the cilia are much greater than the bending rigidity.

By performing discrete fast Fourier transforms on the contour plots in Fig. 3c, we are able to extract the magnitude of wave vector in the direction of wave travel, $|k|$, and the intrinsic frequency, f , of the waves. Incidentally, we also find that f matches the frequency of the individual cilium as it cycles through its motion.

These results are summarized in Fig. 4. From panel (a), we see that, as cilia number density increases from $d^{-2} = 1.15 \times 10^9 m^{-2}$ to $d^{-2} = 4.06 \times 10^9 m^{-2}$, the metachronal wave frequency f is reduced. We attribute this behavior to the fact that as cilia number density increases, the gaps between adjacent cilia are narrowed. The fluid between the increasingly narrow gaps experiences high shear stresses as the cilia deform. The fluid is then a source of resistance to the motion of the cilia. This resistance opposes the active force, \vec{f}_{active} , hence reducing the net

Fig. 4 a Variation of metachronal wave frequency f with cilia bending stiffness EI . **b** Variation of metachronal wave vector magnitude $|k|$ with cilia bending stiffness EI



active force on the cilia and therefore resulting in slower cilia motion and lower wave and cilia frequencies.

Next, we observe that the bending stiffness of the cilia, EI , does not significantly affect the metachronal wave frequency f when $EI < 10^{-19} \text{ Nm}^2$. However, for large bending stiffness $EI > 10^{-19} \text{ Nm}^2$, increasing EI results in a decrease in f . This is attributed to the increasing resistance to cilia motion from increased stiffness. Increased stiffness will similarly reduce the net active force on the cilia, hence reducing the wave and cilia frequencies. This is evident from the contour plots in Fig. 5b and c where the light contours indicate only slight deformations of stiff cilia. However if the bending stiffness of the cilia is small, the active force on the cilia is mainly balanced by the drag from the fluid, resulting in a situation where bending stiffness does not affect the cilia motion.

Figure 4b shows the variations of the magnitude of wave vector in the direction of wave travel, $|k|$, versus EI . It can be seen as cilia number density

increases, there is a corresponding increase in $|k|$. Increase in bending stiffness does not have a significant change in $|k|$ for cilia number densities of

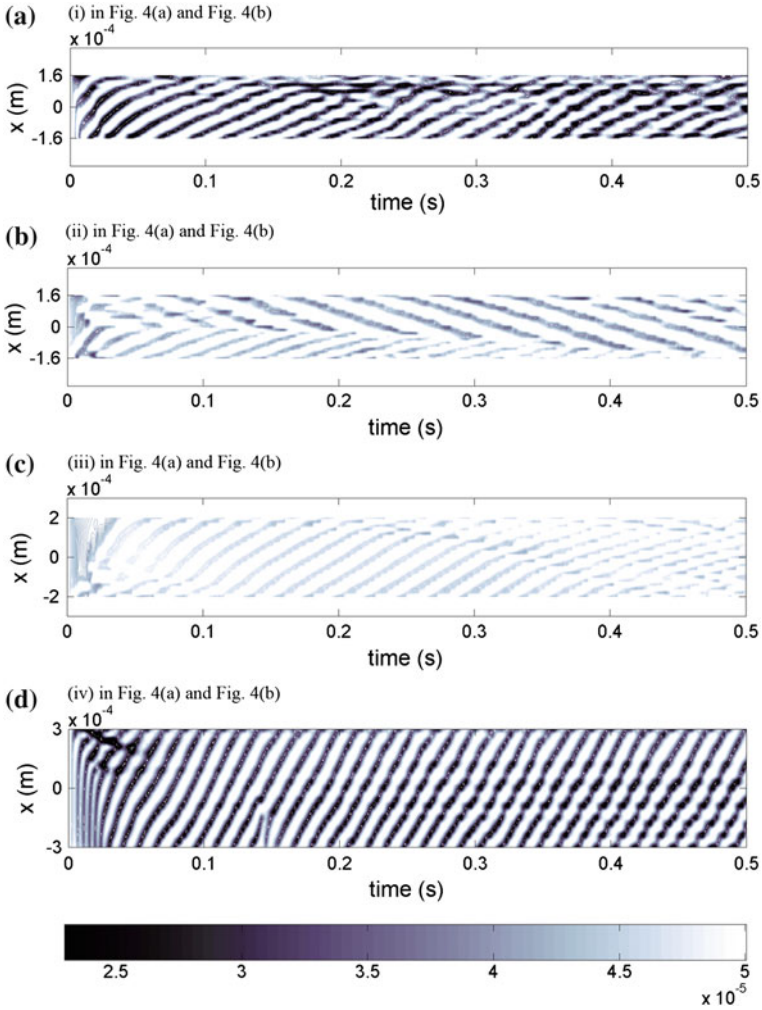


Fig. 5 Variations of cilia tip heights in time for the following scenarios: **a** $EI = 6.90 \times 10^{-21} Nm^2$ and $d^{-2} = 4.06 \times 10^9 m^{-2}$, **b** $EI = 8.27 \times 10^{-19} Nm^2$ and $d^{-2} = 4.06 \times 10^9 m^{-2}$, **c** $EI = 1.38 \times 10^{-18} Nm^2$ and $d^{-2} = 2.60 \times 10^9 m^{-2}$ and **d** $EI = 6.90 \times 10^{-21} Nm^2$ and $d^{-2} = 1.15 \times 10^9 m^{-2}$. (a), (b), (c) and (d) are correspondingly marked as (i), (ii), (iii) and (iv) in Fig. 4a and b. In all four scenarios, slices at mid plane $y = 0$ are shown. Cilia in the reverse stroke have their tips lower than cilia in the forward stroke, giving rise to light and dark bands representing wave fronts

$d^{-2} = 1.15 \times 10^9 m^{-2}$ and $d^{-2} = 2.60 \times 10^9 m^{-2}$. However we observe that for a cilia number density of $d^{-2} = 4.06 \times 10^9 m^{-2}$ at high stiffness, symplectic metachronal waves become unstable and antiplectic waves momentarily form (Fig. 5b). At $EI \sim 10^{-18} Nm^2$, metachronal waves of low amplitudes are formed.

These waves eventually display discontinuous crests and troughs and are unable to transverse the entire cilia bed (Fig. 5c).

By comparing Fig. 5a and d, we observe that wave fronts in Fig. 5a display lower gradients than wave fronts in Fig. 5d. This suggests that as cilia number density decreases, metachronal wave velocity increases. This observation is reinforced by Fig. 4a and b. As d^{-2} decreases, f increases. This is accompanied by a decrease in $|k|$ and hence an increase in wavelength λ . Since metachronal wave speed $c = f\lambda$, we can conclude that as cilia number density d^{-2} decreases, metachronal wave speed increases.

It is also of interest to study how the propagation of metachronal waves can be affected by external perturbations. For example, Naremtsu et al. (2013) showed that when the motions of a localized patch of cilia are reversed through the localized photorelease of caged calcium ions, metachronal waves are still able to pass through the patch, with no change in the wave's wavelength and frequency. This suggests that the propagation of metachronal waves are robust to localized perturbations, and further studies are needed to establish what is the spatial extent of perturbations needed to destabilize metachronal wave propagation. As a first step towards this, we attempt to use our model to simulate the cilia motion reversal in a localized cilia patch. We do this by explicitly reversing the forward and backstroke strokes in Eqs. 15 and 16 in a patch of 3×3 cilia. The results of this localized reversal of a cilia patch are shown in Fig. 6. We observe that the metachronal wave fronts become broken as they pass over the localized cilia patch (black line in Fig. 6e and f). As the wave fronts leave the cilia patch, the disruption in the wave front quickly vanishes as adjacent cilia again couple their movements through the reverse stroke (Fig. 6g).

It is evident in our simulations that cilia spacing and stiffness play a role in the metachronal wave characteristics. Our results show large values of the cilia stiffness, EI , reduce the frequency and amplitude of metachronal waves. Antiplectic metachronal waves are abundant in nature. It happens, for example, over the cilia of *Paramecium*. We find that antiplectic metachronal waves can be produced when cilia stiffness is taken into account. However our results show that antiplectic waves occur when cilia bending stiffness is several orders of magnitude larger than those found in nature. It is therefore likely another mechanism besides cilia stiffness is responsible for the production of antiplectic waves in natural biological systems.

3.2 *Optimal Cilia Number Density for Maximum Slip Velocity*

The flow field around a large cilia bed is often complex and difficult to resolve. One simple way to treat the flow field around a cilia bed is to assume that the cilia tips form a rigid wall but with a non-zero slip velocity boundary condition. We hereby attempt to quantify the slip velocities at the cilia tips in our simulations.

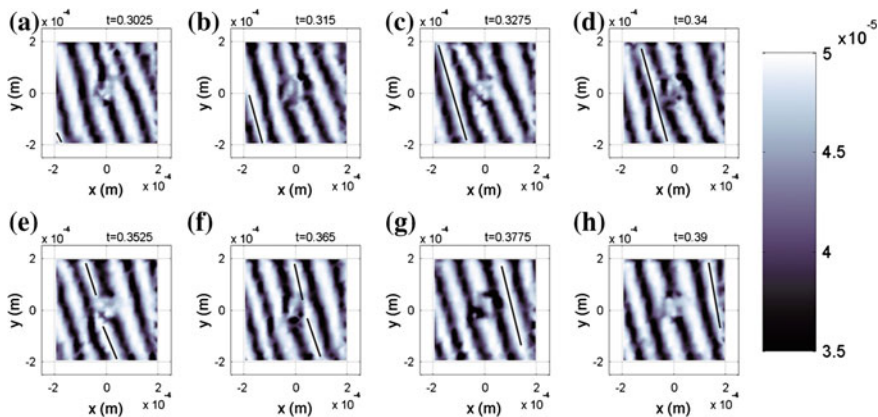


Fig. 6 By imposing cilia stroke reversals on a 3×3 array at the center of the cilia bed, we simulate the disruptive effects of local photorelease of caged calcium ions. We observe the breaking of metachronal waves as they pass through the localized patch. The metachronal waves quickly reform after they pass over the localized patch. The solid black line indicates the location of a wave crest as it transverses the entire cilia bed. In these simulations $EI = 6.90 \times 10^{-23} Nm^2$ and $d^{-2} = 2.60 \times 10^9 m^{-2}$

Figure 7a shows the average forward-stroke component of the velocity profiles in the chamber with a cilia number density of $d^{-2} = 2.60 \times 10^9 m^{-2}$. The average velocity profile for each cilia stiffness is obtained by averaging the velocities across a chosen area A at various heights z above the chamber floor. The average velocity at a particular z is calculated as

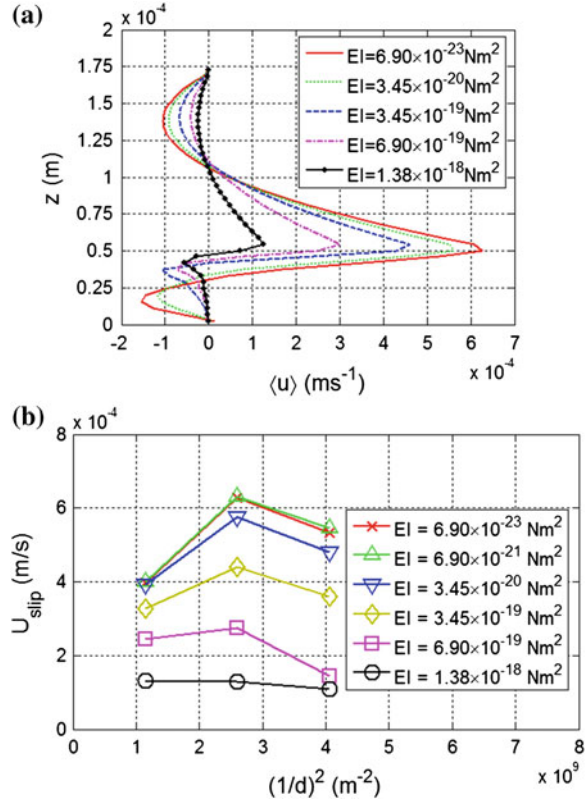
$$\langle \vec{u}_z \rangle = \frac{1}{TA} \iint \vec{u}_z dt dA, \tag{22}$$

where A is an area parallel to the x - y plane centered on the area occupied by the cilia bed A_c , \vec{u}_z the velocity at a particular height z above the chamber floor, and T a time interval large enough such that $\langle \vec{u}_z \rangle$ does not vary with T . In our simulations A is a square of area fixed at $0.19A_c$ and $T \sim 0.6 s$.

We observe that the velocity profiles display qualitatively the same features as described experimentally by Shields et al. (2010). These features consist of a parabolic profile above the cilia tips which include a recirculation region near the chamber ceiling, and a maximum velocity magnitude at the cilia tips which resembles a sliding plane boundary condition in Poiseuille-Couette flow. In other words, the cilia bed can be replaced by a boundary with a non-zero slip velocity. We now proceed to quantify this slip velocity.

We note that the average velocity profiles become less pronounced for higher cilia stiffness. This is because as the stiffness of each cilium is increased, the deformations of the cilium is reduced. This causes a reduction in cilium oscillation amplitude and hence a reduction in the amount of fluid the cilium pumps with each

Fig. 7 a Profile of $\langle u \rangle$, the component of velocity in the forward stroke as defined in Eq. 22, for different cilia stiffness at fixed number density $d^{-2} = 2.60 \times 10^9 m^{-2}$. **b** Slip velocity at cilia tip, as defined in Eq. 23, versus. cilia number density for various EI



cycle. Collectively, lesser fluid is pumped by the cilia bed and therefore average velocity profiles become less pronounced.

Figure 7b shows the magnitude of slip velocities for different cilia densities. Slip velocities are given as

$$U_{slip} = \langle \vec{u} \rangle_{z=L}. \quad (23)$$

We observe that for small values of cilia stiffness where $EI < 6.90 \times 10^{-21} Nm^2$, EI does not affect the slip velocity. However as EI increases, the slip velocity decreases. This is because cilia with high bending stiffness are resistant to deformation and do not pump fluid effectively.

We observe that a cilia number density of $d^{-2} = 2.60 \times 10^9 m^{-2}$ generally gives the highest slip velocity. This shows the existence of an optimum cilia number density which gives the highest slip velocity.

We suggest a mechanism that accounts for the existence of this optimum. As cilia number density increases over the optimum, the narrower fluid gaps in between cilia impose higher shear drag on the cilia during cilia motion, thus reducing the pumping efficiency of the cilia bed. Also as cilia number density

decreases, the larger fluid gaps between cilia form regions where fluid is not actively propelled by cilia, hence reducing the average slip velocity.

In our simulations, a reduction in U_{slip} occurs at a cilia spacing of $d = 0.3 L$. Osterman and Vilfan (2011) have reported a reduction in cilia pumping efficiency for $d < 0.25 L$. Excellent electron microscopy images of *Paramecium* by Allen (1971) show the distance of cilia on the surface are separated by $d \sim 1 \mu m$. Assuming a cilia length of $L = 5 \mu m$, we obtain $d \sim 0.2 L$. However, Carson et al. (1981) studied the formation of cilia in the human nasal epithelium and report an average inter-cilia spacing of $0.41 \mu m$. Again assuming $L = 5 \mu m$, we obtain $d \sim 0.1 L$. This suggests cilia spacing in the nasal epithelium is too small to be optimized. However, we note that cilia in the respiratory tract are surrounded by a complex arrangement of fluids. These fluids consist of a Newtonian-like periciliary layer below a viscoelastic mucus layer. The dynamics of cilia in this environment is therefore highly complex and more work is required to understand the dynamics of such a system.

It is well known that cilia in the respiratory tract may be damaged by the presence of inhaled pollutants. For example, research on mouse models show prolonged exposure to cigarette smoke reduces cilia beat frequency and results in shedding of cilia and loss of ciliated epithelial cells (Simet 2010). Our results indicate that as cilia number density decreases beyond the optimum, there is a drop in slip velocity. This indicates that advection velocities of particles above the cilia tips are reduced, thereby having a negative impact on the functioning of the respiratory system.

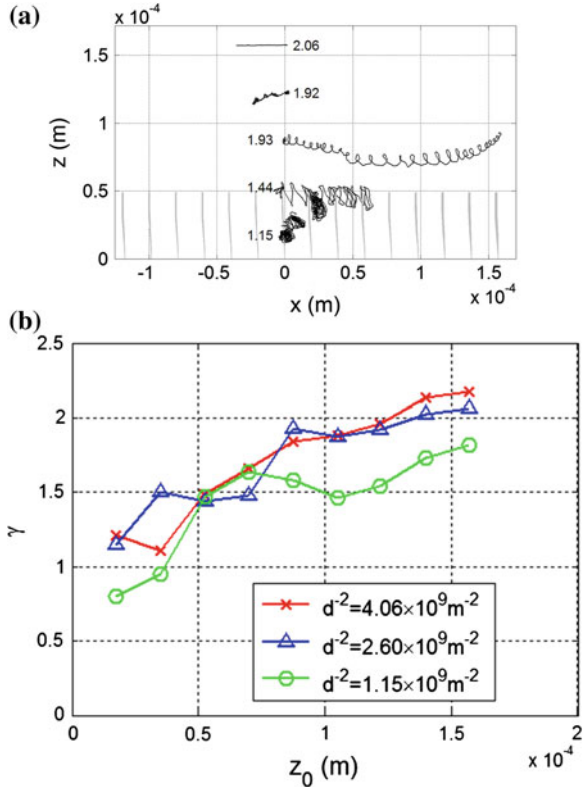
3.3 *Transport of Particles About the Cilia Bed Displays Both Diffusive and Advective Behaviors*

To study the transport properties of particles around a cilia bed, we place massless, passive tracer particles in the chamber and track their motion with time. These particles exert no forces and therefore do not have any effect on fluid motion. These particles are advected in a manner identical to the cilia control points. Their velocities are interpolated from the fluid grid using Eqs. 20 and 21. Figure 8a shows typical particle trajectories projected onto the x - z plane for a simulation with cilia number density of $d^{-2} = 2.60 \times 10^9 m^{-2}$ and $EI = 3.45 \times 10^{-20} Nm^2$. It is observed that particles below and around the cilia tips display spiral trajectories while particles far above the cilia tips display linear trajectories.

We calculate the least squares linear fit for the mean square displacement of the tracers, $\log|\bar{X}|^2$ versus $\log \tau$, to obtain the gradient γ :

$$\log|\bar{X}|^2 \propto \gamma \log \tau. \quad (24)$$

Fig. 8 a Particle trajectories projected onto the $x-z$ plane for particles seeded at different initial heights. Here, cilia number density is $d^{-2} = 2.60 \times 10^9 m^{-2}$ and cilia stiffness is $EI = 3.45 \times 10^{-20} Nm^2$. The numbers next to the trajectories indicate γ as defined in Eq. 24. **b** The exponent γ versus. initial height of tracer particle for various cilia number densities



Here τ is the time taken for the average particle to travel displacement $|\vec{X}|$. A value of $\gamma = 1$ indicates diffusive behavior of the particles and a value of $\gamma = 2$ indicates advective or ballistic behavior of the particles.

Figure 8b shows the variation of γ as a function of the initial height at which the particles are seeded. We observe that for cilia densities of $d^{-2} = 1.15 \times 10^9 m^{-2}$ to $d^{-2} = 4.06 \times 10^9 m^{-2}$, there is no significant difference in transport behavior. Particles close to the chamber floor generally have $\gamma \sim 1$ while particles close to the chamber ceiling generally have $\gamma \sim 2$.

We again note the complex fluid arrangements found in actual respiratory tracts. Particles above the cilia tips embedded in the mucus layer are actively pushed along while particles below the cilia tips are embedded in the periciliary layer and are advected less. Our results show particles below the cilia tips have a tendency to be slowly advected upwards toward the cilia tips. This can be seen in Fig. 8a where the particle closest to the chamber floor seeded at height of $1.74 \times 10^{-5} m$ displays a net upward spiraling motion. The flow conditions ensure particles close to the chamber floor eventually become embedded in the upper layers and are swept from the respiratory system. This phenomenon happens despite the net negative velocities close to the chamber floor (Fig. 7a).

4 Conclusions

In this chapter we have made use of the Immersed Boundary Method to develop a highly efficient simulation of the coupled dynamics of a bed of cilia and the fluid surrounding the cilia. We have shown that metachronal waves can spontaneously form over cilia beds. The metachronal wave characteristics of wave vector magnitude $|k|$, frequency f , and wave speed are functions of cilia stiffness EI and cilia number density d^{-2} . We show that cilia that are too stiff cannot support the propagation of metachronal waves. Also, we observe that metachronal waves can pass through a patch of cilia disrupted by local photorelease of caged calcium ions.

We have also investigated the effects of cilia stiffness EI and cilia number density d^{-2} on cilia slip velocity. We have shown the existence of an optimal cilia number density and suggest a reason for the optimum. Cilia in high densities are subjected to large shear stresses from narrow fluid gaps between cilia, thus lowering the slip velocity. Cilia in low densities have large regions of undriven fluid between them, again lowering the slip velocity.

Finally we study the transport of passive tracers in the fluid chamber. We show that particles close to the chamber floor exhibit diffusive behavior while particles close to the chamber ceiling display advective behavior.

In conclusion, we have demonstrated that realistic and high performance simulations can be used as a serious tool to give an understanding of the various forms of mechanisms involving active cilia in nature, examples of which include respiratory processes and microscale propulsion.

References

- Alexeev A et al (2008) Designing synthetic, pumping cilia that switch the flow direction in microchannels. *Langmuir* 24(21):12102–12106
- Allen RD () Fine structure of membranous and microfibrillar systems in the cortex of *Paramecium caudatum*. *J Cell Biol* 49(1):1–20
- Barataheri A et al (2011) Tethered fleximags as artificial cilia. *J Fluid Mech* 678:5–13
- Berg H (1975) How bacteria swim. *Sci Am* 233:36–44
- Breuning J et al (2008) Primary cilia regulate hippocampal neurogenesis by mediating sonic hedgehog signaling. *Proc Nat Acad Sci* 105:13127–13132
- Breuning J et al (2010) Cilia in the brain: going with the flow. *Nat Neurosci* 13(6):654–655
- Brokaw C (2001) Simulating the effects of fluid viscosity on the behavior of sperm flagella. *Math Methods Appl Sci* 24(17–18):1351–1365
- Carson J et al (1981) Morphometric aspects of ciliary distribution and ciliogenesis in human nasal epithelium. *Proc Nat Acad Sci* 78(11):6996–6999
- Center for Applied Scientific Computing, Lawrence Livermore National Laboratory (2006) *Hypre* high performance preconditioners
- Dillion R et al (1996) Modeling biofilm processes using the immersed boundary method. *J Comput Phys* 129:57–73

- Dillion R et al (2003) Mathematical modeling of axoneme mechanics and fluid dynamics in ciliary and sperm motility. *Dyn Contin, Discrete Impulsive Syst Ser A: Math Anal* 10(5):745–757
- Drescher K et al (2009) Dancing volvox: hydrodynamic bound states of swimming algae. *Phys Rev Lett* 102:168101
- Fauci L, Dillion R (2006) Biofluidmechanics of reproduction. *Ann Rev Fluid Mech* 38:371–394
- Felgner H et al (1996) Flexural rigidity of microtubules measured with the use of optical tweezers. *J Cell Sci* 109:509–519
- Gao W et al (2010) Magnetically powered flexible metal nanowire motors. *J Am Chem Soc* 132:14403–14405
- Gittes F et al (2003) Flexural rigidity of microtubules and actin filaments measured from thermal fluctuations in shape. *J Cell Biol* 120:932–934
- Guasto J et al (2011) Chemotactic maneuverability of sperm. arXiv preprint 1110.2835
- Guirao B et al (2010) Coupling between hydrodynamic forces and planar cell polarity orients mammalian motile cilia. *Nat Cell Biol* 12:341–350
- Hsu CY, Dillion R (2009) A 3D motile rod-shaped monotrichous bacterial model. *Bull Math Biol* 71(5):1228–1263
- Iwadate Y, Nakaoka Y (2008) Calcium regulates independently ciliary beat and cell contraction in paramecium cells. *Cell Calcium* 44:169–179
- Khaderi S et al (2011) Microfluidic propulsion by the metachronal beating of magnetic artificial cilia: a numerical analysis. *J Fluid Mech* 688:44–65
- McQueen DM, Peskin C (2001) Heart simulation by an immersed boundary method with formal second order accuracy and reduced numerical viscosity mechanics for a new millennium. In: *Proceedings of the international conference on theoretical and applied mechanics 2000*. Kluwer Academic Publishers, Dordrecht
- Mitran SM (2007) Metachronal wave formation in a model of pulmonary cilia. *Comput Struct* 85:763–774
- Murase M (1992) *Dynamics of cellular motility*. Wiley, New York, USA
- Narematsu N, Quek R, Chiam KH, Iwadate Y (2013) Metachronal wave propagation on the compliant surface of *Paramecium* cells. Unpublished
- Osterman N, Vilfan A (2011) Finding the ciliary beating pattern with optimal efficiency. *Proc Nat Acad Sci* 105(38):15727–15732
- Peskin C (2002) The immersed boundary method. *Acta Numer* p 1–39
- Purcell EM (1977) Life at low Reynolds number. *Am J Phys* 45:3–11
- Sanderson M, Sleight M (1981) Ciliary activity of cultured rabbit tracheal epithelium: beat pattern and metachrony. *J Cell Sci* 47:331–347
- Shields A et al (2010) Biomimetic cilia arrays generate simultaneous pumping and mixing regimes. *Proc Nat Acad Sci* 107(36):15670–15675
- Simet SM et al (2010) Long-term cigarette smoke exposure in a mouse model of ciliated epithelial cell function. *Am J Respir Cell Mol Biol* 43(6):635–640
- Sugina K, Naitoh Y (1982) Simulated cross-bridge patterns corresponding to ciliary beating in *Paramecium*. *Nature* 295:609–611
- Tannehill J et al (1997) *Computational fluid mechanics and heat transfer*, 2nd edn. Taylor and Francis, Washington, USA
- Vilfan A, Julicher F (2006) Hydrodynamic flow patterns and synchronization of beating cilia. *Phys Rev Lett* 96:058102

Flow on the Surface of the Tracheal Lumen by Ciliary Motion of Asymmetric Axonemal Structures

Hironori Ueno

Abstract Recently, advances in optics and digital image processing techniques have been accompanied by an improvement in the visualization of biologically complex flow by using fluorescent particles, such as particle image velocimetry (PIV) and particle tracking velocimetry (PTV). In addition, visualization of cellular ultrastructure using cryoelectron tomography has revealed the structural arrangements of cytoskeletal complexes and macromolecules in intracellular membranes and organelles. In this chapter, we focus on cilia-generated directional flow. Many eukaryotic cells have developed cilia, an organelle present on cell surfaces that enables motion and generates fluid flow on the cell surface. The complex flow and axonemal structure in mouse airways were previously not well understood. Here, we describe the flow field generated by asymmetric ciliary motion on the surface of sparsely distributed ciliated cells in mouse tracheal epithelial cells by the μ -PIV/PTV method. Moreover, we describe the axonemal structure of respiratory cilia by using data from cryoelectron tomography and image processing.

Abbreviations

MT	Microtubule
PCL	Periciliary liquid layer
IDA	Inner dynein arm
μ -PTV	Micro-particle tracking velocimetry
μ -PIV	Micro-particle image velocimetry
CF	Cystic fibrosis
COPD	Chronic obstructive pulmonary disorder
QDs	Quantum dots
CCD	Charge-coupled device

H. Ueno (✉)

Molecular Function and Life Sciences, Aichi University of Education,
1 Hirosawa, Igaya-cho, Kariya 448-8542, Japan
e-mail: hueno@aecc.aichi-edu.ac.jp

EMCCD	Electron multiplier type CCD camera
PBS	Phosphate buffered saline
ODA	Outer dynein arm
DRC	Dynein regulatory complex
IC	Intermediate chain

1 Introduction

1.1 Ciliary Motion and Flow in Microorganisms

Cilia are microtubule (MT)-based organelles that have an evolutionarily conserved structure of nine doublet MTs surrounding two central singlet MTs (9 + 2 structure) (Fig. 1). The ciliary motion is driven by dynein motors, which generates fluid flow on the surface of various cellular organisms. For example, ciliate and algae such as unicellular *Paramecium*, *Tetrahymena*, *Chlamydomonas*, or multicellular *Volvox*, tunnel through low Reynolds number fluidic field by coordinating their ciliary and flagellar beating patterns (Fig. 2a–c). The ability to do plays an important role in numerous biological functions such as avoiding reaction, reproduction, pathogenic infection, mixing, CO₂/O₂ capture, and photoreaction in lakes, ponds, and oceans. However, how do the unicellular and multicellular organisms reach their destinations by coordinating their individual cilia and flagella? In the case of unicellular organisms such as *Tetrahymena* and *Chlamydomonas*, the base of the cilia and flagella, known as the basal body, is connected by some kinds of filamentous structure that includes MTs (Ringo 1967; Wloga and Frankel 2012) (Fig. 2d). These filamentous structures are thought to be involved in determining the direction of ciliary beating by establishing cell polarity. In multicellular organisms, for example, *Volvox*, cell-cell communication networks such as those that occur through signal transduction via cell junctions, might be the basis for the coordination of phototactic behaviour (Harold and Hoops 2005; MAST 1907). In addition, the hydrodynamic interaction between each cilium is thought to be a candidate for the coordination of ciliary synchronization (Goldstein et al. 2011; Gueron and Levit-Gurevich 1999; Guirao and Joanny 2007; Niedermayer et al. 2008; Vilfan and Julicher 2006). This hydrodynamic interaction of cilia and flagella might be responsible for flagellar and ciliary synchronization across the whole eukaryote from unicellular to multicellular organisms.

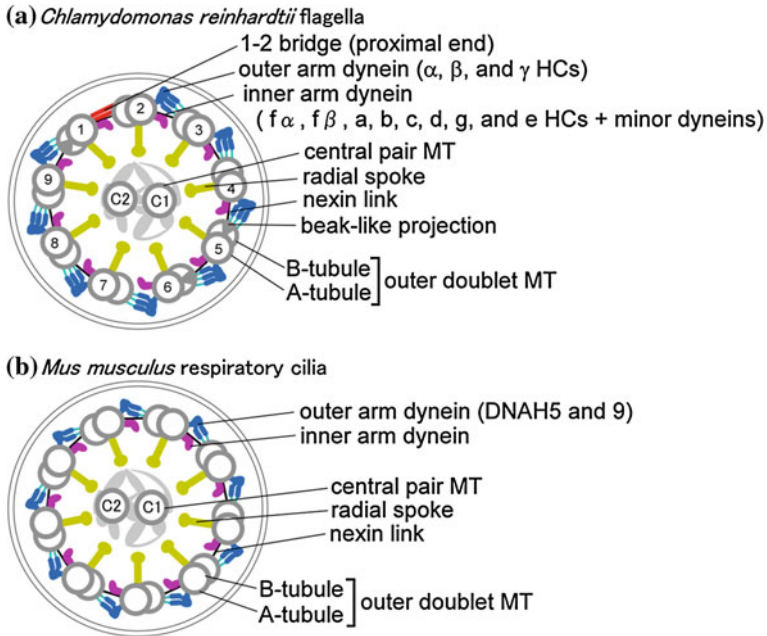


Fig. 1 Illustration of components in the *cross-section* of a *Chlamydomonas* flagellum (a) and a respiratory cilium in mouse airways (b). The dynein arms extend from A-tubule and make temporary cross-bridges with the B-tubule of adjacent outer doublet MT. Neighboring doublets MT are connected by nexin links and are attached to the central pair through radial spokes. ODA is composed of two to three nonidentical heavy chains (HCs). ODA in *Chlamydomonas* flagella contains three HCs, α -, β -, and γ -HCs, while ODA in respiratory cilia contains two HCs, DNAH5 and DNAH9 (Fliegau et al. 2005; Hornef et al. 2006; Olbrich et al. 2006) corresponding to γ - and β -HCs in the *Chlamydomonas* ODA, respectively. The proximal region of doublet MT 1 has the 1–2 bridge structure instead of ODA in the *Chlamydomonas* flagella (Hoops and Witman 1983). Doublet MT 1, 5 and 6 has the beak like projections in the *Chlamydomonas* flagella (Hoops and Witman 1983). IDA contains eight different types of dynein HCs, $f\alpha$, $f\beta$, a, b, c, d, g, and e in the *Chlamydomonas* flagella (Kagami et al. 1990), while structural constitution of IDA in mammalian cilia was unclear

1.2 Mammalian Cilia

Ciliary motion is also critical in generating the fluid flow and transportation of biological molecules and pathogens in various mammalian tissues, including the tracheal lumen, oviduct lumen, sperm, lateral ventricles, and the ventral node in the mouse embryo (Guirao et al. 2010; Halbert et al. 1989; Hirota et al. 2010; Lechtreck et al. 2009; Sawamoto et al. 2006). Therefore, defective ciliary activity causes pathological features in a number of diseases, including chronic bronchitis and sinusitis, male/female sterility, and hydrocephalus (Afzelius 1976; Hirokawa et al. 2006; Jonassen et al. 2008; Nigg and Raff 2009; Nonaka et al. 1998; Okada et al. 1999; Pazour et al. 2000). In this chapter, we focus on mucociliary clearance

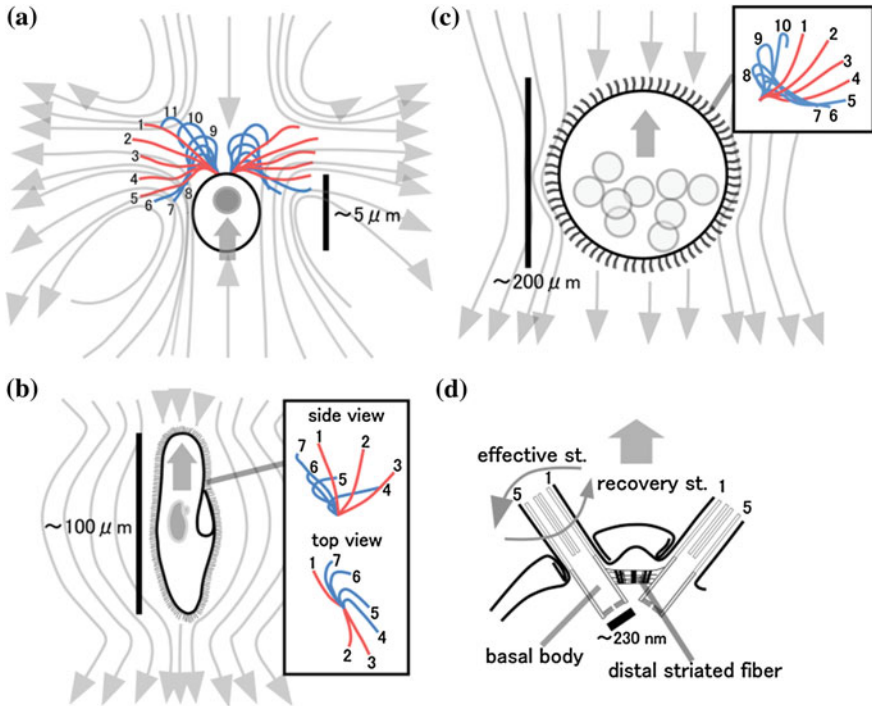


Fig. 2 **a** Diagram of the flagellar waveform (Ruffer and Nultsch 1985) and instantaneous streamlines of flow around a *Chlamydomonas reinhardtii* cell during effective stroke (Guasto, Johnson, and Gollub 2010). **b** Ciliary waveform (Sugino and Naitoh 1982) and streamlines of flow around a ciliated protozoan *Paramecium caudatum* (Ishikawa and Hota 2006). **c** Flagellar waveform and streamlines of flow around a *Volvox rousselatii* (Ueki et al. 2010) and *Volvox carteri* (Drescher et al. 2010). **d** A schematic drawing of a longitudinal section through both basal bodies in *Chlamydomonas reinhardtii*. Two basal bodies are connected by some filamentous structures including the distal striated fibre probably to maintain flagellar polarity and beating direction (Ringo 1967). The swimming direction is indicated by large arrows

by ciliary motion in mouse airways. During breathing, the airways transport into lungs large quantities of air that is contaminated with a variety of dust, bacteria, and viruses; however, the airways have developed a defence system of mucociliary clearance by effective ciliary motion. The airways contain five different types of epithelial cells that perform this clearance: Goblet cells (mucus cells) that secrete mucus, ciliated cells that have about 200 cilia per single cell, brush cells that are columnar cells bearing microvilli, and endocrine cells (Kulchitsky cells) that secrete serotonin and peptides that act as local mediators in reflexes regulating the airway or vascular caliber (Fig. 3a). Moreover, there are a number of basal cells located below the epithelial cells, which serve as stem cells by helping to maintain the epithelium (Figs. 3a, 4a). The base of the cilia in mammalian ciliated cells, known as the basal body, is similar in construction to that found in unicellular organisms.

Fig. 3 a This diagram shows the components of the mucociliary clearance: the mucus, periciliary layer, cilia, epithelial cells, and basal cells. **b** Series of ciliary motion show the change of bending pattern during a ciliary beating cycle (Sanderson and Sleight 1981)

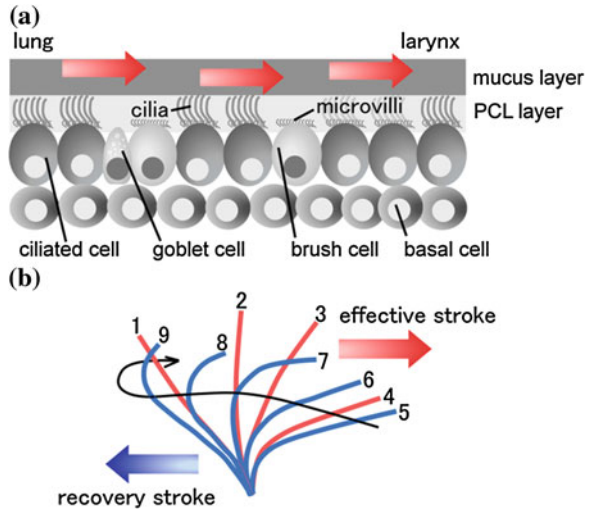
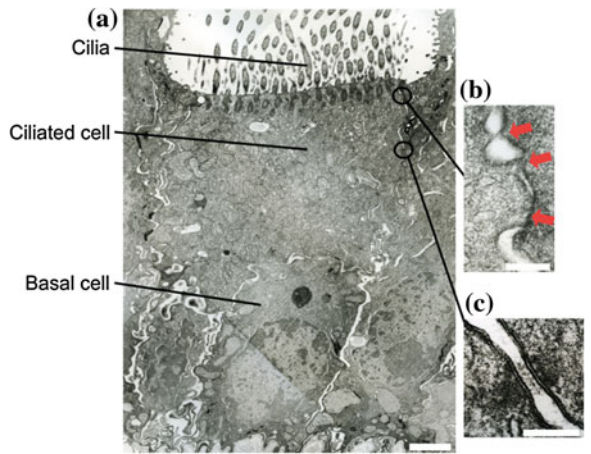


Fig. 4 a Transmission electron micrograph showing several mature ciliated cells and a basal cell from a mouse trachea. **b** Ciliated cells communicate with neighbouring cells through tight junctions (indicated by red arrows) and **c** desmosome with cadherin. Scale bars **a** 1 μm ; **b** 200 nm; **c** 100 nm (colour figure online)



Because the basal bodies are connected to each other by MT with basal feet, disruption of the basal foot affects the coordinated ciliary beating and flow direction (Kunimoto et al. 2012). Signal transduction via cell junctions with structural membrane connection (Fig. 4b, c) is thought to be crucial in the coordination of flow direction and frequency of ciliary beating in mammals as well (Sanderson and Sleight 1981).

1.3 Property of External Fluid and Diseases

The liquid on the tracheal surface consists of two layers, a watery layer and a mucus layer (Fig. 3a). The watery layer surrounds the cilia on the apical surface of ciliated cells (also known as the periciliary liquid layer (PCL)), whereas the mucus layer, which is rich in mucins, lies on top of the PCL. The mucus layer is transported towards the oropharynx from the lungs through effective ciliary motion, whereas the PCL layer is required for smooth beating of respiratory cilia. Unlike the PCL layer, the mucus layer has a high viscosity (Lucas and Douglas 1934). The viscosity of the mucus layer has been examined by a number of researchers. They found that the viscosity of sputum collected from normal healthy human was 12–15 Pa at 1 rad/s (Lai et al. 2009). Pulmonary disease conditions, such as cystic fibrosis (CF), chronic obstructive pulmonary disorder (COPD), and asthma, generally result in an increase in the viscoelasticity of mucus, owing in part to reduced water content and an increased fraction of glycoproteins. The viscosity of sputum collected from asthma patient was 18.4 ± 3.2 Pa ($P < 0.0001$) at 1 rad/s (Daviskas et al. 2007). CF sputum is significantly more elastic than viscous (Lai et al., 2009). These understanding of the physical properties of mucus are important to advancing the field of drug and gene delivery.

1.4 Ciliary Motion

The diameter and length of the respiratory cilium are approximately 230 nm and 6 μ m, respectively. Respiratory cilia have a high beat frequency of 15–30 Hz. Ciliary motion consists of two different strokes: ‘effective stroke’ and ‘recovery stroke’. In the effective stroke, cilia stroke towards the larynx, catch the mucous at the tip of each cilium, and propel it forwards (Fig. 3). They then perform a ‘recovery stroke’ in which they return to their initial position without dragging the mucus backwards, thereby producing a positive flow (Fig. 3). High-speed cinematography and scanning electron microscopy data indicated that the average duration of the recovery stroke is longer than that of the effective stroke in the respiratory cilia of cultured rabbit cells. Moreover, the ciliary motion normally rest at the end of the effective stroke, so that respiratory cilia produce the asymmetric ciliary motion to produce directional flow (Sanderson and Sleight 1981). However, it is difficult to investigate the more detail motion of individual cilia by which directional flow on the airway epithelium is generated, because hundreds of cilia are closely packed on each individual ciliated cell. In addition, three dimensional structure of respiratory cilia has not been reported so far.

1.5 Ciliary Structure

The ciliary movement is driven by some kinds of dynein motor that constitute the inner (IDA) and outer dynein arms (ODA) of axonemes, which consist of dyneins α – g and a complex containing the α , β , and γ heavy chains in *Chlamydomonas* flagella, respectively (Fig. 1a), whereas ODA of axoneme in respiratory cilia has the two different heavy chains, DNAH5 and nine (Fig. 1b). Dynein generates sliding force between adjacent outer doublet MTs, which is converted to axonemal bending. Although the mechanism that converts the sliding movement into ciliary bending is still unknown, it is thought to involve the coordination of activities of each dynein molecule with various properties. Recent advances in cryoelectron tomography have facilitated a number of ultrastructural studies of ciliary components, the axonemal structures of *Chlamydomonas* flagella, sea urchin sperm flagella, and *Trypanosome* flagella are frequently reported (Ishikawa et al. 2007; Nicastro et al. 2005). In addition, it was reported that the axonemal structures of *Chlamydomonas* flagella has the asymmetric arrangement of IDA species in *Chlamydomonas* flagella (Bui et al. 2009). We show the three dimensional ultrastructure of respiratory cilia in this chapter.

1.6 Flow, Ciliary Motion, and Axonemal Structure in Mouse Airways

Here, we describe directional fluid flow on the surface of the tracheal lumen based on the distribution of ciliated cells by μ -PTV and μ -PIV using fluorescent tracer particles. In addition, the motion of individual cilia was analyzed using a Nipkow lens type confocal microscopy with quantum dots (QDs), which are spherical nano-scale crystals made of semiconductor materials 2–20 nm in diameter and having size-dependent optical properties. We developed the imaging technique of individual ciliary motion by labelling the tip of cilia with QDs, and detected asymmetric ciliary motion with a spatial precision of 7–9 nm (Ueno et al. 2012). Moreover, we describe the molecular structure of respiratory cilia by cryoelectron tomography to better understand the molecular mechanisms that control mouse respiratory ciliary motion.

2 Ciliary Flow on the Surface of the Tracheal Lumen

2.1 Preparation of Tracheal Samples

To visualize the dynamics of cilia-generated flow on the surface of the tracheal lumen, mouse tracheas were exclusively obtained from wild-type C57Bl/6 mice. In

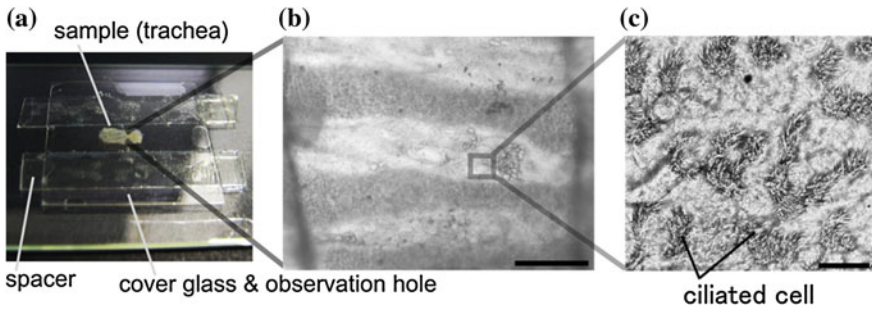


Fig. 5 **a** Photograph of the specimen of a mouse tracheal sample. Specimen is placed between two spacers to prevent compression by the cover-glass, which contains an observation hole. **b** Bright-field image of the mouse tracheal lumen. *Dark areas* indicate tracheal cartilage. *Scale bar* 300 μm . **c** Bright-field light micrograph showing ciliated cells and non-ciliated cells. Ciliated cells are sparsely distributed in the tracheal lumen. *Scale bar* 10 μm

most studies, 3–6 week-old mice were used. Muscle and vascular tissues were dissected from the tracheas in cold phosphate buffered saline (PBS). The tracheas were opened longitudinally to expose the tracheal lumen. The exposed tracheal lumen was soaked with PBS containing fluorescent beads (1 μm), and covered using a cover glass with an observation hole (Fig. 5a, b). Fluid flow was visualized by observing the fluorescent beads under a fluorescence microscope (DM4000B; Leica, Wetzlar, Germany) equipped with a non-cover 100 \times NA0.85 objective lens (Leica). The images were projected onto a charge-coupled device (CCD) camera (DFC 340 FX; Leica) and were contrast enhanced using Image J software. Images were taken at a rate of 30 frames per second. The positions of fluorescent particles in selected video frames were traced using Image J. To characterize the flow fields on the surface of the tracheal lumen, we performed μ -PIV analysis.

2.2 Analysis of Cilia-Generated Flow

We were interested in determining how sparsely distributed ciliated cells (Fig. 5c) contribute to directional flow on the surface of the tracheal lumen. In order to analyze the flow, we identified the positions of ciliated cells on the luminal surfaces of mouse tracheas from a movie of bright field microscopy (Fig. 6a), and monitored the fluid flow generated by ciliary motion by using fluorescent tracer particles (1 μm). The trajectories of the tracer particles were labelled with different colours using the supplied software (Macro of Image J developed by Yuichi Hiratsuka) (Fig. 6b). A high-NA lens with a narrow focal plane is useful for good visualization as it limits out-of-focus fluorescence. We observed a strong directional flow from the lung to the larynx in the middle area of this field. There were also a number of ciliated cells in the same area. Analysis of μ -PIV also showed

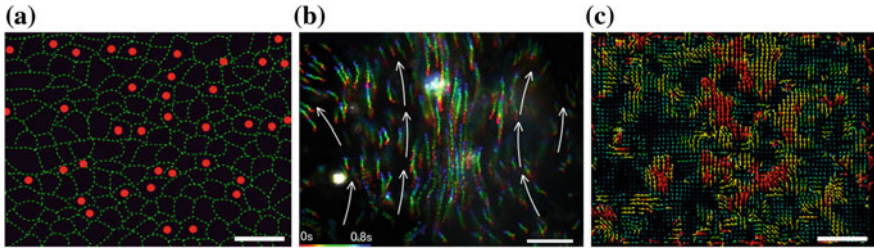


Fig. 6 **a** Positions of the ciliated cells. The outlines of tracheal epithelial cells (*green dotted lines*) and the position of ciliated cells (*red circles*) were estimated from the movie. **b** Trajectories of fluorescent tracer particles, which were made from a 0.8-s movie by taking macro using Image J software. **c** μ PIV analysis of the flow field generated by effective ciliary motion. Each *arrow* denotes the direction and velocity of flow. *Below lung; above oropharynx*. Scale bar 20 μ m (colour figure online)

that a strong directional flow was generated around ciliated cells (Fig. 6c). The tracer particles were eventually transported from the lungs towards the oropharynx, even though ciliated cells were sparsely distributed on the epithelial cells. It will be important to understand how the direction of ciliary beating is coordinated and regulated between each ciliated cell in the tracheal lumen.

3 Ciliary Motion on the Surface of the Tracheal Lumen

3.1 Imaging Setup for Ciliary Motion

The optical system for particle tracking of individual ciliary motion consisted of an epifluorescent microscope (IX-71, Olympus, Tokyo, Japan), a Nipkow lens type confocal unit (CSU10, Yokokawa, Tokyo, Japan), and an electron multiplier type CCD camera (EM-CCD, Ixon DV887, Andor Technology, Belfast, Northern Ireland). A PlanApo 60 \times numerical aperture (NA) 1.40 objective lens (Olympus) was used to visualize individual ciliary movement. QDs were illuminated using a green laser (wavelength, 488 nm; Spectra-Physics). The laser-excited fluorescence was filtered with a 580 nm long-pass filter to image the QDs (Fig. 7a, b). Tracheal samples were analyzed at room temperature, typically within 120 min of euthanasia, and soaked in PBS. We then traced the QD signal on the surface of the tracheal tissue with a spatial precision of 7–9 nm under a Nipkow disk confocal microscope linked to an EMCCD (Fig. 7c).

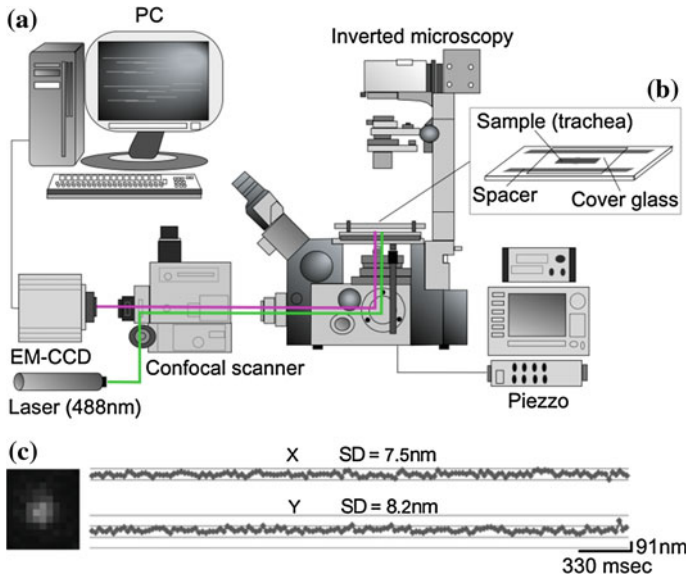


Fig. 7 **a** Schematic of the optical system for observation of tracheal ciliary movement. This optical microscope consists of an epi-fluorescent microscope (IX-71, Olympus, Tokyo, Japan), a Nipkow lens type confocal unit (CSU10, Yokokawa, Tokyo, Japan), and an electron multiplier type charge-coupled device (EM-CCD, Ixon DV887, Andor Technology, Belfast, Ireland). **b** Accuracy of the present methods. **c** The QD(s) were fixed on a tracheal lumen tissue before the position of the QD(s) was determined by temporal resolution with a noise of 7.5–8.2 nm (x-axis and y-axis)

3.2 Tracking the Motion of Individual Cilia

In some of the studies for ciliary motion, in which tracheal ciliated cells were used, the gray intensity of the images resulting from the repetitive motion of the cilia was measured by selecting regions. However, details of the motion of individual cilia with high spatial precision were still unclear. To analyze the motion of individual cilia with nano-scale precision throughout the whole beating cycle, cilia were labelled individually using QDs by hooking them over the claw-like structures of the ciliary tip known as the ciliary crown (Dirksen and Satir 1972; Kuhn and Engleman 1978). However, recording speed was still very slow due to the limitation of the EMCCD recording speed. We are currently attempting to analyze the ciliary motion with high-speed frequency using a high-speed CMOS camera. In this study, however, we could successfully track the motion of individual cilia throughout the whole ciliary beating cycle by tracking the intensity of QD with G-Track (G-Angstrom, Sendai, Japan). Ciliary motion took the form of an asymmetric beating pattern (Fig. 8a–c). The velocity of the effective stroke was 1.24 times higher than that of the recovery stroke. There is a rest phase at the end of the effective stroke in individual ciliary motion, whereas overall ciliary motion

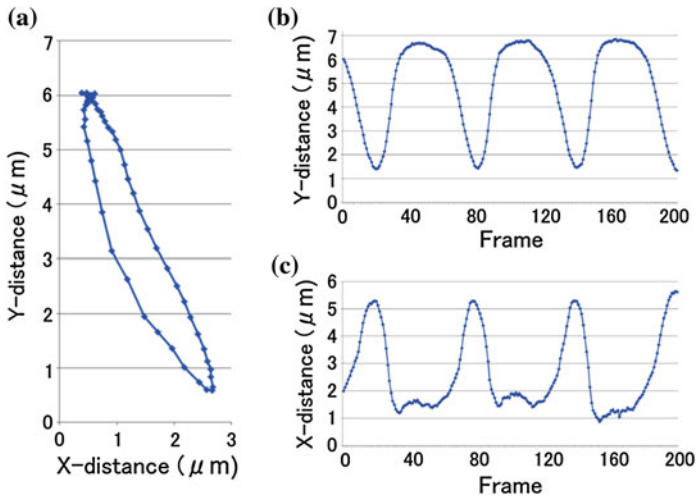


Fig. 8 Motion of an individual cilium during the whole ciliary beating cycle. **a** Trajectory of ciliary movement. The movement of QDs during the whole ciliary beating cycle was tracked using G-Track software. *Below lung; above oropharynx.* **b, c** Trajectory of QD movement in **a** was divided into *x-* (**c**) and *y-axis* (**b**)

smoothly returns from the effective stroke to the recovery stroke. The pattern of trajectory, especially X-distance, at the end of effective stroke was unsteady (Fig. 8c). These results suggest that the switching mechanism from effective to recovery stroke is associated with the delay and unsteady of ciliary motion. They also suggest that each individual respiratory cilium has asymmetric ciliary motion. This was found in a previous study using high-speed cinematography (Sanderson and Sleight 1981); our study results affirmed those previous results by tracing individual ciliary motion in more detail using QD and confocal microscopy.

4 Axonemal Structure of Mouse Respiratory Cilia

4.1 Specimen Preparation and Quick Freezing for Electron Cryoelectron Tomography

Tracheas were opened and gently scratched with the wall of a tube, which was then washed in Tris buffer containing 5 mM DTT to isolate respiratory cilia suspensions. To remove the ciliary membrane, cilia suspensions were centrifuged at 13,000 rpm for 15 min to obtain cell pellets, which were then gently dispersed in Tris buffer containing 2 % NP-40, incubated on ice for 1 h, and re-centrifuged at 13,000 rpm for 15 min. This procedure was then repeated twice, after which the

demembrated cilia were frozen in liquid ethane. Images were taken as described previously (Bui et al. 2008; Ishikawa et al. 2007) using a transmission electron microscope (Tecnai F20 and F30; FEI) equipped with a field emission gun, an energy filter (GIF Tridiem, Gatan), and a $2,048 \times 2,048$ charge-coupled US1000 device (Gatan). The accelerating voltage was set to 200 kV, the magnification, to $27,000\times$; and the under focus, to 4–4.5 μm . Tomographic images from -60 to 60° were acquired using Explore3D software (FEI). The image analysis method used to obtain the 96 nm average from the tomogram was similar to that used in a previous study (Bui et al. 2009). Briefly, tomograms were reconstructed using IMOD software (Mastronarde 1997) with fiducial marker alignment and R-weighted back projection. Sub-tomograms with pixel dimensions of $200 \times 200 \times 200$, each with a 96 nm periodic unit, were created from the original tomograms by using Bsoft (Heymann 2001) and aligned along the MT by using SPIDER software (Frank et al. 1996). Nine MTs were then aligned. Averages were always deconvoluted by the total contribution of the missing wedge to ensure that data sampling was isotropic (Bui et al. 2008). Surface rendering was performed using Chimera (Pettersen et al. 2004) after masking, band-pass filtering, and contrast inversion.

4.2 3D Structure of Respiratory Cilia

In order to understand the location of dynein motor proteins in respiratory axoneme, we examined the three-dimensional structures of mouse respiratory cilia by cryoelectron tomography and image processing. Single tomographic images of transverse sections and longitudinal sections are shown in Fig. 9a, b. Respiratory axoneme has the conventional $9 + 2$ structure including the dynein motor, radial spoke. We found an outer dynein arm (ODA) and eight inner dynein arm (IDA) densities in the averaged structure (Fig. 10a, b) which correspond to the position of *Chlamydomonas* inner arm dynein α , β , a , b , c , d , g , and e (Bui et al. 2012) (Fig. 10d). Previous phylogenetic analysis using *Chlamydomonas* and human genes shows that there are 16 DHC genes including 8 IDA genes in human (Pazour

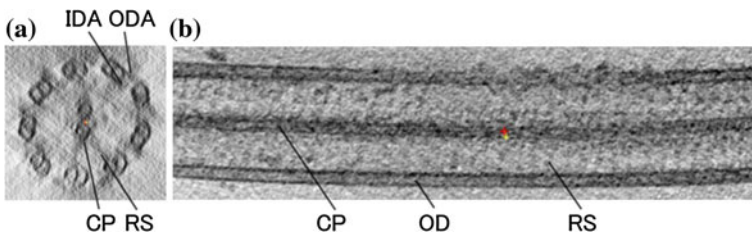


Fig. 9 Single tomographic slices showing **a** the transverse section and **b** longitudinal sections in the central region of respiratory cilia. *ODA* outer arm dynein; *IDA* inner arm dynein; *OD* outer doublet MT; *CP* central pair MT; *RS* radial spoke

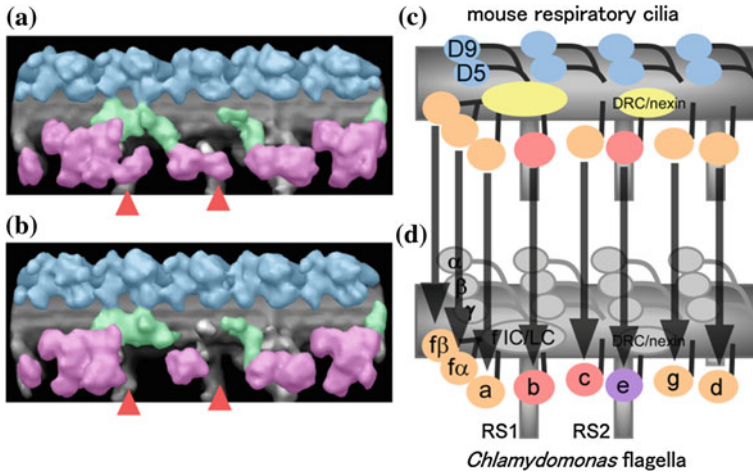


Fig. 10 Analysis of the axonemal structure in mouse respiratory cilia by cryoelectron tomography. **a, b** Surface-rendering models with averages of all doublets and the average of only doublets missing two kinds of IDA species. Mouse IDA corresponding to the position of *Chlamydomonas* inner arm dynein *b* and dynein *e* are missing in at least two doublet MTs in a respiratory axoneme (**a** and **b**, red arrowheads) drawing of the 96-nm unit of doublet MT structure in respiratory cilia, showing the IDA and the pattern of the other structures. **d** Schematic drawing of the 96-nm unit doublet MT structure in *Chlamydomonas* flagella, showing the IDA and the pattern of the other structures. *Chlamydomonas* dynein *b* is missing on the doublet MT number nine in *central/distal* regions of axoneme (Bui et al. 2009). *Chlamydomonas* dynein *c* is missing on the doublet MT number one in the *central/distal* regions of axoneme (Bui et al. 2009). Dynein *e* might be replaced another minor dynein on the doublet MT number 1 in *central/distal* regions of axoneme (Bui et al. 2012). The proximal end is to the left in **a, b** and **c**. DRC, dynein regulatory complex (nexin link); IC intermediate chain, RS, radial spoke

et al. 2006; Yagi 2009). We also examined the phylogenetic analysis using *Chlamydomonas* and mouse genes (Fig. 11), indicating that 8 IDA densities in the respiratory axoneme by cryo electron tomography correspond to 8 IDA genes in mouse. We also observed the dynein regulatory complex (DRC) that is identical to the nexin link identified by Heuser et al. (Heuser et al. 2009) and three radial spokes in 96 nm repeats along the axoneme (Fig. 10a, b). Using the averaged data of each doublet, we found that 2 IDA species corresponding to *Chlamydomonas* dynein *b* and *e* were missing in at least two doublet MTs in a respiratory axoneme. In addition, it has been reported that respiratory cilia from these knockout (KO) mice of a tubulin glutamylation-performing enzyme, tubulin tyrosine ligase-like protein 1, lost asymmetric ciliary motion with the loss of axonemal curvature (Ikegami et al. 2010). Recently, it's reported that dynein *e* is the main target of motility regulation by tubulin polyglutamylation (Kubo et al. 2012). Therefore, the asymmetric ciliary motion would require the asymmetric distribution of dynein *e* in the nine outer doublet MTs in an axoneme.

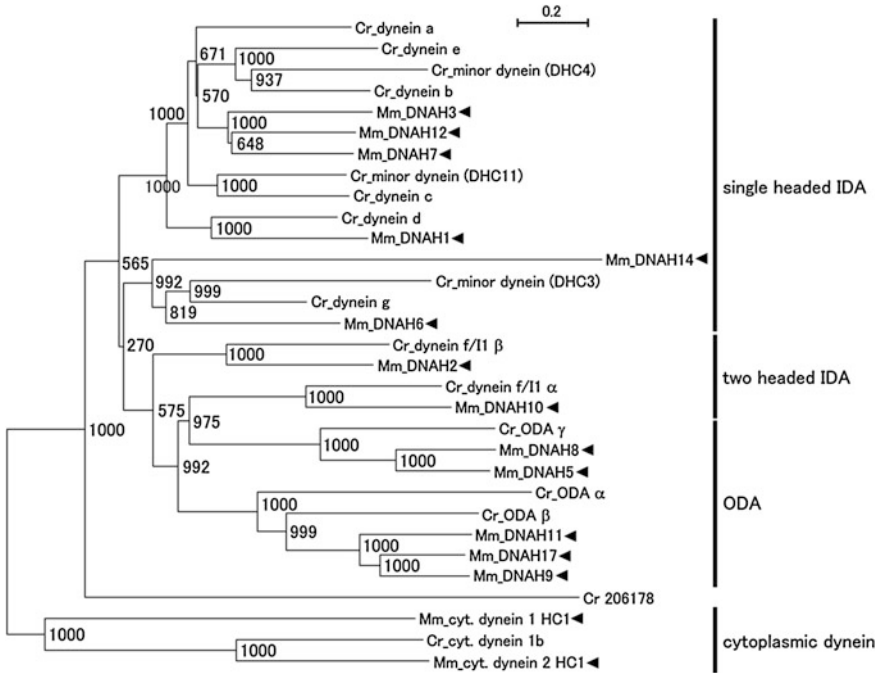


Fig. 11 Phylogenetic tree showing the relationship between the dynein heavy chains of *Chlamydomonas* and mouse. The full-length amino acid sequences of *Chlamydomonas* and mouse DHCs was aligned by ClustalW and developed into a phylogenetic tree. The numbers show the bootstrap values from 1,000 iterations. *Cr* *Chlamydomonas reinhardtii*, *Mm*, *Mus musculus*

5 Conclusions

In order to understand cilia-generated directional flow, we examined the flow field and individual ciliary motion on the surface of tracheal lumen. Although the flow was unsteady and diverse by asymmetric ciliary beating, the tracer particles were eventually transported from the lungs towards the oropharynx. Cryoelectron tomography revealed that the densities of 2 IDAs, mouse inner dynein arm *b* and *e*, were missing from at least two doublet MTs in the axonemal structure of respiratory cilia. These results indicate that the asymmetric ciliary motion is driven by the asymmetric axonemal structure, which generates overall directional flow from the lungs to the oropharynx on sparsely distributed ciliated cells.

Acknowledgments We would like to thank Takashi Ishikawa and Khanh Huy Buy for helpful advice of cryoelectron tomography and image processing, Takuji Ishikawa and Takami Yamaguchi for discussion of ciliary flow, and Toshiki Yagi for advice of the phylogenetic analysis. We took some cryo electron microscopic images using Tecnai G3 Polara in the Medical Institute of Bioregulation, Kyushu University. This study was supported by a Grant-in-Aid for Young

Scientists (B) from the JSPS (No. 24770145) to Hironori Ueno and by a Grant-in-Aid for Scientific Research on Innovative Areas “Nanomedicine Molecular Science” (No. 24107504) to Hironori Ueno from Ministry of Education, Culture, Sports, Science, and Technology of Japan.

References

- Afzelius BA (1976) A human syndrome caused by immotile cilia. *Science* 193(4250):317–319
- Bui KH, Sakakibara H, Movassagh T, Oiwa K, Ishikawa T (2008) Molecular architecture of inner dynein arms in situ in *Chlamydomonas reinhardtii* flagella. *J Cell Biol* 183(5):923–932
- Bui KH, Sakakibara H, Movassagh T, Oiwa K, Ishikawa T (2009) Asymmetry of inner dynein arms and inter-doublet links in *Chlamydomonas* flagella. *J Cell Biol* 186(3):437–446
- Bui KH, Yagi T, Yamamoto R, Kamiya R, Ishikawa T (2012) Polarity and asymmetry in the arrangement of dynein and related structures in the *Chlamydomonas axoneme*. *J Cell Biol* 198(5):913–925
- Daviskas E, Anderson SD, Young IH (2007) Inhaled mannitol changes the sputum properties in asthmatics with mucus hypersecretion. *Respirology* 12(5):683–691
- Dirksen ER, Satir P (1972) Ciliary activity in the mouse oviduct as studied by transmission and scanning electron microscopy. *Tissue Cell* 4(3):389–403
- Drescher K, Goldstein RE, Michel N, Polin M, Tuval I (2010) Direct measurement of the flow field around swimming microorganisms. *Phys Rev Lett* 105(16):168101
- Fliegauf M, Olbrich H, Horvath J, Wildhaber JH, Zariwala MA, Kennedy M, Knowles MR, Omran H (2005) Mislocalization of DNAH5 and DNAH9 in respiratory cells from patients with primary ciliary dyskinesia. *Am J Respir Crit Care Med* 171(12):1343–1349
- Frank J, Radermacher M, Penczek P, Zhu J, Li Y, Ladjadj M, Leith A (1996) SPIDER and WEB: processing and visualization of images in 3D electron microscopy and related fields. *J Struct Biol* 116(1):190–199
- Goldstein RE, Polin M, Tuval I (2011) Emergence of synchronized beating during the regrowth of eukaryotic flagella. *Phys Rev Lett* 107(14):148103
- Guasto JS, Johnson KA, Gollub JP (2010) Oscillatory flows induced by microorganisms swimming in two dimensions. *Phys Rev Lett* 105(16):168102
- Gueron S, Levit-Gurevich K (1999) Energetic considerations of ciliary beating and the advantage of metachronal coordination. *Proc Natl Acad Sci U S A* 96(22):12240–12245
- Guirao B, Joanny JF (2007) Spontaneous creation of macroscopic flow and metachronal waves in an array of cilia. *Biophys J* 92(6):1900–1917
- Guirao B, Meunier A, Mortaud S, Aguilar A, Corsi JM, Strehl L, Hirota Y, Desoeuvre A, Boutin C, Han YG, Mirzadeh Z, Cremer H, Montcouquiol M, Sawamoto K, Spassky N (2010) Coupling between hydrodynamic forces and planar cell polarity orients mammalian motile cilia. *Nat Cell Biol* 12(4):341–350
- Halbert SA, Becker DR, Szal SE (1989) Ovum transport in the rat oviductal ampulla in the absence of muscle contractility. *Biol Reprod* 40(6):1131–1136
- Harold J, Hoops IN, David LK (2005) Cytoplasmic bridges in volvox and its relatives. In: Baluska F, Volkmann D, Barlow PW (eds) *Cell-Cell channels*. *Eurekah.com*, Georgetown, p 1–20
- Heuser T, Raytchev M, Krell J, Porter ME, Nicastro D (2009) The dynein regulatory complex is the nexin link and a major regulatory node in cilia and flagella. *J Cell Biol* 187(6):921–933
- Heymann JB (2001) Bsoft: image and molecular processing in electron microscopy. *J Struct Biol* 133(2–3):156–169
- Hirokawa N, Tanaka Y, Okada Y, Takeda S (2006) Nodal flow and the generation of left-right asymmetry. *Cell* 125(1):33–45
- Hirota Y, Meunier A, Huang S, Shimozawa T, Yamada O, Kida YS, Inoue M, Ito T, Kato H, Sakaguchi M, Sunabori T, Nakaya MA, Nonaka S, Ogura T, Higuchi H, Okano H, Spassky N,

- Sawamoto K (2010) Planar polarity of multiciliated ependymal cells involves the anterior migration of basal bodies regulated by non-muscle myosin II. *Development* 137(18):3037–3046
- Hoops HJ, Witman GB (1983) Outer doublet heterogeneity reveals structural polarity related to beat direction in *Chlamydomonas* flagella. *J Cell Biol* 97(3):902–908
- Hornef N, Olbrich H, Horvath J, Zariwala MA, Fliegauf M, Loges NT, Wildhaber J, Noone PG, Kennedy M, Antonarakis SE, Blouin JL, Bartoloni L, Nusslein T, Ahrens P, Griese M, Kuhl H, Sudbrak R, Knowles MR, Reinhardt R, Omran H (2006) DNAH5 mutations are a common cause of primary ciliary dyskinesia with outer dynein arm defects. *Am J Respir Crit Care Med* 174(2):120–126
- Ikegami K, Sato S, Nakamura K, Ostrowski LE, Setou M (2010) Tubulin polyglutamylolation is essential for airway ciliary function through the regulation of beating asymmetry. *Proc Natl Acad Sci U S A* 107(23):10490–10495
- Ishikawa T, Hota M (2006) Interaction of two swimming Paramecia. *J Exp Biol* 209(Pt 22):4452–4463
- Ishikawa T, Sakakibara H, Oiwa K (2007) The architecture of outer dynein arms in situ. *J Mol Biol* 368(5):1249–1258
- Jonassen JA, San Agustin J, Follit JA, Pazour GJ (2008) Deletion of IFT20 in the mouse kidney causes misorientation of the mitotic spindle and cystic kidney disease. *J Cell Biol* 183(3):377–384
- Kagami O, Takada S, Kamiya R (1990) Microtubule translocation caused by three subspecies of inner-arm dynein from *Chlamydomonas flagella*. *FEBS Lett* 264(2):179–182
- Kubo T, Yagi T, Kamiya R (2012) Tubulin polyglutamylolation regulates flagellar motility by controlling a specific inner-arm dynein that interacts with the dynein regulatory complex. *Cytoskeleton* 179(2):222–228
- Kuhn C 3rd, Engleman W (1978) The structure of the tips of mammalian respiratory cilia. *Cell Tissue Res* 186(3):491–498
- Kunimoto K, Yamazaki Y, Nishida T, Shinohara K, Ishikawa H, Hasegawa T, Okanoue T, Hamada H, Noda T, Tamura A, Tsukita S, Tsukita S (2012) Coordinated ciliary beating requires Odf2-mediated polarization of basal bodies via basal feet. *Cell* 148(1–2):189–200
- Lai SK, Wang YY, Wirtz D, Hanes J (2009) Micro- and macro-rheology of mucus. *Adv Drug Deliv Rev* 61(2):86–100
- Lechtreck KF, Sanderson MJ, Witman GB (2009) High-speed digital imaging of ependymal cilia in the murine brain. *Methods Cell Biol* 91:255–264
- Lucas AM, Douglas LC (1934) Principles underlying ciliary activity in the respiratory tract II. A comparison of nasal clearance in man, monkey and other mammals. *Arch Otolaryngol* 20(4):518–541
- MAST, SO (1907) Light reaction in lower organisms: II. *Volvox globator*. *J Comp Neurol Psychol* 17(2): 99–180
- Mastrorade DN (1997) Dual-axis tomography: an approach with alignment methods that preserve resolution. *J Struct Biol* 120(3):343–352
- Nicastro D, McIntosh JR, Baumeister W (2005) 3D structure of eukaryotic flagella in a quiescent state revealed by cryo-electron tomography. *Proc Natl Acad Sci U S A* 102(44):15889–15894
- Niedermayer T, Eckhardt B, Lenz P (2008) Synchronization, phase locking, and metachronal wave formation in ciliary chains. *Chaos* 18(3):037128
- Nigg EA, Raff JW (2009) Centrioles, centrosomes, and cilia in health and disease. *Cell* 139(4):663–678
- Nonaka S, Tanaka Y, Okada Y, Takeda S, Harada A, Kanai Y, Kido M, Hirokawa N (1998) Randomization of left-right asymmetry due to loss of nodal cilia generating leftward flow of extraembryonic fluid in mice lacking KIF3B motor protein. *Cell* 95(6):829–837
- Okada Y, Nonaka S, Tanaka Y, Saijoh Y, Hamada H, Hirokawa N (1999) Abnormal nodal flow precedes situs inversus in *iv* and *inv* mice. *Mol Cell* 4(4):459–468

- Olbrich H, Horvath J, Fekete A, Loges NT, Storm van's Gravesande K, Blum A, Hormann K, Omran H (2006) Axonemal localization of the dynein component DNAH5 is not altered in secondary ciliary dyskinesia. *Pediatr Res* 59(3): 418–422
- Pazour GJ, Agrin N, Walker BL, Witman GB (2006) Identification of predicted human outer dynein arm genes: candidates for primary ciliary dyskinesia genes. *J Med Genet* 43(1):62–73
- Pazour GJ, Dickert BL, Vucica Y, Seeley ES, Rosenbaum JL, Witman GB, Cole DG (2000) *Chlamydomonas* IFT88 and its mouse homologue, polycystic kidney disease gene *tg737*, are required for assembly of cilia and flagella. *J Cell Biol* 151(3):709–718
- Pettersen EF, Goddard TD, Huang CC, Couch GS, Greenblatt DM, Meng EC, Ferrin TE (2004) UCSF Chimera—a visualization system for exploratory research and analysis. *J Comput Chem* 25(13):1605–1612
- Ringo DL (1967) Flagellar motion and fine structure of the flagellar apparatus in *Chlamydomonas*. *J Cell Biol* 33(3):543–571
- Ruffer U, Nultsch W (1985) High-speed cinematographic analysis of the movement of *Chlamydomonas*. *Cell Motil Cytoskelet* 5(3):251–263
- Sanderson MJ, Sleigh MA (1981) Ciliary activity of cultured rabbit tracheal epithelium: beat pattern and metachrony. *J Cell Sci* 47:331–347
- Sawamoto K, Wichterle H, Gonzalez-Perez O, Cholfin JA, Yamada M, Spassky N, Murcia NS, Garcia-Verdugo JM, Marin O, Rubenstein JL, Tessier-Lavigne M, Okano H, Alvarez-Buylla A (2006) New neurons follow the flow of cerebrospinal fluid in the adult brain. *Science* 311(5761):629–632
- Sugino K, Naitoh Y (1982) Simulated cross-bridge patterns corresponding to ciliary beating in *Paramecium*. *Nature* 295(5850):609–611
- Ueki N, Matsunaga S, Inouye I, Hallmann A (2010) How 5000 independent rowers coordinate their strokes in order to row into the sunlight: phototaxis in the multicellular green alga *Volvox*. *BMC Biol* 8:103
- Ueno H, Ishikawa T, Bui KH, Gonda K, Ishikawa T, Yamaguchi T (2012) Mouse respiratory cilia with the asymmetric axonemal structure on sparsely distributed ciliary cells can generate overall directional flow. *Nanomedicine* 8(7):1081–1087
- Vilfan A, Julicher F (2006) Hydrodynamic flow patterns and synchronization of beating cilia. *Phys Rev Lett* 96(5):058102
- Wloga D, Frankel J (2012) From molecules to morphology: cellular organization of *Tetrahymena thermophila*. *Methods Cell Biol* 109:83–140
- Yagi T (2009) Bioinformatic approaches to dynein heavy chain classification. *Methods Cell Biol* 92:1–9

Index

A

Active Contours, 140, 142
Advection equation, 50, 64
Advective, 197, 216, 217
Aggregability, 76, 97
Aneurysms, 1, 167
Area dilation modulus, 62, 101, 102, 106–108, 110
Arterial branches, 2
Arterial fluid mechanics, 43
Arterial hemodynamics, 2, 3, 9, 19
Arterial homeostasis, 1
Articular chondrocytes, 173
Automatic, 121, 124, 125, 128
Axial migration, 76

B

Bending model, 67
Best fit circles, 141, 144
Bifurcations, 121, 123
Binarization, 121, 128
Bioavailability, 95–97
Biofluid mechanics, 175
Biofluids, 175
Biologically complex flow, 219
Biomechanics, 5
Biomicrofluidics, 122
Biotransport, 91
Blood cells, 183
Blood flow, 1, 2, 3, 7, 10, 12, 15, 18, 26, 90, 92, 93, 95, 120, 121, 154, 167, 169–171, 188
Blood vessels, 166–168, 173
Bone cells, 173
Boundary element method, 63, 101, 103, 112
Bulk flow, 3, 7–11, 14, 18

C

Cancer cells, 182
Capsule, 101–103, 112–114
Cardiovascular diseases, 2
Cardiovascular flows, 2, 17
Carotid artery, 13, 14, 19
Cell alignment, 173
Cell deformation, 141
Cell-deplete layer, 76
Cell differentiation, 165
Cell-free layer (CFL), 76–79, 91, 97, 121, 127, 183, 185–188, 190, 194, 195
Cell migration, 167, 169, 171
Cell proliferation, 169–171
Cells, 168, 169, 171–175
Cell surface, 219
Cellular flow, 173, 175
Cellular mechanics, 175
Cellular ultrastructure, 219
Cerebral aneurysms, 25–27, 42
Cerebral artery, 27
Cilia, 197–200, 205, 207, 209–217, 219, 220, 222, 224, 225, 228–232
Cilia bed, 199, 200, 207, 209, 212–215
Cilia bending stiffness, 199, 212
Cilia-fluid interactions, 197
Ciliary flow, 206, 232
Ciliary motion, 219–222, 224–229, 231, 232
Cilia stiffness, 197, 212–214, 217
Cilia stroke, 197
Complex flow, 219
Computational biofluid mechanics, 26
Computational biomechanics, 89
Computational blood flow, 10
Computational fluid dynamics, 14
Computational model, 14
Computational simulation, 96, 97

- Confluences, 122, 123
 Continuum constitutive law, 101, 102, 106, 107
 Contractions, 121, 153
 Contrast enhancement, 134, 135, 138, 139, 141, 144
 Cryoelectron tomography, 219, 225, 229, 230, 232
 Cytokine secretion, 165
- D**
- Deformability, 92, 97, 120–122, 133, 134, 152, 157
 Deformability degree, 157
 Deformation gradient tensor, 50
 Deformation index, 154, 156, 157, 159
 Deformation of cells, 152
 Deviatoric stress, 53, 54
 Diagnosis, 130
 Diffusion, 91, 93–98
 Diffusion barrier, 77
 Diffusive, 197, 215–217
 Diffusivity, 146
 Diffusivity coefficients, 146
 Dirac delta function, 66
- E**
- Edge detection, 82, 83
 Endothelium, 91–94, 96–98
 Enzyme NO synthase, 90
 Epithelial Cells, 166, 172–175
 Eukaryotic cells, 219
 Eulerian frame, 61, 70
 Evans-Skalak model, 67
 Expansions, 158, 159
 Extensional flows, 153, 154, 157, 159
 Extensional stress, 152
 Extracellular matrix, 173, 174
- F**
- Fåhræus-Lindqvist effect, 95
 Fibroblasts, 170, 171, 173
 Fifth-order WENO method, 65
 Filtering methods, 146
 Finite element method, 103, 112
 Flow-induced deformation, 103
 Flow rates, 185, 186, 190, 126, 127
 Flow resistance, 77
 Flow visualization, 13
 Fluid-membrane coupling, 48, 60
 Fluid propulsion, 197, 198, 205
 Fluid-structure interaction, 102
- Fluid-structure interaction modeling, 25
 Fluid transport, 197
 Fluorescent particles, 219, 226
 FSI computations, 25–27, 33, 36, 38, 43
- G**
- Gas transport, 92, 95, 96–98
 Glass capillaries, 121, 152
 Grayscale image, 80, 82
- H**
- Hematocrit, 92, 95, 97, 120, 121, 126, 127, 128, 185, 195
 Hemodynamics, 2, 4, 7, 9, 11, 14, 18, 92, 98
 High molecular weight dextran, 84
 Histogram, 79–82
 Hough transform, 140–142, 144
 Human blood, 154
 Hyperbolic contraction, 155
 Hyperbolic microchannel, 151
 Hyperbolic shape, 154, 155
 Hyperelastic material, 49, 50, 54, 56, 106
 Hyper-elastic material, 106
 Hyperthermia, 182, 195
- I**
- Image analysis, 121, 122, 124, 152, 192
 Image Filtering, 135
 Image processing, 133, 134, 144, 219, 230
 Image segmentation, 79, 80, 82, 84, 148
 Immersed boundary method, 197, 198, 200, 217
 In silico, 2, 7, 14, 19
 Intercellular membranes, 175
 Interstitial fluid flow, 165
 Intravital microscope, 78
 In vivo, 2, 3, 10, 12, 14–19
 Iron oxide, 181, 183, 184, 194
- L**
- Lagrangian frame, 49
 Laminar Flow, 167, 168
 Large elastic deformation, 103
 Left Cauchy-Green deformation tensor, 47, 49, 61, 66, 70, 50, 55
 Low aspect ratio, 154
 Lubricating role, 77
 Lymphatic vessels, 165

M

Macromolecules, 219
 Magnetic fields, 181, 183, 185, 190
 Magnetic nanoparticles, 182, 183, 188, 190, 195
 Manual, 121, 124, 128
 Material phase, 47, 49, 50, 61
 Medical imaging, 14
 Membrane mechanics, 104
 Mesh generation, 25, 27, 30, 31
 Metachronal waves, 197–200, 209, 212, 217
 Michaelis-Menten kinetics, 90, 94
 Microchannel, 121, 122, 124, 181, 185
 Microcirculation, 76, 78, 79, 92, 98, 120, 121, 133, 152, 183
 Microfabrication, 152
 Microgeometries, 119
 Microhemodynamics, 77
 Microscale propulsion, 152
 Microvessel, 92, 93, 95, 98, 120, 121
 Minimum thresholding algorithm, 81
 Mixture representation, 51, 53
 Mixture stress, 53
 Modeling of a biological cell, 102
 Modified left Cauchy-Green deformation tensor, 54, 55, 65
 Mooney-Rivlin model, 53, 54, 56
 Magnetic resonance imaging (MRI), 10, 12, 15, 17, 18, 19
 MTHINC method, 64, 66
 Multi-ciliated swimmer, 200
 Multi-flagellated swimmers, 200

N

Nanoparticle, 181, 184–188, 190, 192, 194, 195
 Neo-Hookean model, 54, 62, 66, 67
 Newtonian fluid, 61, 67
 Nitric oxide, 77, 90, 94
 Numerical method, 197, 200
 Numerical simulation, 68, 107, 114, 199

O

Organelles, 219, 220
 Oscillatory shear index, 25, 27, 29
 Otsu's thresholding algorithm, 81
 Oxygen, 90

P

Parallel computing, 197
 Paramecium, 199, 200, 212, 215

Particle image velocimetry (PIV), 219
 Particle-in cell approach, 66
 Particles, 181–184, 187, 190, 192
 Particle tracking velocimetry (PTV), 219
 Patientspecific cerebral aneurysm model, 25, 27, 40
 Photorelease, 197, 212, 217
 μ -PIV/PTV method, 219
 Plasma layer, 181, 183
 Platelet, 4, 9, 47, 67–70, 134, 154
 Poisson ratio, 101, 102, 106, 107, 108, 109, 110
 Polydimethylsiloxane, 121, 134, 155
 Probability, 81, 82

Q

Quasi-implicit formulation, 65

R

RBC tracking, 133
 Reaction, 90, 91, 93
 Red blood cell (RBC), 47, 67, 75, 76, 91, 102, 120, 133, 134, 146, 147, 151, 152, 154, 183, 185, 187, 188, 190, 192
 Red blood cell aggregation, 188
 Respiratory epithelium, 197
 Respiratory processes, 217
 Reversibility, 56–58, 70

S

Saint Venant-Kirchhoff material, 54, 56
 Scavenging rate, 94–97
 Segmentation methods, 146, 147
 Segmenting RBCs, 141
 Semi-automatic, 152
 Shear elastic modulus, 101, 102, 106, 107, 108
 Shear flow, 101, 103, 107, 112–114, 152, 154, 159
 Shear stress, 152, 166–175
 Simplified MAC method, 55
 Smooth muscle cells, 170
 Softlithography, 122
 Solvothermal process, 183
 Solvothermal synthesis, 181, 183
 Spring network model, 101, 102, 107–111
 Steady-state, 96
 Stokes flow, 101
 Superparamagnetic particles, 182
 Surface gradient operator, 61
 Surface Jacobian, 61

Surface left Cauchy-Green deformation tensor, 61, 70
Surface projection tensor, 61
Surface singular force, 62
Suspension flow, 47, 49, 66, 67
Synthesis, 183, 184

T

Tank-treading motion, 76
Three-dimensional simulations, 197
Thresholding, 79–83
Time-dependent, 96, 97
Tissues, 166, 167, 173
Tracking RBCs, 140, 146

U

Upper-convected time derivative (Oldroyd derivative), 50
Upstream-downstream, 125–127

V

Vascular cells, 165, 175
Vascular diseases, 2
Vascular endothelial cells, 166
Vascular wall pathologies, 3
Viscous flow, 103
VOF (volume-fraction/volume-of-fluid)
 function, 49, 50, 61, 64–66
Volvox, 199, 200
Voxel data, 199, 200

W

Wall shear stress, 3, 4, 8, 25, 27, 28, 77, 90, 92, 94, 96–98

Y

Young modulus, 101, 102, 106, 108–110